

PHOTON SCIENCE 2024.

Highlights and Annual Report

Deutsches Elektronen-Synchrotron DESY
A Research Centre of the Helmholtz Association



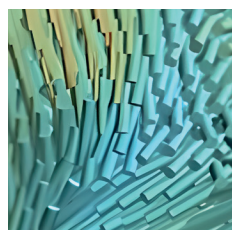


PHOTON SCIENCE 2024.

Highlights and Annual Report

Cover

The cover picture shows the three-dimensional orientation distribution of the collagen fibres in the breast cancer specimen. Recent advances in X-ray imaging technologies, such as small-angle X-ray scattering tensor tomography (SAXS-TT) and X-ray fluorescence computed tomography (XRF-CT), provide new and effective methods for exploring collagen structures and metal distribution in tumours in three dimensions. SAXS-TT provides further insights by visualising nanoscale collagen structures, deepening our understanding of their role in tumour progression (details see page 36).



(Based on original data measured at the PETRA III beamline P62)



Contents

> Introduction	4
> News and Events	8
> Science Highlights	16
• Nano and materials science	18
• Energy conversion and sustainability	28
• Health and life science	34
• Atomic and molecular science	46
• Quantum materials and magnetism	58
• Earth and environment	68
• Laser and X-ray sources – methods and developments	72
> Light Sources and User Infrastructures	88
> Campus and Cooperations	110
> Facts and Numbers	120

Publications

The list of publications based on work done at DESY Photon Science is accessible online:

http://photon-science.desy.de/research/publications/list_of_publications/index_eng.html

DESY tries to keep this list complete and up-to-date and relies on the support by all users who are kindly requested to register their publications in our database (login via door.desy.de).

The year 2024 at DESY

Chairman's foreword

Dear Colleagues and Friends of DESY,

In a time of significant challenges—financial constraints, geopolitical instabilities, and heightened international competition—DESY faces a demanding landscape. Rising personnel costs, volatile energy prices, and inflation-driven reductions in purchasing power puts us under considerable pressure and the priority is to lead DESY safely into the future.

At the heart of our strategy stands the ambitious PETRA IV upgrade project. The conversion of PETRA III into a state-of-the-art 4th generation X-ray light source is essential not only for DESY's advancement but also for strengthening international research and securing Germany's technological sovereignty. As the world's most advanced and brilliant X-ray source, PETRA IV will enable unprecedented precision

in studying materials and biological macromolecules, paving the way for pioneering innovations like AI-driven material design.

The DESY infrastructure focus also includes transformative projects. The new DESYUM visitor centre, whose construction is progressing according to plan, will soon be a public landmark and could become the iconic symbol of the Bahrenfeld campus. Through CAST, our Center for Accelerator Science and Technology, and the innovation hub, DESY Innovation Factory, the integrated technology and start-up centre, we are expanding the 'Bahrenfeld ecosystem' by linking research and innovation to drive technology and economic development.



Celebrating 60 years of research with synchrotron light at DESY: Robert Feidenhans'l, Poul Nissen, Edgar Weckert, Saša Bajt, Massimo Altarelli, Jerome Hastings, Jochen Schneider, Tetsuya Ishikawa, Laurent Chapon, Francesco Sette, Harald Reichert, Rolf Heuer, Helmut Dosch (from left to right). (Credit: DESY)



Visualisation of the DESY Center for Accelerator Science and Technology (CAST), close to the PETRA III experimental hall 'Max von Laue' (right). (Credit: pbr/nh studio)



The Science Data Management Centre building for the Cherenkov Telescope Array Observatory on the DESY campus in Zeuthen. (Photo: DESY / Susann Niedworok)

This is my last foreword for an annual report as the chairman of the DESY Board of Directors and I would like to take this opportunity to make a few personal remarks: It has been an honour to serve in this role. I would like to thank all DESY employees and national and international partners for their trust over the past 15 years and especially to the board members for their unique team spirit and constructive cooperation. Together, we achieved numerous successes, including the remarkable construction of the European XFEL from 2009 to 2017, a masterpiece 'made by DESY', establishing the astroparticle physics division, strategically expanding nanoscience and laser-plasma research and the successful operation of PETRA III, FLASH, and European XFEL as Hamburg's flagship photon sources. We are not only continuing a long tradition: Since the commissioning of the first particle accelerator in 1964, DESY has been one of the pioneers of research with synchrotron radiation worldwide.

I reflect with pride on the growth of the two DESY sites in Hamburg and Zeuthen together with our partners. The new interdisciplinary research centres—CFEL, CSSB, CXNS for Photon Science and the recently opened Science Data Management Centre (SDMC) for Astroparticle Physics as well as the ongoing projects mentioned above and the planned Wolfgang Pauli Centre for theoretical physics (WPC) and Centre for Molecular Water Science (CMWS)—are visionary initiatives that will contribute to strengthen Germany's research landscape as a whole and innovation regions of Hamburg and Zeuthen in particular.

A highlight of my time at DESY has been the recruitment of renowned scientists. With the appointment of over 30 W3 professorships, including 15 women and close collaborations with universities in Hamburg, Schleswig-Holstein,

Berlin, Brandenburg and beyond, we have enhanced our scientific network and supported our university partners' excellence. Of particular note are the new members on the DESY Board in 2025: Beate Heinemann, Wim Leemans, Britta Redlich, Christian Stegmann and Arik Willner, bringing science, innovation and technology transfer expertise. With this exceptional team, DESY is well-equipped to master future challenges.

When I hand over the helm to Beate Heinemann in spring 2025, I do so in a turbulent time not only for DESY. Research and social issues can no longer be addressed only on the national level. Sharing expertise and infrastructures and thereby strengthening international cooperations is becoming more important: Innovation is the key for our future. Therefore, the pending political decision for PETRA IV is crucial for DESY and our national and international partners and users, and I hope for swift action in the next period.

I extend my best wishes to all DESY staff, hoping you will continue leading this remarkable research centre into a bright future. Thank you all and also our partners for constant support and excellent cooperation over the years. I wish DESY continued success and that essential extra bit of luck.

*Yours
Helmut Dosch*

Helmut Dosch
Chairman of the DESY Board of Directors

Photon Science at DESY

Introduction

Dear Colleagues and Friends of DESY Photon Science,

It is with great pride and enthusiasm that we present the DESY Photon Science Report 2024, a reflection of the groundbreaking advancements, collaborative efforts and transformative research facilitated by DESY's photon science facilities and inhouse research over the past year despite severe budgetary constraints.

2024 was a special year for DESY Photon Science. We celebrated '60 years of Research with Synchrotron Radiation at DESY' in August. First measurements with synchrotron radiation were carried out as early as 1964, soon after the commissioning of the synchrotron 'DESY'. What began with a small number of scientists at DESY has now developed into an important field of research. This rapid growth was also reflected through the strong interest in the 'International Conference on Synchrotron Radiation Instrumentation' (SRI), which took place from 24–30 August 2024. More than 1200 experts from around the world met in the Hamburg Congress Center with an accompanying industrial exhibition to exchange their latest research results, new developments in instrumentation and also for networking of the leading researchers in this field.

Luckily, some of the budgetary constraints of 2023 caused by the high energy and gas prices lessened in 2024. Experiments using Helium were no longer hampered, thanks also to our effort to improve on closed-cycle cooling devices wherever possible. Still, we have to tackle the high inflation-related cost increases that are far higher than the annual increase in funding. This negatively impacts our services that we can provide and what we can achieve in science and technology. In that context, the expansion of the India@DESY collaboration for an additional term of two years, where India supports the operation of 1.5 beamlines at DESY, is very significant.

Due to the delay of the PETRA IV upgrade project by several years, DESY is confronted with an outdated PETRA III infrastructure: In June one of the damping wiggler absorbers in the PETRA III accelerator failed resulting in a loss of beam for two weeks. At the end of October, a fire in the injector complex DESY II due to failing power supplies brought the accelerator down for an additional month. Comprehensive cleaning of all electronic equipment near the fire hazard from fire extinguisher residue was neces-

sary. We thank colleagues from different divisions at DESY for the excellent organisation of the machine repair, clean-up and flawless restart of the machine within only a few hours after repair. To lessen the impact of loss in beamtime for our users, additional test time was dedicated to user operation from 19–23 December 2024.

Despite these significant accelerator problems, user operation at our photon science facilities has been very successful in 2024. At PETRA III about 4200 hours user run could be offered to the community with an availability of almost 90%. In total, more than 3400 individual users, including mail-in and remote access, were registered at PETRA III.

Research capabilities at PETRA III are further expanded. The HIKA instrument operated by KIT at beamline P23 for hierarchical X-ray imaging utilizes a dedicated instrumentation for X-ray tomography and laminography and will also offer a Bragg-Magnifier for an enlarged field of view. The construction of the envisaged beamline P25 dedicated to instrument development and industrial applications made further progress. The beamline will offer fluorescence imaging and fully automated high-resolution powder diffraction. The experimental hutch is expected to receive first beam in the second half of next year. The last free PETRA III beamline, P63, will be dedicated to catalysis and is built and operated with partners from Fritz-Haber Institut Berlin and Institute for Chemical Energy Conversion Mülheim (both Max-Planck-Society). The corresponding design was finalised and calls for tender were published.

PETRA IV, DESY's main future facility project, took up speed. The PETRA IV pre-project, approved by the federal budget committee end of 2023, is committed to prepare DESY and its campus for this project. The particular challenge of the large civil engineering project is to execute all constructions on time and on budget. Another good news is that the German Federal Ministry of Education and Research (BMBF) started its 'roadmap process' for large research infrastructures to which the PETRA IV team submitted an exceptionally strong proposal addressing the scientific, innovation and societal impact of PETRA IV. The prioritisation of projects by the ministry is projected to be completed by June 2025. During 2024, work continued towards an engineering design report with more detailed planning of the accelerator complex, the civil engineering tasks, beamlines and experimental stations. We hope



Signing of the cooperation agreement 'India@DESY' in New Delhi in October 2024. Front (from left): Eswaramoorthy Muthusamy, Dean of the Jawaharlal Nehru Centre for Advanced Scientific Research (JNCASR); Franz Kärtner, Interim Director DESY Photon Science. Background, middle (from left): Jitendra Singh, Indian Minister for Science and Technology; Bettina Stark-Watzinger, German Federal Minister for Education and Research. (Credit: DESY)

that the new German Bundestag forming in spring 2025 will follow the roadmap process with the PETRA IV project hopefully at the top of the short list. A final decision on project funding is expected for the following year.

User operation at FLASH continued until 9 June 2024, with the last month being used for a standardised access mode, a novelty in FEL operation. Here, grouping of experiments using the same accelerator and similar pump-probe laser settings for a given set of experiments allowed executing the experiments at higher speed without the usual tuning time in between. This access mode showed that roughly twice as many FEL experiments can be executed when compared to the usual access scheme, which is very promising for the future. The current second part of the FLASH upgrade will be completed by August 2025. By then, the old fixed gap undulators at FLASH1 will be replaced by APPLE-III undulators, tuneable in photon energy as well as in polarisation. In addition, external seeding will be implemented at FLASH1, which will lead to significantly higher spectral and temporal stability compared to the self-amplified spontaneous emission (SASE) FEL operation mode, thus enabling spectroscopic methods at the FEL that were previously, if at all, only possible with low temporal or spectral resolution.

DESY scientists continue to carry out very successful experiments at the European XFEL, especially within the large user consortia SFX, HIBEF and hRIXS with major DESY contributions. DESY's activities at XFEL will continuously

increase especially with the advent of attosecond pulse generation at the European XFEL.

Also, the Centre for Molecular Water Science (CMWS), dedicated to study peculiar properties of water from fundamental properties to possible applications in science and technology, achieved an additional milestone. A total of 47 partners from Germany and Europe signed the CMWS founding declaration and a first general assembly meeting was held online in October. The inauguration of the CMWS is planned for February 2025 during the annual 'Water Days'.

I would like to close by thanking all DESY staff, in particular all people at Photon Science, our advisory and funding bodies and user community for their dedication and continuous support to keep the user operation at our facilities running and to carry out excellent research during these challenging times. On a personal note, it was a real pleasure to serve as interim director to this exceptionally talented and committed to excellence DESY Photon Science division for a year, and to welcome the new director Professor Britta Redlich, who will take over in January 2025.

Franz X. Kärtner

Franz X. Kärtner
Interim Director DESY Photon Science



News and Events

News and Events

A busy year 2024

January

12 January: Nobel Laureate Anne L'Huillier visits DESY

Anne L'Huillier, a physicist from Lund University and 2023 Nobel Laureate in Physics, visited DESY. She shared the Nobel Prize with two colleagues for their groundbreaking work on experimental methods that generate attosecond pulses of light, enabling the study of electron dynamics in matter. During her visit, she toured DESY and the Center for Free-Electron Laser Science (CFEL), at the invitation of Francesca Calegari, lead scientist at

DESY and professor at the University of Hamburg, who is also conducting pioneering research in attosecond physics. Attosecond physics explores the behaviour of matter on the timescale of electrons—extremely brief intervals around a ten-millionth of a billionth of a second. L'Huillier and her colleagues discovered an extremely nonlinear optical process that allowed them to overcome the femtosecond 'barrier' and access the attosecond domain.



16 January: Holger Sondermann appointed new Scientific Director of CSSB

DESY lead scientist Holger Sondermann has become the new Scientific Director of the Centre for Structural Systems Biology (CSSB) for two years.



The CSSB is one of the campus' core cooperative institutes involving DESY and eight other universities and research centres. On 1 December 2023, the CSSB Council confirmed the CSSB directorate's nomination of Sondermann. Sondermann joined CSSB in 2020 from Cornell University in the US. As head of the 'Molecular and Structural Microbiology' research group at CSSB, Sondermann investigates the molecular mechanisms of how biofilms develop and how they could be eliminated.

24 January: Users' Meeting 2024 under the 'Kuppel Hamburg'

This year, DESY and European XFEL Users' Meetings busted out of its usual auditorium setting and instead made their way to the huge tents of the 'Kuppel Hamburg' across the street from DESY. More than 1100 participants from around 210 different institutions registered for the Users' Meeting at this special event venue. The Users' Meeting 'Research with Synchrotron Radiation and FELs', offered over three days of presentations on the current status and plans for the European XFEL and DESY's light sources PETRA III and FLASH, as well as talks and 340 posters on research highlights and developments. The two poster sessions were accompanied by a vendor exhibition with more than 50 exhibitors. In addition, 20 satellite workshops took place at DESY and at the European XFEL.



24 January: 'DESY Photon Science User Award' for exceptional achievements goes to Heshmat Noei

On the occasion of the DESY Photon Science Users' Meeting 2024, Heshmat Noei was honoured with the first 'DESY Photon Science User Award'. This award is given to a user or group of users of FLASH and/or PETRA III and acknowledges singular and exceptional contributions to the general advancement of science using DESY's large-scale photon science facilities. Heshmat Noei is the scientist responsible for the surface spectroscopy at the DESY NanoLab at the Centre for X-ray and Nano Science (CXNS). She was selected for the DESY Photon Science User Award 2024 for 'her innovative and pioneering developments in the field of synchrotron- and FEL-based X-ray techniques; in particular in the field of ultrafast, time-resolved femtosecond photoelectron spectroscopy for the study of photocatalysts in action, thus bridging the gap between fundamental knowledge of catalysts and their application'.



February

18 February: CFEL group leader Beata Ziaja-Motyka awarded honour by Polish science ministry

Beata Ziaja-Motyka, group leader at the Center for Free-Electron Laser Science (CFEL) at DESY and professor



at the Henryk Niewodniczański Institute of Nuclear Physics of the Polish Academy of Sciences in Krakow, received the prestigious award of the Polish Ministry of Science and Higher Education. The award ceremony took place at the annual Polish Science Gala on 18 February 2024, where Ziaja-Motyka was honoured for her scientific achievements in recent years. The award recognises her pioneering work in the field of femtosecond physics and the study of materials under intense irradiation with pulses from X-ray free-electron lasers, e.g. the European XFEL.

29 February: Focus on molecular water science – CMWS Water DAYS 2024

The CMWS Water DAYS 2024 took place at DESY in Hamburg from 26–28 February as the 7th general CMWS meeting. More than 80 participants discussed the key challenges in molecular water research and the status and future of the Centre for

Molecular Water Science (CMWS). The CMWS initiative brings together key experts to advance the understanding of the fundamental questions about molecular processes in water and at water interfaces systematically.



April

18 April DESY researcher Robin Santra elected as AAAS Fellow

Robin Santra, lead scientist at DESY, professor of physics at the University of Hamburg and expert in ultrafast processes in intense radiation fields, received one of the highest scientific honours in the US: He was elected an AAAS Fellow. The 'Class of 2023', announced on 18 April, is made up of a total of 502 high-ranking scientists from disciplines such as biology, chemistry, medicine and physics. The AAAS—American Association for the Advancement of Science—is the largest scientific community in the world and publisher of the journal *Science* as well as other journals in the *Science* family. Robin Santra, who heads the theory group at the Center for Free-Electron Laser Science CFEL, investigates how to better understand microscopic processes in the interaction of X-rays with matter to further improve modern radiation sources' use. He was honoured for 'seminal contributions to the field of computational and theoretical physics by developing theoretical tools for modelling and predictions in X-ray free-electron-laser science and in attosecond science'.



June

1 June Science City Day: Welcome to DESY!

Research for everyone: On 1 June, DESY opened the doors to the future. As part of the 'Science City Day', the research centre invited people to the big open day on the campus in Bahrenfeld—finally again after seven years. During the day, DESY opened its huge experimental halls and presented science with more than 100 activities and lectures. DESY is located in the heart of Hamburg's future pro-



ject Science City Hamburg Bahrenfeld. By the 2040s, this new district will be created here in which research, work and life will take place.

20 June Jackson Barp wins Student Award at the IEEE Photovoltaic Specialists Conference 2024

Jackson Luis Barp Junior, a PhD student of the 'X-Ray Nanoscience and X-Ray Optics' group at DESY and University of Hamburg, won the highly coveted award for the best student paper in the area 'Characterization Methods' of the IEEE Photovoltaic Specialists Conference (IEEE PVSC) that took place in June 2024 in Seattle (Washington, USA). The topic of his award-winning presentation was 'Assessing the local charge-carrier kinetics in buried structures through time-resolved X-ray beam-induced voltage measurements'.



July

1 July DESY researcher Simone Techert has been elected as Fellow of the Royal Society

Simone Techert has been named a Fellow of the Royal Society of Chemistry, a professional society based in the United Kingdom with over 50000 members worldwide. Each year, the Fellows of the Royal Society elect up to 85 new Fellows. The designation of Fellow of the Royal Society of Chemistry is given to scientists who have made 'a substantial contribution to the improvement of natural knowledge, including mathematics, engineering science and medical science'. Simone Techert is a lead scientist in the group 'Chemical Structural Dynamics' at DESY and a professor for ultra-short pulsed X-ray physics at the University of Göttingen within the network of the 'Göttingen Research Campus'. She develops methods for time-resolved X-ray experiments and their applications and optimisation for analysis of chemical molecular processes and of structural dynamics and relations in chemical reactions.

18 July Andrea Trabattoni becomes a professor at Leibniz University Hanover

DESY and CFEL scientist Andrea Trabattoni accepted an appointment as Associate Professor in Ultrafast Photoelectron Science at Leibniz University Hanover (LUH). Working as a researcher at DESY since 2016 and as a junior professor at LUH since 2022, Trabattoni was recently awarded an ERC starting grant to develop novel laser-based

imaging tools for large molecules and interfaces with unprecedented spatiotemporal resolution. He will continue to divide his time between Hanover and Hamburg. In his research, Trabattoni investigates the photo-induced electron dynamics in matter with particular emphasis on atoms, molecules and nanosystems.



19 July Start of the DESY Summer School and DESY-Ukraine Summer School

Like every summer, the summer students came to DESY as well in 2024. This year, a total of 112 participants from 27 countries conducted research for seven weeks on the Hamburg and

Zeuthen campuses. Particularly interesting this summer was that the DESY-Ukraine Summer School took place in parallel for the first time, with 14 participants coming from Ukraine.



22 July Otto Haxel Dissertation Prize for Kaja Schubert



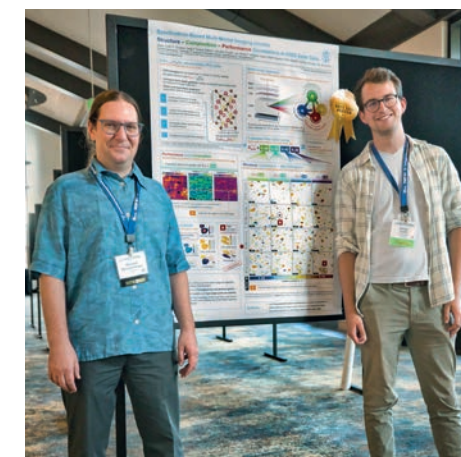
For her dissertation, the DESY physicist Kaja Schubert was awarded the Otto Haxel Dissertation Prize 2021 (Rank 3). Kaja completed her doctoral thesis with the title 'The electronic

structure and deexcitation pathways of biomolecular ions' in Sadia Bari's former Helmholtz Young Investigators group and now DESY Photon Science group for 'Biomolecules in the Gas Phase' and at the University of Göttingen under supervision of Simone Techert. The prestigious Otto Haxel Dissertation Prize is awarded annually by the KIT Freundeskreis und Fördergesellschaft e.V. together with the German Physical Society to the three best dissertations in physics at the Universities of Göttingen and Heidelberg and at the KIT, where the German physicist Otto Haxel (1909–1998) worked.

August

21 August Niklas Pyrlik wins 'Best XRD Poster Award' at the Denver X-ray Conference 2024

Niklas Pyrlik, a master's student of the 'X-Ray Nanoscience and X-Ray Optics' group at DESY and the University of Hamburg, has been honoured with the 'Best XRD Poster Award' award at the Denver X-ray Conference which took place in Colorado (USA) from 5–9 August 2024. The title of his award-winning poster presentation was 'Synchrotron-Based Multi-Modal Imaging Unveils Structure–Composition–Performance Correlations in CIGS Solar Cells'.



August

26 August SRI 2024: Top elite in X-ray light research meets in Hamburg

From 26 to 30 August 2024, the DESY and European XFEL welcomed more than 1200 experts from 34 countries and 210 institutions from all over the world to the 15. International Conference on Instrumentation of Synchrotron Radiation Sources (SRI) at the CCH Congress Centre in Hamburg. The conference is regarded as the world's most important exchange forum for the further development of large X-ray radiation sources such as the

European XFEL in Schenefeld near Hamburg or DESY's light sources in Hamburg-Bahrenfeld. The first conference was organised in Hamburg in 1982 and has since been held every three years at different locations around the world. The attendance of the conference was remarkable: There were 541 registered posters and 273 talks with 37 micro symposia sessions, 3 keynote talks, 11 plenary talks, 111 invited talks and 148 contributed talks.



26 August 60 years of research with synchrotron radiation at DESY

The anniversary '60 years of research with synchrotron radiation at DESY' was celebrated with a festive colloquium on 26 August 2024. Around 300 former companions came to Hamburg to mark the occasion. After commissioning its first particle accelerator 'DESY' in 1964, it has been one of the world's pioneers of research with synchrotron light. Since then, DESY's light sources have been used to conduct high-calibre research which was even

awarded a Nobel Prize in 2009. DESY's expertise also created a completely new type of large-scale research facilities: free-electron lasers that can record chemical reactions in real time.



October

24 October DESY strengthens cooperation with Indian partners at PETRA III



DESY and numerous Indian research institutes want to work more closely together in the future. To this end, representatives of these institutes have made an agreement during a delegation visit of the German federal government to New Delhi (India). In the context of the seventh German-Indian governmental consultations and celebration of 50 years of Indian-German scientific collaboration, a continuation of an earlier collaboration agreement was signed in the presence of the Federal Minister for Education and Research, Bettina Stark-Watzinger, and her Indian counterpart, Jitendra Singh. The DESY delegation was led by the interim director of the Photon Science division Franz Kärtner.

28 October Access to attoseconds and more: DESY joins Lasers4EU network

The network Lasers4EU will now include five laser setups at DESY dedicated to ultrafast science. The setups are based on tabletop lasers that either are pulsed to access the attosecond timescale, which is a billionth of a billionth of a second, or that generate secondary radiation that can attain ultrashort processes or lasers that can emit several different frequencies simultaneously. DESY joins over two dozen other organisations that are part of Lasers4EU, including several Helmholtz research centres. Lasers4EU is a European Union-funded network that supports scientists wanting to do research at laser lab setups in Europe. The network aims to provide coordinated and transnational access for users to 27 different laser installations, structure the European landscape of laser research and increase human resources in regions where laser technologies are not as prominent.

November

5 November ERC Synergy Grant for Thomas Marlovits

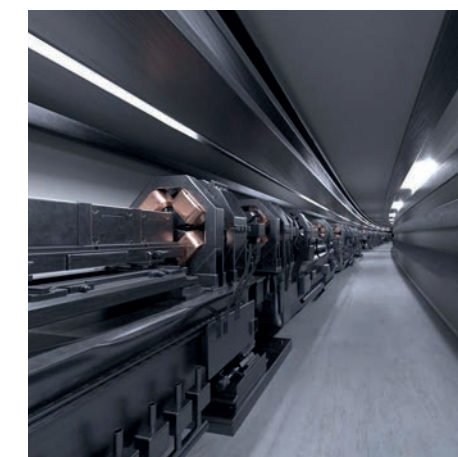
The scientist Thomas Marlovits from DESY, CSSB and University Medical Center Hamburg-Eppendorf (UKE), together with three other researchers, Edith Houben from Vrije Universiteit in Amsterdam, Tracy Palmer from Newcastle University and John McKinney from EPFL Lausanne, received an ERC Synergy Grant for their project 'CombaT7', for which they will receive funding of 10.8 million Euro to be used over six years. The project aims to provide a deep mechanistic understanding of the diverse roles of mycobacterial T7SSs and to develop insights into how exploiting these systems may help combat infections.



8 November André L. C. Conceição received the Gold Poster Award at the SAS2024 conference

At the XIX International Small Angle Scattering Conference (SAS2024), DESY scientist André Conceição was honoured with the Gold Award for his outstanding poster presentation entitled 'Quantifying Myelin in Multiple Sclerosis by SAXS-CT'. The SAS2024 conference took place from 3–8 November 2024 in Taipei (Taiwan) and is one of the most important gatherings in the field. It is held every three years and highlights the latest advances by scientists from around the world.

15 November PETRA IV – moving forward towards funding



The German Federal Ministry of Education and Research (BMBF) has officially confirmed that the PETRA IV proposal is participating in the 'National Prioritization Procedure for Large-scale Research Infrastructures'. A team from DESY has prepared a short concept according to the BMBF's specifications and submitted it on 25 October 2024. The title: 'PETRA IV – the ultimate 4D X-ray microscope'. The evaluation of the submitted concepts by international teams of experts is now underway. The BMBF plans to publish a shortlist of the best projects in summer 2025. In addition to the expected gain in scientific knowledge, the evaluation will consider the innovation and transfer potential, the sustainability of the construction and operation as well as the costs and risks.



Dezember

4 December ERC Consolidator Grant for DESY physicist Christoph Heyl



Christoph Heyl, research group leader at DESY Photon Science and the Helmholtz Institute Jena, has been awarded a prestigious ERC Consolidator Grant, providing him with funding of 2 million Euro over five years for his research project 'Gas Phase Sonophotonics' GASONIC. With the highly competitive Consolidator Grants, the European Research Council (ERC) supports excellent scientists in further expanding and consolidating their innovative research and pursuing their most promising scientific ideas. Christoph Heyl leads the Ultrafast Photonics Research and Innovation group at DESY Photon Science. His work focusses on the development of ultrafast optical methods and technologies with applications, e.g. for ultrafast science, particle accelerators and industry.

Science Highlights

Nano and materials science	
> XFEL pulses drive the out-of-equilibrium dynamics of nanogels	18
> Ionic superdiscs form nanowires in nanopores	20
> Spinel-structured materials – durable and flexible	22
> Capturing the uncapturable in electron beam powder bed fusion	24
> Shaping matter's transparency with ultrashort X-rays	26
Energy conversion and sustainability	
> Linking surface structure and chemistry in electrocatalysis	28
> New insights into the Haber-Bosch reaction	30
> Uncovering catalyst structures for removing trace ammonia	32
Health and life science	
> Unravelling magnetic properties of individual cells in brain tissue	34
> New imaging technique at PETRA III revolutionising breast cancer research	36
> Structural insights for Parkinson's therapy	38
> How structure-activity relationships shape the future of rational design nucleic acid carriers	40
> Filming DNA repair	42
> Structural biology of bacterial insecticides	44
Atomic and molecular science	
> X-rays create exotic forms of ice	46
> Freezing nuclear motions with attosecond X-rays	48
> Combining XUV light sources for coupled molecular dynamics	50
> Electron bubble in a water cage	52
> Twisting currents: electron vortices in chiral molecules	54
> A tiny droplet of acid	56
Quantum materials and magnetism	
> A new type of magnetism experimentally confirmed in RuO	58
> Storing X-ray wave packets	60
> Towards ultrafast energy-efficient data recording	62
> Where do energy and angular momentum go?	64
> 4f electronic excitations in rare-earth metals	66
Earth and environment	
> A 'hidden route' for transporting water into the Earth's deep interior	68
> A new approach against 'forever chemicals'	70
Laser and X-rays sources - methods, developments	
> A record resolution	72
> Extending frontiers with X-ray multibeam ptychography	74
> Leveraging AI to extract weak signals	76
> Dose-efficient in vivo X-ray imaging of small samples	78
> The dark side of transmission X-ray microscopy	80
> Chip-integrated ultrafast laser sources	82
> Laser pulse control at extreme parameters using intense gas-borne ultrasound	84
> Terahertz-driven ultrafast photogun: a practical novelty	86

XFEL pulses drive the out-of-equilibrium dynamics of nanogels

Real-time swelling-collapse of PNIPAm revealed by MHz X-ray photon correlation spectroscopy

Stimuli-responsive hydrogels such as poly-N-isopropylacrylamide (PNIPAm) are a class of materials that undergo a volume phase transition as a response to variations in their local environment such as changes in pH, pressure or temperature, enabling a wide range of applications from nanorobotics to drug delivery or adaptive optics. While the equilibrium response of such systems has been intensively investigated [1], only in recent years the kinetics of the collapse mechanisms have been studied in time-resolved experiments, providing new information on the details of these processes [2]. The study provides direct access to the timescales of this volume phase transition in hydrogel particles.

The swelling-collapse kinetics of hydrogel particles with radii in the mm to μm range is well described by the Tanaka model [3] which predicts a characteristic time τ_c proportional to the square of the fully swollen particle radius a . This behaviour has been observed in experiments where the time evolution of a certain observable, e.g. optical density, is followed after creating a sudden temperature jump. Different results are found if the energy is delivered first to the solvent [4] or directly to the nanoparticles [5], pointing to limitations of the established model on short timescales.

We performed a direct measurement of the hydrodynamic radius of silica-PNIPAm core-shell particles dispersed in water. The studied systems are synthesised with two

different cross-linker concentrations and two different shell thicknesses. Upon heating from room temperature, the PNIPAm shell reduces its thickness slightly and collapses fully at the lower critical solution temperature T_{lcst} around 312 K as verified by dynamic light scattering (DLS) measurements. We applied X-ray photon correlation spectroscopy (XPCS), using the MHz X-ray pulse trains of the European XFEL at the MID instrument to measure the diffusion properties of the dispersion. We followed the time evolution of driven and out-of-equilibrium systems over time- and length-scales that cannot be reached with other, more conventional experiments. In this scheme, illustrated in Fig. 1a, the ultrashort X-ray pulses act both as pumps, heating the sample, and as probes of the dynamics with sub- μs time resolution following the collapse, (Fig. 1b).

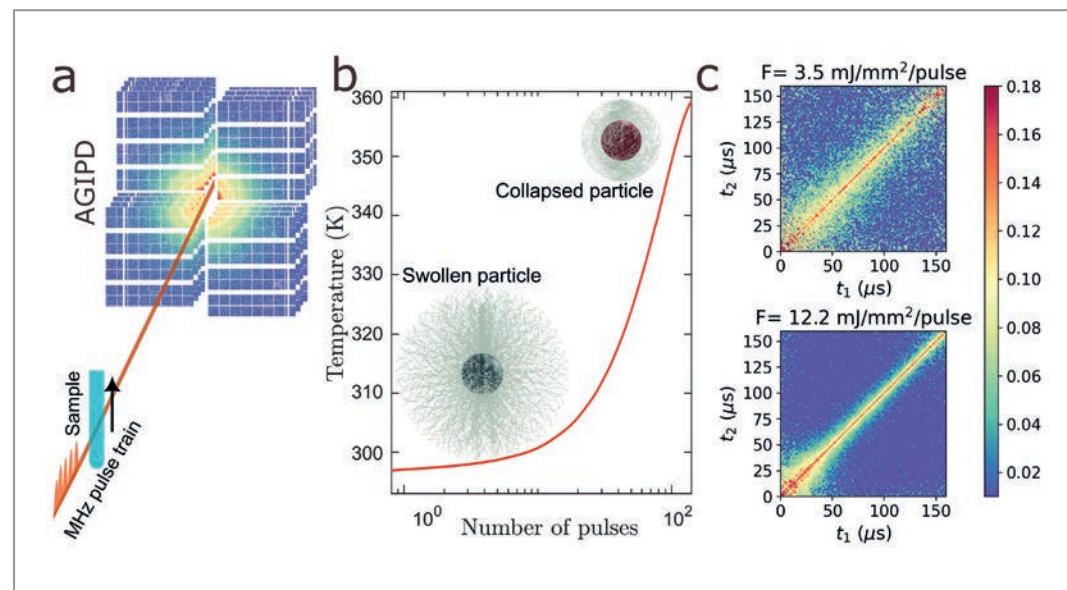
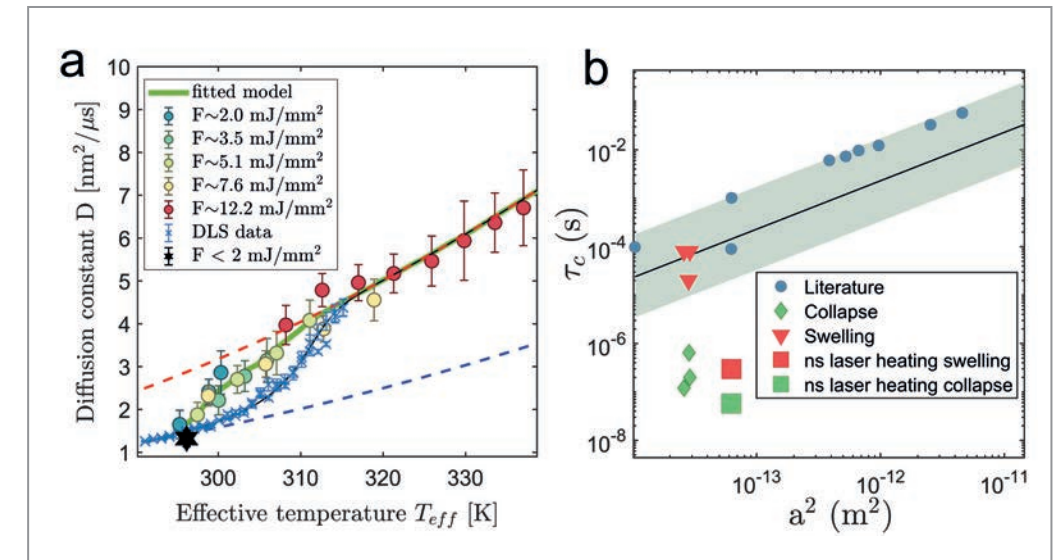


Figure 1
a) Experiment scheme. A train of X-ray pulses at MHz repetition rate hits the sample which is continuously moved to minimise radiation damage. Small angle X-ray scattering is collected by the AGIPD detector. b) Varying the X-ray fluences allows for control over the solvent temperature surrounding the particles, thereby driving the collapse of the PNIPAm shell. c) Two times correlation matrices at different fluences for $q=0.09 \text{ nm}^{-1}$. Correlation decreases faster at the end of the matrix signalling a speeding up of the dynamics. This process increases for higher fluences.

Figure 2
a) Experimental diffusion constant as a function of effective temperature for fluences between 2 and 12 mJ/mm^2 (circles). The collapse of the PNIPAm shell is indicated by the transition from the Stokes-Einstein law (dashed lines) of a swollen particle (blue) to the one of a collapsed particle (red). The XFEL data indicates a collapse at lower T_{eff} compared to the equilibrium data (crosses). b) The resulting τ_c for collapse (green diamond) and swelling (red triangles) are compared with literature values of global (blue circles) and local (squares) heating experiments.



The samples were probed by trains of 9 keV X-ray pulses with repetition rates of up to 2.24 MHz. A fast heating takes place as a response to the first pulse, followed by cooling before the next pulse hits the sample volume. The scattering volume cannot fully dissipate the thermal energy within the μs time separation between different pulses, so overall a steady heating is present. The PNIPAm shell will respond to all these transients reaching a collapsed state. Knowledge of the routes of this transition provides valuable insight into the kinetics of collapse and swelling. The response of the nanoparticles is critically dependent on the X-ray intensity and pulse repetition rate. The XPCS analysis gives access to the evolving dynamics (an example is shown in Fig. 1c) and consequently to the nonequilibrium diffusion constant D of the particles. Knowing the fluence, an effective temperature is associated with the number of pulses obtaining $D(T_{\text{eff}})$, reported in Fig. 2, for the case of 1.1 MHz pulse repetition rate. It is possible to identify several fluence regimes: From the weakest in which no collapse is triggered (black star) to the strongest that results either in a collapse after one pulse or a complete destruction of the PNIPAm shell (not shown). Intermediate fluencies show a collapse with apparent lower T_{lcst} compared to the equilibrium data. However, considering the time-dependent collapse and swelling of the PNIPAm during the pulse-induced temperature jump, the time-resolved model introduced in [6] can be extended (green line in Fig. 2) to extract the experimental values for τ_c for swelling and collapse of the particle radius a , reported in the inset of Fig. 2. The results indicate a swelling time consistent with the one observed in literature for global heating conditions and a collapse time consistent with the one for local heating. These findings are important not only for the investigation of the kinetics of the PNIPAm collapse

but also for future studies in more complex environments such as protein folding kinetics.

Author contact:
Francesco Dallari, francesco.dallari@unipd.it
Felix Lehmkuhler, felix.lehmkuehler@desy.de

References

- M. A. C. Stuart et al., 'Emerging applications of stimuli-responsive polymer materials', *Nat. Mater.* 9, 101–113 (2010).
- P. I. Yunker et al., 'Physics in ordered and disordered colloidal matter composed of poly(n-isopropylacrylamide) microgel particles', *Rep. Prog. Phys.* 77, 056601 (2014).
- T. Tanaka and D. J. Fillmore, 'Kinetics of swelling of gels', *J. Chem. Phys.* 70, 1214–1218 (1979).
- B. Tagdell et al., 'Temperature-jump spectroscopy of gold-poly(N-isopropylacrylamide) core-shell microgels', *J. Phys. Chem. C* 126, 4118–4131 (2022).
- S. Murphy, S. Jaber, C. Ritchie, M. Karg and P. Mulvaney, 'Laser flash photolysis of Au-PNIPAm core-shell nanoparticles: Dynamics of the shell response', *Langmuir* 32, 12497–12503 (2016).
- F. Lehmkuhler et al., 'Emergence of anomalous dynamics in soft matter probed at the European XFEL', *Proc. Natl. Acad. Sci. U.S.A.* 117, 24110–24116 (2020).

Original publication

'Real-time swelling-collapse kinetics of nanogels driven by XFEL pulses', *Science Advances* 10, eadm7876 (2024).
DOI: 10.1126/sciadv.adm7876



Francesco Dallari^{1,2}, Irina Lokteva^{1,3}, Johannes Möller⁴, Wojciech Roseker¹, Claudia Goy¹, Fabian Westermeier¹, Ulrike Boesenberg⁴, Jörg Hallmann⁴, Angel Rodriguez-Fernandez⁴, Markus Scholz⁴, Roman Shayduk⁴, Anders Madsen⁴, Gerhard Grübel^{1,3,4} and Felix Lehmkuhler^{1,3}

- Deutsches Elektronen-Synchrotron DESY, Hamburg, Germany
- Department of Physics and Astronomy, University of Padova, Padova, Italy
- The Hamburg Centre for Ultrafast Imaging CUI, University of Hamburg, Hamburg, Germany
- European XFEL, Schenefeld, Germany

Ionic superdiscs form nanowires in nanopores

Realisation of controllable self-assembly of ionic liquid crystals under external stimuli

Synchrotron radiation-based X-ray scattering and optical birefringence measurements were used to study the phase behaviour of discotic ionic liquid crystals (DILCs) in nanopores. The study revealed a remarkably rich phase behaviour influenced by the molecular anchoring to the pore walls. Continuous and reversible nanowire as well as nanoring formation was observed as a function of cooling and heating, suggesting that infiltration of DILCs into nanoporous solids allows tailoring their nanoscale texture and ion channel formation and thus potentially extending their electrical and optical functionalities beyond what is achievable in the bulk state.

Liquid crystals have become an integral component of our everyday lives. The optical technologies that employ liquid crystals are numerous and diverse. They are responsible for the brilliant colours we see on our mobile phones, televisions and computers. They also play a significant role in many other advanced photonic technologies. We have recently observed a novel liquid-crystalline self-assembly behaviour that has the potential to expand the applications of liquid crystals in the fields of bio- and nanoelectronics as well as in the development of novel membrane technologies for battery design and water purification.

We studied discotic ionic liquid crystals (DILCs). They consist of self-assembled superdiscs of cations and anions that spontaneously stack in linear columns with high one-dimensional ionic and electronic charge mobility, making them prominent model systems for functional soft matter [1]. Compared to classical nonionic discotic liquid crystals, many liquid crystalline structures with a combination of electronic and ionic conductivity have been reported for these systems which are of interest for separation mem-

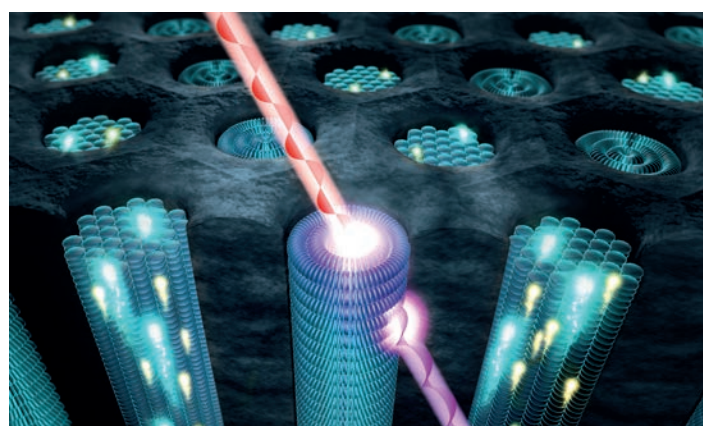
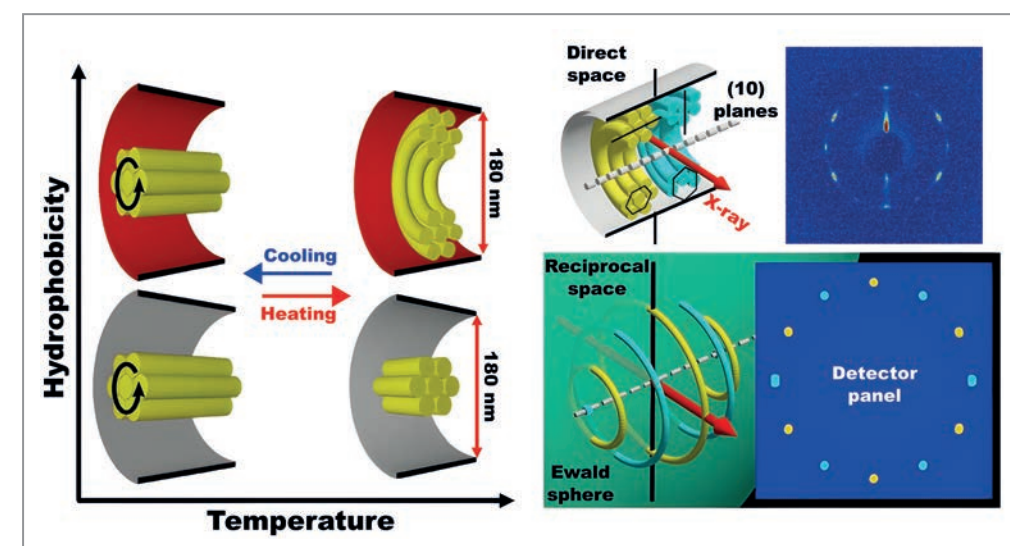


Figure 1 Possible arrangements of DILCs when confined within a nanoporous solid scaffold. Depending on temperature and anchoring at the pore walls the ionic superdiscs spontaneously form well-aligned concentric rings or straight nanowires. These structures can be used to tailor the polarisation of laser light or to create novel smart membranes with simultaneous ion and electron transport.

branes, artificial ion/proton conducting membranes and optoelectronics [1]. Unfortunately, a homogeneous alignment of the DILCs on the macroscale is often not achievable which significantly limits the applicability of DILCs. Infiltration into nanoporous solid scaffolds can, in principle, overcome this drawback [2,3]. However, due to the experimental challenges to scrutinise liquid crystalline order in extreme spatial confinement, little is known about the structures of DILCs in nanoscale confinement. To address this challenge, we performed temperature-dependent high-resolution optical birefringence measurement and 3D reciprocal space mapping based on synchrotron radiation-based X-ray scattering to investigate the thermotropic phase behaviour of dopamine-based DILCs in cylindrical channels of 180 nm diameter in macroscopic anodic aluminium oxide membranes.

As illustrated in Fig. 1, the passage of a linearly polarised laser beam through the combined materials results in a modification of its polarisation state. The linear polarisation of light is modified into elliptical polarisation following its passage through the sample. The self-assembly of a concentric circular ring is characterised by positive optical anisotropy which may be defined as positive birefringence and may be expressed as a prolate optical indicatrix.

Figure 2 By modulating the temperature and molecular hydrophobicity, it is possible to achieve a reversible transition between an axial and a radial/circular concentric (log-pile) structure (left). The illustration depicts two differently oriented circular concentric domains in direct space, accompanied by its X-ray diffraction image (top figure on the right). The corresponding reciprocal space pattern and Bragg peak distribution is illustrated in the bottom figure on the right.



Conversely, the axial alignment results in negative optical anisotropy which may be defined as oblate optical indicatrix. By a systematic study of this optical anisotropy state as a function of temperature, we could infer that the confined DILCs exhibit a reversible transition between axial and circular concentric structures, as depicted in Fig. 2 (left).

A synchrotron radiation-based temperature-dependent small-angle X-ray scattering experiment performed at beamline P08 at PETRA III and beamline BM02 at the European Synchrotron Radiation Facility (ESRF) confirmed these findings. As exemplified in Fig. 2 (right), the diffraction pattern developed by the distinct textures produce unique scattering patterns. In the course of the experiment we investigated the impact of a number of different parameters on the self-assembly behaviour of the DILCs (temperature, surface chemistry, pore size and molecular size).

As a function of the membranes' hydrophilicity and thus the molecular anchoring to the pore walls (edge-on or face-on) and the variation of the hydrophilic-hydrophobic balance between the aromatic cores and the alkyl side chain motifs of the superdiscs by tailored chemical synthesis, a particularly rich phase behaviour was found. This phase behaviour is not present in the bulk state and governed by a complex interplay of liquid crystalline elastic energies (bending and splay deformations), polar interactions and pure geometric confinement. It also includes the aforementioned textural transitions between radial and axial alignment of the columns with respect to the long nanochannel axis. Furthermore, confinement-induced continuous order formation is observed in contrast to discontinuous first-order phase transitions which can be described quantitatively by Landau-de Gennes' free energy models for liquid crystalline order transitions in confinement [2]. Our obser-

vations suggest that the infiltration of DILCs into nanoporous solids allows tailoring their nanoscale texture and ion channel formation and thus their electrical and optical functionalities over an even wider range than in the bulk state in a homogeneous manner on the centimetre scale as controlled by the monolithic nanoporous scaffolds.

Author contact: Zhuoqing Li, zhuoqing.li@tuhh.de
Patrick Huber, patrick.huber@tuhh.de

References

1. K. Goossens, K. Lava, C. W. Bielawski and K. Binnemans, 'Ionic liquid crystals: versatile materials', *Chem. Rev.* **116**, 4643–4807 (2016).
2. K. Sentker, A. W. Zantop, M. Lippmann, T. Hofmann, O. H. Seeck, A. V. Kityk, A. Yildirim, A. Schönhals, M. G. Mazza and P. Huber, 'Quantized self-assembly of discotic rings in a liquid crystal confined in nanopores', *Phys. Rev. Lett.* **120**, 067801 (2018).
3. K. Sentker, A. Yildirim, M. Lippmann, A. W. Zantop, F. Bertram, T. Hofmann, O. H. Seeck, A. V. Kityk, M. G. Mazza, A. Schönhals and P. Huber, 'Self-assembly of liquid crystals in nanoporous solids for adaptive photonic metamaterials', *Nanoscale* **11**, 23304–23317 (2019).

Original publication

'Self-assembly of ionic superdiscs in nanopores', *ACS Nano* **18**, 14414–14426 (2024). DOI: 10.1021/acsnano.4c01062



Zhuoqing Li^{1,2}, Aileen Raab³, Mohamed Aejaz Kolmangadi⁴, Mark Busch^{1,2}, Marco Grunwald³, Felix Demel³, Florian Bertram⁵, Andriy V. Kityk⁶, Andreas Schönhals^{4,7}, Sabine Laschat³ and Patrick Huber^{1,2}

1. Institute for Materials and X-ray Physics, Hamburg University of Technology, Hamburg, Germany
2. Centre for X-ray and Nano Science CXNS, DESY, Hamburg, Germany
3. Institut für Organische Chemie, Universität Stuttgart, Stuttgart, Germany
4. Bundesanstalt für Materialforschung und -prüfung (BAM), Berlin, Germany
5. Deutsches Elektronen-Synchrotron DESY, Hamburg, Germany
6. Faculty of Electrical Engineering, Czestochowa University of Technology, Czestochowa, Poland
7. Institut für Chemie, Technische Universität Berlin, Berlin, Germany

Spinel-structured materials – durable and flexible

Possible material for optical diagnostic windows in future fusion reactors

Magnesium aluminate spinel has received significant practical interest because of the predicted tolerance to ionising irradiation. This material is currently on the priority list of the EUROFUSION consortium for optical windows in future deuterium-tritium fusion reactors to enable diagnostic systems in order to look into the plasma. A wide range of the exceptional properties of these spinel-structured materials is related to their unique crystalline structure which is highly stable and flexible at the same time. Figuratively speaking, this crystalline lattice with relatively loose cations in a rigid anionic framework is exceptionally durable due to the self-healing of radiation-induced defects.

Variable composition of cations enables flexible control of the electronic structure of the mineral magnesium aluminate spinel (MgAl_2O_4). The low occupancy of cationic sites together with a high mobility of cations is leading to a partial swapping of cations between intrinsic tetrahedral and octahedral lattice sites in crystals. They are forming a huge concentration of the so-called antisite defects, when Mg and Al cations exchange their positions. Influence of antisites on the electronic structure and functional properties of spinel materials is of paramount importance and regularly discussed. Even in the most studied MgAl_2O_4

spinel not much was known experimentally about the nature of antisite lattice defects, their energy levels and mechanisms of the electron/energy transfer.

Their concentration is inherently very high and always exceed $1.5 \times 10^{21} \text{ cm}^{-3}$ (>10 % of inversion) in the synthetic solids, detailing its formula as $(\text{Mg}_{1-i}\text{Al}_i)^{\text{T}}(\text{Mg}_i\text{Al}_{2-2i})^{\text{O}}\text{O}_4$, where $()^{\text{T}}$ and $()^{\text{O}}$ signify tetrahedral and octahedral sites in lattices, respectively, and i is the inversion parameter ranging from 0 for the normal spinel $(\text{Mg})^{\text{T}}(\text{Al}_2)^{\text{O}}\text{O}_4$ to 1 for the inverse spinel $(\text{Al})^{\text{T}}(\text{MgAl})^{\text{O}}\text{O}_4$. Moreover, up to now the degree of inversion can only be evaluated in the limited range $0 \leq i < 0.4$ via high precision X-ray diffraction measurements.

A research team of scientists from France, Estonia and Japan accomplished photoluminescence (PL) and PL excitation experiments on MgAl_2O_4 spinel materials at the PETRA III beamline P66, also at beamlines with synchrotron radiation excitation in the UV-visible spectral range of UVSOR (Japan) and MAX IV Laboratory (Sweden) as well as cathodoluminescence at the setup of the Institute of Physics (Estonia).

The nature of the most intense luminescence band in the UV-C region at $\sim 250 \text{ nm}$, whose intensity varies greatly with the sample origin and processing and which has remained an issue up to now, was of a particular concern in this work. The origin and excitation mechanism of this

intriguing UV-C luminescence was analysed in the pristine crystal and in the crystal irradiated with He^+ ions (of energy 150 keV and fluence $10^{17} \text{ particles/cm}^2$).

The detailed analysis revealed a characteristic behaviour of this band inherent to donor-acceptor pairs (DAP). In particular, the spectral shift of the UV-C band towards lower energies was observed with an increase in the time delay from the excitation pulse. The PL decay followed a power law, explained by the distant DAP recombination sequence. Furthermore, the PL spectra showed that the spectral position of the UV-C band depends on the excitation photon energy. The observed progressive PL red shift reinforced the assignment to DAP transitions.

A comparison of two spinel crystals with different inversions demonstrated an enhancement of absorption at $\sim 7.1 \pm 0.2 \text{ eV}$ with an increase of inversion (corresponding to the distant low-energy DAPs). This distance between donor and acceptor matches the spinel cell length. Accordingly, the emitting centres were related to the cations inversion forming intragap energy levels in the vicinity of the CB/VB edges. The acceptor was assigned to Mg^{2+} substituting Al^{3+} site in the octahedral voids and donor to a deep oxygen vacancy V^{O} : Mg_{Al} (shallow acceptor) – V^{O} (deep donor). The correlation of the UV-C band intensity with the inversion degree i supports this assignment. The UV-C luminescence thus appearing due to the electron transfer from Mg_{Al} to Al_{Mg} , (excitation) following by that from V^{O}

to Mg_{Al} (emission) and the extremely high concentration of antisite defects is the main reason for the strong 5 eV luminescence.

The irradiation with He^+ ions up to high fluences of $10^{17} \text{ particles/cm}^2$ randomly displaced cations to empty sites of the spinel lattice resulting in more intragap defect levels, which induce a non-radiative energy relaxation channel quenching closely spaced while unaffected distant DAP luminescence. The material could therefore be considered as radiation tolerant.

Author contact: Eduard Feldbach, eduard.feldbach@ut.ee
Andrei Kanaev, andrei.kanaev@lspm.cnrs.fr



Figure 2
The photo shows three different samples on the sample holder (Credit: DESY).

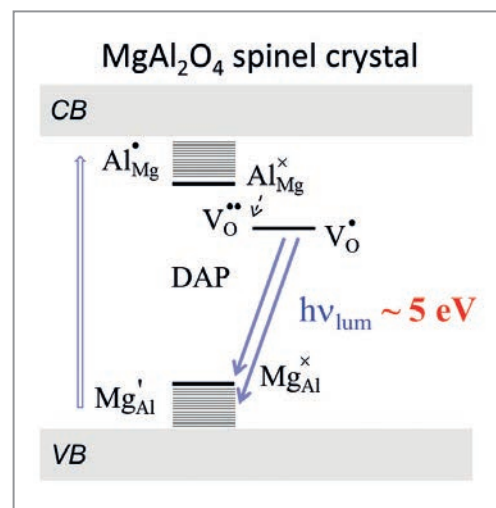


Figure 1
Antisite PL mechanism in MgAl_2O_4 spinel crystal (VB: valence band, CB: conduction band). (Credit: Original publication)

Original publication

'Donor-acceptor pair transitions in MgAl_2O_4 spinel', *Journal of Luminescence* 265, 120235 (2024). DOI: 10.1016/j.jlumin.2023.120235



Luc Museur¹, Eduard Feldbach², Aleksei Kotlov³, Mamoru Kitaura⁴ and Andrei Kanaev⁵

- Laboratoire de Physique des Lasers - LPL, CNRS UMR 7538, Université Sorbonne Paris Nord, Villetaneuse, France
- Institute of Physics, University of Tartu, Tartu, Estonia
- Deutsches Elektronen-Synchrotron DESY, Hamburg, Germany
- Faculty of science, Yamagata University, Yamagata, Japan
- Laboratoire des Sciences des Procédés et des Matériaux - LSPM, CNRS UPR 4307, Université Sorbonne Paris Nord, Villetaneuse, France

Capturing the uncapturable in electron beam powder bed fusion

High-speed radiography unveils the hidden dynamics behind a process instability: the 'Smoke' phenomenon

Electron Beam–Powder Bed Fusion (PBF-EB) has demonstrated significant potential for the manufacturing of complex metal parts due to its unique capabilities, including high productivity, minimal contamination and efficient use of raw materials. However, this technique suffers from a so-called 'Smoke' phenomenon which severely impacts the process stability. We used high-speed radiography to capture this phenomenon for the first time with enhanced temporal and spatial resolution. We gathered key insight into understanding this phenomenon on a particle-level scale subsequent to the powder's melting.

One of the key challenges unique to PBF-EB compared to other PBF technologies is the 'Smoke' phenomenon. It is characterised by the rapid and uncontrolled scattering of powder particles, forming a cloud above the work surface during processing that resembles smoke. This phenomenon disrupts the necessary powder layer for the powder bed fusion process, and recovering a healthy powder layer often requires halting or even fully interrupting the build process. While it is generally attributed to electrostatic forces from negative charge accumulation on the powder particles [1], the complex electron beam–substrate interaction suggests other forces may also play a role.

To better understand the Smoke phenomenon, effective monitoring is essential but challenging due to several

unique aspects of PBF-EB. These include the high vacuum environment, elevated process temperatures, pre-sintered powder layers and the presence of metal vapor. Typically, high-speed cameras can be used to monitor Smoke, mounted outside the vacuum chamber. However, these cameras often lack sufficient temporal and spatial resolution which makes tracking particle movements difficult as they move out of focus during Smoke development. Consequently, a comprehensive understanding of Smoke dynamics remains constrained.

The engineering materials station P61A at PETRA III beam-line P61 is equipped with a PBF-EB sample environment called MiniMelt, equipped with a camera system as part of the Röntgen-Ångström-Cluster project 'Track-AM' since

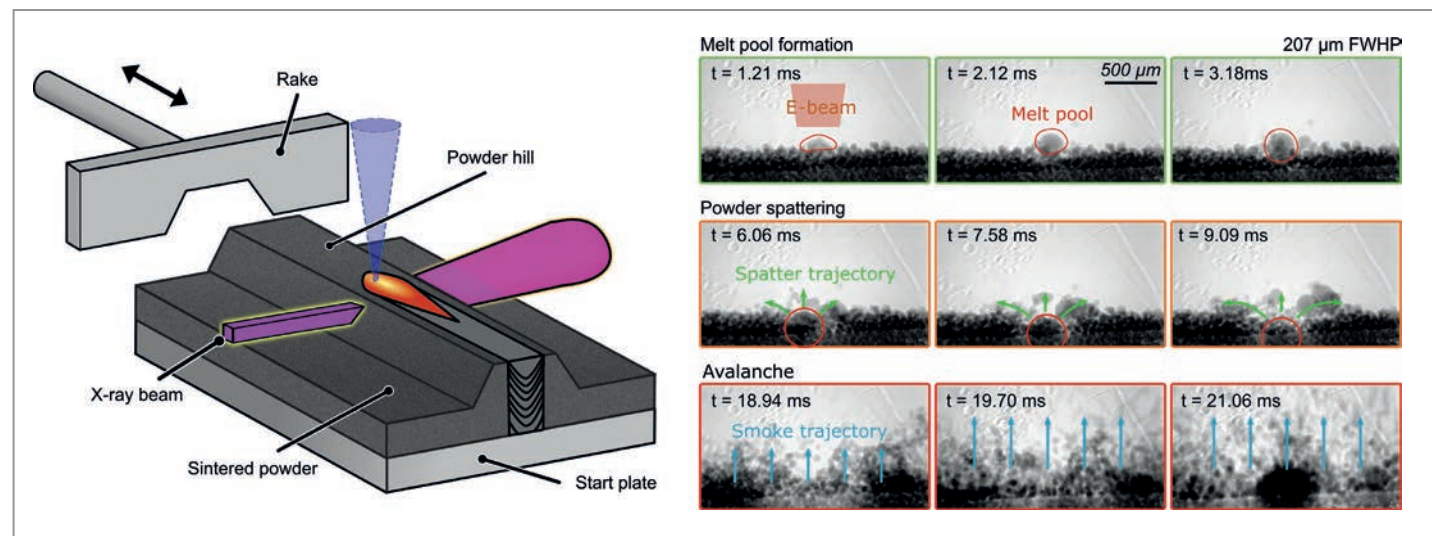


Figure 1 Illustration of an unconfined powder bed as the imaging object. The powder hill is created using a pre-cut rake blade, with the electron beam interacting with the surface of the powder hill. Simultaneously, X-rays transmit through the powder hill from the side [3]. The observed Smoke development pattern can be divided into three stages: melt pool formation (e-beam creates a melt pool), powder spattering (overheating of the melt pool and powder ejected from the surface), Smoke avalanche (powder lifts at a significantly higher speed).

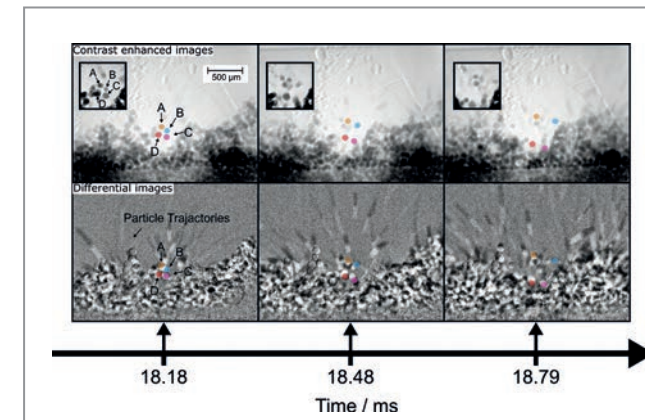
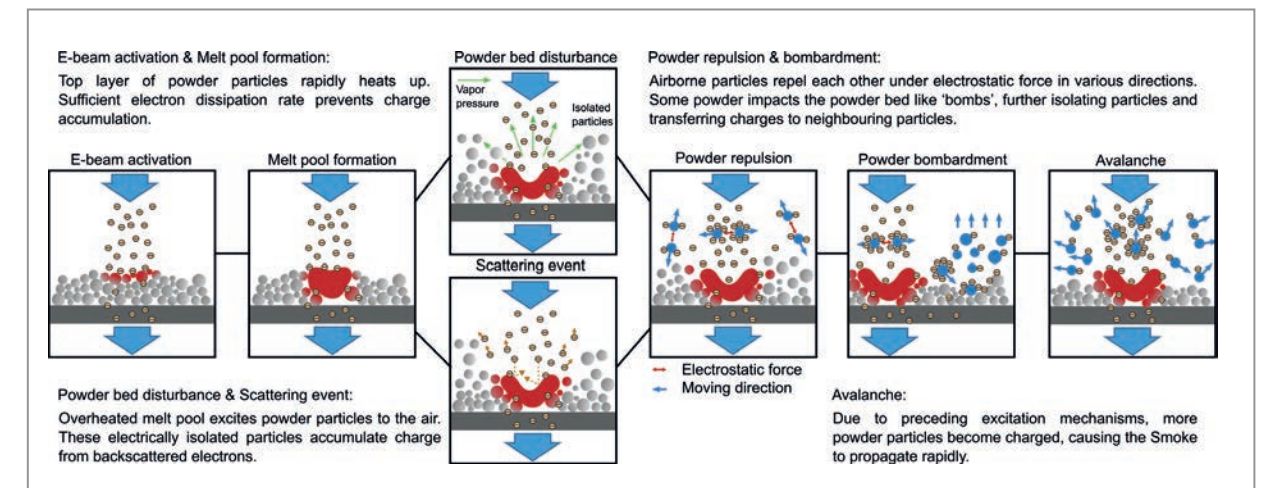


Figure 2 Powder behaviour during the transition phase. Three consecutive frames from the transition phase are presented, each processed using two different methods for enhanced analysis. Contrast enhancement: visualises the state of the powder bed. It highlights the movement of four particles (A-D) repelling each other. This behaviour is presumed to be caused by electrostatic force (upper row). Image subtraction: demonstrates the dynamics of powder particles. The black-and-white lines represent the trajectories of rapidly moving particles. Their quantity visibly escalates over time (lower row).

Figure 3 A sequential illustration of Smoke development under a stationary e-beam, highlighting key mechanisms.



2023. The camera has a frame rate of up to 25 kHz. The maximum recorded resolution is 2048 × 1952 pixels with an effective pixel size of 1.35 μm. This setup [2] allows monitoring process phenomena in PBF-EB under thermal and electrical conditions similar to those found in industrial-scale processes, making it ideal for investigating the Smoke phenomenon. For this procedure we used a standard PBF-EB powder feedstock (CMSX-4) on the MiniMelt. The Smoke was triggered by a stationary electron beam with varying beam sizes on an unconfined powder bed, as shown in Fig. 1. Monitoring revealed a novel Smoke development pattern previously unreported. Under a sharp electron beam, 207 μm full width half power (FWHP), a spherical melt pool initially forms. Subsequently, spattering particles are ejected from the melt pool at a moderate speed. After 18.94 ms, the movement of these particles changes abruptly, with their speed dramatically increasing as they move away from the start plate. By analysing the characteristic movement patterns of these particles (Fig. 2 as an example), we identified Smoke as a physical phenomenon involving multiple driving forces. For instance, the Smoke is initiated by recoil pressure resulting from melt pool evaporation under a sharp electron beam. This initiation generates particles that are electrically isolated from the ground. These isolated particles are likely captured by the electron beam, and as they become heavily charged, electrostatic forces dominate their movement causing rapid acceleration. These observations resolve the discrepancies between the conventional

Smoke model and experimental results, guiding the development of a new model for the Smoke phenomenon, as depicted in Fig. 3. This new model enables a more detailed Smoke optimisation method, thereby enhancing the stability of the PBF-EB process.

Author contact: Jihui Ye, jihui.ye@fau.de

References

1. Z. C. Cordero, H. M. Meyer, P. Nandwana and R. R. Dehoff, 'Powder bed charging during electron-beam additive manufacturing', *Acta Mater.* 124, 437–445 (2017).
2. P. M. Bidola et al., 'A high-speed x-ray radiography setup for in-situ electron beam powder bed fusion at PETRA III', *Advances in X-Ray/EUV Optics and Components XVIII* 12694, 1269402 (2023).
3. H. H. König et al., 'MiniMelt: An instrument for real-time tracking of electron beam additive manufacturing using synchrotron x-ray techniques', *Rev. Sci. Instrum.* 94, 125103 (2023).

Original publication

'Revealing the Mechanisms of Smoke during Electron Beam–Powder Bed Fusion by High-Speed Synchrotron Radiography', *Journal of Manufacturing and Materials Processing* 8, 103 (2024). DOI: 10.3390/jmmp8030103



Jihui Ye^{1,2}, Nick Semjatov², Pidassa Bidola³, Greta Lindwall⁴ and Carolin Körner^{1,2}

1. Center of Advanced Materials and Processes, Friedrich-Alexander University Erlangen-Nürnberg, Fürth, Germany
2. Chair of Materials Science and Technology for Metals, Department of Material Science and Engineering, Friedrich-Alexander University Erlangen-Nürnberg, Erlangen, Germany
3. Institute of Materials Physics, Helmholtz-Zentrum Hereon, Geesthacht, Germany
4. Department of Materials Science and Engineering, KTH Royal Institute of Technology, Stockholm, Sweden

Shaping matter's transparency with ultrashort X-rays

Transient absorption of copper reveals transformation from opaque to transparent with increasing X-ray pulse intensity

Warm dense matter (WDM) is at the boundary between a plasma and a condensed phase and plays a role in astrophysics, planetary science and inertial confinement fusion research. However, its structure and interaction with radiation remain poorly understood. Creating and probing WDM in a laboratory setting are difficult due to its extreme density and temperature; neither can the theoretical modelling provide reliable predictions. Here, we employ an intense and ultrafast soft X-ray free-electron laser (XFEL) pulse to simultaneously create and characterise warm dense copper using transient X-ray absorption spectroscopy over a large irradiation intensity range.

Focused ultrashort XFEL pulses deposit significant energy into solids, with each atom likely absorbing one or more photons via inner-shell photoionisation. Within femtoseconds, processes such as Auger-Meitner decay and electron-impact ionisation create a highly-excited, non-equilibrium electronic state while ions remain largely stationary. XFEL pulses can also probe these transient states, and X-ray absorption near-edge spectroscopy (XANES), achieved through measuring the energy-resolved transmission near the ionisation edge, provides detailed insights into both electronic structure and ionic order. The transmission signal forms during the XFEL pulse, capturing information from the initial femtoseconds of the WDM state. Until now, XANES has been mostly applied to infrared- and optically-heated WDM with picosecond to subpicosecond time resolutions [1].

This study was conducted at the Spectroscopy and Coherent Scattering instrument at European XFEL. Intense 15 fs long XFEL pulses were focused on a 100 nm thick copper film, with photon energy tuned to the Cu L_3 and L_2 absorption edges. The broadband XFEL spectrum enabled XANES measurements over a 15 eV window around the edges. By varying the X-ray intensity across five orders of magnitude, dramatic changes in the absorption spectrum were observed (Fig. 1a). At intensities above 10^{13} W/cm², pre-edge absorption increases due to the creation of 3d vacancies, which causes an overall drop in X-ray transmission, referred to as Reverse Saturable Absorption (RSA). Another spectral feature is a ~ 1 eV wide peak at 936.7 eV, indicative of a van Hove singularity in the copper density of states, reflecting long-range crystalline order. Its persistence confirms that the 15 fs pulse is too short to induce structural changes.

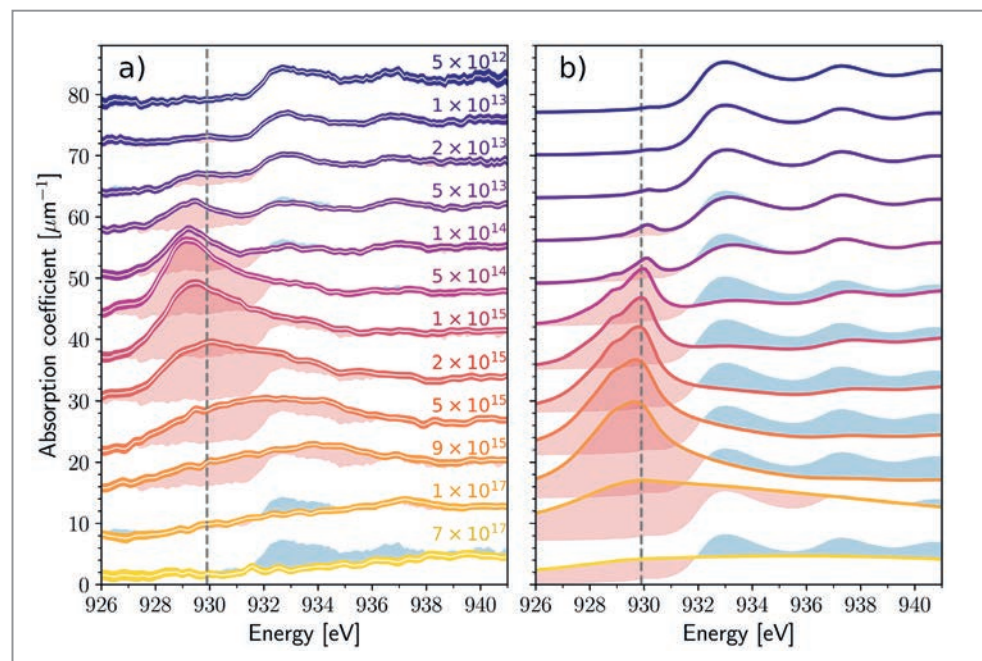
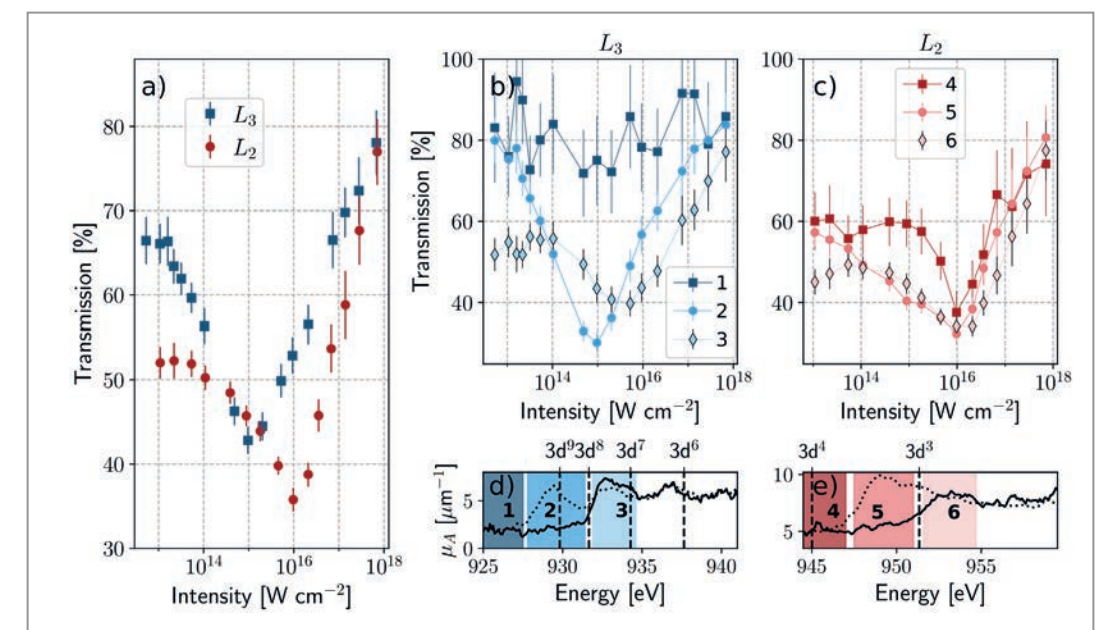


Figure 1 Transient XANES of XFEL-created warm dense copper. a) Experimental absorption spectra at the L_3 edge for XFEL intensities as indicated in the figure, in W/cm². The spectra are vertically offset by $7 \mu\text{m}^{-1}$. The red (blue) areas show the stronger (weaker) absorption relative to the cold spectrum obtained at $I = 5 \times 10^{12}$ W/cm². The dashed line indicates the position of the pre-edge peak at low intensity. b) Corresponding theoretical XANES calculations.

Figure 2 Transition from RSA to SA. a) Transmission of an XFEL pulse centred at the L_2 and L_3 edges as a function of pulse intensity. b) Transmission at the L_3 edge and c) L_2 edge in selected spectral regions (1,4: below the pre-edge, 2,5: on the pre-edge, 3,6: on the edge) d) Absorption coefficient around L_3 edge for the cold reference spectra (solid line) and for the high-intensity case (dashed line). e) Same as d) for L_2 edge. The vertical dashed lines show the calculated $2p_{3/2}3d^N \rightarrow 3d^{N+1}$ excitation energies of various ions.



At intensities above 10^{15} W/cm², absorption peak shifts to higher energies and broadens due to ion states with fewer than eight 3d electrons (see Fig. 2d,e). At sufficiently high intensities, absorption lines shift beyond the spectral range of the pulse, closing these channels and leading to increased transmission—Saturable Absorption (SA). This RSA-to-SA transition is clearly shown in Fig. 2a where measured transmissions at the L_3 and L_2 edges are plotted as a function of pulse intensity. For selected spectral regions near both edges, the RSA-to-SA transition is analysed in Fig. 2b,c. At the L_2 edge, additional absorption channels from highly ionised states (e.g. Cu^{4+} , Cu^{5+} , Cu^{6+}) shift the RSA-to-SA transition to higher intensities.

Modelling of the WDM state and its X-ray opacity is challenging. Plasma-based approaches, like the kinetic Boltzmann code [2], effectively describe ionisation dynamics, electron configurations and non-equilibrium energy distributions. However, they lack the ability to capture bonding and electronic band hybridisation which are essential for XANES calculations. To address this, finite-temperature DFT via the FEFF10 code [3] was employed. By combining the Boltzmann and FEFF10 codes, XANES spectra were calculated as depicted in Fig. 1b. While this approach serves to reproduce the observed trends and explain them, further advancements are needed to develop self-consistent electronic structure models and spectral response functions for quantitative predictions.

While ions remain largely stationary, electron equilibration occurs on a comparable timescale to the XFEL pulse duration, suggesting that time-integrated XANES spectra reflect significant contributions from non-equilibrium stages. Higher temporal resolution could offer deeper insights into ionisation dynamics and improve non-equilibrium structure models. With advances in attosecond XFEL pulses generation and transient absorption spectroscopy,

this approach holds great promise for exploring matter under extreme conditions.

Author contact:

Andrei Benediktovitch, andrei.benediktovitch@desy.de
Nina Rohringer, nina.rohringer@desy.de
Laurent Mercadier, laurent.mercadier@xfel.eu
Beata Ziaja-Motyka, beata.ziaja-motyka@cfel.de

References

1. N. Jourdain, L. Lecherbourg, V. Recoules, P. Renaudin and F. Dorchies, 'Ultrafast thermal melting in nonequilibrium warm dense copper', *Phys. Rev. Lett.* **126**, 065001 (2021).
2. B. Ziaja, V. Saxena, S.-K. Son, N. Medvedev, B. Barbel, B. Woloncewicz and M. Stransky, 'Kinetic Boltzmann approach adapted for modeling highly ionized matter created by X-ray irradiation of a solid', *Phys. Rev. E* **93**, 053210 (2016).
3. T. S. Tan, J. J. Kas and J. J. Rehr, 'Real-space Green's function approach for X-ray spectra at high temperature', *Phys. Rev. B* **104**, 035144 (2021).

Original publication

'Transient absorption of warm dense matter created by an X-ray free-electron laser', *Nature Physics* **20**, 1564–1569 (2024). DOI: 10.1038/s41567-024-02587-w



Laurent Mercadier¹, Andrei Benediktovitch², Špela Krušič³, Joshua J. Kas⁴, Justine Schlappa⁵, Marcus Agåker^{5,6}, Robert Carley¹, Giuseppe Fazio⁷, Natalia Gerasimova¹, Young Yong Kim¹, Loïc Le Guyader¹, Giuseppe Mercurio¹, Sergii Parchenko¹, John J. Rehr⁴, Jan-Erik Rubensson⁵, Svitozar Serkez¹, Michal Stransky^{1,8}, Martin Teichmann¹, Zhong Yin^{1,10}, Matjaž Žitnik³, Andreas Scherz¹, Beata Ziaja^{2,9} and Nina Rohringer^{2,9}

1. European XFEL, Schenefeld, Germany
2. Center for Free-Electron Laser Science CFEL, DESY, Hamburg, Germany
3. J. Stefan Institute, Ljubljana, Slovenia
4. Department of Physics, University of Washington, Seattle, WA, USA
5. Department of Physics and Astronomy, Uppsala University, Uppsala, Sweden
6. MAX IV Laboratory, Lund University, Lund, Sweden
7. Laboratorium für Physikalische Chemie, ETH Zürich, Zurich, Switzerland
8. Institute of Nuclear Physics, Polish Academy of Sciences, Krakow, Poland
9. Department of Physics, University of Hamburg, Hamburg, Germany
10. International Center for Synchrotron Radiation Innovation Smart, Tohoku University, Sendai, Japan

Linking surface structure and chemistry in electrocatalysis

A combined surface X-ray diffraction and infrared spectroscopy experiment

Electrocatalysis is the decisive factor for a future energy system based on renewable resources. The most active electrocatalysts usually exhibit a high degree of complexity in terms of structure and chemical composition. During operation, the electrocatalytic properties of such systems change dynamically and are controlled by the interfacial chemistry at the electrified interface. Under these conditions, surface structure and surface chemistry are intimately entangled, both statically and dynamically. To understand the structure-activity relationship in electrocatalysis, it is therefore essential to study surface structure and surface chemistry in a correlated manner.

An interdisciplinary team from Friedrich-Alexander-Universität Erlangen-Nürnberg (FAU) and DESY has developed a versatile experimental setup [1] funded as part of the BMBF joint research project CIXenergy (05K19WE1). It combines two complementary *in situ* techniques under electrochemical conditions: High Energy Surface X-ray Diffraction (HE-SXRD) and Infrared Reflectance Absorption Spectroscopy (IRRAS). This *in situ* approach simultaneously provides structural and chemical information about the

same sample. The concept of this approach is illustrated in Fig. 1. An electrochemical IRRAS cell with a three-electrode configuration is located in an external chamber of a dedicated IR spectrometer. A planar model electrode, e.g. single crystal supported nanoparticles on a planar electrode or a nanostructured film serves as a working electrode (WE) and is pressed against an IR-transparent window. This creates a thin layer just a few micrometres thick which is required for electrochemical IRRAS. While the IR light for IRRAS enters through the IR-transparent window, the high-energy X-ray beam for HE-SXRD enters directly through the cell walls made of materials with low absorption. The diffracted beam passes through the IR-transparent window. By rotating the electrochemical cell with the sample, different azimuthal planes can be sampled with HE-SXRD.

The schematic representation of the technical implementation of this concept is shown in Fig. 1b. The setup consists of a Fourier transform infrared (FTIR) spectrometer with a customised external chamber on an adjustable optical table. The chamber contains the electrochemical cell which is mounted on an aluminium arm attached to a goniometer. The design allows the sample to be aligned and the rotation required for HE-SXRD to be possible. The height and tilt of the optical table can be adjusted via Z-stages to align the

Figure 1
Combined setup for simultaneous structural and chemical analysis using electrochemical HE-SXRD and IRRAS methods. a) Concept and b) schematic representation of the setup. (Reprinted with permission from [1]. Copyright 2023 American Chemical Society)

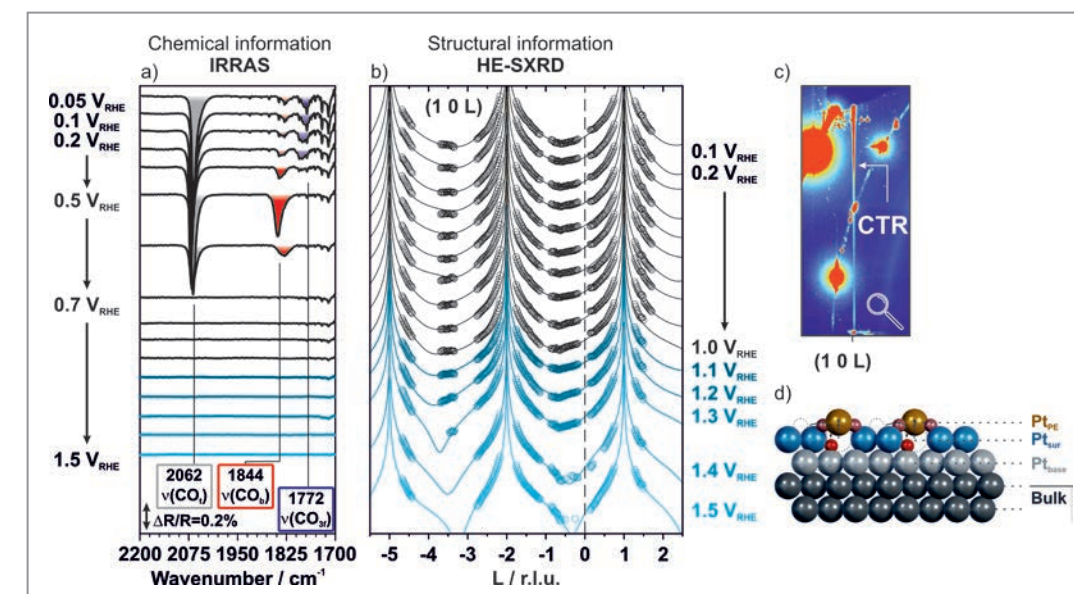
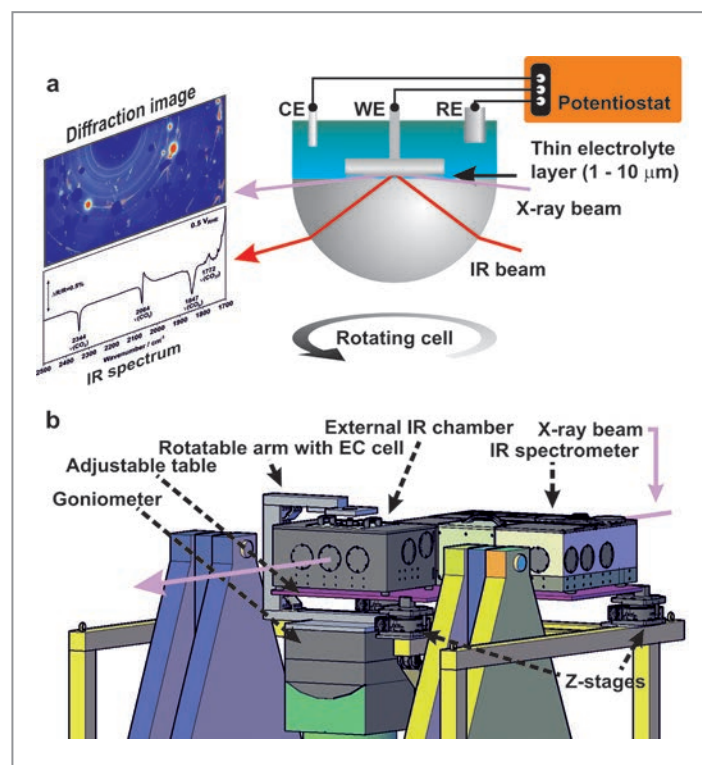


Figure 2
Oxidation of CO and a Pt surface observed in the combined HE-SXRD and IRRAS experiment. a) Potential-dependent IRRAS spectra, b) and c) corresponding X-ray diffraction data. d) Spherical model illustrating the oxidation mechanism at the Pt surface. (Reprinted with permission from [1]. Copyright 2023 American Chemical Society)

optical path of the IR spectrometer to the fixed measurement position for HE-SXRD. The spectrometer can be operated with static polarisation or polarisation modulation, depending on the requirements of the application.

To demonstrate the potential of the setup, the researchers performed a model experiment with the electrochemical oxidation of an adsorbate (CO_{ads}) and the electrode (Pt(111)) itself in an acidic aqueous electrolyte. The data shown in Fig. 2 were obtained by simultaneously recording the IRRAS spectra (Fig. 2a, chemical information) and imaging the reciprocal space with a 2D detector and high-energy X-rays at defined potentials during an experiment performed at beamline P07 at PETRA III (Fig. 2b and 2c, structural information). The IR spectra (Fig. 2a) provide information on adsorbates, their potential-dependent adsorption geometries and the reaction products formed. To analyse the surface structure and morphology of the Pt(111) electrode, the scientists examined the crystal truncation rods (CTR) which appear as vertical stripes (Fig. 2c). Analysing the CTR intensity profiles (Fig. 2b) provides information about the lattice parameters, surface relaxations and the roughness of the Pt(111) electrode (Fig. 2d).

With this combined experiment, the researchers were finally able to distinguish between the adsorbate-induced restructuring and the electrochemical oxidation of the Pt(111) surface under potential control. By recording the data simultaneously, correlations between structure and reactivity could be established much more reliably and reproducibly. Finally, it should be pointed out that the instrument described here is compatible with various beamlines at DESY and the European Synchrotron Radiation

Facility (ESRF) and became part of the DESY infrastructure which is available to users via the usual application procedures [2].

Author contact: Olaf Brummel, olaf.brummel@fau.de
Yaroslava Lykhach, yaroslava.lykhach@fau.de
Andreas Stierle, andreas.stierle@desy.de
Jörg Libuda, joerg.libuda@fau.de

References

- O. Brummel, L. Jacobse, A. Simanenko, X. Deng, S. Geile, O. Gutowski, V. Vonk, Y. Lykhach, A. Stierle and J. Libuda, 'Chemical and structural in-situ characterization of model electrocatalysts by combined infrared spectroscopy and surface X-ray diffraction', *J. Phys. Chem. Lett.* **14**, 39, 8820–8827 (2023).
- H. Noei, V. Vonk, T. Keller, R. Röhlisberger and A. Stierle, 'DESY NanoLab, Deutsches Elektronen Synchrotron (DESY)', *J. Large-Scale Res. Facil.* **2**, A76 (2016).

Original publication

'Chemical and structural in-situ characterization of model electrocatalysts by combined infrared spectroscopy and surface X-ray diffraction', *The Journal of Physical Chemistry Letters* **14**, 8820–8827 (2023). DOI: 10.1021/acs.jpcl.3c01777

Olaf Brummel¹, Leon Jacobse², Alexander Simanenko¹, Xin Deng^{1,2}, Simon Geile², Olof Gutowski³, Vedran Vonk², Yaroslava Lykhach¹, Andreas Stierle^{2,4} and Jörg Libuda¹

- Friedrich-Alexander-Universität Erlangen-Nürnberg, Erlangen, Germany
- Centre for X-ray and Nano Science CXNS, DESY, Hamburg, Germany
- Deutsches Elektronen-Synchrotron DESY, Hamburg, Germany
- University of Hamburg, Hamburg, Germany

New insights into the Haber-Bosch reaction

High-pressure XPS resolves questions on 100 year old reaction

Ammonia production feeds over 50% of the world's population, but also consumes 1–2% of all energy generated worldwide. Yet, the exact mechanisms behind the industrial catalytic ammonia production has remained unknown until very recently. With the first true high-pressure XPS setup installed at DESY's P22 beamline, researchers have been able to reveal the chemistry behind the previously elusive reaction and show how the most important catalyst of the 20th century operates.

Although the production of ammonia is essential for sustaining the world's population [1] a detailed understanding of its catalytic processes has long remained speculative. The limitations stemmed from the extreme pressures required for the catalyst to operate typically in the range of hundreds of bars [2]. This high pressure restricted previous studies to either theoretical calculations or analysis of the catalyst's bulk chemistry [3]. While these past studies provided valuable insights, understanding the chemistry at the interface between the gas and the solid catalyst is critical to the design of the next generation of catalysts.

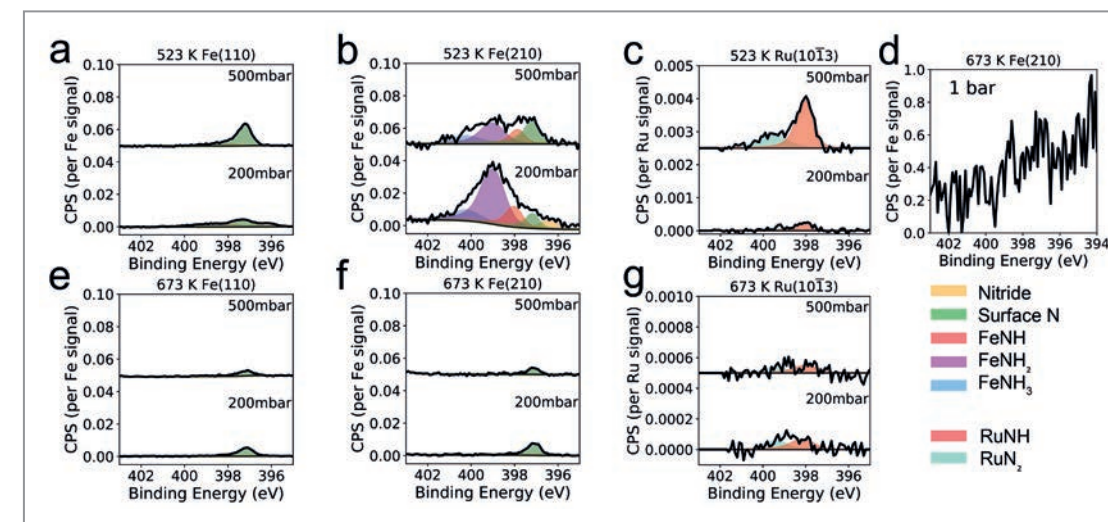
It is technically possible to study the ammonia synthesis' reaction at very low pressures, but ammonia production becomes negligible. This issue is especially important for hydrogenation reactions like ammonia formation where reactivity does not increase in simple proportion to pressure [4]. Thus, conducting studies not only *in situ* (in expected operational conditions) but also *operando* (under proven operational conditions) is essential to ensure practical reliable results.

To enable such studies at pressures up to 1 bar, scientists at Stockholm University have developed the high-pressure XPS setup POLARIS [5]. Figure 1a shows a schematic of the setup and how gas flows around the same orifice that collects photoelectrons and reaction products. The synchrotron light strikes the sample at a grazing angle in the virtual pressure cell, generating photoelectrons precisely where the reaction occurs. The collected photoelectrons and a portion of the gas enter into an electrostatic lens that separates the electrons from the gas for individual analysis. The gas composition is measured in a quadrupole mass spectrometer (MS) while the electrons are analysed in a hemispherical electron analyser.

To measure ammonia conversion, the gas composition was changed from an inert nitrogen environment to a nitrogen-hydrogen mixture. In Fig. 1b, the MS signal for ammonia rises as the reaction starts, indicated by change from a blue (nitrogen-only) to a green (nitrogen and hydrogen), showing the flow which is plotted on the left axis. The black line shows the ammonia signal rising from the background level as the reaction begins.

By measuring multiple samples under various conditions, the relative activity of each catalyst can be measured independently, as shown in Fig. 1c.

Figure 2
Photoelectron spectra are gathered at various reaction conditions a-c) from below the highest activity 523 K at both 200 mbar and 500 mbar, for each catalyst, as well as d) high pressure 1 bar at 673 K, and at the highest activity conditions, 673 K at the same pressure. The spectra are deconvoluted, displaying the various chemical states of the catalyst's surfaces.



With the use of POLARIS, scientists achieved the pressure required to produce ammonia. By testing different catalysts, they identified not only the active states of the catalysts but also the reactivity in terms of rate-limiting steps and thereby detected new insights into each catalyst's operation and limitations.

Figure 2 illustrates the chemical state of the nitrogen on the catalyst surface during the reaction as a function of temperature and pressure. Figure 2a-c show the chemical states at two pressures with a temperature where the reaction rate is low. There may be a slight pressure dependence based on the catalyst, with our data suggesting that hydrogenation increases with rising pressure. From Fig. 2d, taken at 1 bar, it appears that the catalyst is almost a pure metal; under industrial conditions the surface may consist of completely pristine metal.

At low temperatures, where the reaction proceeds slowly, the surface of the catalyst may have a significant coverage of NH_x species. This shows that at low temperatures the rate-limiting step is the hydrogenation of surface nitrogen, not nitrogen fixation. In contrast, the ruthenium (Ru) surface shows much lower nitrogen content, independent of temperature or pressure, compared to the Fe surface, despite Ru being the most active catalyst. These results confirm that iron binds nitrogen more readily than ruthenium, even though ruthenium is a more active catalyst.

After the reaction temperature is raised to real operating conditions at high rates, the surface chemistry changes dramatically. Figures 2e-g demonstrate that the nitrogen on the Fe surfaces decreases significantly, with little or no hydrogenated nitrogen remaining. Meanwhile, the nitrogen on the Ru surface is almost indistinguishable from the background signal. The low occupancy of the surface occurs due

to the high turnover of the surface, proving that the reaction is rate-limited at the initial step of nitrogen adsorption, followed by dissociation for all the catalysts studied.

Through the detailed analysis and a novel experimental approach, the researchers answered many long-standing questions about the reaction mechanism of the most important catalyst of the past century.

Author contact: Christopher Goodwin, cgoodwin@cells.es

References

1. A. E. Yüzbaşıoğlu, C. Avcı and A. O. Gezerman, 'The current situation in the use of ammonia as a sustainable energy source and its industrial potential', *Curr. Res. Green Sustain. Chem.* 5, 100307 (2022).
2. V. Smil, 'Detonator of the population explosion', *Nature* 400, 415–415 (1999).
3. B. Herzog, D. Herein and R. Schlögl, 'In situ X-ray powder diffraction analysis of the microstructure of activated iron catalysts for ammonia synthesis', *Appl. Catal. A: Gen.* 141, 71–104 (1996).
4. G. A. Somorjai and N. Materer, 'Surface structures in ammonia synthesis', *Top. Catal.* 1, 215–231 (1994).
5. P. Amann et al., 'A high-pressure x-ray photoelectron spectroscopy instrument for studies of industrially relevant catalytic reactions at pressures of several bars', *Rev. Sci. Instrum.* 90, 103102 (2019).

Original publication

'Operando probing of the surface chemistry during the Haber-Bosch process', *Nature* 625, 282–286 (2024).
DOI: 10.1038/s41586-023-06844-5



Christopher M. Goodwin¹, Patrick Lömker¹, David Degerman¹, Bernadette Davies², Mikhail Shipilin¹, Fernando Garcia-Martinez³, Sergey Koroidov¹, Jette Katja Mathiesen¹, Raffael Rameshan⁴, Gabriel L. S. Rodrigues¹, Christoph Schlueter³, Peter Amann² and Anders Nilsson¹

1. Department of Physics, Stockholm University, Stockholm, Sweden
2. Department of Materials and Environmental Chemistry, Stockholm, Sweden
3. Deutsches Elektronen-Synchrotron DESY, Hamburg, Germany
4. Institute for Physical Chemistry, Montan University Leoben, Leoben, Austria

Figure 1

a) The experimental setup demonstrates the illuminated sample in a virtual pressure cell where gas flows towards the sample through the same device that gathers the photoelectrons and samples gas of the reaction environment. The gas is separated from the photoelectrons and analysed by MS, an example of the results can be found in b). As the gas changes from inert nitrogen (blue) to a 1:1 mixture of hydrogen and nitrogen (green) the MS signal for ammonia increases (black). Finally, by comparing different catalysts, the relative reactivity can be determined, shown here in c).

Uncovering catalyst structures for the removal of trace ammonia

Operando spectroscopy reveals structure of efficient clean air catalysts

Ammonia, generated from green hydrogen and nitrogen, is a potential CO₂-free fuel, allowing for storage and transport of renewable energy [1]. However, its use for energy production results in traces of toxic unconverted ammonia slipping in the atmosphere. For widespread industrial application this slip needs to be prevented which is done with help of ammonia slip catalysts (ASCs) facilitating oxidation of toxic ammonia to environmentally benign nitrogen. This requires a delicate balance between, on the one hand, a catalyst active enough to activate ammonia, and on the other hand, avoiding overoxidation of nitrogen to nitrogen oxides which are even more toxic greenhouse gases.

X-ray absorption spectroscopy (XAS) is an ideal tool to probe heterogeneous catalysts at work (i.e. *operando*) due to element selectivity and the penetration power of X-rays. It allows studies directly in chemical reactors under realistic conditions such as temperature and gas or liquid environment at relevant pressures. Catalytic conversion most often occurs on the surface of catalyst particles which comprises a single-digit percent of all atoms probed by XAS. This limits the applicability of the bulk-averaging XAS and requires the use of highly sensitive detection modes, providing good statistics, as well as advanced data analysis

techniques. In this work, we exploited the excellent statistics offered by the high brilliance beam and the quick-scanning XAS (QEXAFS) monochromator with the corresponding detection system installed at the PETRA III P64 beamline. These measurements were combined with multivariate curve resolution–alternating least squares (MCR-ALS) and augmented by kinetic studies, *operando* infrared (IR) spectroscopy and quantum chemical (DFT) calculations. This allowed identifying small contributions from different surface and subsurface Pt species at different temperatures and correlate them with an onset of catalytic activity and production of desired and unwanted products, i.e. selectivity.

The study was performed on an industrially relevant Pt/Al₂O₃ catalyst with ca. 2 nm mean Pt nanoparticle size leading to the highest specific activity of platinum [2]. It was further validated on a derivative sample with > 13 nm

Figure 1
Contour plot of Pt L₃ XANES region of normalised *operando* QEXAFS spectra of the tested Pt/Al₂O₃ catalyst recorded during temperature-programmed ammonia oxidation reaction, covering three different activity and selectivity regimes (500 ppm of NH₃ and 10% O₂, inert balance). a) conventional representation of three most different XANES spectra corresponding to three temperature regimes with different catalytic properties. b) contour plot of the *operando* QEXAFS dataset highlighting the evolution of spectral features during the catalytic experiment. c) temporal evolution of the X-ray absorption profile at the energy near the maximum absorption (11568.9 eV) during the temperature-programmed reaction.

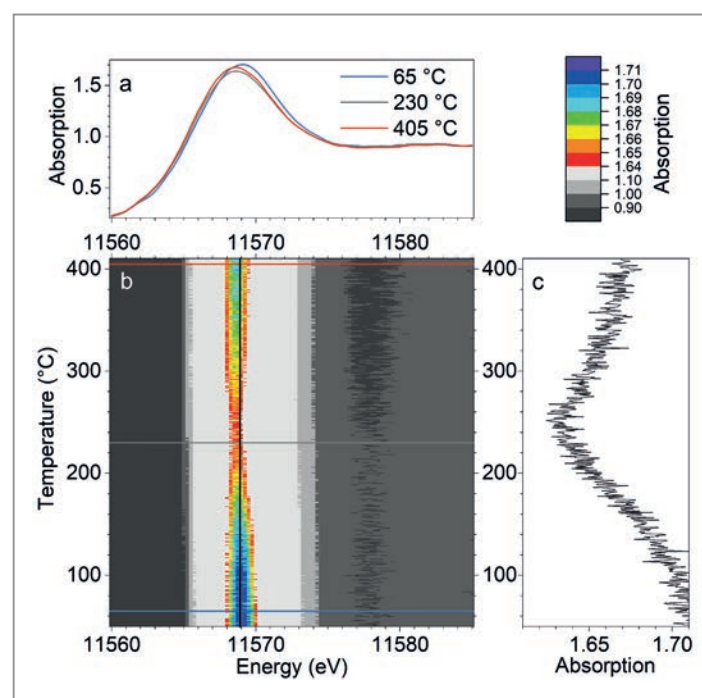
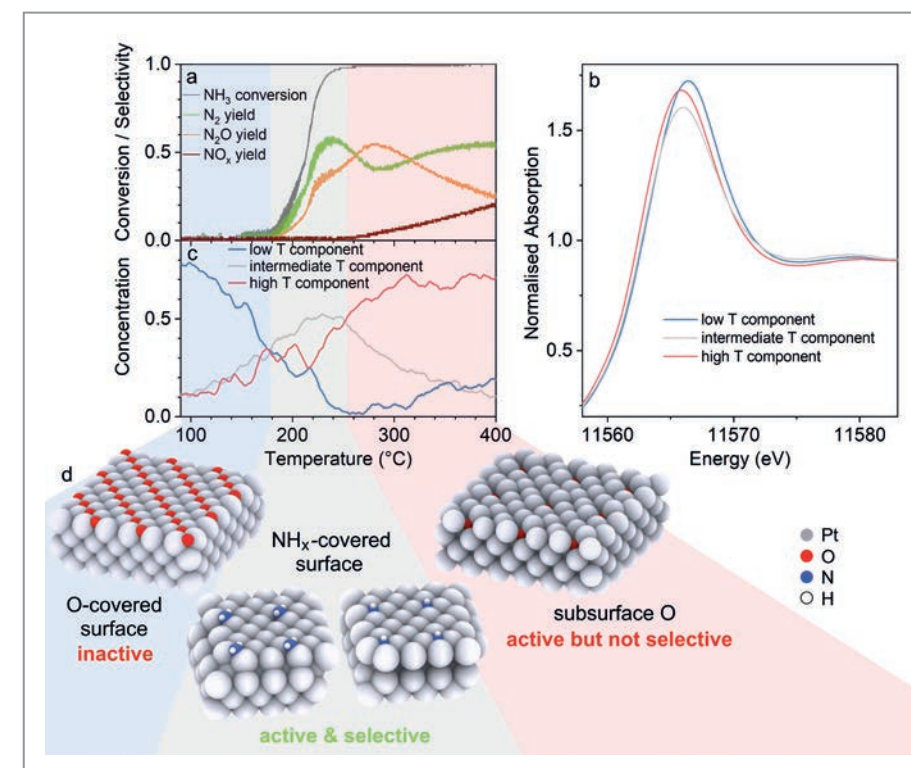


Figure 2
Structure-activity relationship demonstrating surface and subsurface Pt species at the origin of different activity and selectivity modes of platinum ammonia oxidation catalysts. a) ammonia conversion and yields of desired (N₂) and undesired (N₂O and NO_x) products plotted alongside b) the most distinct XANES spectral components of the *operando* QEXAFS dataset and c) quantification of the corresponding Pt species. d) Models of surface and subsurface structure of Pt nanoparticles corresponding to different activity/selectivity/spectral regimes derived from comparison of the experimental and theoretically predicted XANES spectra.



nanoparticles typical of sub-optimally prepared or aged catalysts. First, catalytic tests identified temperature regimes with different activity and selectivity. Next, a kinetic study found that surface species detrimental to activation of NH₃ at temperatures below 180°C contain oxygen. Further advance was achieved with IR spectroscopy, identifying NH_x species on the catalyst surface in the temperature region corresponding to the highest selectivity to the desired N₂. Likewise, adsorbed nitrates were found on the catalyst surface at higher temperatures when undesired products were formed. IR spectroscopy, however, could not show if the observed species were located on the surface of catalytically active Pt nanoparticles or on the alumina support.

The final clue was provided by *operando* QEXAFS. Despite very similar spectral shape throughout the whole cycle, QEXAFS allowed reliable identification of three distinct spectral patterns at different temperature regions (Fig. 1a) corresponding to the different activity and selectivity regimes (Fig. 2a). Interestingly, the maximum absorption intensity, related to electronic density on Pt, went through the minimum indicating partial reduction followed by reoxidation of Pt surface (Fig. 1c) even if the energy position of the maximum shifted, pointing to different nature of oxide species (Fig. 1b). Potential Pt surface structural models were identified, taking into account insights from kinetic and IR studies and were optimised by DFT calculations. Finally, the theoretical spectra of all potential structures were matched with experimental ones, confirming the three relevant Pt species: PtO_x surface oxides hindering activation of ammonia at low temperatures (inactive), metallic Pt surface covered with NH_x in the

intermediate temperature region (active and selective), Pt with subsurface oxygen which results in undesired NO_x (Fig. 2d). For the first time the work provides a clear view of Pt surface structure required for active and selective ammonia oxidation catalysts that needs to be maintained over the broadest possible range of operating conditions. This goal can be achieved via both target-driven synthesis of new generation catalysts and optimisation of industrial reaction conditions.

Author contact: Vasyi Marchuk, vasyi.marchuk@esrf.fr
Dmitry E. Doronkin, dmitry.doronkin@kit.edu

References

- F. Schüth, R. Palkovits, R. Schlögl and D. S. Su, 'Ammonia as a possible element in an energy infrastructure: catalysts for ammonia decomposition', *Energy Environ. Sci.* 5, 6278–6289 (2012).
- V. Marchuk, X. Huang, J.-D. Grunwaldt and D.E. Doronkin, 'Structure sensitivity of alumina- and zeolite-supported platinum ammonia slip catalysts', *Catal. Sci. Technol.* 13, 2946–2965 (2023).

Original publication

'Surface states governing the activity and selectivity of Pt-based ammonia slip catalysts for selective ammonia oxidation', *ACS Catalysis* 14, 1107–1120 (2024). DOI: 10.1021/acscatal.3c05019



Vasyi Marchuk¹, Dmitry I. Sharapa², Jan-Dierk Grunwaldt^{1,2} and Dmitry E. Doronkin^{1,2}

- Institute for Chemical Technology and Polymer Chemistry (ITCP), Karlsruhe Institute of Technology, Karlsruhe, Germany
- Institute of Catalysis Research and Technology (IKFT), Karlsruhe Institute of Technology, Eggenstein-Leopoldshafen, Germany

Unravelling magnetic properties of individual cells in brain tissue

Toward in-cell magnetometry with MRI and X-ray fluorescence.

The toxic properties of metals, which depend on their binding state in the brain, may play a critical role in disorders such as Parkinson's and Alzheimer's disease. Quantifying brain metals and determining their binding state can therefore provide insights into their pathological roles. We developed a multimodal method to measure these properties in tissues by combining ultra-high-field magnetic resonance imaging (MRI) and X-ray fluorescence. The technique allows insights into the binding state and thus toxicity of iron at the single-cell level. It was shown that dopaminergic neuronal iron, a potential contributor to Parkinson's disease, may be more toxic than previously thought. This approach brings us closer to non-invasive biomarkers for earlier disease diagnosis.

In the human body iron allows oxygen transport, aids cellular energy production, the immune system and brain function. But like many metals, iron is a double-edged sword; The toxic effects of excessive amounts of iron are associated with cell death in neurodegenerative conditions such as Alzheimer's disease, multiple sclerosis and Parkinson's disease (PD). The toxicity of iron likely depends on how it is stored: When firmly bound, it may be less toxic than when loosely bound and more accessible to cell-damaging processes. Neuromelanin, for instance, the major iron-binding polymer in dopaminergic neurons, has been suggested to bind iron in two sites: a low-affinity high-toxicity site and a high-affinity low-toxicity site (Fig. 1c) [1]. However, until now it has not been possible to identify the binding state of iron without removing the binding compound from its physiological environment. This has greatly limited our ability to understand the iron's function, as the removal of

iron-binding molecules from tissue is known to alter the binding state [1]. We wanted to overcome these obstacles by combining ultra-high-field MRI with proton-induced X-ray emission and X-ray fluorescence, allowing us to examine iron storages directly in tissue.

Magnetic resonance imaging provides 3D images of the body's interior due to its sensitivity to hydrogen protons, mainly present as water (Fig. 1a). Bodily tissues have different microstructural environments in which water molecules diffuse, leading to different relaxation times of tissue magnetisation and variable contrasts in the final image [2]. The presence of magnetisable metals—such as iron—due to the fields they generate, can be inferred through relaxation time-changes of water. While this has already advanced our understanding of iron in the brain, findings have been limited because the binding state has remained elusive.

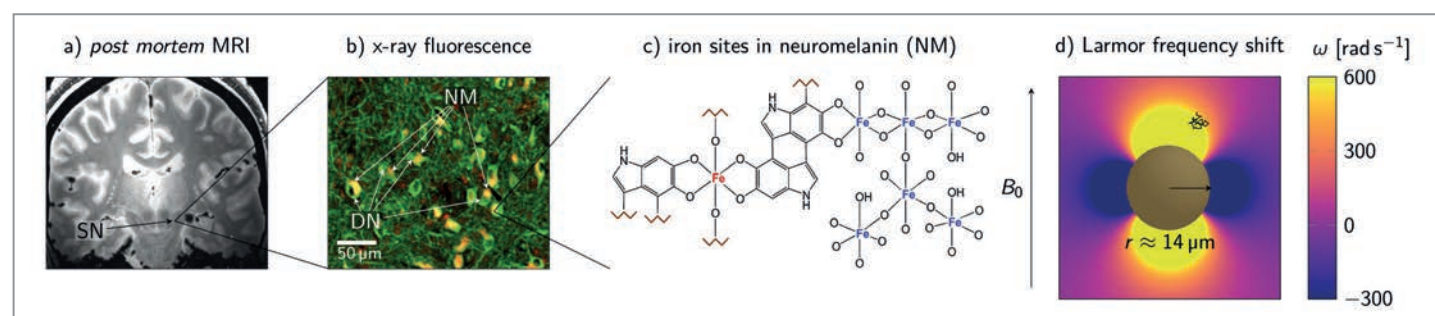


Figure 1 Combining MRI microscopy and X-ray fluorescence for susceptometry of dopaminergic neurons. a) An MRI image shows the dark substantia nigra (SN), the focus point of dopaminergic neuron degeneration in Parkinson's disease. b) Dopaminergic neurons (DNs, green) store iron in the molecule neuromelanin (NM, yellow). DN's were stained with nickel-enhanced immunohistochemistry, allowing their detection with X-ray fluorescence. c) Neuromelanin has two iron-binding sites with distinct magnetic properties: a low-affinity high-toxicity (red) and a high-affinity low-toxicity binding site (blue). d) For single neuron magnetometry, we modelled dopaminergic neurons approximating them as magnetised spheres which induce a dipole field in their vicinity that is sensed by water protons (indicated with a black line). (Figures adapted from the original publication).

Figure 2

Estimating the susceptibility of iron in dopaminergic neurons. a) MRI microscopy phase images show dopaminergic neurons as dipolar phase perturbations. b) We estimated the susceptibility of iron in dopaminergic neurons from the ratio of individual neuron's magnetic moment and iron mass. The value we obtained was close to the susceptibility of iron bound to the low-affinity site (Fig. 1c). c) An individual neuron appears as dipolar phase perturbation in the MRI microscopy data and as iron hot spot in the iron concentration maps. d) We used X-ray fluorescence and proton-induced X-ray emission to obtain iron concentration maps on consecutive tissue sections, allowing to quantify the iron mass within entire cells.

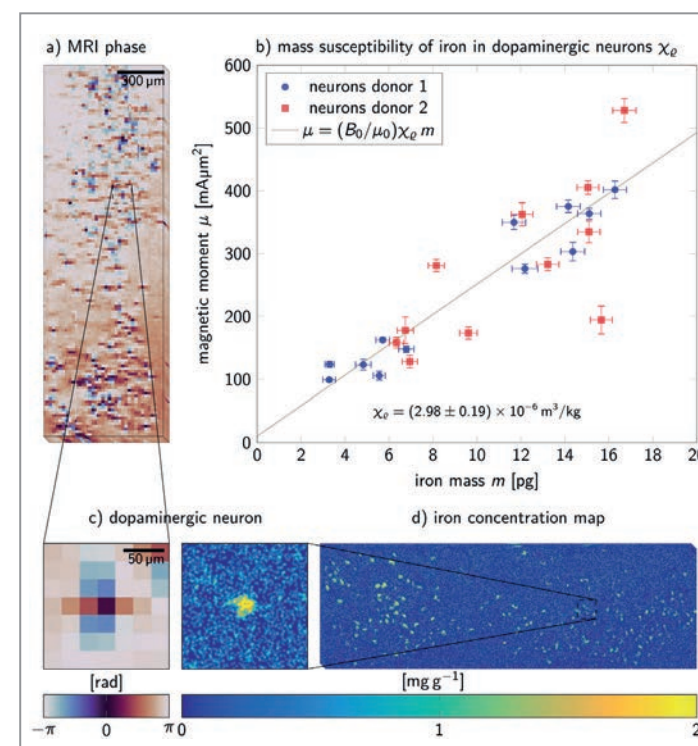
Quantifying how easily a material is magnetised, can solve this dilemma but raises another. Though tightly bound iron differs in terms of magnetic susceptibility from loosely bound iron, one cannot know what combination of low-susceptibility low-toxicity and high-susceptibility high-toxicity contributes to the overall measurement. Resolving this ambiguity also requires knowing the amount of magnetisable material within a voxel. This was accomplished with proton-induced X-ray emission and X-ray fluorescence for metal quantification (Fig. 1b) [3].

The voxel size was reduced as much as possible with ultra-high-field MRI scanning, so that resolutions at the cellular scale were achieved. Fortunately, the iron-containing neurons in the post-mortem sample were well separated from each other which made it possible to quantify precisely the impact of single cells on the MRI signal. The image data were then fit with signals predicted by describing the iron sources as isolated magnetic dipoles—an accurate approximation in the far field (Fig. 1d). Separately, measurements of iron quantity were obtained from the tissue samples with proton-induced X-ray emission and ultrasensitive X-ray fluorescence conducted at the PETRA III beamline P06. Finally, the 'super-resolution MRI microscopy' (Fig. 2a) was compared with those from two X-ray techniques (Fig. 2d), yielding the susceptibility of the metal bound in a cell (Fig. 2b).

With this novel combined method, we managed to measure the susceptibility of iron contained within individual human dopaminergic neurons in the post-mortem brain tissue samples. Surprisingly, contrary to common belief, most iron in the dopaminergic neurons examined was not tightly bound in the high-affinity site of neuromelanin but loosely bound to the low-affinity site. This suggests higher iron toxicity in dopaminergic neurons than previously presumed, with major implications for neurodegenerative disorders that involve iron. If the findings hold, the new method may help advance MRI exploration of iron toxicity and contribute to the development of new MRI-readable biomarkers for earlier detection of various neurodegenerative diseases.

Author contact:

Malte Brammerloh, mbrammerloh@cbs.mpg.de
 Nikolaus Weiskopf, weiskopf@cbs.mpg.de
 Joshua Grant, grant@cbs.mpg.de
 Evgeniya Kirilina, kirilina@cbs.mpg.de



References

1. L. Zecca et al., 'The Role of Iron and Copper Molecules in the Neuronal Vulnerability of Locus Coeruleus and Substantia Nigra during Aging', *Proc. Natl. Acad. Sci. U.S.A.* **101**, 9843–48 (2004).
2. N. Weiskopf, L. J. Edwards, G. Helms, S. Mohammadi and E. Kirilina. 'Quantitative Magnetic Resonance Imaging of Brain Anatomy and in Vivo Histology', *Nat. Rev. Phys.* **1–19** (2021)
3. I. Friedrich et al., 'Cell Specific Quantitative Iron Mapping on Brain Slices by Immuno-MPIXE in Healthy Elderly and Parkinson's Disease', *Acta Neuropath.* **Commun.** **9**, 47 (2021).

Original publication

'In Situ Magnetometry of Iron in Human Dopaminergic Neurons Using Superresolution MRI and Ion-Beam Microscopy', *Physical Review X* **14**, 021041 (2024). DOI: 10.1103/PhysRevX.14.021041



Malte Brammerloh^{1,2,3}, Renat Sibgatulin⁴, Karl-Heinz Herrmann⁴, Markus Morawski^{1,5}, Tilo Reinert^{1,5}, Carsten Jäger^{1,5}, Roland Müller¹, Gerald Falkenberg⁶, Dennis Brückner⁶, Kerrin J. Pine¹, Andreas Deistung⁷, Valerij G. Kiselev⁸, Jürgen R. Reichenbach⁴, Nikolaus Weiskopf^{1,3,9} and Evgeniya Kirilina¹

1. Max Planck Institute for Human Cognitive and Brain Sciences, Leipzig, Germany
2. International Max Planck Research School on Neuroscience of Communication: Function, Structure, and Plasticity
3. Felix Bloch Institute for Solid State Physics, Faculty of Physics and Earth System Sciences, Leipzig University, Leipzig, Germany
4. Institute of Diagnostic and Interventional Radiology, Jena University Hospital, Jena, Germany
5. Paul Flechsig Institute—Centre of Neuropathology and Brain Research, Leipzig University, Leipzig, Germany
6. Deutsches Elektronen-Synchrotron DESY, Hamburg, Germany
7. University Clinic and Outpatient Clinic for Radiology, University Hospital Halle (Saale), Halle (Saale), Germany
8. Department of Diagnostic and Interventional Radiology, University Medical Center Freiburg, University of Freiburg, Freiburg, Germany
9. Wellcome Centre for Human Neuroimaging, Institute of Neurology, University College London, London, United Kingdom

New imaging technique at PETRA III revolutionising breast cancer research

Simultaneous 3D information on the nanostructure, fiber orientation and chemical composition of the tumour

Breast cancer caused 685000 deaths globally in 2020 according to the World Health Organisation. It is not life-threatening in its earliest form. But if the cancer cells are able to spread further in the tissue to nearby lymph nodes or important organs, this metastasis can be fatal. We developed an advanced multimodal imaging approach and applied it to investigate breast cancer metastasis. The results show how key molecules collectively influence the metastatic mechanism. This breakthrough paves the way for an in-depth investigation of breast cancer metastasis, promising novel therapeutic approaches and personalised treatment strategies, which could ultimately save patients' lives if recognised early enough.

It is imperative that we understand the mechanisms of metastasis if we are to develop effective treatments for breast cancer. Metastasis remains the leading cause of death [1]. Changes in the extracellular matrix, particularly the remodelling of collagen fibrils, are a key factor in this process. Collagen provides structural support and influences cell behaviour. Alterations in its organisation are closely tied to tumour growth and spread, making it an important and promising focus for therapeutic research. Researchers have identified 'tumour-associated collagen signatures' which show how cancer cells interact with their surroundings through changes in fibre orientation, density, and cross-linking in the tumour environment.

While much of the research has been conducted on cell cultures or animal models, studying real tissue samples from breast cancer patients is essential for fully understanding the disease. Investigating breast cancer in three dimensions offers a better representation of the complexity of metastasis compared to traditional models.

In addition to collagen remodelling, other molecules like matrix metalloproteinases (MMPs) and vascular endothelial growth factor (VEGF) are also key players in metastasis. MMPs break down the extracellular matrix, including collagen, enabling cancer cells to invade nearby tissues. VEGF is a key driver of new blood vessel formation, supporting tumour growth and cancer cell spread.

Recent advances in X-ray imaging technologies, such as small-angle X-ray scattering tensor tomography (SAXS-TT) and X-ray fluorescence computed tomography (XRF-CT), provide new and effective methods for exploring collagen structures and metal distribution in tumours in three dimensions. SAXS has already provided invaluable insights into the structural arrangement of collagen in breast tumours. When combined with computed tomography (SAXS-CT), it allows for detailed 3D mapping of collagen in both benign and malignant tissues [2]. SAXS-TT provides further insights by visualising nanoscale collagen structures, deepening our understanding of their role in tumour progression (Fig. 1).

XRF-CT is an invaluable addition to SAXS-TT, allowing researchers to visualise and quantify metal elements such as zinc and iron which are associated with cancer development. These metals in tumours affect cancer cell behaviour [3]. At the SAXSMAT beamline P62 at PETRA III [4], we developed a multimodal approach, combining SAXS-TT and XRF-CT. This gave us a comprehensive view of how collagen remodelling and metal accumulation interact during breast cancer metastasis.

Figure 1

Artistic view of the Advanced Multimodal X-ray Tomography Imaging setup at the SAXSMAT beamline P62. The three-dimensional orientation distribution of the collagen fibres in the breast cancer specimen is highlighted here. (Credit: S. Haas, DESY)

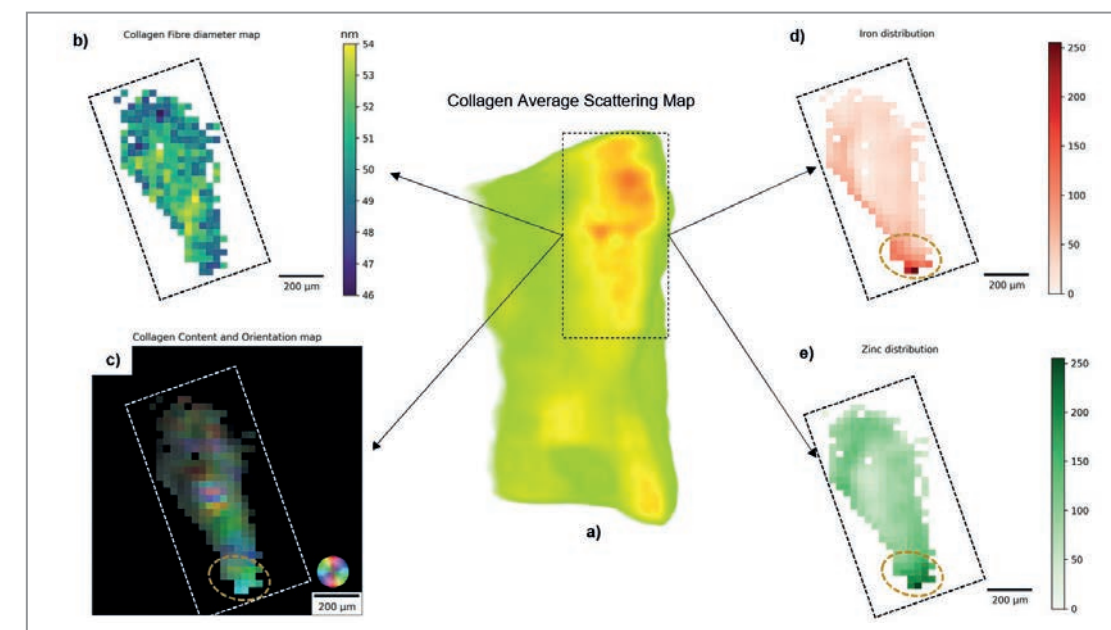
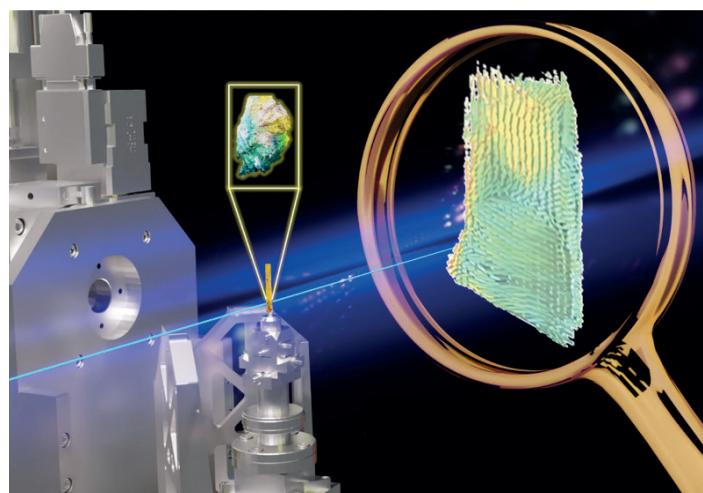


Figure 2

Multimodal X-ray tomography. a) Three-dimensional map of the average scattering of the collagen fibrils. The dashed rectangle indicates the higher scattering intensity region. The green area inside the dashed rectangle was masked out for further maps due to none or very low collagen content. b) The distribution of the calculated collagen fibril diameter within the region of interest (ROI). c) The orientation map retrieved from the SAXS-TT reconstruction in Fig. 1. The orientation is colour-coded according to the colour wheel inset. Highly-oriented collagen fibrils show up with bright colours, whereas dense fibrils without preferential orientation are darker. d) and e) Normalised distribution of Fe and Zn, respectively. The brown ellipse dashed area in c), d) and e) highlights a potential metastatic site. (Figure from original publication)

Our observations revealed a clear and significant correlation between zinc accumulation, linked to MMP activity and the highly-oriented collagen structure (see the maps shown in Fig. 2). MMPs degrade the extracellular matrix, aligning collagen fibres in ways that facilitate cancer cell migration and create pathways that allow the cells to invade other tissues. Iron accumulation, associated with VEGF, undoubtedly promotes angiogenesis, ensuring the blood supply needed for tumour growth and metastasis.

This study bridges the gap between experimental models and real tissue samples, opening the door for deeper exploration of breast cancer metastasis and pre-metastatic niches. These imaging techniques allow us to create comprehensive 3D maps of tumours and secondary organs in various breast cancer subtypes which will lead to more targeted diagnostic and treatment strategies.

This approach is currently limited to a few large-scale facilities due to the significant resources required. However, these techniques will undoubtedly become more accessible with advancements in imaging technology and machine learning, transforming breast cancer research and treatment. These methods will lead to personalised treatment strategies that improve patients' outcomes, as they provide better insights into tumour environments, collagen behaviour and metal accumulation.

Author contact:

André L. C. Conceição, andre.conceicao@desy.de

References

1. C. L. Chaffer and R. A. Weinberg, 'A perspective on cancer cell metastasis', *Science* 331, 1559-1564 (2011).
2. A. L. C. Conceição, J. Perlich, S. Haas and S. S. Funari, 'SAXS-CT: A nanostructure resolving microscopy for macroscopic biologic specimens', *Biomed. Phys. Eng. Express* 6, 35012 (2020).
3. M. P. Silva, D. M. Silva, A. L. C. Conceição, A. Ribeiro-Silva and M. E. Poletti, 'Role of Ca, Fe, Cu and Zn in breast cancer: Study by X-ray fluorescence techniques and immunohistochemical analysis', *X-Ray Spectrom.* 42, 303-311 (2013).
4. S. Haas, X. Sun, A. L. C. Conceição, J. Horbach and S. Pfeffer, 'The new small-angle X-ray scattering beamline for materials research at PETRA III: SAXSMAT beamline P62', *J. Synchrotron Radiat.* 30, 1156-1167 (2023).

Original publication

'Unveiling breast cancer metastasis through an advanced X-ray imaging approach', *Scientific Reports* 14, 1448 (2024). DOI: 10.1038/s41598-024-51945-4



André L. C. Conceição¹, Volkmar Müller², Eike-Christian Burand³, Malte Mohme⁴, Leonard C. Nielsen⁵, Marianne Liebi^{5,6,7} and Sylvio Haas¹

1. Deutsches Elektronen-Synchrotron DESY, Hamburg, Germany
2. Department of Gynecology, University Medical Center Hamburg-Eppendorf, Hamburg, Germany
3. Institute of Pathology, University Medical Center Hamburg-Eppendorf, Hamburg, Germany
4. Department of Neurosurgery, University Medical Center Hamburg-Eppendorf, Hamburg, Germany
5. Department of Physics, Chalmers University of Technology, Gothenburg, Sweden
6. Photon Science Division, Paul Scherrer Institute, Villigen, Switzerland
7. Institute of Materials, Ecole Polytechnique Fédérale de Lausanne (EPFL), Lausanne, Switzerland

Structural insights for Parkinson's therapy

Advancing neuroprotective strategies through molecular understanding of the CDNF-GRP78 interaction

Parkinson's disease (PD) is a neurodegenerative disorder marked by the progressive loss of dopamine-producing neurons in the brain leading to motor symptoms such as tremors, stiffness and bradykinesia. Despite extensive research, no treatments can slow or halt disease progression, with current therapies focusing mainly on symptom management. In this context, Cerebral Dopamine Neurotrophic Factor (CDNF) has emerged as a promising candidate for disease-modifying therapy in PD (Fig. 1) [1]. As an unconventional neurotrophic factor, CDNF supports the neurons' growth, survival and differentiation, particularly under stress. However, the mechanisms underlying its protective effects remain largely unclear.

To address this knowledge gap, scientists from Herantis Pharma PLC collaborated with EMBL scientists and BIOSAXS GmbH to investigate the relationship between CDNF and the Unfolded Protein Response (UPR). The UPR is a critical cellular stress response pathway that maintains protein homeostasis in the endoplasmic reticulum. Under stress conditions, such as the accumulation of misfolded proteins, the UPR activates protective mechanisms to restore normal cellular function or induce cell death if the damage is irreparable. A key regulator of the UPR is Glucose-Regulated Protein 78 (GRP78), a 'chaperone' that facilitates proper protein folding and helps cells to cope with stress.

In this study, researchers utilised X-rays at EMBL's BIOSAXS beamline P12 at PETRA III [2] to explore the solution structure of the CDNF-GRP78 complex (Fig. 2a). Employing small-angle X-ray scattering (SAXS), they uncovered es-

ential details regarding the interaction between CDNF and GRP78. Using an adaptable chromatography-coupled setup (SEC-SAXS) [3,4] was crucial, as it allowed for the separation of the fully bound complex from single proteins, thus ensuring monodispersity—a prerequisite for robust analysis (Fig. 2b,c) [5]. To accurately identify the binding site, the team used various *in silico* techniques to interpret the SAXS data, including homology modeling, rigid body modeling, normal mode analysis [6] and molecular dynamics simulations (Fig. 2d) [7].

A significant finding was that the C-terminal domain of CDNF plays a predominant role in binding to GRP78. This was further validated by a second SAXS-based structure of CDNF lacking the N-terminal domain, reinforcing the idea that CDNF primarily interacts with GRP78 through its C-terminal domain. The structure also pointed out the specific

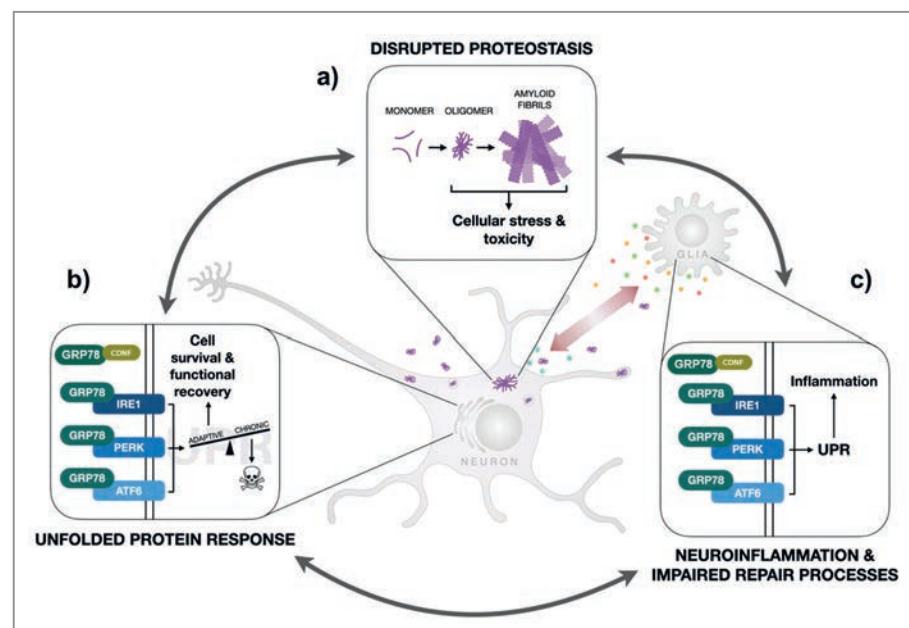
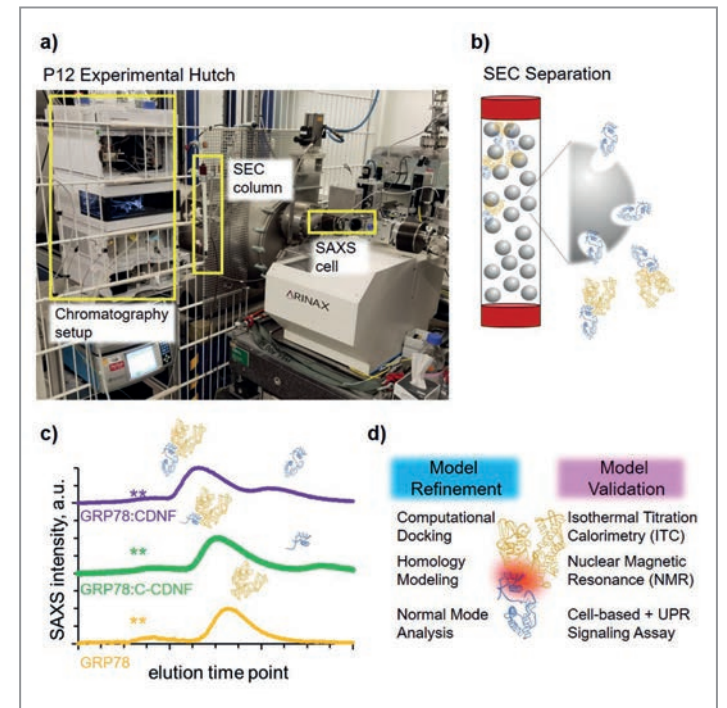


Figure 1 Interconnections of proteostasis, UPR pathway and neuroinflammation in Parkinson's disease. a) Brain accumulation of α -synuclein aggregates is a key neuropathological feature of Parkinson's disease, affecting both neuronal and glial cells. b) CDNF modulates the activity of the UPR pathway by binding to the UPR master regulator GRP78 to promote function and survival c) UPR is also involved in the regulation of immune and glial cell activity. CDNF modulates neuroinflammation in microglial cells via GRP78 and UPR signaling.

Figure 2

Experimental strategy for SAXS analysis of the CDNF-GRP78 binding site. a) Experimental setup at P12, highlighting the chromatography and SAXS modules. b) Size-based separation system of the GRP78:CDNF complex from excess CDNF. c) Elution profiles from SEC-SAXS experiments: GRP78 alone (orange), GRP78:C-CDNF (green) and GRP78:CDNF (purple) with the indication of excess ligand removal as well as higher oligomeric structures (**). d) Overview of model refinement and validation methods with the binding site of CDNF on GRP78 highlighted in red in the cartoon representation: GRP78 (orange), CDNF (blue).



loop in CDNF that is likely to interact with GRP78. To confirm the solution structure (Fig. 2d), complementary biophysical binding studies were conducted. Techniques like isothermal titration calorimetry (ITC), performed at the EMBL sample characterisation and preparation facility (SPC), enabled seamless integration with SAXS data collection and analysis. These studies effectively compared wild-type and modified structures where single amino acid residues were mutated to assess their impact on binding. Notably, mutating critical residues to alanines abolished binding, underscoring their significance in the interaction.

Further examinations, including spectral shift assays and nuclear magnetic resonance (NMR) titration with $^{13}\text{C}/^{15}\text{N}$ -Ala-labeled C-CDNF, confirmed the involvement of key residues in the binding interface as elucidated by SAXS. Ultimately, the functional significance of these structural observations was validated through additional *in vitro* cellular experiments which demonstrated that mutations in key residues not only disrupted binding but also abolished CDNF's neuroprotective function in neuronal cultures. This pivotal evidence establishes a connection between CDNF's interaction with GRP78 and its therapeutic potential, emphasising the need to target this interaction as a crucial step toward advancing Parkinson's disease treatments. Drugs designed based on the CDNF loop (HER-096) [8] involved in GRP78 interaction have been proven to be safe and pass the blood-brain barrier (BBB) in clinical trials.

In conclusion, understanding the structural basis of the CDNF-GRP78 interaction paves the way for next-generation CDNF-based therapies that target the molecular mechanisms of neurodegeneration rather than merely alleviating symptoms. Access to large-scale facilities is vital for establishing robust assays to evaluate drug candidates. Solution SAXS stands out as a valuable tool for examining binding interactions under conditions that closely mimic physiological environments (including variations in concentration and pH). The effects of these parameters can be readily detected in scattering data, highlighting the importance of automation for achieving high-throughput and reliable analysis.

Author contact:
 Melissa Gräwert, melissa.graewert@embl-hamburg.de
 Arnab Bhattacharjee, arnab.bhattacharjee@gmx.com
 Henri Huttunen, henri.huttunen@herantis.com

References

- H. J. Huttunen and M. Saarma, 'CDNF protein therapy in parkinson's disease', *Cell Transpl.* 28, 349–366 (2019).
- C. E. Blanchet et al., 'Versatile sample environments and automation for biological solution X-ray scattering experiments at the P12 beamline (PETRA III, DESY)', *J. Appl. Crystallogr.* 48, 431–443 (2015).
- M. A. Graewert and D. I. Svergun, 'Advanced sample environments and sample requirements for biological SAXS', *Methods Enzymol.* 677, 1–39 (2022).
- M. A. Graewert et al., 'Size exclusion chromatography (SEC) and light scattering (LS) devices to obtain high-quality small angle x-ray scattering (SAXS) data', *Crystals* 10, 975 (2020).
- C. M. Jeffries et al., 'Preparing monodisperse macromolecular samples for successful biological small-angle X-ray and neutron-scattering experiments', *Nat. Protoc.* 11, 2122–2153 (2016).
- A. Panjkovich and D. I. Svergun, 'Deciphering conformational transitions of proteins by small angle X-ray scattering and normal mode analysis', *Phys. Chem. Chem. Phys.* 18, 5707–5719 (2016).
- B. Jiménez-García et al., 'pyDockSAXS: protein-protein complex structure by SAXS and computational docking', *Nucleic Acids Res.* 43, W356–W361 (2015).
- N. Kuleskaya et al., 'HER-096 is a CDNF-derived brain-penetrating peptidomimetic that protects dopaminergic neurons in a mouse synucleinopathy model of Parkinson's disease', *Cell Chem. Biol.* 31, 593–606 (2024).

Original publication

'Structural basis of CDNF interaction with the UPR regulator GRP78', *Nature Communications* 15, 8175 (2024). DOI: 10.1038/s41467-024-52478-0



Melissa Ann Graewert^{1,2}, Maria Volkova³, Klara Jonasson³, Juha A. E. Määttä⁴, Tobias Gräwert², Samara Mamidi³, Natalia Kuleskaya⁵, Johan Evenäs³, Richard E. Johnson³, Dmitri Svergun², Arnab Bhattacharjee⁵ and Henri J. Huttunen⁵

- European Molecular Biological Laboratory EMBL c/o DESY, Hamburg, Germany
- BIOSAXS GmbH, Hamburg, Germany
- Red Glead Discovery AB, Lund, Sweden
- Faculty of Medicine and Health Technology, Tampere, Finland
- Herantis Pharma Plc, Espoo, Finland

How structure-activity relationships shape the future of rational design nucleic acid carriers

PH-dependent transitions in lipid nanoparticle mesophases

Lipid nanoparticles (LNPs) based on cationic ionisable lipids (CILs) represent the most advanced technology for delivery of nucleic acid. LNPs proved to be efficient and safe carriers for mRNA vaccines during the COVID-19 pandemic. Yet the mechanism of pH-dependent response that is believed to cause endosomal release of LNPs is not well understood. Minute variations of the lipid head group result in drastic differences in mRNA transfer. Here we present a systematic study of the liquid crystalline order and spacings of three ionisable lipids/cholesterol water mixtures. A pH-dependent structural transition from inverse micellar to inverse hexagonal order around the pKa value of the lipids is correlated with gene expression onset and hints towards a critical structure-activity relation.

LNPs provide efficient encapsulation and delivery of RNAs to living cells in the human body and are considered a platform technology for nucleic acid therapeutics [1]. Gene therapy enables the production of therapeutic proteins via messenger RNA or the knock-down of disease-related proteins via small interfering RNA. Rapid progress of LNP formulations with regards to efficiency and biocompatibility over the last twenty years led to the first FDA-approved LNP-based therapy in 2018 [1]. A cartoon of a lipid nanoparticle is shown in (Fig. 1a). The particles contain five components: cationic ionisable lipid (CIL), cholesterol, a structural lipid, a polyethyleneglycol functionalised (PEG)-lipid and nucleic acid. The components assemble into a characteristic core-shell architecture with distinct surface and solid core compositions. LNPs are taken up by cells by a process called endocytosis, i.e. the inside budding of the plasma membrane with the LNPs being internalised in endosomal vesicles. Subsequently, the endosomes undergo

acidification due to activity of proton pumps. It is understood that a pH-sensitive response of LNPs lead to endosomal membrane destabilisation and result in nucleic acid escape into the cytoplasm. Here the choice of ionisable lipid plays a crucial role, showing a two orders of magnitude improvement between the first generation of ionisable aminolipids, e.g. DLin-DMA (DD) and the second generation of ionisable aminolipids DLin-MC3-DMA (MC3), DLin-KC2-DMA (KC2), see also (Fig. 1b). In mice studies the AstraZeneca group showed that the difference in lipid efficiency is traced down to their endosomal escape efficacy.

In the following we hypothesise that the three CILs react differently to pH changes in the LNP core. We hence study the structure of macroscopic CIL/cholesterol mixtures in water as mimics for the LNP core phase. Using X-ray scattering at the P12 BioSAXS EMBL beamline at PETRA III, a sequence of ordered CIL/cholesterol mesophases with lowering pH values are observed, showing isotropic inverse micellar, cubic Fd3m inverse micellar, inverse hexagonal H_{II} and bicontinuous cubic Pn3m symmetry (Fig. 2a). The order of lipid phases follows a trend of decreasing spontaneous lipid curvature as the lipid headgroup becomes protonated [2]. Secondly, if polyadenylic acid (polyA) as mRNA surrogate is added to CIL/cholesterol, the lipid phases (Fig. 2b) coexist with a condensed nucleic acid lipid H_{II} phase (not

Figure 1
a) Schematic representation of a lipid nanoparticle (LNP) showing a characteristic core-shell architecture. The core moiety is formed by cationic ionisable lipid, cholesterol and nucleic acid. The outer monolayer contains PEG-lipid that stabilises the particles and promotes biocompatibility.
b) Three aminolipids (MC3, KC2, DD) exhibit the same amino group with pKa 6.5, the same type of lipid tails but different chemical head linker group
c) X-ray small angle X-ray scattering (SAXS) from a MC3/chol/water mesophase. (Credit: Adopted from original publication)

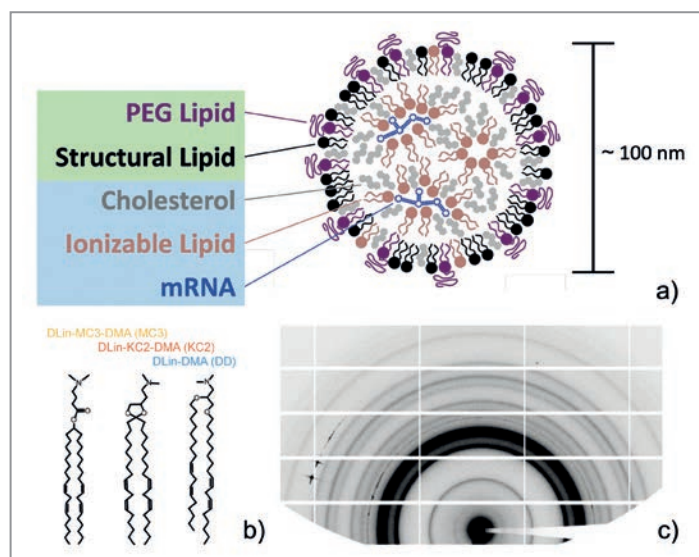
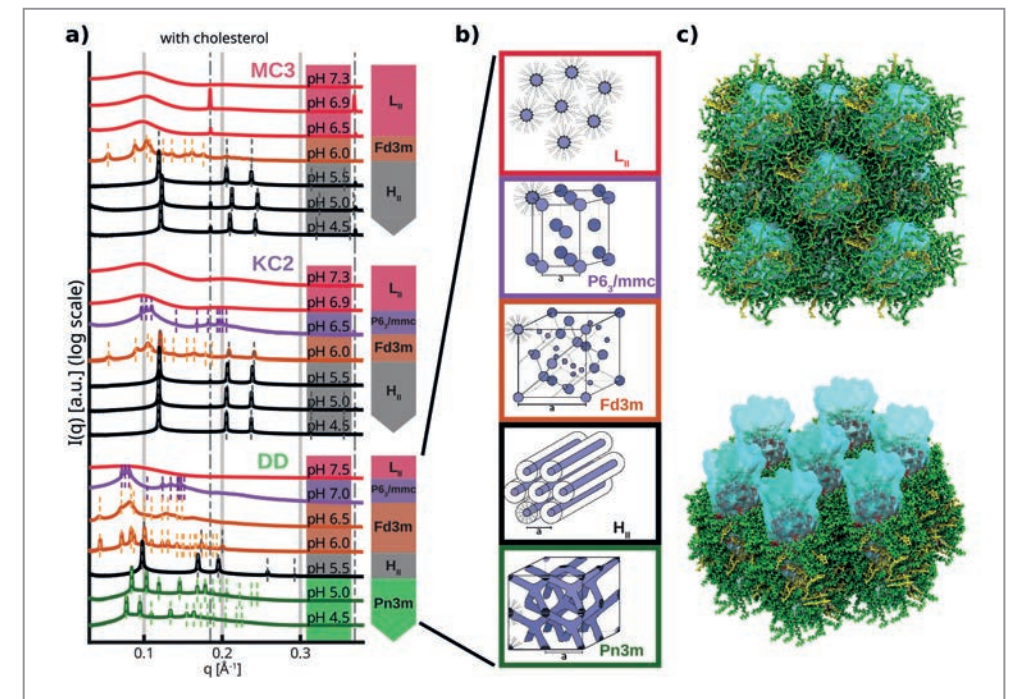


Figure 2
SAXS-based identification of pH-dependent mesophases. a) The three different ionisable lipid (MC3, KC2, DD), cholesterol, buffer exhibit a similar order of phases with decreasing pH value from inverse micellar isotropic L_{II} , inverse micellar cubic with P63/mmc symmetry, inverse micellar cubic with Fd3m symmetry, inverse hexagonal H_{II} , and bicontinuous cubic Pn3m. b) The order agrees with a trend from negative curvature toward zero curvature with increasing headgroup protonation. c) MD simulation of the inverse micellar and inverse hexagonal phase. (Credit: Adopted from original publication)



shown). Such complexed nucleic acid - cationic lipid represents a close to charge-neutral phase separated condensate (coacervate) [3]. We find that the structure of the complexed nucleic acid lipid H_{II} phase is pH-independent, leading us to believe that the pH response of the excess ionisable lipid phase is critical. Note that in clinical formulations cationic-lipid to anionic-nucleic acid charge ratio is typically chosen to be N/A=3 or larger. From the SAXS data we also find that the next-neighbour distance of the excess lipid phase shows a discontinuity at the Fd3m inverse micellar to inverse hexagonal H_{II} transition, occurring at about pH 6. Remarkably, DD shows a distinctly larger spacing and hydration compared to MC3 and KC2. This behaviour is also found in the scattering pattern from LNPs in solutions that show only one dominant length scale.

In order to gain molecular insights into the lyotropic order transition molecular dynamics (MD), simulations were carried out in the Augsburg group. As shown in Fig. 2b, both, stable inverse micellar as well as inverse hexagonal CIL/cholesterol phase, are reproduced for zero and fully headgroup charge, respectively. MD data allows quantitative comparison of the form factor, which in turn is used to fine-tune MD parameters, in particular the water molar fraction. Furthermore, MD simulation revealed an important molecular detail of the lipid headgroup conformation. While the uncharged headgroup is strongly folded back into the hydrophobic tail region, the charged headgroup sticks straight into the water phase.

To show that lyotropic phase behaviour relates to fusogenic mechanisms, we measured the fluorescence after LNP-based in-vitro transfection of eGFP-mRNA. From single-cell expression time courses we find earlier onset and more efficient expression for MC3 and KC2 compared to DD (Fig. 3b). Our data suggests that the pH-driven

Fd3m- H_{II} transition in bulk phases is a critical prerequisite for fusion, and that CIL-specific structural differences affect the propensity for endosomal fusion and hence mRNA release efficacy. These findings provide a novel perception of mode of action, emphasising a structural transition of the inner core phase as trigger for LNP fusogenic activity.

Author contact: Joachim Rädler, raedler@lmu.de
Nadine Schwierz, nadine.schwierz@physik.uni-augsburg.de
Lennart Lindfors, lennart.lindfors@astrazeneca.com

References

- J. A. Kulkarni, D. Witzigmann, S. B. Thomson, S. Chen, B. R. Leavitt, P. R. Cullis and R. Van Der Meel, 'The current landscape of nucleic acid therapeutics', *Nat. Nanotechnol.* **16**, 630 (2021).
- Z. Xu, J. M. Seddon, P. A. Beales, M. Rappolt and A. I. Tyler, 'Breaking Isolation to Form New Networks: PH-Triggered Changes in Connectivity inside Lipid Nanoparticles', *J. Am. Chem. Soc.* **143**, 16556 (2021).
- I. Koltover, T. Salditt, J. O. Rädler, and C. R. Safinya, 'An Inverted Hexagonal Phase of Cationic Liposome-DNA Complexes Related to DNA Release and Delivery', *Science*, **281**, 78-81 (1998).

Original publication

'pH-dependent structural transitions in cationic ionizable lipid mesophases are critical for lipid nanoparticle function', *Proceedings of the National Academy of Sciences* **120**, e2310491120 (2023). DOI: 10.1073/pnas.2310491120



Julian Philipp¹, Alexandra Dabkowska², Anita Reiser¹, Kilian Frank¹, Rafal Krzysztoń¹, Christiane Brummer¹, Bert Nickel¹, Clement. E. Blanchet³, Akhil Sudarsan⁴, Mohd Ibrahim⁴, Svante Johansson², Pia Skantze², Urban Skantze², Sofia Östman², Marie Johansson², Neil Henderson², Kjetil Elvevold², Bård Smedsrød⁵, Nadine Schwierz¹, Lennart Lindfors² and Joachim O. Rädler¹

- Ludwig Maximilians-University, Munich, Germany
- AstraZeneca, Gothenburg, Sweden
- European Molecular Biology Laboratory EMBL c/o DESY, Hamburg, Germany
- University of Augsburg, Augsburg, Germany
- University of Tromsø, Tromsø, Norway

Filming DNA repair

Time-resolved crystallography captures photolyase in action

Anyone who has suffered a sunburn knows first-hand that sunlight can be harmful. Discomfort isn't the only reason to take shelter, though. Direct sunlight can wreak havoc on cells' DNA and in the worst case lead to cancer. To cope, all organisms employ DNA repair enzymes that are constantly working to keep our genomes healthy. We studied the inner workings of one such enzyme, photolyase, using the power of X-ray free electron lasers (XFELs) to image and understand the DNA repair process as it took place.

Photolyase repairs the most common form of sunlight-induced damage where two pieces of DNA become incorrectly chemically bonded to one another following UV irradiation [1] (Fig. 1). Elegantly, photolyase captures and uses a second photon to drive this repair chemistry, making it one of the few known photoenzymes. If one looks around on a sunny day, photolyase is repairing DNA in the plants, animals and microbes all around us. Unfortunately, we humans suffer more from this UV damage than most other organisms because we lost the gene coding for photolyase some time ago during our evolutionary history. We believe this happened when our ancestors were nocturnal and didn't need to worry about the sun as they went about their nighttime rituals [2]. As a result, all placental mammals lack photolyase.

Our study focused on three questions. First, we knew the enzyme stabilised a photoexcited state of its chromophore, flavin adenine dinucleotide (FAD), sufficiently long

in order to conduct the repair chemistry. Outside of the enzyme system, FAD decays back to the ground state rapidly (10s ps) whereas it requires 100s ps to perform the electron transfer necessary to drive DNA repair [3]. The enzyme stabilises FAD for 2 ns, more than enough time to facilitate electron transfer, but how this quantum mechanical engineering is achieved was unclear.

Second, we wanted to know more about the DNA repair reaction itself. The damaged DNA has two chemical bonds that shouldn't be there. We knew photolyase broke both bonds, but for decades scientists debated whether they split simultaneously or one at a time [4].

Finally, when photolyase discovers a piece of damaged DNA, it grabs it and then waits until it absorbs enough sunlight to repair the damage. Once this job is done, it quickly releases the repaired DNA and starts looking for

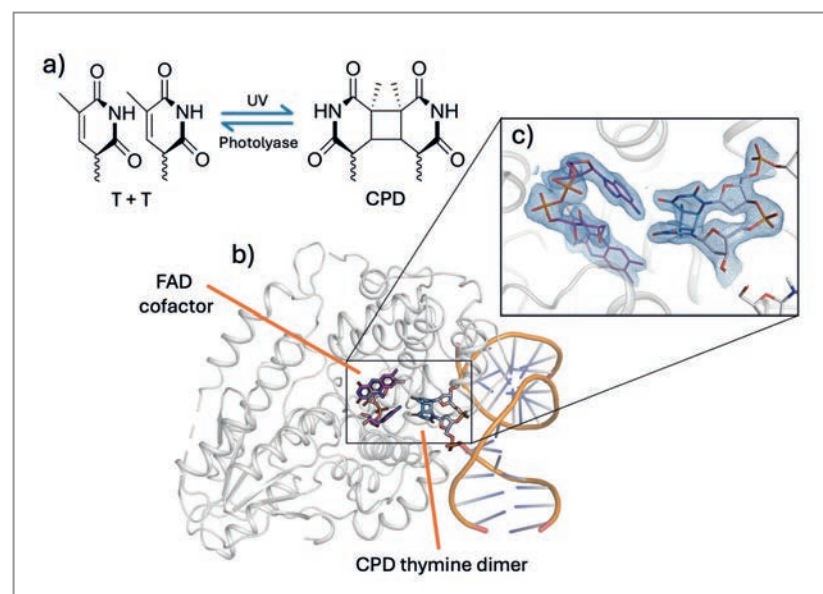


Figure 1

Photolyase repairs UV-induced DNA damage. a) Healthy, sequence-adjacent pyrimidine bases, such as the two thymines shown on the left (T+T), can cross-link upon UV irradiation to form cyclobutane pyrimidine dimers (CPDs), a form of DNA damage. CPDs are highly mutagenic. b) Photolyase is an enzyme capable of light-driven chemistry that repairs CPD lesions. c) The enzyme binds a FAD cofactor that acts as a chromophore and positions it proximal to a CPD lesion. Photoactivation drives an electron transfer reaction from FAD to CPD which is sufficient to cleave the two non-native carbon-carbon bonds that form the lesion and restore the healthy DNA structure.

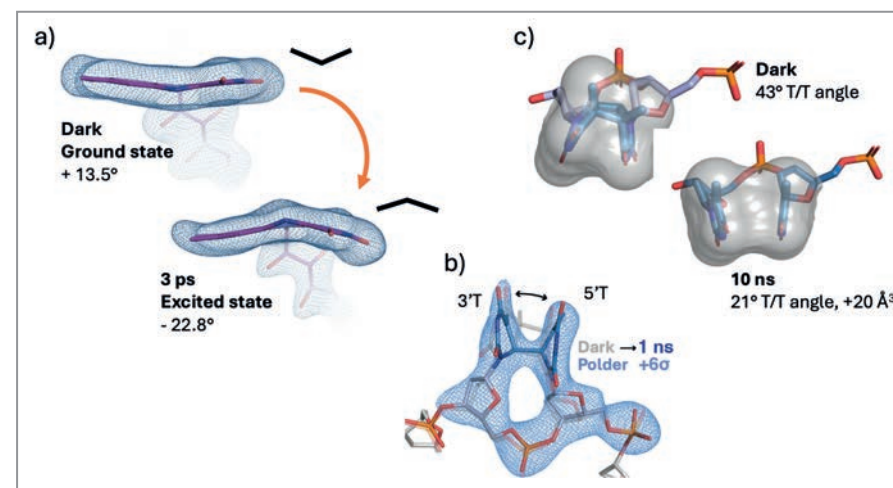


Figure 2

Time-resolved crystallography reveals the details of photolyase-catalysed DNA repair. a) The reaction progresses via a FAD-excited state that is stabilised by the enzyme in a highly bent geometry. b) After electron transfer, bond cleavage proceeds sequentially via a metastable one-bond intermediate. c) Following repair (10 ns), the thymines attempt to π -stack, swelling the active site and driving product release.

another bit of damage to repair [5]. We wanted to know how, exactly, photolyase distinguishes between damaged and healthy DNA.

To answer these questions, our DESY-led collaboration conducted a pump-probe serial crystallography experiment at SwissFEL (Fig. 2,3). We found that the enzyme stabilises a bent excited state geometry using an ingenious network of interactions, including two water molecules that can toggle into a new arrangement within 3 ps. Moreover, we were able—for the first time—to confirm that the two incorrect bonds are repaired one at a time and not simultaneously. Finally, we saw that after these bonds are broken, the repaired DNA bases attempt to π -stack in a coplanar geometry. They are prevented from reaching this ideal arrangement, though, by the limited space in the active site pocket. The resulting strain forces product release, leaving an empty active site ready for another repair reaction.

Ultrafast XFEL pulses allowed us to directly answer our questions by making them visible with X-rays, giving us a view into how life can survive and thrive under the sun.

Author contact: Thomas Lane, thomas.lane@desy.de

References

1. A. Sancar, 'Structure and function of DNA photolyase and cryptochrome blue-light photoreceptors', *Chem. Rev.* **103**, 2203–2238 (2003).
2. J. I. Lucas-Lledó and M. Lynch, 'Evolution of mutation rates: Phylogenomic analysis of the photolyase/cryptochrome family', *Mol. Biol. Evol.* **26**, 1143–1153 (2009).
3. Y. T. Kao, C. Saxena, T. F. He, L. Guo, L. Wang, A. Sancar and D. Zhong, 'Ultrafast dynamics of flavins in five redox states', *J. Am. Chem. Soc.* **130**, 13132–13139 (2008).
4. H. Ando, B. P. Fingerhut, K. E. Dorfman, J. D. Biggs and S. Mukamel, 'Femtosecond Stimulated Raman Spectroscopy of the Cyclobutane Thymine Dimer Repair Mechanism: A Computational Study', *J. Am. Chem. Soc.* **136**, 14801–14810 (2014).
5. A. Espagne, M. Byrdin, A. P. M. Eker and K. Brettel, 'Very Fast Product Release and Catalytic Turnover of DNA Photolyase', *ChemBioChem* **10**, 1777–1780 (2009).

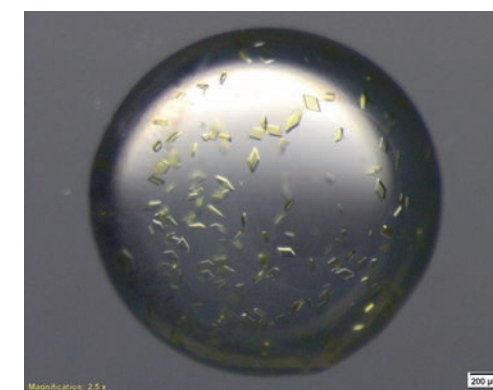


Figure 3

Micrograph of the photolyase:DNA crystals employed in this study which made use of the technique of time-resolved serial crystallography. Shown here are crystals optimised for preliminary work on the PETRA III synchrotron. Crystals employed during the XFEL experiment were smaller, approximately 10 μm , but were otherwise morphologically and compositionally identical.

Original publication

'Time-resolved crystallography captures light-driven DNA repair', *Science* **382**, 1015–1020 (2023). DOI: [10.1126/science.adj4270](https://doi.org/10.1126/science.adj4270)



Nina-Eleni Christou¹, Virginia Apostolopoulou^{1,3}, Diogo V. M. Melo², Matthias Ruppert⁴, Alisia Fadini⁵, Alessandra Henkel¹, Janina Sprenger¹, Dominik Oberthür¹, Sebastian Günther¹, Anastasios Pateras¹, Aida Rahmani Mashhour¹, Oleksandr M. Yefanov¹, Marina Galchenkova¹, Patrick Y. A. Reinke¹, Viviane Kremling¹, T. Emilie S. Scheer¹, Esther R. Lange¹, Philipp Middendorff¹, Robin Schubert², Elke De Zitter⁶, Koya Lumbao-Conradson⁷, Jonathan Herrmann⁸, Simin Rahighi⁸, Ajda Kunavar^{9S}, Emma V. Beale¹⁰, John H. Beale¹⁰, Claudio Cirelli¹⁰, Philip J. M. Johnson¹⁰, Florian Dworakowski¹⁰, Dmitry Ozerov¹⁰, Quentin Bertrand¹⁰, Maximilian Wranik¹⁰, Camila Bacellar¹⁰, Saša Bajt^{1,3}, Soichi Wakatsuki¹¹, Jonas A. Sellberg¹², Nils Huse⁴, Dušan Turk^{13,14}, Henry N. Chapman^{1,3,15} and Thomas J. Lane^{1,3}

1. Center for Free-Electron Laser Science CFEL, DESY, Hamburg, Germany
2. European XFEL, Schenefeld, Germany
3. The Hamburg Centre for Ultrafast Imaging CUI, University of Hamburg, Hamburg, Germany
4. Institute for Nanostructure and Solid-State Physics, University of Hamburg, Hamburg, Germany
5. Department of Life Sciences, Imperial College London, London, United Kingdom
6. Institut de Biologie Structurale, Grenoble, France
7. Linac Coherent Light Source LCLS, SLAC National Accelerator Laboratory, Menlo Park, USA
8. Department of Structural Biology, Stanford University, Stanford, USA
9. Laboratory for Fluid Dynamics and Thermodynamics, Mechanical Engineering, University of Ljubljana, Ljubljana, Slovenia
10. Paul Scherrer Institute, Villigen PSI, Switzerland
11. Stanford Synchrotron Radiation Lightsource SSRL, SLAC National Accelerator Laboratory, Menlo Park, USA
12. KTH Royal Institute of Technology, Stockholm, Sweden
13. Department of Biochemistry and Molecular and Structural Biology, Jožef Stefan Institute, Ljubljana, Slovenia
14. Centre of Excellence for Integrated Approaches in Chemistry and Biology of Proteins, Ljubljana, Slovenia
15. Department of Physics, University of Hamburg, Hamburg, Germany

Structural biology of bacterial insecticides

Using MHz XFEL repetition rate and nanofocused X-rays to unravel the structure of sub-microscopic crystals that kill mosquitoes

Bacterial pesticidal proteins, such as those from *Lysinibacillus sphaericus* and *Bacillus thuringiensis*, play a crucial role in controlling mosquito populations that spread diseases like malaria and dengue. They are also widely used in modern agricultural pest control, as they act very specifically and do not harm beneficial insects. Two of these pesticidal proteins, Tpp49Aa1 and Cry48Aa1, are active together even against mosquito species which have developed resistance against commonly used bacterial insecticides. Using serial femtosecond crystallography with X-rays focused to a few 100 nm, we have unveiled the detailed structure of Tpp49Aa1 from native protein nanocrystals. Knowing the structure at near-atomic detail is vital for designing next-generation bioinsecticides to tackle insect resistance and enhance both public health efforts and efficacy and safety of agricultural pest control.

Bacterial toxins have been a focus of research due to their unique roles in controlling insect populations and diseases they may spread. Gram-positive spore-forming bacteria like *Bacillus thuringiensis* (Bt) and *Lysinibacillus sphaericus* (*L. sphaericus*) are well known for producing specialised proteins that target insects. These bacteria produce crystalline proteins during sporulation which attack the midgut cells of insects. The diversity of these toxins allows them to target a wide range of pests while being safe for humans and other non-target organisms. Bt, for example, is used extensively in agriculture and public health due to its selective toxicity, making it a natural biopesticide [1].

Detailed knowledge of the atomic three-dimensional structure of these toxins and of their native arrangement within the crystals would help in understanding structure-function relationships, relationship with toxins from other organisms and last but not least could be beneficial for designing improved toxins to combat mosquitoes and other insects harmful to humans and human food supply. Due to the small size of the native toxin crystals and challenges in re-crystallising them to obtain larger crystals, only a few structures of these toxins could be elucidated before the advent of serial femtosecond crystallography (SFX). Moreover, in order to obtain larger crystals, the proteins forming these crystals often had to be modified and, in turn, crystal packing differed from the natively grown crystals.

The first native structure of a bacterial insecticide was Cry3A, obtained from SFX data collected at the Linac Coherent Light Source (LCLS) at SLAC National Accelerator Laboratory in the U.S. [2]. The same method was used to solve the structures of Cyt1Aa and Cry11 toxins from Bt and the Tpp1Aa2/Tpp2Aa2 toxin from *L. sphaericus* [3-5]. For our study we were granted beamtime at the experimental station SPB/SFX at the European XFEL (EuXFEL) to solve the structure of Tpp49Aa1, a protein that is part of the Tpp49Aa1/Cry48Aa1 toxin pair, which is investigated for its possible use in the development of new pesticidal agents aimed at overcoming Tpp1Aa2/Tpp2Aa2 resistance. At EuXFEL, we were able to record about 2000 diffraction images per second, compared to 120 images at LCLS, while the nanofocus option delivered X-ray pulses focused to the size of our crystals (Fig. 1) at unprecedented intensity. The use of advanced 3D-printed double flow-focusing micro nozzles [6] was key to our success, as it enabled us to collect more than two million useful diffraction images

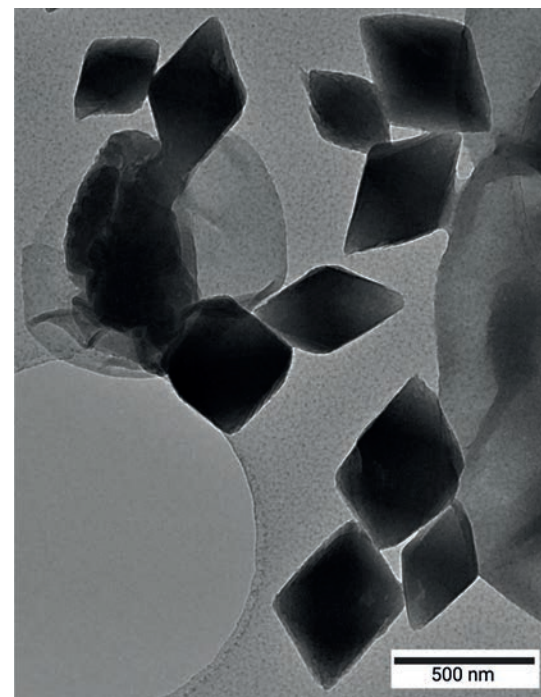


Figure 1
Transmission electron microscopy (TEM) image of Tpp49Aa1 crystals. Crystals of the same batch were used for SFX at EuXFEL. (Credit TEM image: Robin Schubert, EuXFEL)

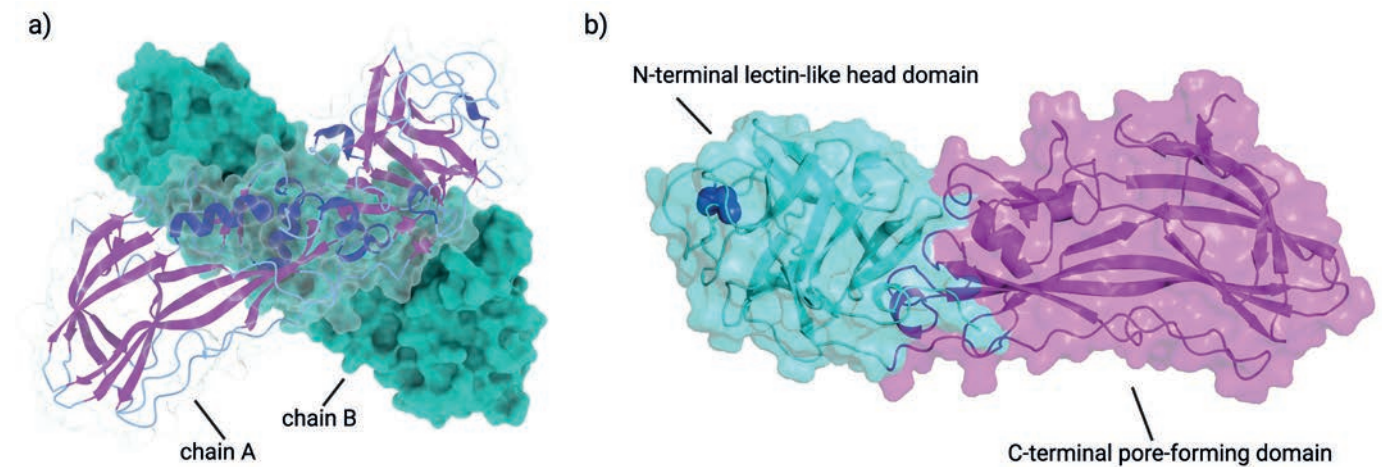


Figure 2

a) Tpp49Aa homodimer, both chains are of identical composition, chain A is depicted as cartoon plot, highlighting alpha-helical (dark blue) and beta-sheet (purple) parts of the protein, as well as loops (light blue) connecting these parts. Chain B is depicted as a solvent-excluded molecular surface. b) Detailed view of one of the chains of the homodimer. Two distinct domains exist within the Tpp49Aa1 monomer. The N-terminal lectin-like head domain (cyan) consists of six β -hairpins that form a β -trefoil fold containing a disulfide bond Cys91-Cys183 (shown as dark blue spheres). The C-terminal pore-forming domain (magenta) comprises an aerolysin-like domain. (Fig. 2b adapted from original publication licensed under a Creative Commons Attribution License 4.0 (CC BY), figures 1 and 2 were created using biorender.com)

within about half an hour, at an overall success rate of 88%.

From these data we solved the structure of Tpp49Aa1 using data to 1.62 Å resolution. Tpp49Aa1 is present as a homodimer forming an X-like structure (Fig. 2a) similar to that described for natural heterodimeric crystals of Tpp1Aa2/Tpp2Aa2 [5]. Each monomer consists of two distinct domains, an N-terminal lectin-like domain and a C-terminal putative pore-forming domain (Fig. 2b), showing strong structural similarity to Tpp2Aa2 from the Tpp1Aa2/Tpp2Aa2 toxin pair.

We also investigated the toxicity of Tpp49Aa1 together with Cry48Aa1 using cellular assays and were able to show that, in addition to the already known toxicity against *C. quinquefasciatus*, they showed promising activity against *Culex tarsalis* cells. This prompted further testing on mosquito larvae, where Cry48Aa1/Tpp49Aa1 demonstrated toxicity against *Aedes albopictus*, *Anopheles stephensi* and *C. tarsalis*, which are significant vectors of

diseases like dengue and West Nile virus. These findings underscore the potential of this toxin pair in targeting multiple mosquito species, including emerging and resilient vectors of human diseases.

Author contact:

Dominik Oberthür, dominik.oberthuer@desy.de

Colin Berry, Berry@cardiff.ac.uk

Original publication

'Structure of the *Lysinibacillus sphaericus* Tpp49Aa1 pesticidal protein elucidated from natural crystals using MHz-SFX', *Proceedings of the National Academy of Sciences* 120, e2203241120 (2023). DOI: 10.1073/pnas.2203241120



Lainey J. Williamson¹, Marina Galchenkova², Hannah L. Best¹, Richard J. Bean³, Anna Munke², Salah Awel², Gisel Pena², Juraj Knoska², Robin Schubert³, Katerina Dörner³, Hyun-Woo Park⁴, Dennis K. Bideshi⁴, Alessandra Henkel², Viviane Kremling², Bjarne Klopprogge², Emyr Lloyd-Evans⁵, Mark T. Young¹, Joana Valerio³, Marco Kloos³, Marcin Sikorski³, Grant Mills³, Johan Bielecki³, Henry Kirkwood³, Chan Kim³, Raphael de Wijn³, Kristina Lorenzen³, Paul Lourdu Xavier^{2,5}, Aida Rahmani Mashhour², Luca Gelisio², Oleksandr Yefanov², Adrian P. Mancuso^{3,6}, Brian A. Federici⁷, Henry N. Chapman^{2,8,9}, Neil Crickmore¹⁰, Pierre J. Rizkallah¹¹, Colin Berry¹ and Dominik Oberthür²

1. School of Biosciences, Cardiff University, Cardiff, United Kingdom
2. Center for Free Electron Laser Science CFEL, DESY, Hamburg, Germany
3. European XFEL GmbH, Schenefeld, Germany
4. Department of Biological Sciences, California Baptist University, Riverside, CA, USA
5. Max-Planck Institute for the Structure and Dynamics of Matter, Hamburg, Germany
6. Department of Chemistry and Physics, La Trobe Institute for Molecular Science, La Trobe University, Melbourne, Australia
7. Department of Entomology and Institute for Integrative Genome Biology, University of California, Riverside, CA, USA
8. Centre for Ultrafast Imaging, University of Hamburg, Hamburg, Germany
9. Department of Physics, University of Hamburg, Hamburg, Germany
10. School of Life Sciences, University of Sussex, Falmer, Brighton, United Kingdom
11. School of Medicine, Cardiff University, Cardiff, United Kingdom

X-rays create exotic forms of ice

Formation of superionic ice is influenced by experimental duration and thermodynamic path

An unusual form of water called superionic (SI) ice is thought to exist at the extreme conditions found in the interior of icy planets. SI ice, which consists of liquid-like hydrogen atoms within an oxygen crystal lattice, has a high ionic conductivity which is thought to contribute to the unusual magnetic fields of Uranus and Neptune [1]. SI ice exists in two forms with different arrangements of oxygen atoms, and the stability fields of these two phases remain heavily debated [2,3]. In experiments performed at the High Energy Density Instrument of the European X-ray Free-Electron Laser (XFEL), intense X-ray pulses were used to generate SI ice in compressed water and to investigate its structure at different pressures.

By tuning the pressure and temperature of water (H₂O), it is possible to access numerous solid phases with different crystal structures, chemical bonding and proton ordering. For example, various hydrogen-bonded molecular phases are observed at low pressures and temperatures [4], whereas hydrogen-bond symmetrisation results in a transformation to a non-molecular phase at high pressures [5]. At high pressures and temperatures H₂O molecules first dissociate to form SI ice before transforming to the fluid phase at higher temperatures. Such variations in chemical bonding strongly influence physical properties such as viscosity, ionic/thermal conductivity and elastic properties which are relevant for modelling the interior of icy planets.

Although the properties of SI ice are of interest for planetary science, experimental studies are scarce due to its reactive nature which makes it difficult to create and confine it in the laboratory. At pressures below approximately 100 GPa, SI ice can only be produced in static compression

experiments, where a small volume of H₂O is compressed between the tips of two diamond anvils and heated with a near-IR or CO₂ laser. Previous static compression experiments [2,3] differ regarding the stability fields of various SI ice phases (SI-bcc and SI-fcc) – in particular, the pressure range over which SI-fcc can form. This is especially important for planetary modelling, as the ionic conductivity depends on the symmetry of the oxygen atoms [6].

This work used a novel, dynamic heating approach to create SI ice. Statically compressed H₂O samples were irradiated with 300 ultrashort XFEL pulses with a spacing of 443 ns and a photon energy of 18 keV, while structural changes were monitored using the same pulses for X-ray diffraction. As direct X-ray heating of H₂O is not very effective, samples were indirectly heated using doughnut-type couplers made from highly absorbing materials (Fig. 1a) which acted as miniature furnaces heating the H₂O via thermal conduction. This resulted in a sawtooth-like

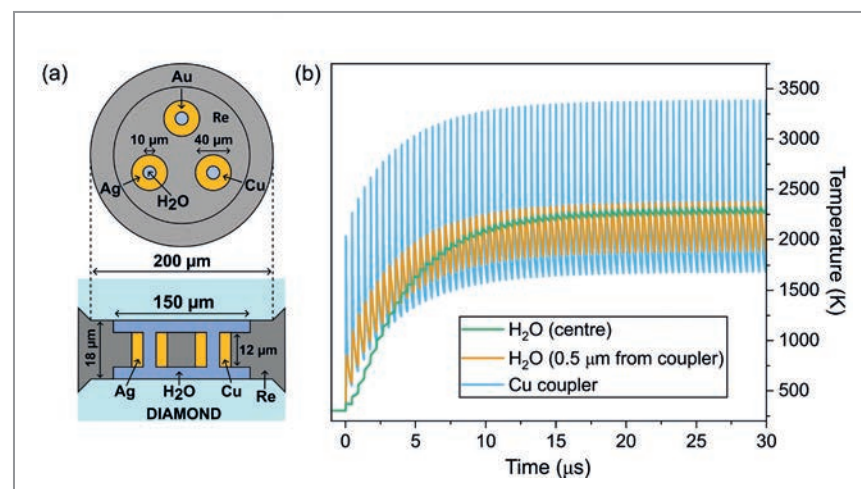


Figure 1

a) Illustration of the sample design. Doughnut-shaped couplers made of highly absorbing materials (Ag, Au, Cu) were used to heat compressed samples of H₂O. b) The temperature evolution of the H₂O sample and Cu coupler resulting from irradiation with 300 X-ray pulses at 2.2 MHz, determined from a Finite Element Analysis (FEA) simulation.

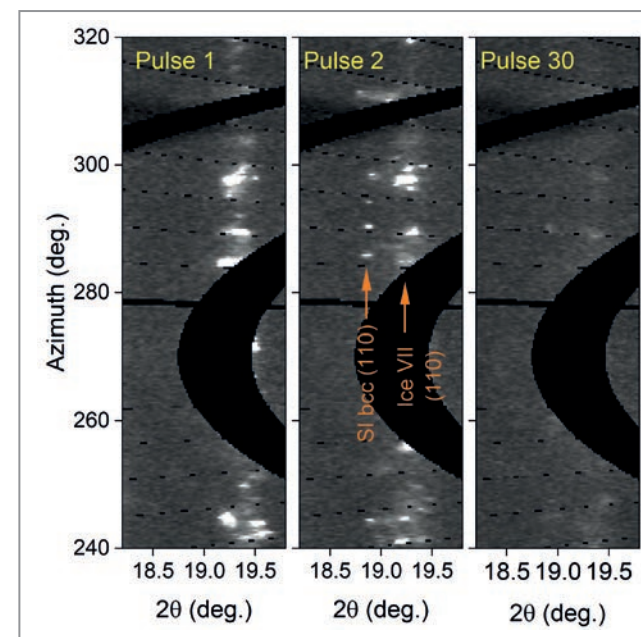


Figure 2

X-ray diffraction images collected from H₂O at 36.7 GPa during irradiation with an increasing number of XFEL pulses. The transformation to a mixture of SI-bcc and fluid at high temperatures was identified based on the appearance of a new reflection in the pulse 2 image and the significant reduction in the intensity of Bragg reflections by pulse 30.

temperature profile (Fig. 1b) with large thermal oscillations in the vicinity of the coupler and smaller oscillations at the centre of the sample hole. Due to the short duration of individual pulses (< 50 fs), diffraction provided an essentially instantaneous snapshot of the sample during dynamic cooling, capturing the structure of quenched crystalline states when H₂O was heated above its melting temperature.

H₂O samples at pressures from 26 to 69 GPa were subjected to multiple irradiation cycles at different X-ray fluences. SI-bcc was observed over the entire pressure range, in agreement with previous studies, whereas SI-fcc was only observed at pressures above 50 GPa. At lower pressures around 40 GPa, H₂O transformed into a SI-bcc/fluid mixture upon heating (Fig. 2). This is in good agreement with previous CO₂ laser heating studies [2] but contrasts with IR laser heating experiments in which SI-fcc was observed at pressures as low as 30 GPa [3]. Although SI-fcc is thought to be thermodynamically stable below the melting line, previous theoretical studies found SI-bcc to have a lower solid/fluid interfacial energy than SI-fcc [7], suggesting that SI-fcc may have a longer nucleation time when crystallising from the melt. The absence of SI-fcc in lower pressure runs was therefore attributed to the unique *P-T* path experienced in serial pulse heating experiments, combined with kinetic hindrance when SI-fcc is formed from the fluid phase. Due to the oscillating temperature profile (Fig. 1b), the sample does not remain in the SI-fcc stability field long enough to form SI-fcc. This result has implications for the stability of SI phases in ice-rich planets, for example during dynamic freezing, where the preferential crystallisation of SI-bcc may result in distinct physical properties across mantle ice layers.

Author contact: Rachel Husband, rachel.husband@desy.de

References

1. R. Redmer, T. R. Mattsson, N. Nettelmann and M. French, 'The phase diagram of water and the magnetic fields of Uranus and Neptune', *Icarus* 211, 798–803 (2011).
2. G. Weck, J.-A. Queyroux, S. Ninet, F. Datchi, M. Mezouar and P. Loubeyre, 'Evidence and stability field of fcc superionic water ice using static compression', *Phys. Rev. Lett.* 128, 165701 (2022).
3. V. B. Prakapenka, N. Holtgrewe, S. S. Lobanov and A. F. Goncharov, 'Structure and properties of two superionic ice phases', *Nat. Phys.* 17, 1233–1238 (2021).
4. C. G. Salzmann, P. G. Radaelli, E. Mayer and J. L. Finney, 'Ice XV: A New Thermodynamically Stable Phase of Ice', *Phys. Rev. Lett.* 103, 105701 (2009).
5. A. F. Goncharov, V. V. Struzhkin, M. S. Somayazulu, R. J. Hemley and H. K. Mao, 'Compression of Ice to 210 Gigapascals: Infrared Evidence for a Symmetric Hydrogen-Bonded Phase', *Science* 273, 218–220 (1996).
6. H. F. Wilson, M. L. Wong and B. Militzer, 'Superionic to Superionic Phase Change in Water: Consequences for the Interiors of Uranus and Neptune', *Phys. Rev. Lett.* 110, 151102 (2013).
7. B. Cheng, M. Bethkenhagen, C. J. Pickard and S. Hamel, 'Phase behaviours of superionic water at planetary conditions', *Nat. Phys.* 17, 1228–1232 (2021).

Original publication

'Phase transition kinetics of superionic H₂O ice phases revealed by Megahertz X-ray free-electron laser-heating experiments', *Nature Communications* 15, 8256 (2024). DOI: 10.1038/s41467-024-52505-0



R. J. Husband¹, H. P. Liermann¹, J. D. McHardy², R. S. McWilliams², A. F. Goncharov³, V. B. Prakapenka⁴, E. Edmund⁵, S. Chariton⁴, Z. Konôpková⁵, C. Strohm¹, C. Sanchez-Valle⁶, M. Frost⁷, L. Andriambariarajona⁸, K. Appel⁹, C. Baetz⁹, O. B. Ball¹⁰, R. Briggs¹⁰, J. Buchen¹¹, V. Cerantola⁵, J. Choi¹², A. L. Coleman¹⁰, H. Cynn¹⁰, A. Dwivedi⁹, H. Graafsma¹, H. Hwang¹, E. Koemets¹³, T. Laurus¹⁴, Y. Lee¹², X. Li¹, H. Marquardt¹⁵, A. Mondal⁶, M. Nakatsutsumi⁵, S. Ninet⁶, E. Pace², C. Pepin¹⁵, C. Prescher¹⁵, S. Stern¹, J. Sztuk-Dambietz⁵, U. Zastrau⁵ and M. I. McMahon^{2,14}

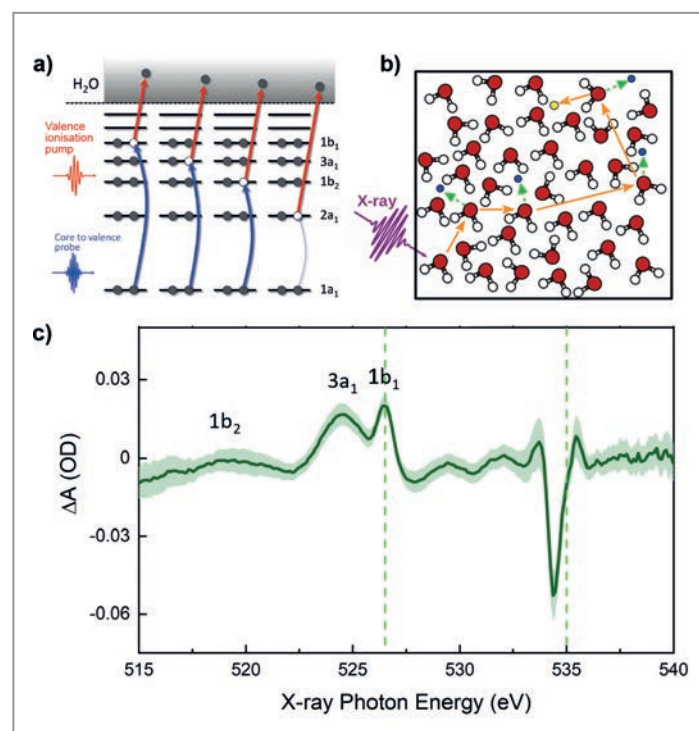
1. Deutsches Elektronen-Synchrotron DESY, Hamburg, Germany
2. The University of Edinburgh, Edinburgh, UK
3. Carnegie Science, Washington DC, USA
4. The University of Chicago, Chicago, USA
5. European XFEL, Schenefeld, Germany
6. Universität Münster, Münster, Germany
7. SLAC National Accelerator Laboratory, California, USA
8. Sorbonne Université, Paris, France
9. Helmholtz-Zentrum Dresden-Rossendorf, Dresden, Germany
10. Lawrence Livermore National Laboratory, Livermore, USA
11. University of Oxford, Oxford, UK
12. Yonsei University, Seoul, Korea
13. CEA, Arpajon, France
14. Université Paris-Saclay, Bruyères-le-Châtel, France
15. University of Freiburg, Freiburg, Germany

Freezing nuclear motions with attosecond X-rays

All-attosecond X-ray pump-probe spectroscopy resolves the long-standing debate on X-ray emission from liquid water

Water is known to exhibit multiple anomalous macroscopic properties owing mainly to its unique ability to form a strong hydrogen bonding network. X-ray emission spectroscopy (XES) is a well-established method to study structural properties of liquids. The X-ray emission spectrum of liquid water under ambient conditions exhibits a doublet $1b_1$ peak, whose origin has been under strong debate. In this joint experimental and theoretical study, we report the first all-X-ray attosecond transient absorption spectroscopy (AX-ATAS) ever performed on a condensed-phase system enabling spectral snapshots free from nuclear motion and resolving this long-standing debate.

The experiment was performed at the Linac Coherent Light Source (LCLS), where a liquid water jet was exposed to two consecutive X-ray pulses of 600 as duration each and with a 700 as delay between them. The first pulse (pump) with a photon energy of 250 eV ionises water from anywhere in the valence band (Fig. 1a). The high-energy photoelectrons, thus produced, initiate a cascade of further ionisations through collisions (Fig. 1b). The second pulse with a photon energy of 525 eV probes pumped liquid water while the collisional ionisation in the sample is going on. The experimental AX-ATAS spectrum of liquid water is depicted in Fig. 1c.



To interpret the AX-ATAS signal, it is necessary to construct a theoretical model incorporating collisional-ionisation dynamics and multichannel-coherence effects. The model shows that during the probe pulse, collisional ionisation causes 4–5 valence holes per absorbed pump photon. The key object for the interpretation is the time-dependent polarisation response to the probe pulse of the dynamically evolving sample. The computed time-dependent polarisation of pumped water is shown in Fig. 2 for different cases, namely, with (green) and without (magenta) considering electronic coherences and in comparison to an isolated water molecule in gas phase (grey). As can be seen, compared to the gas phase, the polarisation response of liquid water is pronouncedly damped, while coherence effects remain limited. The former is a direct effect of the inhomogeneous broadening of the valence-hole spectrum in liquid water. These results lead to the fact that the recorded transient absorption spectrum can be considered as almost instantaneous response. In particular, the AX-ATAS signal is devoid of any influence by nuclear movement in liquid water.

The insights gained from the theoretical model allow one to compare the AX-ATAS and XES results in liquid water as they involve the same electronic transitions but in reverse order, as illustrated in Fig. 3a. While in XES the core level is ionised and reoccupied from the valence orbital, in AX-ATAS

Figure 1
All X-ray attosecond transient absorption spectroscopy (AX-ATAS) in liquid water. a) The pump pulse has sufficient energy to ionise water from anywhere in the valence band and the probe pulse causes core-to-valence/virtual transition close to 530 eV. b) The high-energy photoelectron produced by pump-induced valence ionisation causes collisional ionisation on nearby neutral water molecules. c) Attosecond transient absorption spectrum (ΔA) of liquid water covering the valence hole and pre-edge region.

valence levels are photoionised and then reoccupied from the core level by the absorption of another X-ray photon. The key difference is that the timescale of XES is dictated by the core-hole lifetime (about 4 fs) which is considerably longer than the pump-probe delay in AX-ATAS (about 0.7 fs).

The debated doublet $1b_1$ peak (Fig. 3b) has been attributed either to the presence of two predominant structural motifs in ambient water [1,2] or to ultrafast hydrogen motion in core-excited water [3]. Unlike XES, AX-ATAS does not exhibit a $1b_1$ -doublet structure (Fig. 3b). The difference must arise from the fact that the XES signal is impacted by nuclear dynamics during the oxygen core-hole lifetime. Accordingly, it can be concluded that the splitting of the $1b_1$ peak in XES does not directly reflect two distinct structural motifs in liquid water but rather ultrafast hydrogen motion in core-ionised water.

Our study shows that AX-ATAS is a powerful tool for investigating systems in which rapid hydrogen motion can contaminate the information content of the probe signal, like in XES. Moreover, the ability to perform X-ray pump/probe experiments with subfemtosecond pulse durations allows exploring high-energy radiation-induced processes in condensed-phase samples in an entirely new way.

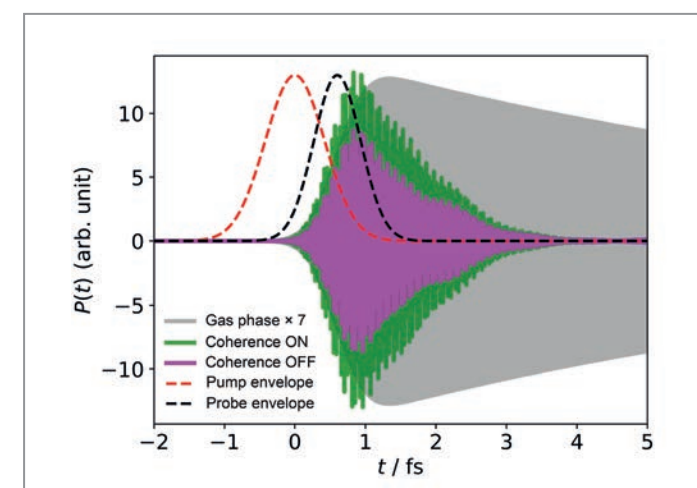


Figure 2
Results from theoretical modelling. Polarisation response, $P(t)$, in liquid water with (green) and without (magenta) coherence effects in comparison to the case of an isolated molecule in the gas phase (grey).

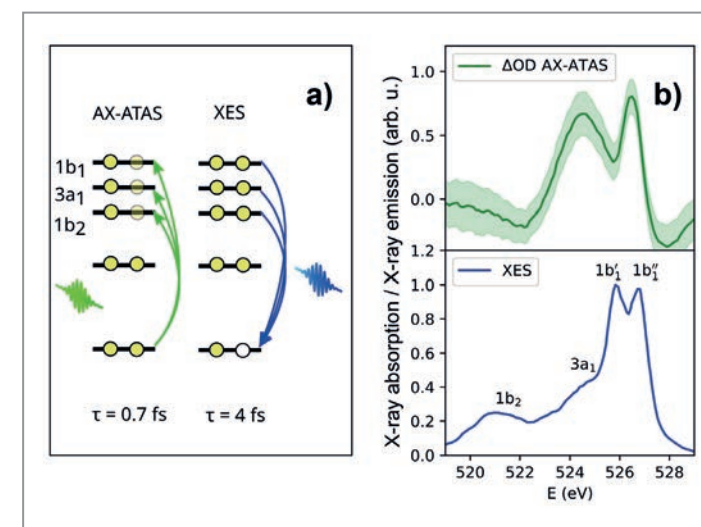


Figure 3
Comparison between AX-ATAS and XES of liquid water. a) AX-ATAS and XES involve the same set of initial and final states but in reverse order. b) (Upper panel) AX-ATAS of liquid water including error range, same as in Fig. 1; (lower panel) XES of liquid water taken from Ref. [2].

Author contact:

Swarnendu Bhattacharyya, swarnendu.bhattacharyya@cfel.de
Ludger Inhester, ludger.inhester@cfel.de
Robin Santra, robin.santra@cfel.de
Linda Young, young@anl.gov

References

1. A. Nilsson and L. G. Pettersson, 'The structural origin of anomalous properties of liquid water', *Nat. Comm.* **6**, 8998 (2015).
2. T. Tokushima, Y. Harada, O. Takahashi, Y. Send, H. Ohashi, L. G. M. Peterson, A. Nilsson and S. Shin, 'High-resolution X-ray emission spectroscopy of liquid water: The observation of two structural motifs', *Chem. Phys. Lett.* **460**, 487–490 (2008).
3. O. Takahashi, R. Yamamura, T. Tokushima and Y. Harada, 'Interpretation of the X-ray emission spectra of liquid water through temperature and isotope dependence', *Phys. Rev. Lett.* **128**, 086002 (2022).

Original publication

'Attosecond-pump attosecond-probe x-ray spectroscopy of liquid water', *Science* **383**, 1118–1122 (2024).
DOI: [10.1126/science.adn6059](https://doi.org/10.1126/science.adn6059)



Shuai Li¹, Lixin Lu², Swarnendu Bhattacharyya³, Carolyn Pearce^{4,5}, Kai Li^{3,6}, Emily T. Nienhuis⁴, Gilles Doumy¹, R. D. Schaller⁷, S. Moeller⁸, M.-F. Lin⁸, G. Dakovski⁸, D. J. Hoffman⁸, D. Garratt⁹, Kirk A. Larsen⁹, J. D. Koralek⁸, C. Y. Hampton⁸, D. Cesar⁸, Joseph Duris⁸, Z. Zhang⁸, Nicholas Sudar⁸, James P. Cryan^{8,9}, A. Marinelli^{8,9}, Xiaosong Li², Ludger Inhester^{3,10,11}, Robin Santra^{3,10,11} and Linda Young^{1,6}

1. Chemical Sciences and Engineering Division, Argonne National Laboratory, Lemont, IL, USA
2. Department of Chemistry, University of Washington, Seattle, WA, USA
3. Center for Free-Electron Laser Science CFEL, DESY, Hamburg, Germany
4. Pacific Northwest National Laboratory, Richland, WA, USA
5. Department of Crop and Soil Sciences, Washington State University, Pullman, WA, USA
6. Department of Physics and James Franck Institute, The University of Chicago, Chicago, IL, USA
7. Center for Nanoscale Materials, Argonne National Laboratory, Lemont, IL, USA
8. SLAC National Accelerator Laboratory, Menlo Park, CA, USA
9. Stanford PULSE Institute, SLAC National Accelerator Laboratory, Menlo Park, CA, USA
10. The Hamburg Centre for Ultrafast Imaging, Hamburg, Germany
11. Department of Physics, University of Hamburg, Hamburg, Germany

Combining XUV light sources for coupled molecular dynamics

Resolving a prototypical complex photochemical reaction on ultrafast time scales

The achievements for deeper understanding of ultrafast electron dynamics in matter are highlighted by the 2023 Nobel Prize in Physics for the first attosecond (10^{-18} seconds) light sources by means of high-order harmonic generation (HHG). Yet, the technique also comes with limitations such as a photon flux that is typically too low for pump-probe experiments or spectra that are too broad for state- or site-specific excitations. This can be overcome with the help of free-electron lasers (FELs). In our work we combine these two extreme-ultraviolet (XUV) light sources for the first time to observe the coupled dissociation dynamics of electrons and the nuclei in molecular oxygen.

The interaction of light with matter, especially with molecules, plays an important role in many areas of nature, for example in biological processes such as photosynthesis. Technologies like solar cells use this process as well. While the individual atoms in a molecule are held together by their outermost electrons – they act as ‘chemical glue’ – inner-shell electrons are bound closer to an atomic nucleus and are therefore more localised in the molecule. It is precisely these electrons that can be specifically excited with XUV radiation, e.g. provided by FEL facilities, and thereby allow for site-specificity of photochemical reactions combined with femto- to picosecond (10^{-15} – 10^{-12} seconds) time resolution. Although resolving the fast motion of electrons in matter is now experimentally possible, their influence on the nuclear degrees of freedom in molecules on similarly fast or slightly slower time scales has just started to be investigated [1].

In our work we study the photodissociation of oxygen molecules via two parallel pathways (Fig. 1). This is enabled by using the FEL pulses at around 28 eV as pump pulses (exciting and ionising the molecules at the same time) to reach a specific electronically excited state in the O_2^+ ion, which is known to dissociate much slower than other XUV-excited states. Yet, the exact time scale of the molecular break-up process for this state has not been precisely measured before, which arises from the complex interplay of the electronic and nuclear degrees of freedom within the molecules. The electronic potential experienced by the atomic nuclei exhibits an energy barrier along the dissociation pathway. Classically, this would trap the molecule in this particular excited state. Yet, quantum-mechanics provides two ways out of the situation: First, the nuclei can tunnel through the potential energy barrier and dissociate afterwards. Second, the trapped electronic state lives

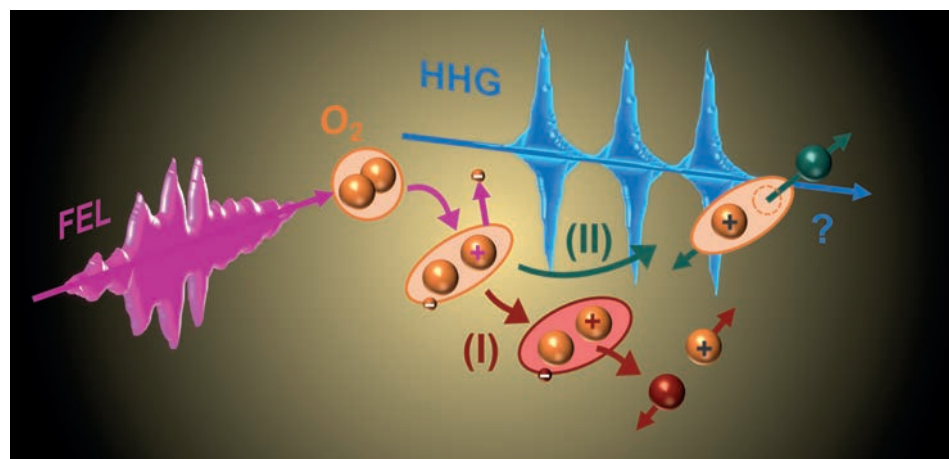


Figure 1
Illustration of the investigated photochemical reaction: the dissociation of an O_2 molecule (orange) initially excited by an FEL pulse (pink). The dissociation involves coupled electronic and nuclear degrees of freedom and can take place via two parallel pathways (red: change of electronic configuration, green: nuclear tunneling). All fragments are probed with a broadband HHG pulse (blue) enabling the measurement of the dissociation time and reaction rates for the first time. (Figure adapted from original publication)

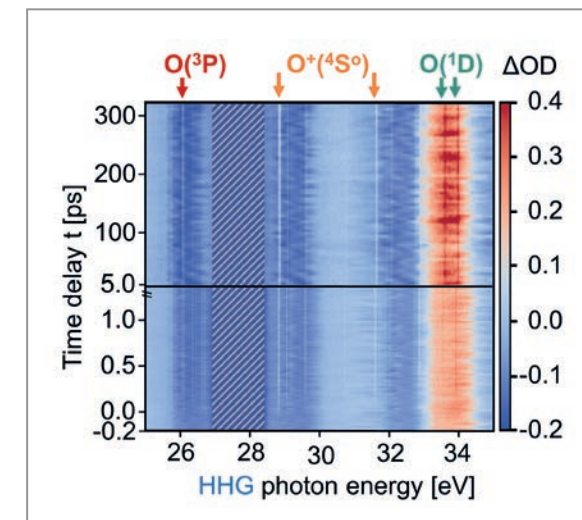
long enough, so it can undergo an internal change of electronic configuration (via a non-adiabatic electronic coupling) and dissociates freely along the new electronic potential energy curve.

But how to detect such a process? By looking at the specific reaction products as a function of time! Both pathways produce one singly-ionised atomic oxygen ion in its electronic ground-state configuration. But the neutral atomic product partners for the two pathways are different. For the electronic configuration change, the resulting neutral oxygen atom is in its electronic ground state whereas in the case of the nuclear tunneling, it is in an excited electronic configuration. To be sensitive to neutral products and their electronic configuration, we employ HHG pulses as probe in transient absorption spectroscopy (Fig. 2). Their broad XUV spectral bandwidth allows to measure absorption fingerprints by means of resonant electronic transitions of all three different relevant fragments at different photon energies, thereby identifying the fragments. Repeating the absorption measurement at different time delays between FEL-pump and HHG-probe pulses enables to track the resonances' evolution and hence the fragments in time. We find that all fragments appear to have the same dissociation time of around 300 picoseconds (10^{-12} seconds) constraining a broad range of earlier theoretical predictions.

In the future, this novel measurement technique based on the combination of FEL and HHG pulses could help to observe and control more complex photochemical reactions, including coupled electronic-nuclear dynamics of polyatom-

Figure 2

Time-resolved absorption spectra capturing the break-up of the oxygen molecules. Spectrally sharp absorption lines (white/red) appear as a function of time delay between pump and probe pulse (from bottom to top). On femtosecond time scales (lower half), all absorption lines appear weakly, whereas five of the lines become more prominent on picosecond time scales (upper half). They belong to the three fragments relevant to the processes investigated, highlighted at the top with arrows (red/orange/green). The exponential increase in the absorption lines as a function of time delay allows to extract the dissociation time of the reaction. The striped area around 28 eV marks FEL stray light illustrating the FEL bandwidth (~ 1 eV) is much too narrow to detect all the relevant resonances and fragments at the same time. (Figure adapted from original publication)



ic molecules with site-specificity, complete fragment detection and identification, all using ultrafast time resolution.

Author contact:

Alexander Magunia, alexander.magunia@mpi-hd.mpg.de

Christian Ott, christian.ott@mpi-hd.mpg.de

Thomas Pfeifer, thomas.pfeifer@mpi-hd.mpg.de

References

1. O. Alexander et al., ‘Chapter Three - Attosecond electron dynamics in molecular systems’, *Adv. At. Mol. Opt. Phys.* 72, 183–251 (2023).

Original publication

‘Time-resolving state-specific molecular dissociation with XUV broadband absorption spectroscopy’, *Science Advances* 9, eadk1482 (2023). DOI: 10.1126/sciadv.adk1482



Alexander Magunia^{1,2}, Marc Rebholz¹, Elisa Appi^{3,4}, Christina C. Papadopolou⁵, Hannes Lindenblatt^{1,2}, Florian Trost^{1,2}, Severin Meister^{1,2}, Thomas Ding¹, Michael Straub^{1,2}, Gergana D. Borisova^{1,2}, Junhee Lee^{1,2}, Rui Jin¹, Alexander von der Dellen¹, Christian Kaiser¹, Markus Braune⁵, Stefan Düsterer⁵, Skirmantas Ališauskas⁵, Tino Lang⁵, Christoph Heyl^{5,6,7}, Bastian Manschwetus⁵, Sören Grunewald⁵, Ulrike Frühling⁵, Ayhan Tajalli⁵, Ammar Bin Wahid⁸, Laura Sillett⁹, Francesca Calegari^{9,9}, Philip Mosel⁵, Uwe Morgner³, Milutin Kovacev³, Uwe Thumm¹⁰, Ingmar Hartl⁵, Rolf Treusch⁵, Robert Moshhammer¹, Christian Ott¹ and Thomas Pfeifer¹

1. Max-Planck-Institut für Kernphysik, Heidelberg, Germany
2. Ruprecht-Karls-Universität Heidelberg, Heidelberg, Germany
3. Leibniz University Hannover, Hannover, Germany
4. Lund University, Lund, Sweden
5. Deutsches Elektronen-Synchrotron DESY, Hamburg, Germany
6. Helmholtz-Institute Jena, Jena, Germany
7. GSI Helmholtzzentrum für Schwerionenforschung, Darmstadt, Germany
8. Center for Free-Electron Laser Science CFEL, DESY, Hamburg, Germany
9. Universität Hamburg, Hamburg, Germany
10. J. R. Macdonald Laboratory, Kansas State University, Kansas, United States of America

Electron bubble in a water cage

Computer simulations and time-resolved X-ray spectroscopy reveal new insights into the solvation of electrons in liquid water.

Ionising radiation in bulk water leads to a sequence of collisional ionisation events. Secondary electrons eventually cause the formation of ions and radicals such as H_3O^+ and OH^\cdot [1]. The electrons released in this context decelerate in the bulk medium and temporarily form a species that is called the solvated electron (e_{aq}^-)—a localised electron bubble that is surrounded by a cage of water molecules, illustrated in Fig. 1. Together with the other ions and radicals, e_{aq}^- plays a major role in the ionisation-induced chemistry. Many details regarding the formation and structure of these species are debated. For example, how quickly does the solvation proceed?

Figure 2a shows the changes in the X-ray absorption spectrum (XAS) of a liquid water jet 2 ps after it has been exposed to an 800-nm strong-field pulse in an experiment at the Linac Coherent Light Source (LCLS) [2]. The change in optical density ΔOD shown in Fig. 2b exhibits, for various energy regions, significant absorption gain (orange) or absorption loss (blue). From calculations of the absorption spectra of individual solvated species in Fig. 2c, these changes in the absorption could be assigned to the presence of ions and radicals in the water after the ionising pulse. Specifically, the

water molecules surrounding the e_{aq}^- lead to pronounced absorption gain at about 533 eV [3]. Combining the computed absorption spectra in Fig. 2c, one obtains an absorption difference spectrum in Fig. 2d that qualitatively matches the measurement in Fig. 2b. These results particularly lead to the conclusion that the gain in the region around 533 eV can be directly connected to the appearance of e_{aq}^- . Time-resolved XAS recorded in the experiment seen in Fig. 3 show indeed a delayed temporal rise in the XAS, suggesting that e_{aq}^- forms on a timescale of 0.26 ± 0.03 ps.

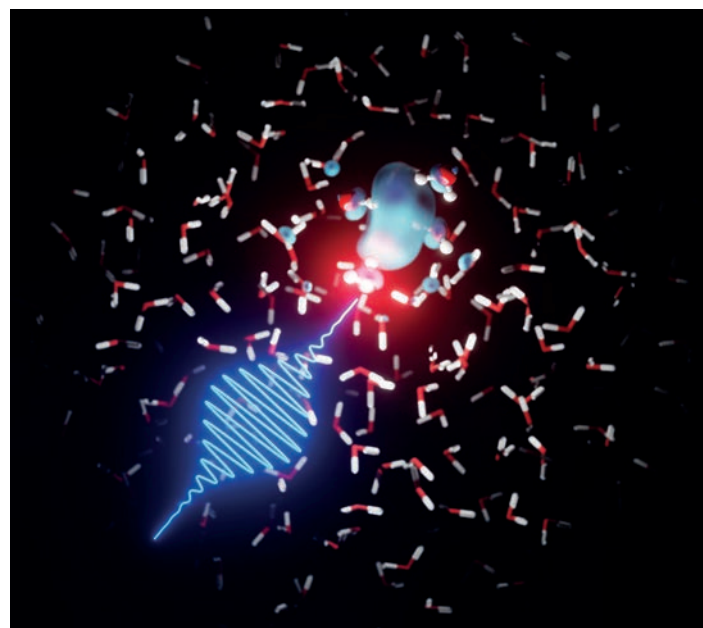


Figure 1

An X-ray pulse probes water molecules in the vicinity of the solvated electron. The solvated electron density is illustrated via its isovolume. The neighbouring water molecules form a cage structure around the electron bubble.

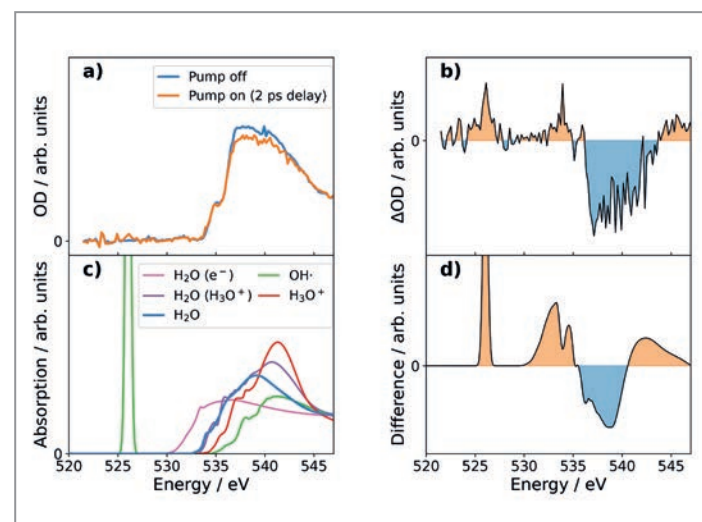


Figure 2

a) Experimental XAS for unpumped and pumped (after a 2 ps pump-probe delay) water. b) Experimental differential XAS. c) Theoretical XAS for solvated OH^\cdot (green line), solvated H_3O^+ (red line), water molecules in the solvation shell of H_3O^+ (purple line), water molecules belonging to the cavity of e_{aq}^- (pink line) and water molecules in the bulk (blue line). d) Calculated differential XAS for water containing the aforementioned species.

Further insight into the solvation process could be gained from computer simulations of the solvation process, incorporating certain nuclear quantum effects and using a neural-network force field trained on high-level *ab initio* electronic structure calculations [4]. Considering an initially delocalised electron injected into bulk water, the simulations confirm the appearance of the absorption gain at 533 eV linked to the solvation of the electron. It turns out that the solvation time is highly sensitive to initial fluctuations in the water structure. Accordingly, at higher temperatures, when the liquid exhibits stronger fluctuations, the solvation takes place considerably faster than at lower temperatures.

The overall picture reveals a so-called trap-seeking-cavity-digging solvation mechanism: The electron waits for a suitable trap, i.e. a local fluctuation in the hydrogen bridge connection, to randomly appear and then starts to actively dig its cavity, a cage of 4–6 water molecules each coordinating one of their hydrogen atoms to the electron. This digging step eventually causes major disruption of the surrounding hydrogen-bond network. While the trap-seeking mechanism is influenced by structural fluctuations, which are notably influenced by temperature and the electron's specific preparation in water, the subsequent collapse into a cavity occurs relatively fast (<100 fs). The elucidation of X-ray spectroscopic signatures for e_{aq}^- , OH^\cdot , and H_3O^+ suggests that future studies will be able to provide more insight into ionisation dynamics, proton transfer and proton hydration in water exposed to ionising radiation.

Author contact: Ludger Inhester, ludger.inhester@cfel.de
Linda Young, young@anl.gov

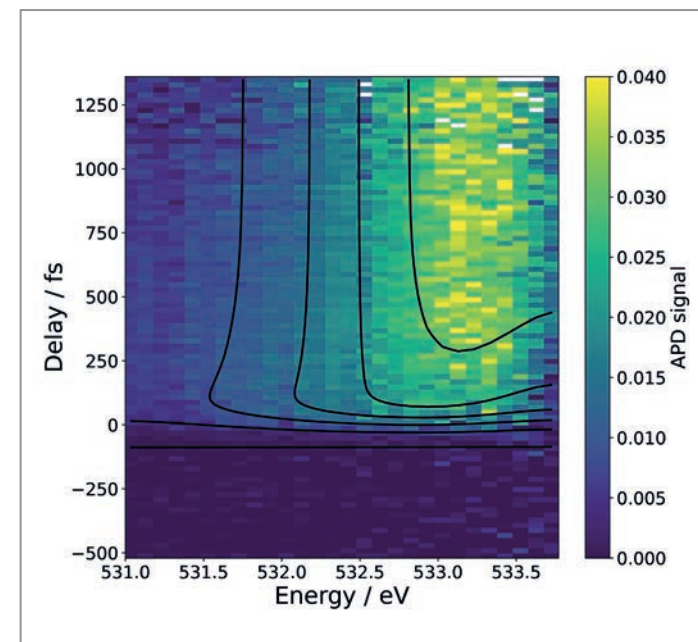


Figure 3

Transient absorption signal from ionised liquid water.

References

1. E. Alizadeh and L. Sanche, 'Precursors of Solvated Electrons in Radiobiological Physics and Chemistry', *Chem. Rev.* **112**, 5578–5602 (2012).
2. Z.-H. Loh, G. Doumy, C. Arnold, L. Kjellsson, S. H. Southworth, A. Al Haddad, Y. Kumagai, M. F. Tu, P. J. Ho, A. M. March, R. D. Schaller, M. S. Bin Mohd Yusof, T. Debnath, M. Simon, R. Welsch, L. Inhester, K. Khalili, K. Nanda, A. I. Krylov, S. Moeller, G. Coslovich, J. Koralek, M. P. Minitti, W. F. Schlotter, J.-E. Rubensson, R. Santra and L. Young, 'Observation of the fastest chemical processes in the radiolysis of water', *Science* **367**, 179–182 (2020).
3. X. Li, X. Jia, A. S. P. Paz, Y. Cao and W. J. Glover, 'Evidence for Water Antibonding Orbital Mixing in the Hydrated Electron from Its Oxygen 1s X-ray Absorption Spectrum', *J. Am. Chem. Soc.* **144**, 19668–19672 (2022).
4. J. Lan, V. Kapil, P. Gasparotto, M. Ceriotti, M. Iannuzzi and V. Rybkin, 'Simulating the ghost: quantum dynamics of the solvated electron', *Nat. Commun.* **12**, 766 (2021).

Original publication

'Tracking Cavity Formation in Electron Solvation: Insights from X-ray Spectroscopy and Theory', *Journal of the American Chemical Society* **146**, 3262–3269 (2024). DOI: 10.1021/jacs.3c11857



Arturo Sopena Moros¹, Shuai Li², Kai Li^{2,3}, Gilles Doumy², Stephen H. Southworth², Christopher Otolski², Richard D. Schaller^{2,4}, Yoshiaki Kumagai⁵, Jan-Erik Rubensson⁶, Marc Simon⁷, Georgi Dakovski⁸, Kristjan Kunnus⁹, Joseph S. Robinson⁹, Christina Y. Hampton⁹, David J. Hoffman⁸, Jake Koralek⁸, Zhi-Heng Loh⁹, Robin Santra^{1,10}, Ludger Inhester¹ and Linda Young^{2,3}

1. Center for Free-Electron Laser Science CFEL, DESY, Hamburg, Germany
2. Argonne National Laboratory, Lemont, United States
3. The University of Chicago, Chicago, United States
4. Northwestern University, Evanston, United States
5. University of Agriculture and Technology, Tokyo, Japan
6. Uppsala University, Uppsala, Sweden
7. Sorbonne Université, CNRS, Paris, France
8. LCLS, SLAC, Menlo Park, United States
9. Nanyang Technological University, Singapore, Singapore
10. Department of Physics, Universität Hamburg, Hamburg, Germany

Twisting currents: electron vortices in chiral molecules

A window on molecular chirality at the timescale of electron motion

Enantiomers are molecules that are mirror images of each other but cannot be superimposed even after rotation—just like our hands. Referred to as chiral, (S)- and (R)- enantiomers react with other chiral molecules in distinct ways. They play a crucial role in human metabolism because many biological molecules, such as amino acids and sugars, exist predominantly in a single enantiomeric form, giving them specific biochemical properties. For example, (S)-methamphetamine acts as nasal decongestant while its opposite (R)-enantiomer is known as crystal meth. This chiral discrimination is therefore important for drug design but also for a range of fields, from analytical chemistry to material sciences and spintronics.

A molecule's chirality is defined by the three-dimensional arrangement of its atoms, but its chiral response can drastically change over time when it is excited by light. Recent work has shown how a chiral molecule responds to light as its nuclei move and eventually dissociate over time [1]. However, it was not known how chirality evolves before the nuclei start to move on the much faster few-femtosecond (fs) timescale where electron motion can also contribute significantly. In our work, we aimed at addressing the following question: How do photoinduced electron dynamics influence molecular chirality? Indeed, by understanding the role of electrons in the very first moment after photoexcitation of a chiral molecule, we may be able to influence its reactivity at later times.

To study the rapid electron dynamics in photoexcited chiral molecules, we used a laser technique known as time-

resolved photoelectron circular dichroism (tr-PECD) [2,3]. PECD uses circularly polarised ionising laser pulses in which the electric field rotates as the light moves forward. When such pulses interact with an ensemble of enantiopure chiral molecules, photoelectrons are ejected in a preferred direction along the laser propagation axis, resulting in a forward/backward asymmetry. This asymmetry, which is highly sensitive to chirality, is reversed when pulses of the same helicity interact with an ensemble of molecules of the opposite enantiomer.

In our experiment, we used one of the shortest few-fs ultraviolet (UV) pulses available to date [4,5], to first photoexcite an ensemble of chiral methyl lactate molecules. With a time-delayed, circularly polarised ionising pulse of only 5 fs duration, we then probed the temporal evolution of the ultrafast chiral response using PECD. An electron detector was used to measure the time and kinetic energy-dependent angular distributions of the photoelectrons produced by ionisation (Fig. 1). This approach allowed us to capture a periodic evolution of the coherent electron motion on the few-fs timescale (Fig. 1b).

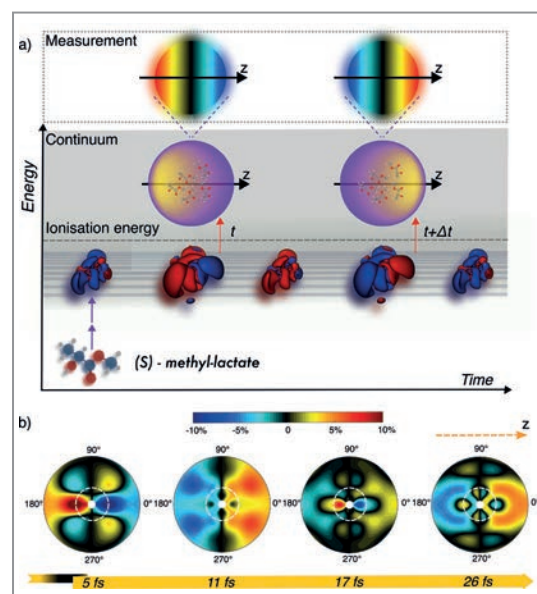


Figure 1

a) A few-femtosecond linearly polarised UV pulse excites an ensemble of randomly oriented chiral molecules, creating a coherent superposition of electronic states. The chiral response of the ensemble is probed by a time-delayed circularly polarised near-infrared pulse, leading to the ejection of photoelectrons along the light-propagation axis defined along the z direction. The red and blue structures show the temporal evolution of the coherent electron density in the excited neutral molecule, leading to a reversal of the 3D photoelectron angular distribution at two distinct time delays, t and $t + \Delta t$, captured by the measurements. b) For each time delay, an image is captured for both left- and right-circular polarisation of the probe pulse. The differential images are shown for time delays of 5, 11, 17, and 26 fs, displaying photoelectrons with kinetic energies ranging from 25 to 300 meV along the radial axis. The white dashed circles highlight photoelectrons with energies below 100 meV that undergo an ultrafast reversal in their emission direction.

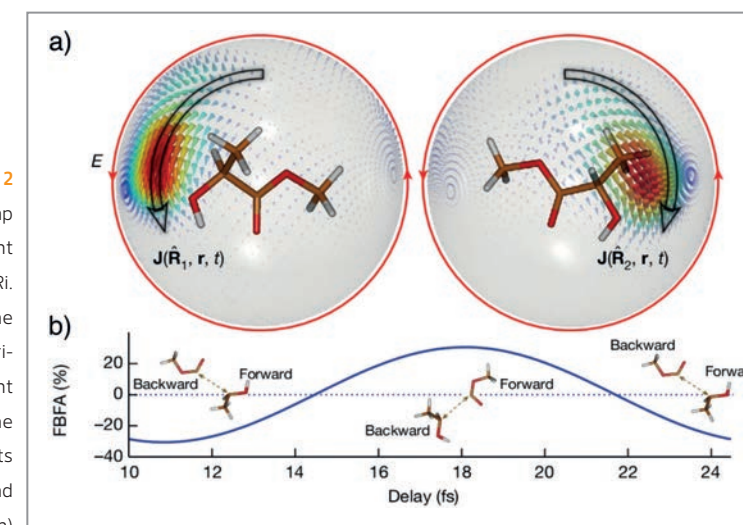


Figure 2

a) Snapshots of the electronic current generated by the pump pulse on a sphere with a radius of 10 atomic units. The current surrounds the molecule for two distinct orientations, R₁. Photoionisation is enhanced for orientation R₁, in which the current (black arrow) rotates together with the circularly polarised field (red arrow). b) Calculated forward/backward fragment asymmetry (FBFA) along the laser propagation axis during the dissociative ionisation of methyl lactate cations. The insets illustrate the preferential directions of emission of CO₂CH₃ and CH₃CHOH⁺ fragments. (Figure adopted from original publication)

We found that the emission direction of photoelectrons from a given enantiomer of methyl lactate can reverse in less than 10 fs, even though the molecular structure remains unchanged. Our theoretical model was able to confirm that this ultrafast chiral response is due to quantum beatings as a result of a superposition of electronic states created by the UV radiation.

The model also showed that the electron motion driven by quantum beatings generates a chiral current—a flow of charge that reflects the handedness of the molecule. The direction of rotation of this current periodically reverses on the same ultrafast timescale observed experimentally, providing an important tool for the photocontrol of chiral molecules.

Indeed, the properties of the chiral currents we discovered depend strongly on the orientation of the molecule (Fig. 2a). Our calculations predict that by using an ensemble of randomly oriented enantiomers, it is possible to exploit this feature in order to selectively ionise a subset of molecules that share the same orientation, using a circularly polarised pulse that rotates in the same direction as the electronic current. This unique filtering effect is achievable only because both the chiral current and the ionising laser pulses possess spin angular momentum, resulting in enantiospecific interactions. By using this effect, we intend to control the fragmentation direction of chiral molecules induced by dissociative ionisation as an experimental proof-of-principle for enantio-sensitive charge-directed reactivity [6]. This will be achieved by measuring the forward/backward fragment asymmetry (FBFA, Fig. 2b) of ions produced after photoionisation by circularly polarised pulses with few-fs time resolution.

In conclusion, our findings provide valuable insights into the quantum-level interactions between chiral molecules and light, revealing a previously unknown aspect of electron dynamics and opening up possibilities for photochemical

control through enantio-sensitive, charge-directed reactivity. From a broader perspective, this work demonstrates that the laser technology required for the perturbative study of ultrafast electron dynamics in neutral molecules has finally come of age.

Author contact: Vincent Wanie, vincent.wanie@desy.de
Bernard Pons, bernard.pons@u-bordeaux.fr
Francesca Calegari, francesca.calegari@desy.de

References

- V. Svoboda et al., 'Femtosecond photoelectron circular dichroism of chemical reactions', *Sci. Adv.* 8, eabq2811 (2022).
- S. Beaulieu et al., 'Probing ultrafast dynamics of chiral molecules using time-resolved photoelectron circular dichroism', *Faraday Discuss.* 194, 325–348 (2016).
- A. Comby et al., 'Relaxation Dynamics in Photoexcited Chiral Molecules Studied by Time-Resolved Photoelectron Circular Dichroism: Toward Chiral Femtochemistry', *J. Phys. Chem. Lett.* 7, 4514–4519 (2016).
- V. Wanie et al., 'A flexible beamline combining XUV attosecond pulses with few-femtosecond UV and near-infrared pulses for time-resolved experiments', *Rev. Sci. Instrum.* 95, 083004 (2024).
- M. Galli et al., 'Generation of deep ultraviolet sub-2-fs pulses', *Opt. Lett.* 44, 1308–1311 (2019).
- A. Ordonez et al., 'Geometric magnetism and anomalous enantio-sensitive observables in photoionization of chiral molecules', *Commun. Phys.* 6, 257 (2023).

Original publication

'Capturing electron-driven chiral dynamics in UV-excited molecules', *Nature* 630, 109–115 (2024). DOI: 10.1038/s41586-024-07415-y



Vincent Wanie¹, Etienne Bloch², Erik P. Månsson¹, Lorenzo Colaizzi^{1,3}, Sergey Ryabchuk^{3,4}, Krishna Saraswathula^{1,3}, Andres F. Ordonez⁵, David Ayuso^{5,6}, Olga Smirnova^{6,7}, Andrea Trabattini^{1,8}, Valérie Blanchet², Nadia Ben Amor⁹, Marie-Catherine Heitz⁹, Yann Mairesse², Bernard Pons² and Francesca Calegari^{1,3,4}

- Center for Free-Electron Laser Science, CFEL, DESY, Hamburg, Germany
- Université de Bordeaux, CNRS, CEA, CELIA, Talence, France
- Department of Physics, University of Hamburg, Hamburg, Germany
- The Hamburg Centre for Ultrafast Imaging, University of Hamburg, Hamburg, Germany
- Department of Physics, Imperial College London, London, United Kingdom
- Max-Born-Institut, Berlin, Germany
- Technische Universität Berlin, Berlin, Germany
- Institute of Quantum Optics, Leibniz Universität Hannover, Hannover, Germany
- Laboratoire de Chimie et Physique Quantiques, CNRS, UPS, Toulouse, France

A tiny droplet of acid

Hyperfine-resolved rotational spectroscopy reveals the HCl dissociation with minimal hydration

A key challenge in molecular science is to understand how properties of matter transition from the molecular scale to the bulk phase. The dissociation of acids, which is relevant for their acidic properties, in the presence of just a few water molecules is particularly important for grasping fundamental chemical processes, from interstellar reactions to atmospheric nucleation. In our recent study focusing on complexes of hydrochloric acid (HCl) with up to seven water molecules, we measured the coupling between chlorine's nuclear spin and the angular momentum of the HCl-water clusters to determine whether the H-Cl bond is covalent or ionic. HCl was found to dissociate after forming three hydrogen bonds with water molecules upon the addition of a fifth water molecule, resulting in a dissociated $\text{H}^+\text{Cl}^-(\text{H}_2\text{O})_5$ cluster with a contacting ionic bond.

Molecules often display distinct properties in their isolated gaseous forms compared to their condensed phases. In the gas phase an acid monomer remains intact with the proton covalently bonded to its conjugate base. However, in aqueous solution, acids dissociate, releasing the proton to form hydrated ions which then drive various chemical reactions of interests. This raises a fundamental question: How many water molecules are required to trigger acid dissociation? This fundamental knowledge is essential for understanding key molecular processes such as the formation of aerosol particles that contribute to atmospheric pollution or catalytic reactions occurring on ice surfaces.

One effective method for uncovering the aggregation process at the molecular level is to study acid-water clusters

of varying sizes formed in cold, isolated environments. By adding individual water molecules in a stepwise manner, one could observe how geometry and reactivity evolves with cluster growth. In the case of HCl microsolvation, pioneering infrared spectroscopic studies successfully characterised HCl-water clusters containing up to three water molecules in superfluid helium nanodroplets and molecular jets [1,2]. At this stage of aggregation, the dissociation of HCl was not observed. With four or more water molecules, theoretical calculations predicted dissociation. However, the resulting clusters exhibit three-dimensional structures with similar yet distinct atomic configurations, complicating the analysis of vibrational signals at the limits of the detection methods and their link to the specific properties of the acid-water clusters.

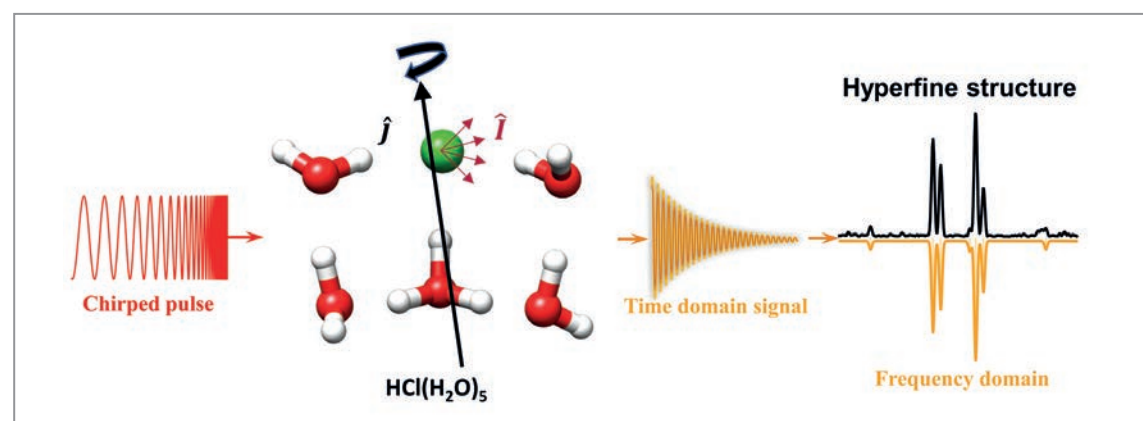
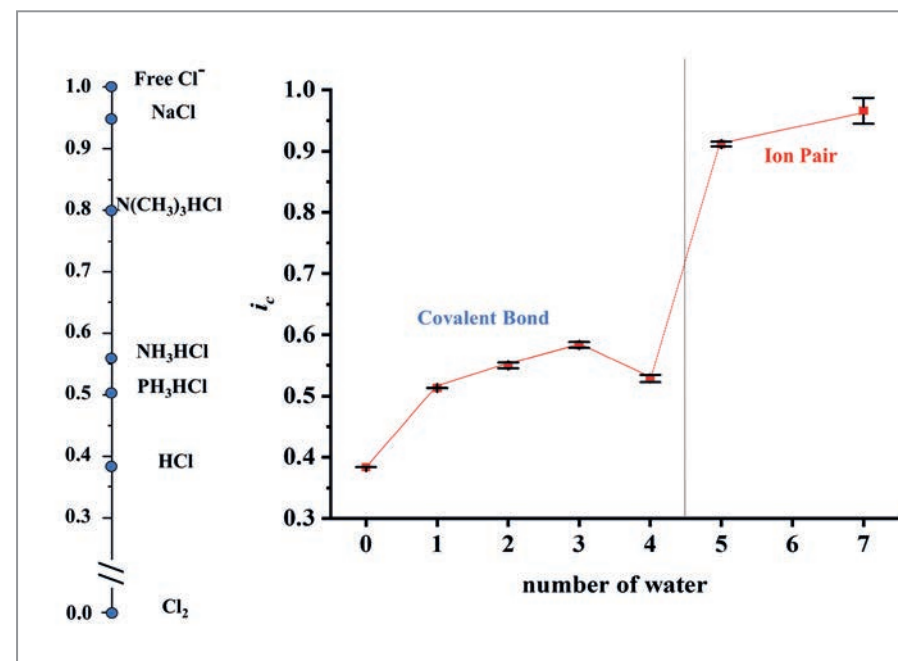


Figure 1
Representation of a rotational spectroscopy measurement of HCl-water clusters. A broadband microwave pulse (red) induces coherence between rotational energy levels of the clusters, resulting in a macroscopic dipole moment as an ensemble effect. Subsequently, the decay of this macroscopic dipole moment is recorded as a function of time in the form of a free induction decay (yellow). Due to the coupling of the nuclear spin of the chlorine (Cl) atom with the molecular rotation, the resulting spectrum exhibits a characteristic hyperfine structure which provides valuable insight into the bonding character and thus the amount of ionicity of the chlorine atom.

Figure 2
The ionicity i_c of the H-Cl bond in a series of $\text{HCl}(\text{H}_2\text{O})_n$ clusters derived from the Cl nuclear hyperfine structures (right). For comparison, the degree of ionicity for a variety of chlorine-containing molecules, ranging from a fully covalent bond ($i_c=0$) in the Cl_2 molecule to a highly ionic species like in NaCl is provided on the left side. For the series of $\text{HCl}(\text{H}_2\text{O})_n$ clusters, a clear change in ionicity is observed for HCl micro-solvation with five water molecules and more, indicating the HCl dissociation associated with proton migration to the surrounding water molecules.



This complexity has sparked decades of debate within the scientific community.

To offer new insights to this topic, we revisited HCl-water clusters formed in a supersonic jet expansion using high-resolution broadband rotational spectroscopy which we designed and operate in our in-house laboratory. As shown in Fig. 1, these clusters were irradiated with frequency-chirped microwave pulses, which excited transitions between quantised rotational states, which are strongly dependent on the structures of the complexes and thus provided their distinct rotational spectroscopic signatures. These signatures carry highly detailed structural information, enabling us to unambiguously identify the different structural arrangements of the HCl-water clusters. Most importantly, our microwave spectroscopy experiments revealed the coupling between chlorine's nuclear spin and the angular momentum of the clusters which manifests as a characteristic hyperfine structure in the spectra. This hyperfine structure adds an additional layer of complexity to the spectral analysis, but it is extremely valuable as it provides direct information about the electron distribution around the chlorine nucleus. This electron distribution is a direct indicator of the bonding environment, giving us insight into how the chlorine atom interacts with nearby water molecules and how its bonding character changes as the cluster evolves.

As shown in Fig. 2, the analysis of this hyperfine structure gives direct measurement of the H-Cl bond ionicity as a function of the number of surrounding water molecules. It was observed that the addition of a fifth water molecule leads to the dissociation of HCl, resulting in a dissociated $\text{H}^+\text{Cl}^-(\text{H}_2\text{O})_5$ cluster, which goes along with the formation of three hydrogen bonds of HCl with water. In this configura-

tion, the H-Cl bond undergoes a transformation from covalent to ionic, marking a significant shift in the cluster's chemical nature.

Our definitive rotational spectral assignments provided unambiguous determinations of both the geometry and electronic configuration of the HCl-water clusters. This clarity is essential for understanding the stepwise process of HCl microsolvation and how it leads to dissociation under increasing hydration. Furthermore, these findings could also offer valuable reference points for interpreting the results of other experimental and theoretical studies on the topic of small HCl-water clusters.

Author contact: Fan Xie, fan.xie@desy.de
Denis S. Tikhonov, denis.tikhonov@desy.de
Melanie Schnell, melanie.schnell@desy.de

References

1. A. Gutberlet et al., 'Aggregation-induced dissociation of $\text{HCl}(\text{H}_2\text{O})_2$ below 1 K: the smallest droplet of acid', *Science* 324, 1545–1548 (2009).
2. D. Skvortsov et al., 'Hydrated HCl clusters, $\text{HCl}(\text{H}_2\text{O})_{1-3}$, in helium nanodroplets: studies of free OH vibrational stretching modes', *J. Phys. Chem. A* 113, 26, 7360–7365 (2009).

Original publication

'Electric nuclear quadrupole coupling reveals dissociation of HCl with a few water molecules', *Science* 384, 1435–1440 (2024).
DOI: 10.1126/science.ado7049

Fan Xie¹, Denis S. Tikhonov² and Melanie Schnell^{1,2}

1. Deutsches Elektronen-Synchrotron DESY, Hamburg, Germany
2. Institut für Physikalische Chemie, Christian-Albrechts-Universität zu Kiel, Kiel, Germany



A new type of magnetism experimentally confirmed in RuO₂

Time-reversal symmetry breaking despite compensated magnetic order

Ferromagnetism and antiferromagnetism have long been known as the two classes of magnetic order in materials. As early as 2020 a third class of magnetic order was predicted called altermagnetism. Recently, experimental evidence for altermagnetism has been provided by the observation of a circular dichroism effect, which is considered to be a signature of altermagnetism. Altermagnets combine the advantages of ferromagnets and antiferromagnets. Their neighbouring magnetic moments are antiparallel, as in antiferromagnets, but at the same time they exhibit a spin-polarised current, as in ferromagnets.

In an altermagnet electrons moving in one direction have a uniform opposite spin direction in respect to the spin direction of those electrons moving in the other direction [1] (see Fig. 1a). This alignment phenomenon has nothing to do with the position of the electrons but only with the direction of the electron's velocity. Thus, altermagnetism is a phenomenon in reciprocal rather than in direct space. The complete spin polarisation of the conduction electrons in altermagnets is advantageous in spintronic devices, resulting in much larger magnetoresistance effects than in antiferromagnets. In contrast to ferromagnets, the switching time of the altermagnetic order is not limited by the Larmor precession due to the compensated magnetic moments.

An essential distinction between altermagnets and antiferromagnets is their different symmetry [2]. In antiferromagnets, the time reversal operation T flips all magnetic moments. Combined with the translational symmetry of

the lattice, t , collinear antiferromagnets are symmetric with respect to Tt . In altermagnets the Tt symmetry is broken due to their specific crystal symmetry where the two magnetic sublattices have different crystal fields. Instead, altermagnets are symmetric with respect to T combined with a rotation R .

The broken time-reversal symmetry combined with the spin polarisation pattern of the valence electrons in reciprocal space make altermagnetism an ideal subject for the study of circular dichroism in angle-resolved photoemission. The photoelectrons were excited by circularly polarised soft X-rays (open port I of beamline P04, PETRA III, DESY, Hamburg) from epitaxial RuO₂(110) films grown by pulsed laser deposition on TiO₂(110) substrates. For their detection we used the time-of-flight momentum microscope with an energy resolution of 60 meV at a sample temperature of 70 K [3]. The azimuthal orientation of the

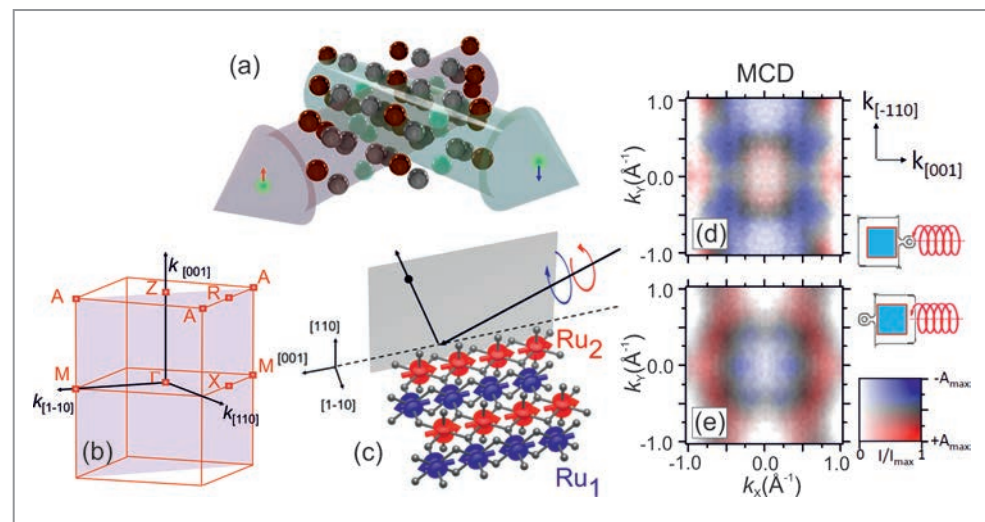


Figure 1
a) Opposite spin direction for electrons moving in two different directions with respect to the crystal geometry. b) Brillouin zone showing the high symmetry points relevant to the spectra shown in the data. c) Sketch of the RuO₂ magnetic crystal structure with the surface oriented along the [110] direction and the experimental setup of scattered photoelectrons from circularly polarised light. d) MCD and intensity shown in a combined colour scale. e) Similar data for the sample rotated by 180° as indicated by the sketches on the right.

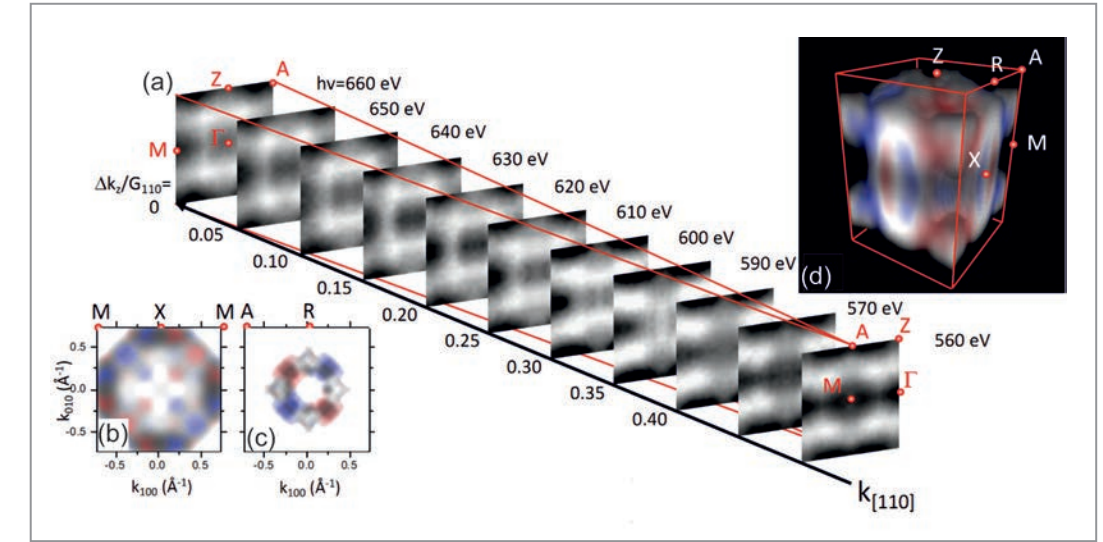


Figure 2
The 3D Fermi surface is constructed from photoemission data measured for a series of photon energies. a) Series of photoelectron intensity maps at the Fermi level for indicated photon energies. b-c) Photoelectron intensity at the Fermi surface for planes perpendicular to the c -axis [110] at $k_z = 0$ and $0.5G_{110}$. d) Three-dimensional Fermi surface colour marked with the MCD asymmetry.

sample was adjusted, so that the plane of photon incidence coincided with the easy spin axis of RuO₂, i.e. the [001] c axis (Fig. 1c). We measured the intensity distribution of the direct transitions in four-dimensional energy-momentum space $I(E_B, k_x, k_y, k_z)$ where E_B – binding energy; k_x, k_y, k_z – wave vectors. This intensity distribution is the spectral density function modulated by matrix elements accounting for the photoexcitation probability for a given initial k_i and final state k_f . The kinetic energy of the emitted photoelectrons is recorded by their time of flight, and the Fermi edge serves as reference for $E_B = 0$. The intensity asymmetry is calculated pixel by pixel as $A = (I^+ - I^-)/(I^+ + I^-)$, with I^+ and I^- denoting the intensity measured at circular right and left polarisation, and the asymmetry of magnetic circular dichroism (MCD) as $A_{MCD}(k_x, k_y) = A(k_x, k_y) + A(k_x - k_y)$. Figure 1d-e shows the MCD maps at the Fermi level. The MCD data show negative asymmetry for the vertical stripes parallel to Γ -M and positive values for the horizontal stripes parallel to Γ -Z. The maximum values of the A_{MCD} are $\pm 15\%$. To confirm that the observed A_{MCD} values are related to the magnetic order of the sample, we rotated the sample around the surface normal by 180 degree and repeated the photoemission experiment. The corresponding results are shown in Fig. 1e. The A_{MCD} has reversed its sign which is a direct observation of the broken time-reversal symmetry in the sample. The scanning of the perpendicular momentum by photon energy is shown in Fig. 2. This topographic mapping is performed by varying the photon energy, mapping a complete 3D Brillouin zone. The distribution of positive and negative MCD values reflects the d -wave symmetry of the altermagnetic exchange splitting as predicted for RuO₂.

Author contact:
Olena Fedchenko, ofedchen@uni-mainz.de
Hans-Joachim Elmers, elmerts@uni-mainz.de

References

1. L. Šmejkal, R. González-Hernández, T. Jungwirth and J. Sinova, 'Crystal time-reversal symmetry breaking and spontaneous Hall effect in collinear antiferromagnets', *Sci. Adv.* **6**, eaaz8809 (2020).
2. L. Šmejkal, J. Sinova and T. Jungwirth, 'Emerging research landscape of altermagnetism', *Phys. Rev. X* **12**, 040501 (2022).
3. K. Medjanik, O. Fedchenko, S. Chernov, D. Kutnyakhov, M. Ellguth, A. Oelsner, B. Schönhense, T. R. F. Peixoto, P. Lutz, C.-H. Min, F. Reinert, S. Däster, Y. Acremann, J. Viehhaus, W. Wurth, H. J. Elmers and G. Schönhense, 'Direct 3D mapping of the Fermi surface and Fermi velocity', *Nat. Mater.* **16**, 615 (2017).

Original publications

'Observation of time-reversal symmetry breaking in the band structure of altermagnetic RuO₂', *Science Advances* **10**, ead4883 (2024). DOI: [10.1126/sciadv.adj4883](https://doi.org/10.1126/sciadv.adj4883).



Olena Fedchenko¹, Jan Minár², Akashdeep Akashdeep¹, Sunil Wilfred D'Souza², Dmitry Vasilyev¹, Olena Tkach^{1,3}, Lukas Odenbreit¹, Quynh Nguyen⁴, Dmytro Kutnyakhov⁵, Nils Wind^{6,7,8}, Lukas Wenthaus⁵, Markus Scholz⁶, Kai Rossnagel^{6,8}, Moritz Hoesch⁵, Martin Aeschlimann⁹, Benjamin Stadtmüller¹, Mathias Kläui^{1,8}, Gerd Schönhense¹, Tomas Jungwirth^{10,11}, Anna Birk Hellenes¹, Gerhard Jakob¹, Libor Šmejkal^{1,10}, Jairo Sinova^{1,10} and Hans-Joachim Elmers¹

1. Institut für Physik, Johannes Gutenberg-Universität, Mainz, Germany
2. University of West Bohemia, New Technologies Research Centre, Plzeň, Czech Republic
3. Sumy State University, Sumy, Ukraine
4. Linac Coherent Light Source, Menlo Park, USA
5. Deutsches Elektronen-Synchrotron DESY, Hamburg, Germany
6. Ruprecht Haensel Laboratory, Deutsches Elektronen-Synchrotron DESY, Hamburg, Germany
7. Institut für Experimentalphysik, Universität Hamburg, Hamburg, Germany
8. Institut für Experimentelle und Angewandte Physik, Christian-Albrechts-Universität zu Kiel, Kiel, Germany
9. Universität Kaiserslautern, Kaiserslautern, Germany
10. Institute of Physics Academy of Sciences of the Czech Republic, Praha, Czech Republic
11. School of Physics and Astronomy, University of Nottingham, Nottingham, United Kingdom

Storing X-ray wave packets

A pathway to an X-ray quantum memory

Light is an excellent carrier of information. It is used not only for classical communication technologies but also increasingly for quantum applications such as quantum computing. However, processing light signals is far more difficult compared to the more common electronic signals. We demonstrated how X-ray pulses can be stored and released by a frequency comb in a novel way that could be applicable for future X-ray quantum technologies.

In quantum computing, much like in classical computing, synchronisation of various computational processes is an elemental part. This renders a memory device essential, where the quantum information, so called qubits, can be stored and released at predetermined times without loss of information. In optical quantum computing, qubits are encoded in the various degrees of freedom of photon wave packets, such as their polarisation state, number of photons or waveform. Storing such a wave packet without losing its quantum information is a major challenge for optical quantum applications [1].

Typically, the problem is solved by transferring the quantum information to long-lived collective quantum excitations in matter systems. Various protocols have been established that can force the matter system to re-emit the photon wave packet at a predetermined time, allowing the qubit to

be read out. One particularly appealing protocol uses a 'frequency comb' structure. In this method, the absorption spectrum of the matter system features a series of evenly spaced atomic resonances – the comb teeth. When a photon wave packet with a suitable spectrum gets absorbed by such a comb structure, all resonances are simultaneously excited. This collective state represents a coherent excitation of many frequency modes by a single photon [2]. While at the time of excitation all modes are in-phase, the different frequencies cause a rapid dephasing. With the specific structure of the frequency comb, however, the modes will rephase at certain 'echo' time instants that are inversely proportional to the frequency spacing of the comb. This results in a highly increased photon emission probability—a photon echo which is essentially a copy of the absorbed photon wave packet [2, 3]. Thus, by preparing a certain frequency comb state in the matter system before the arrival of a photon wave packet, the re-emission of the photon wave packet can be well-controlled to occur at predetermined time instants.

This 'quantum memory' protocol has been demonstrated for visible light using strong laser sources to create a frequency comb in the absorption spectrum of an atomic ensemble. This becomes increasingly difficult with decreasing wavelengths because light sources are much weaker at X-ray energies. We overcame this problem by using a novel approach to form a frequency comb [4]. Instead of an

Figure 1
Sketch of the experimental setup for the nuclear frequency comb. a) Seven stainless-steel foils enriched in the isotope ^{57}Fe (^{57}SS) are moved along the beam direction, each with a different velocity. The velocities of adjacent foils are set to differ by a constant velocity spacing Δv . b) The motion-induced Doppler shifts form a frequency comb in the nuclear absorption structure which can absorb photon wave packets with suitable spectral shapes (gray, exemplary).

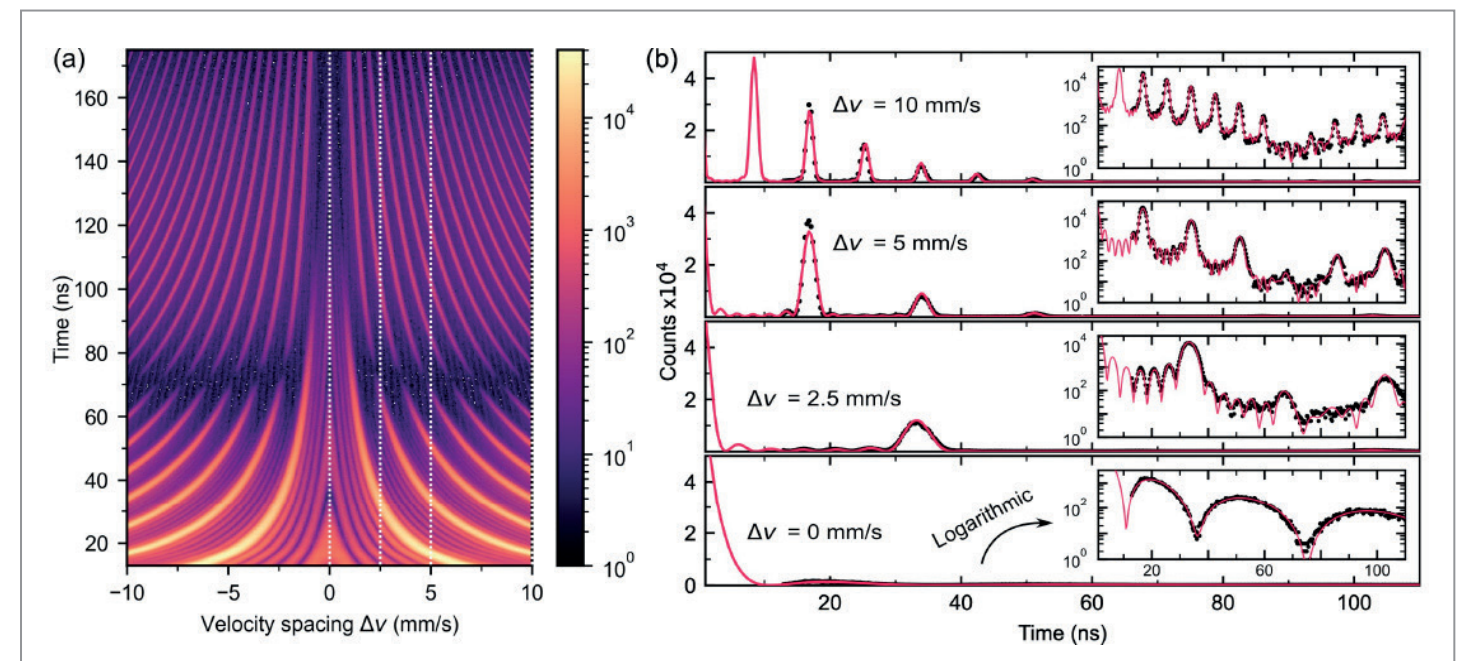
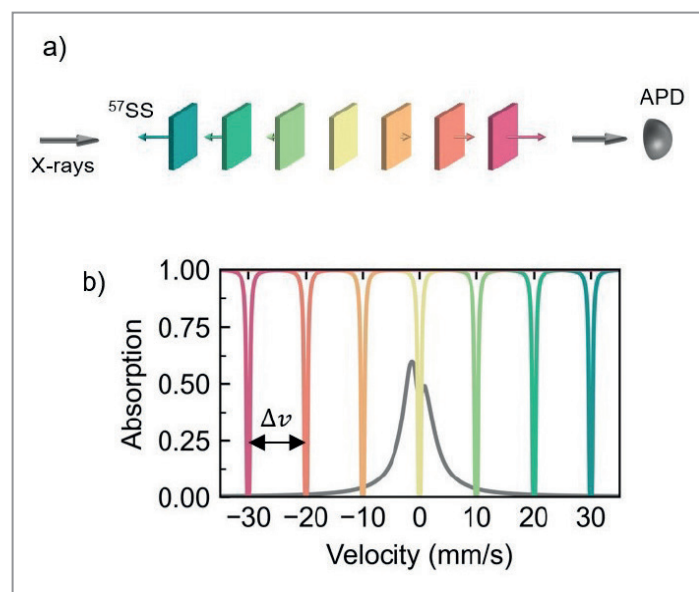


Figure 2
Photon emission after excitation of the nuclear frequency comb. a) Each emitted photon is counted as a function of its arrival time at the detector after X-ray excitation and the velocity spacing of the frequency comb. The colour scale is logarithmic, showcasing the time instants of high emission probability as sharp bright lines. b) Line-cuts from a) for specific velocity spacing in linear and logarithmic scale, nicely following the simulated patterns (red).

electronic transition in the atom, the nuclear transition of the isotope ^{57}Fe at an energy of 14.4 keV is utilised. Nuclear transitions feature extremely narrow energy linewidths. The transition of ^{57}Fe , for example, has a natural linewidth of 5 neV – nearly 13 orders of magnitude smaller than its transition energy. For these narrow transitions, Doppler shifts caused by mechanical motions can substantially shift the transition energy. In the experiments performed at beamline P01 (PETRA III) and ID18 (ESRF), we used mechanical motions to form a frequency comb structure by using multiple moving absorber foils as depicted in Fig. 1. After excitation of all moving foils with a short resonant X-ray pulse, a collective frequency comb state is generated which emits an X-ray wave packet into the same direction with high probability at the comb's echo time instants. The wave packet's release time is adjustable by the velocity spacing (Fig. 2). For increasing velocity spacing of the foils, the echo separation decreases. In addition, the nuclear frequency comb demonstrated that an X-ray wave packet can be stored with moderate efficiency (33%) while preserving its temporal waveform, as quantified by a 'fidelity' of up to 97%.

The synchrotron pulses used in these experiments contain far below one resonant photon on average. The ability to work on a single-photon level without loss of information qualifies the nuclear frequency comb as a quantum memory [5] and is its first demonstration at X-ray energies. Our work highlights the potential for applying quantum technologies at short wavelengths regimes where devices can be more compact and flexible while operating at room temperature. The nuclear frequency comb also allows for the formation of 'time-bin' waveforms, a specific type of

photonic qubit. Manipulating and controlling X-ray wave packets at the single-photon level opens up intriguing possibilities for technical applications such as excitation and detection of ultra-narrow nuclear transitions as well as advancing the field quantum optics at X-ray energies.

Author contact: Sven Velten, sven.velten@desy.de

References

1. A. I. Lvovsky, B. C. Sanders and W. Tittel, 'Optical quantum memory', *Nat. Photonics* **3**, 706–714 (2009).
2. M. Afzelius, C. Simon, H. de Riedmatten and N. Gisin, 'Multimode quantum memory based on atomic frequency combs', *Phys. Rev. A* **79**, 052329 (2009).
3. H. de Riedmatten, M. Afzelius, M. U. Staudt, C. Simon and N. Gisin, 'A solid-state light-matter interface at the single-photon level', *Nature* **456**, 773–777 (2008).
4. X. Zhang, W.-T. Liao, A. Kalachev, R. Shakhmuratov, M. Scully and O. Kocharovskaya, 'Nuclear quantum memory and time sequencing of a single γ photon', *Phys. Rev. Lett.* **123**, 250504 (2019).
5. Y. Lei, F. K. Asadi, T. Zhong, A. Kuzmich, C. Simon and M. Hosseini, 'Quantum optical memory for entanglement distribution', *Optica* **10**, 1511–1528 (2023).

Original publication

'Nuclear quantum memory for hard X-ray photon wave packets', *Science Advances* **10**, eadn9825 (2024). DOI: 10.1126/sciadv.adn9825



Sven Velten^{1,2}, Lars Bocklage^{1,2}, Xiwen Zhang³, Kai Schlage⁴, Anjali Panchwane¹, Sakshath Sadashivaiah^{4,5}, Ilya Sergeev¹, Olaf Leupold¹, Aleksandr I. Chumakov⁶, Olga Kocharovskaya³ and Ralf Röhlsberger^{5,4,7,1,2}

1. Deutsches Elektronen-Synchrotron DESY, Hamburg, Germany
2. The Hamburg Centre for Ultrafast Imaging CUI, Hamburg, Germany
3. Texas A&M University, College Station, USA
4. Helmholtz-Institut Jena, Jena, Germany
5. GSI Helmholtzzentrum für Schwerionenforschung GmbH, Darmstadt, Germany
6. ESRF - The European Synchrotron, Grenoble, France
7. Friedrich-Schiller Universität Jena, Jena, Germany

Towards ultrafast energy-efficient data recording

The nature of terahertz-driven coherent spin dynamics in magnetic recording media

Not at last due to the advent of artificial intelligence, crypto currencies and autonomous driving, the transformation into the digital age is accompanied by an enormous increase in data generated and energy consumed. These developments ask for ever faster data-recording solutions with high energy efficiency. Among the most promising ones is the use of terahertz pulses that can drive coherent spin dynamics at unprecedented high frequencies and with low power consumption. In this project, we were pioneering terahertz pump-probe experiments at the free-electron laser FLASH, unravelling the nature of ultrafast coherent spin dynamics in nanometre-sized magnetic domains.

Femtomagnetism is the research field studying magnetisation dynamics induced by femto- to picosecond laser pulses. Extreme laser fields with frequencies in the terahertz (THz) regime thereby revealed the existence of ultrafast coherent magnetisation oscillations in ferromagnetic thin films [1]. In analogy to the nutation of a spinning top in classical mechanics, this is believed to be a higher-order effect of the THz magnetic field exerting a Zeeman torque on the magnetisation vector. Ultimately, interactions of THz light with magnetic matter promise an efficient all-optical reversal of the magnetisation direction on ultra-short timescales [2]. Completely unknown so far, however, is the THz-driven magnetisation dynamics in technologically relevant magnetic materials with perpendicular magnetic anisotropy (PMA) and nanometre-sized magnetic domains. Combining THz pumping with X-ray resonant magnetic scattering (XRMS) at FLASH beamline BL3, we could resolve the coherent magnetisation oscillations with nanometre-spatial resolution in a state-of-the-art magnetic recording medium for the first time. An image of the investigated domain network, recorded at PETRA III beamline P04, and

the corresponding XRMS signal, obtained at obtained at FLASH, are shown in Fig. 1a and b, respectively. Our results reveal that, indeed, the THz-driven dynamics are local coherent oscillations of nanometre-sized spin structures, whereas nonlocal effects like spin superdiffusion in lateral dimensions are lacking. Hence, the results suggest the feasibility of spatially controlled THz all-optical recording in magnetic nanostructures where the perpendicular magnetic anisotropy acts as an energy barrier limiting the speed of the data writing.

The two main challenges of this project were to identify the THz-pulse characteristics and the spatio-temporal overlap of the THz and FEL pulses at the sample position. The former was improved over the past years under the lead of Nikola Stojanovic (now DLR) and Rui Pan (DESY), enabling radiometric power measurements, electro-optic sampling, spatial beam profiling and Fourier-transform infrared spectroscopy at BL3 [3]. The latter could be solved within the FS-CXS group under the lead of Gerhard Grübel (now EuXFEL), developing a THz end station for time-

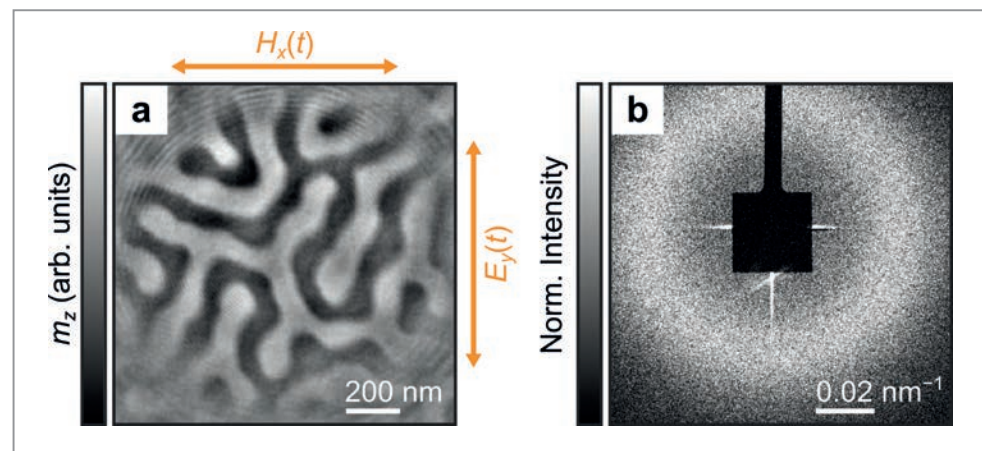
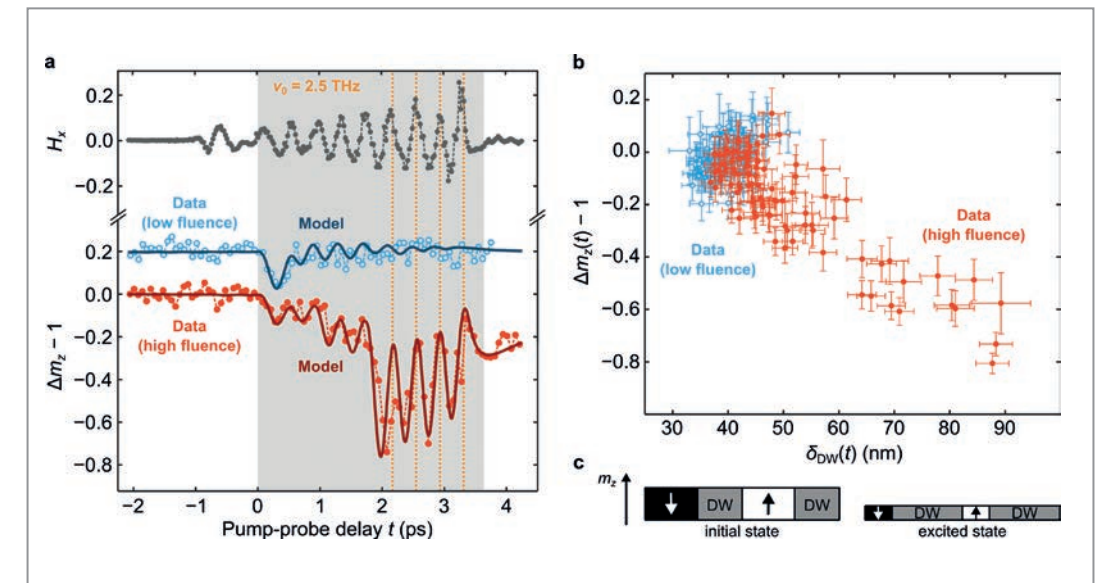


Figure 1
a) Image of the labyrinth-type magnetic domain network in ferromagnetic Co/Pt multilayers obtained by Fourier-transform holography. Arrows indicate the oscillation directions of the THz electric and magnetic fields. b) Normalised magnetic scattering image obtained by THz-pump-XRMS-probe measurements at delay time of -1 ps (initial state).

Figure 2
a) Top: Time trace of the THz magnetic field measured by electro-optic sampling. The THz undulator was tuned to generate 3.6 ps long THz pump pulses with fundamental frequency of 2.5 THz and a magnetic field of 1.4 T. Bottom: response of the magnetisation m_z component to low- and high-fluence THz excitation. The low fluence is shifted for clarity, dotted and dashed lines are guides to the eye. b) Correlation between average local magnetisation $m_z(t)$ and average domain-wall dynamics $\delta_{DW}(t)$. c) One-dimensional illustration of the initial- and maximum-excited domain network.



resolved XRMS experiments at BL3 that comprises an in-vacuum beamstop photodiode [4] and sample holder with fluorescent screen and coarse-timing tools.

Furthermore, low- and high-fluence THz pulses caused qualitatively different dynamics as compared to magnetic materials without PMA [1]. Inspired by the thermal stability of the magnetisation direction in nanoscale magnetic particles, we could understand our results by a time-dependent magnetic damping that is determined by the heat-induced compensation of the anisotropy energy barrier, providing a guideline to tune the dynamics via PMA and the THz-pump fluence (Fig. 2a). Time-resolved XRMS, moreover, provides information on the ultrafast spin dynamics in lateral dimensions, given by the time-evolution of the domain network's form- and structure-factor contributions. Our results show no signs of domain and domain-wall dynamics on femto-second timescales (in the presence of PMA) but a high degree of correlation between domain and domain-wall dynamics (Fig. 2b) on picosecond timescales (upon heat-induced compensation of PMA). This demonstrates the local character of the ultrafast coherent spin oscillations and suggests the applicability of THz all-optical recording in magnetic nanostructures without substantial spin leakage in lateral dimensions.

The availability of extreme THz pulses paved the way for studying ultrafast coherent phenomena in condensed matter at FLASH. The upcoming beamline FL11 will replace beamline BL3, expanding the range of dynamic investigations in THz pump-probe experiments [5,6]. A semi-permanent end station with cryogenic magnet and sample environments called SPINFLASH is currently manufactured via ErUM-Pro funding.

Author contact: Matthias Riepp, matthias.riempf@ipcms.unistra.fr

References

- M. Shalaby, A. Donges, K. Carva, R. Allenspach, P. M. Oppeneer, U. Nowak and C. P. Hauri, 'Coherent and incoherent ultrafast magnetization dynamics in 3d ferromagnets driven by extreme terahertz fields', *Phys. Rev. B* 98, 014405 (2018).
- C. H. Back, D. Weller, J. Heidmann, D. Mauri, D. Guarisco, E. L. Garwin and H. C. Siegmann, 'Magnetization Reversal in Ultrashort Magnetic Field Pulses', *Phys. Rev. Lett.* 81, 3251-3254 (1998).
- R. Pan, E. Zapolnova, T. Golz, A. J. Krmpot, M. D. Rabasovic, J. Petrovic, V. Asgekar, B. Faatz, A. Perucchi, S. Kovalev, B. Green, G. Geloni, T. Tanikawa, M. Yurkov, E. Schneidmiller, M. Gensch and N. Stojanovic, 'Photon diagnostics at the FLASH THz beamline', *J. Synchrotron Radiat.* 26, 700-707 (2019).
- L. Müller, M. Walther, M. Riepp, A. Philippi-Kobs, W. Jo, W. Roseker, K. Bagschik, R. Frömter, R. Pan, D. Lott, J. Möller, U. Bösenberg, J. Hallmann, A. Rodriguez-Fernandez, M. Scholz, G. Ansaldo, J. Wrigley, A. Zozulya, A. Madsen and G. Grübel, 'The beam stop as an intensity monitor', *J. Phys.: Conf. Ser.* 2380, 012081 (2022).
- E. Zapolnova, T. Golz, R. Pan, K. Klose, S. Schreiber and N. Stojanovic, 'THz pulse doubler at FLASH: double pulses for pump-probe experiments at X-ray FELs', *J. Synchrotron Radiat.* 25, 39-43 (2018).
- E. Zapolnova, R. Pan, T. Golz, M. Sindik, M. Nikolic, M. Temme, M. Rabasovic, D. Grujic, Z. Chen, S. Toleikis and N. Stojanovic, 'XUV-driven plasma switch for THz: new spatio-temporal overlap tool for XUV-THz pump-probe experiments at FELs', *J. Synchrotron Radiat.* 27, 11-16 (2020).

Original publication

'Terahertz-driven coherent magnetization dynamics in labyrinth-type domain networks', *Physical Review B* 110, 094405 (2024). DOI: 10.1103/PhysRevB.110.094405



M. Riepp^{1,2}, A. Philippi-Kobs^{2,3}, L. Müller², W. Roseker², R. Rysov², R. Frömter⁴, K. Bagschik², M. Hennes⁵, D. Gupta¹, S. Marotzke^{2,3}, M. Walther², S. Bajt^{6,7}, R. Pan², T. Golz², N. Stojanovic⁸, C. Boeglin⁸ and G. Grübel²

- Institut de Physique et Chimie des Matériaux de Strasbourg, Université de Strasbourg, CNRS, France
- Deutsches Elektronen-Synchrotron DESY, Hamburg, Germany
- Institut für Experimentelle und Angewandte Physik, Christian-Albrechts-Universität zu Kiel, Germany
- Institute of Physics, Johannes Gutenberg-Universität Mainz, Germany
- Sorbonne Université, CNRS, Institut des NanoSciences de Paris, INSP, Paris, France
- Center for Free-Electron Laser Science CFEL, DESY, Hamburg, Germany
- The Hamburg Centre for Ultrafast Imaging CUI, University of Hamburg, Germany
- Institute for Optical Sensor Systems, Deutsches Zentrum für Luft- und Raumfahrt, Berlin, Germany

Where do energy and angular momentum go?

Identifying the microscopic nature of non-equilibrium energy and angular momentum transfer mechanisms

Femtosecond lasers can quench the magnetism of metallic ferromagnets within ~100 fs. Flipping of electronic spins was expected to be nanosecond slow, hence the question how this loss of angular momentum happens remains enigmatic even after 25 years of the pioneering experiment. Researchers at Uppsala University, in a collaboration with researchers from Germany, have exploited the fundamental conservation laws of energy and momentum to track the scattering of spins after laser excitations in time-momentum space. These results illustrate the influence of lattice-mediated scattering processes and pave the way for deciphering the still elusive microscopic mechanism of angular momentum transfer between spin and lattice.

Understanding elementary scattering processes due to the interactions between electrons and lattice vibrations is of importance in a wide range of condensed matter phenomena such as superconductivity, electronic and spin transport, ultrafast demagnetisation and laser-induced phase transitions.

In a pioneering experiment in 1996 [1], it was shown that femtosecond-optical pulses can be used to demagnetize nickel, i.e., the ferromagnetic alignment of the nickel electron spins, on the femtosecond timescale. However, it took more than 25 years before experiments with femtosecond X-ray and electron pulses could detect the missing spin angular momentum as chiral lattice vibrations. Similar to experimental methods, for which the Nobel

Prize in Physics 2023 was awarded, a short pulse light source, known as free-electron laser (FEL), was used to observe electrons moving on their natural timescale as they interact with lattice vibrations. The time- and angle-resolved photoemission spectroscopy (tr-ARPES) measurements were performed at the PG2 beamline of the FLASH FEL at the HEXTOF end station.

The researchers observe electrons moving in nickel on their natural timescale (femtoseconds) as they interact with lattice vibrations. This results in electrons that disappear in some states (marked green in Fig. 1) and reappear in others (marked blue in Fig. 1) while the change in electron energy and momentum corresponds to transiently occupied lattice vibrations (orange arrow in Fig. 1).

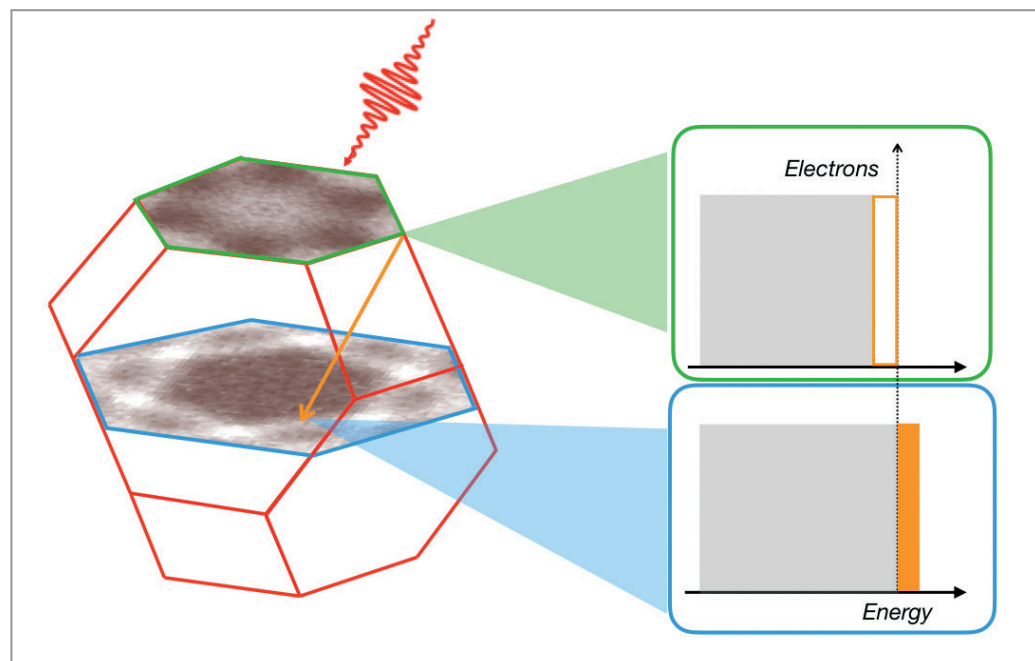
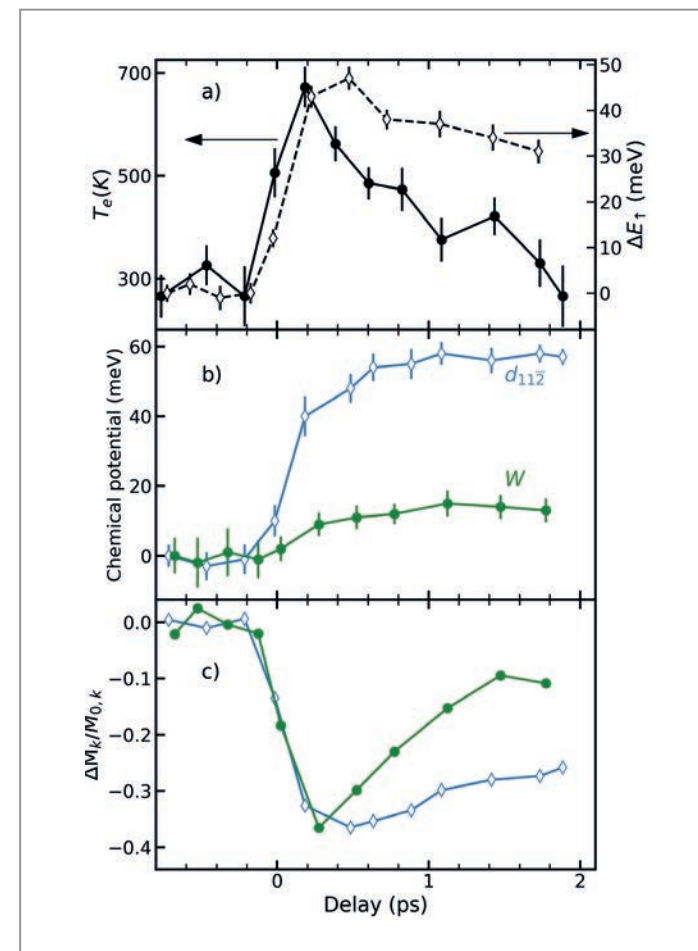


Figure 1
The scattering of electrons from one plane of a Brillouin zone to another in a laser excited system defined by the exchange momentum vector (orange arrow) in reciprocal space. The Brillouin zone (red polyhedron) is the space encompassing all the momentum of electrons in a solid.

Figure 2
Femtosecond laser excitation changes the electronic temperature, T_e , and spin dependent quasiparticle energy, ΔE_{\uparrow} , as shown in a). The band occupations of electrons in green and blue states marked in Fig. 1 are shown in b) as a state-resolved chemical potential. The change in the state-resolved magnetic moment is shown in c).



Momentum microscopy at FLASH enabled the direct visualisation of these processes as shown in Fig. 2. The changes in electronic state occupations (marked orange in the insets of Fig. 1, where the open orange area corresponds to a loss of electrons while solid orange area signifies a gain of electrons) are shown in Fig. 2b as changes in a state-dependent chemical potential. The observed energy difference between the chemical potential changes of green and blue states corresponds closely to the energy of transient phonons observed previously [2]. These transient phonons are characterised by large momentum wavevectors corresponding to the orange arrow in Fig. 1. Their population was found to rapidly increase during the first picosecond following laser excitation and lingers for many picoseconds. In thermal equilibrium, these large momentum states are always less occupied than other low-momentum states. Even increasing the sample temperature does not change this but risks damaging the material. Hence, the build up of a significant population of large momentum phonons using lasers provides a unique pathway to control the non-equilibrium properties. Furthermore, the observed time evolution of the chemical potential changes is distinctly different than the one expected from scattering processes with hot electrons and magnons as visualised by the evolution of electronic temperature and exchange splitting in Fig. 2a, respectively. Interestingly, the phonon-electron scattering events described above are also accompanied by a change in the electron spin polarisation at their respective states. This is clearly visible in Fig. 2c where the spin polarisation of green and blue electronic states initially displays identical dynamics but for longer times above 0.5 ps are distinctly different. This clearly demonstrates that spin angular momentum flow accompanies such phonon-driven electronic scattering events.

These results provide the first direct visualisation of electron-phonon scattering processes. Moreover, during these scattering processes, a net flow of spins results in the distribution of magnetic moments breaking the equilibrium picture of equivalence of magnetism and exchange splitting in nickel.

Author contact:

Vishal Shokeen, vishal.shokeen@physics.uu.se
Hermann Dürr, hermann.durr@physics.uu.se

References

1. E. Beaurepaire, J.-C. Merle, A. Daunois and J.-Y. Bigot, 'Ultrafast Spin Dynamics in Ferromagnetic Nickel', *Phys. Rev. Lett.* **76**, 4250–4253 (1996).
2. P. Maldonado, T. Chase, A. H. Reid, X. Shen, R. K. Li, K. Carva, T. Payer, M. Horn von Hoegen, K. Sokolowski-Tinten, X. J. Wang, P. M. Oppeneer and H. A. Dürr, 'Tracking the Ultrafast Non-Equilibrium Energy Flow between Electronic and Lattice Degrees of Freedom in Crystalline Nickel', *Phys. Rev. B* **101**, 100302(R) (2020).

Original publication

'Real-time observation of non-equilibrium phonon-electron energy and angular momentum flow in laser-heated nickel', *Science Advances* **10**, ead4207 (2024). DOI: 10.1126/sciadv.ad4207



Vishal Shokeen¹, Michael Heber², Dmytro Kutnyakhov², Xiaocui Wang¹, Alexander Yaroslavtsev¹, Pablo Maldonado¹, Marco Berritta⁴, Nils Wind^{3,4}, Lukas Wenthaus², Federico Pressacco², Chul-Hee Min^{4,5}, Matz Nissen³, Sanjoy K. Mahatha⁴, Sjarhei Dziarzhyski², Peter M. Oppeneer¹, Kai Rossnagel^{4,5}, Hans-Joachim Elmers⁶, Gerd Schönhense⁶ and Hermann A. Dürr¹

1. Department of Physics and Astronomy, Uppsala University, Uppsala, Sweden
2. Deutsches Elektronen-Synchrotron DESY, Hamburg, Germany
3. Department for Experimental Physics, University of Hamburg, Hamburg, Germany
4. Ruprecht Haensel Laboratory, Deutsches Elektronen-Synchrotron DESY, Hamburg, Germany
5. Institut für Experimentelle und Angewandte Physik, Christian-Albrechts-Universität zu Kiel, Kiel, Germany
6. Institut für Physik, Johannes Gutenberg-Universität Mainz, Mainz, Germany

4f electronic excitations in rare-earth metals

Towards ultrafast control of magneto-crystalline anisotropy

Magneto-crystalline anisotropy (MCA) is the property of a magnetic material to lock its macroscopic magnetisation direction. MCA stabilises magnetically stored information against decay, making it an essential property of materials for information technologies. As, in turn, strong MCA complicates information writing, efficient control of magnetisation in materials with strong MCA is a leading objective in ultrafast spin physics. One possible approach is controlling MCA itself. MCA originates from spin-orbit coupling together with an anisotropic electron orbital wavefunction. At FLASH, we could demonstrate a way to manipulate MCA on ultrashort time scales by addressing the 4f electronic wave function with femtosecond optical excitation.

Magnetism in the most relevant magnetic elements arises either from itinerant 3d-bands of transition metals or from strongly localised 4f states of rare earth (RE) ions. The delocalised character of the 3d electrons in solids quenches their orbital magnetic moment [1] while 4f electrons remain atomic-like even in solids; their electronic ground state follows Hund's rules, leading to large orbital magnetic moments and strong MCA.

The itinerant 5d6s valence electrons in RE metals mediate the exchange interaction between the localised 4f spins but otherwise contribute little to the magnetic properties of RE metals [1,2]. However, the valence electrons become important during excitation with infrared (IR) laser pulses,

as 4f electrons have too high binding energies to be excited directly. Consequently, excitations changing the 4f electronic configuration were not considered relevant for ultrafast magnetisation dynamics in RE metals so far.

In our study at the TRIXS end station for time-resolved resonant inelastic X-ray scattering (RIXS) at the PG1 beamline of FLASH1, we could now prove that 4f electronic excitations do occur upon IR pumping and transiently alter MCA: For the exemplary RE metal Terbium (Tb) we found that 5d-4f electron-electron scattering efficiently drives 4f multiplet excitations.

We used RIXS at the $4d \rightarrow 4f$ ($N_{5,4}$) transition which provides a highly sensitive probe for the electronic state of the 4f shell. Fig. 1 shows the energy levels of Tb and illustrates the RIXS process. The eight electrons in the Tb 4f shell occupy the 7F_6 ground state. Resonant X-ray absorption at 147eV induces a transition from the $4d^{10}4f^8$ ground state into a $4d^94f^9$ intermediate state (Fig. 1, left). The subsequent decay into various $4d^{10}4f^8$ final state

Figure 1
Optical excitation (curved red line) initially affects the $(5d6s)^3$ electrons. Via inelastic 5d-4f scattering, higher lying states like the 7F_5 multiplet 0.26 eV above the 7F_6 ground state are populated. In RIXS, this process is prominently visible: RIXS involving, e.g., the 5D_4 final state multiplet (at 2.64 eV energy loss when excited from the ground state), shows an energy shift of the loss feature by 0.26 eV when the 7F_5 multiplet becomes populated.

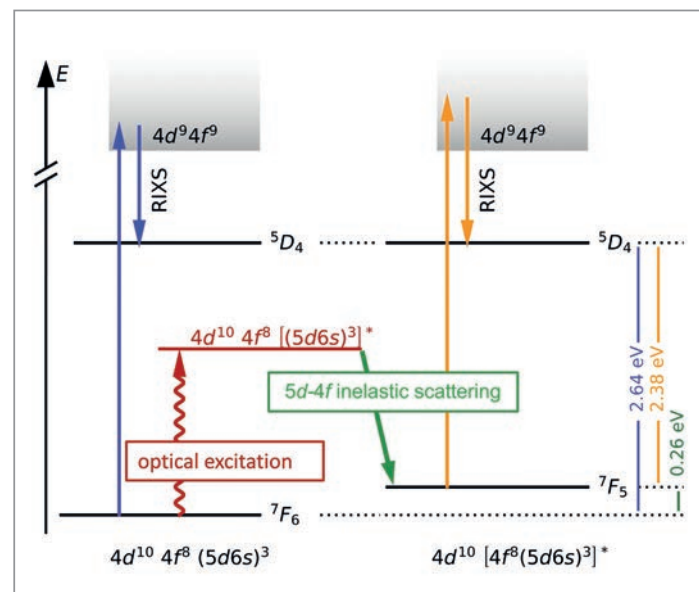
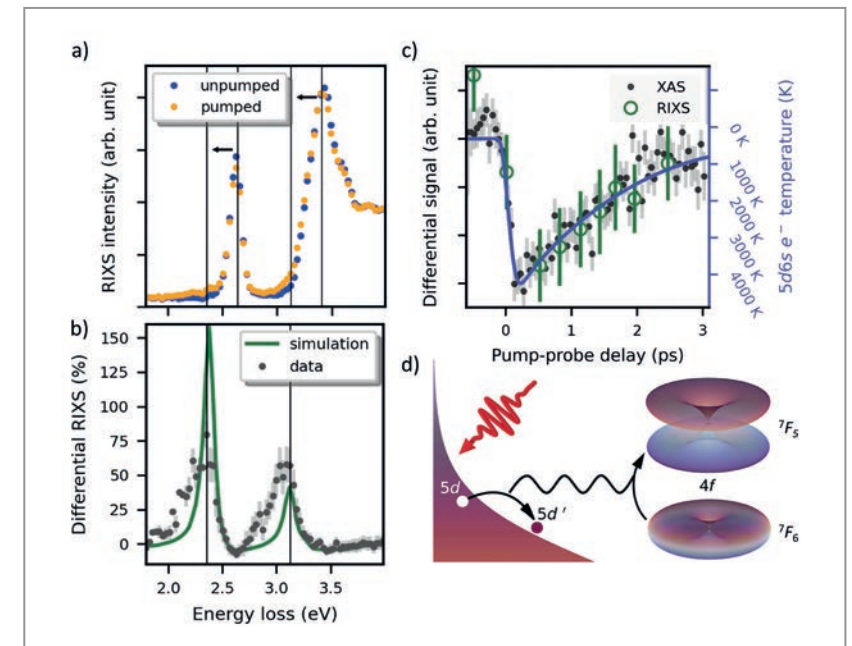


Figure 2

a) $N_{5,4}$ RIXS spectrum (147 eV incident energy) of Tb metal in its 7F_6 ground state and 300 fs after pump-pulse arrival (blue and orange dots). The pumped sample shows a RIXS intensity shifted by 0.26 eV to lower loss energy, corresponding to an excitation into the 7F_5 multiplet. b) The differential RIXS signal (black) shows the relative change of intensity for spectra in a) well described by atomistic calculations (green line). c) Time-resolved spectral changes in RIXS (green) and M_5 XAS (black) follow the temperature of the laser-heated 5d6s electrons (blue line calculated from a 2-temperature model, involving 5d electrons and lattice). d) Sketch of ultrafast inelastic scattering between optical excited 5d and 'cold' 4f electrons, driving 4f multiplet excitations.



multiplets at higher energies leads to emission of photons with lower energies which we detected in the RIXS measurement. For our study, we used the decay into the 5D_4 multiplet, leading to a well-separable inelastic energy loss line around 2.64 eV, as referred to in Fig. 1 and shown in Fig. 2a. IR-pumping of the 5d6s valence electrons (red arrow in Fig. 1) followed by $(5d6s)$ -4f inelastic scattering (green arrow) can lead to a $4d^{10}[4f^8(5d6s)^3]^*$ excited initial state such as the 7F_5 configuration (Fig. 1, right). The higher energy of this state will be conserved in the RIXS process. We thus expect to observe an emission shifted to higher photon energy just by the energy difference between 7F_6 and pump-excited 7F_5 initial states. In fact, the excitation in the 4f shell after IR pumping, showed a distinct blue shift of spectral weight indicated by the arrows in Fig. 2a and well observable in the differential RIXS signal (Fig. 2b).

The RIXS study on Tb was complemented by time-resolved X-ray absorption (XAS), studied at the SCS instrument of EuXFEL. The temporal evolution of the pump effect in XAS and RIXS shows the 4f electronic transitions to follow the temperature of the directly laser-heated 5d6s valence electrons (Fig. 2c). 5d-4f electron-electron scattering hence transfers energy and angular momentum between the 5d and 4f system (Fig. 2d). With moderate pump fluences up to 20% of the probed volume, 4f ions are found in the excited 7F_5 multiplet with $\Delta E=0.26$ eV and $\Delta J = -1$ relative to the 7F_6 ground state. Our DFT calculations show that this excitation changes MCA such that the local magnetic easy axis flips from in-plane to out-of-plane (Fig. 2d). We also found signatures of higher excitations into 7F_1 multiplets with $J = 4,3,2,1$ as well as fingerprints of $5d \leftrightarrow 4f$ charge transfer excitations. Upcoming experimental capabilities at

FLASH will allow us to directly connect altered 4f electronic states with magnetic dynamics in RE metals and thus to identify efficient routes for magnetic order control in RE-based materials.

Author contact: Nele Thielemann-Kühn, nele.thielemann-kuehn@fu-berlin.de

References

- J. M. D. Coey and S. S. P. Parkin, 'Handbook of Magnetism and Magnetic Materials' (Springer Nature Switzerland AG 2021).
- T. Kasuya, 'A Theory of Metallic Ferro- and Antiferromagnetism on Zener's Model', Prog. Theor. Phys. 16, 45–57 (1956).

Original publication

'Optical control of 4f orbital state in rare-earth metals', Science Advances 10, eadk9522 (2024). DOI: 10.1126/sciadv.adk9522



Nele Thielemann-Kühn¹, Tim Amrhein¹, Wibke Bronsch^{1,2}, Somnath Jana³, Niko Pontius³, Robin Y. Engel⁴, Piter S. Miedema⁴, Dominik Legut^{5,6}, Karel Carva⁶, Unai Atxitia^{1,8}, Benjamin E. van Kuiken⁷, Martin Teichmann⁷, Robert E. Carley⁷, Laurent Mercadier⁷, Alexander Yaroslavtsev^{7,9}, Giuseppe Mercurio⁷, Loïc Le Guyader⁷, Naman Agarwal⁷, Rafael Gort⁷, Andreas Scherz⁷, Siarhei Dzarzhyski⁷, Günter Brenner⁴, Federico Pressacco⁴, Ru-Pan Wang^{4,11}, Jan O. Schunck^{4,11}, Mangalika Sinha⁴, Martin Beye⁴, Gheorghe S. Chiuzbăian¹⁰, Peter M. Oppeneer⁹, Martin Weinelt¹ and Christian Schübler-Langeheine³

- Freie Universität Berlin, Fachbereich Physik, Berlin, Germany
- Elettra-Sincrotrone Trieste S.C.p.A., Trieste, Italy
- Helmholtz-Zentrum Berlin für Materialien und Energie GmbH, Berlin, Germany
- Deutsches Elektronen-Synchrotron DESY, Hamburg, Germany
- VSB - Technical University Ostrava, IT4Innovations, Ostrava, Czech Republic
- Charles University, Faculty of Mathematics and Physics, DCMP, Prague, Czech Republic
- European XFEL, Schenefeld, Germany
- Instituto de Ciencia de Materiales de Madrid, CSIC, Madrid, Spain
- Uppsala University, Department of Physics and Astronomy, Uppsala, Sweden
- Sorbonne Université, CNRS, Laboratoire de Chimie Physique, Paris, France
- Department of Physics, University of Hamburg, Hamburg, Germany

A 'hidden route' for transporting water into the Earth's deep interior

In situ high-pressure and high-temperature X-ray diffraction to experimentally simulate subducting clays from the surface to the lower mantle

Water is the most important volatile, covering approximately 70% of the Earth's surface. Equally important is the water distributed in the Earth's mantle, as it alters the properties of the mantle rocks thereby influencing their movement and, in some cases, melting. Recent research suggests that there is about the same amount of water in the mantle transition zone (~410–660 km) as on the surface, while about four times of the surface water is estimated to reside in the lower mantle (~660–2900 km) [1]. Subduction zones play a critical role in the water cycle between the surface and the interior of the Earth. However, the ways how water has become distributed in such a way remain largely unknown. Our research sheds light on the role subducting clays play in distributing water in the Earth's deep interior.

Subduction zones play an important role as global inlet of water into the Earth's interior as a variety of hydrous minerals composing a subducting lithospheric plate act as the carriers of water to a range of depth destinations [2].

This is because water is generally expelled from those hydrous mineral carriers at certain depths as they transform into less hydrous or anhydrous ones. Within the subducting plate, the topmost part is composed of oceanic sediments where hydrated clay minerals rich in alumina and silica in the ternary $\text{Al}_2\text{O}_3\text{-SiO}_2\text{-H}_2\text{O}$ (ASH) system are the major components, together with available free water.

Pyrophyllite ($\text{Al}_2\text{Si}_4\text{O}_{10}(\text{OH})_2$) is one of the representative hydrous clay minerals in the ASH system composing the oceanic sediments containing ~5.0 weight-% of water in form of structural hydroxyls. We have investigated the stability of subducting pyrophyllite in water-containing sediments up to ~23 GPa and ~900 °C, corresponding to depths down to approximately 700 km in the lower mantle, following cold subduction thermal models (Fig. 1). *In situ* synchrotron X-ray powder diffraction measurements were performed at the Extreme Conditions Beamline (ECB) P02.2 at PETRA III, with simultaneous pressure and

Figure 1

Experimental pressure and temperature conditions of pyrophyllite and its breakdown products along water-rich cold subduction geotherms. Continuous and dashed curves (upper panel) denote the geotherms of two subducting slab surfaces and corresponding slab Moho (i.e. boundary between Earth's crust and mantle, 7 km beneath the slab surface), respectively. The geotherm models within the mantle transition zone (lower panel) have been extrapolated. The horizontal dotted lines define the upper and lower boundaries of the mantle transition zone.

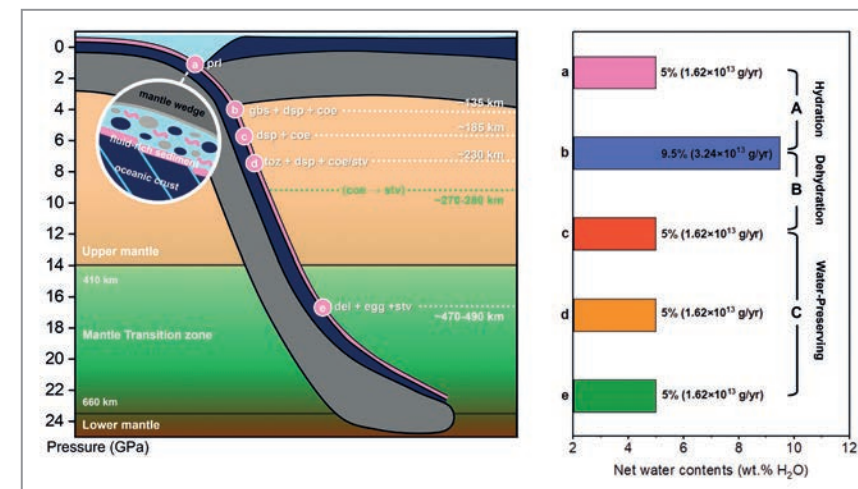
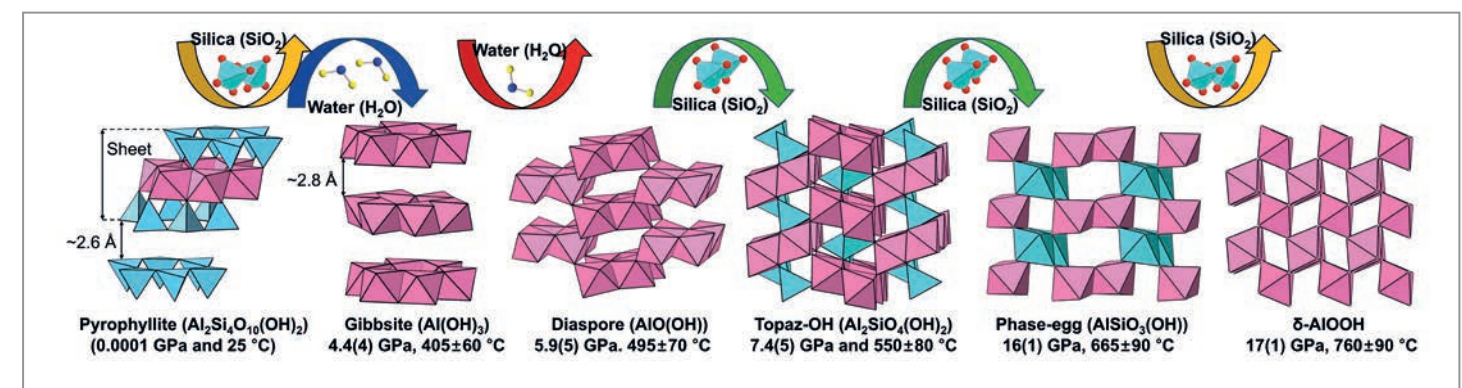


Figure 2

Water transport down to the lower mantle via sequential transformations of subducting pyrophyllite. Top) Structural evolution of pyrophyllite into its breakdown products in the ASH system. Bottom left) Depths of sequential breakdowns from pyrophyllite are marked in a schematic subduction diagram. Phase assemblages from pyrophyllite are: a (prl), b (gbs + dsp + coe), c (dsp + coe), d (toz + dsp + coe/stv), e (del + Egg + stv). *Phase abbreviations: pyrophyllite (prl), gibbsite (gbs), diaspore (dsp), coesite (coe), topaz (toz), stishovite (stv), phase Egg (egg), δ -AIOOH (del). Bottom right) Estimated net water contents (wt.% H_2O) of the respective phase assemblages. Values in the parenthesis are the estimated global H_2O flux from pyrophyllite.

temperature conditions created using a graphite resistive-heated diamond anvil cell (RH-DAC). This RH-DAC setup offers the advantage of providing homogeneous and stable temperature across the entire sample [3].

Our observations revealed pyrophyllite breaks down into the gibbsite ($\text{Al}(\text{OH})_3$)—the most hydrated mantle mineral with ~34 weight-% H_2O —diaspore ($\text{AlO}(\text{OH})$) and coesite (SiO_2) assemblage, at a depth condition of ~135 km thereby removing water from the subducting fluid by ~1.8 weight-% (Fig. 2a). Subsequently, dehydration occurs at deeper depth conditions of ~185 km and releases back the amount of water taken up before. In course of the following breakdown steps mineral assemblage change, but the net water content is preserved down to ~660 km depth (Fig. 2). In summary, this would deliver a net amount of ~5.0 weight-% H_2O —same as contained in the initial pyrophyllite—in a phase assemblage containing δ -AIOOH and phase Egg ($\text{AlSiO}_3(\text{OH})$) to the lower mantle (Fig. 2).

Assuming that such type of subduction-driven mineral transformations have been operating for the past 2.5 billion years, we may infer that approximately 2.5% of the current ocean water could have been transported down to the lower mantle.

Author contact: Yoonah Bang, yoonaibang@kaeri.re.kr
Yongjae Lee, yongjaelee@yonsei.ac.kr

References

1. A. H. Peslier, M. Schonbachler, H. Busemann and S.-I. Karato, 'Water in the Earth's interior: Distribution and origin', *Space Sci. Rev.* **212**, 743-810 (2017).
2. P. E. van Keken, B. R. Hacker, E. M. Syracuse and G. A. Abers, 'Subduction factory: 4. Depth-dependent flux of H_2O from subducting slabs worldwide', *J. Geophys. Res. Solid Earth* **116**, B01401 (2011).
3. H. Hwang, Y. Bang, J. Choi, H. Cynn, Z. Jenei, W. J. Evans, A. Ehnes, I. Schwark, K. Glazyrin, G. D. Gatta, P. Lotti, C. Sanloup, Y. Lee and H.-P. Liermann, 'Graphite resistive heated diamond anvil cell for simultaneous high-pressure and high-temperature diffraction experiments', *Rev. Sci. Instrum.* **94**, 083903 (2023).

Original publication

'A role for subducting clays in the water transportation into the Earth's lower mantle', *Nature Communications* **15**, 4428 (2024). DOI: 10.1038/s41467-024-48501-z



Yoonah Bang^{1,2}, Huijeong Hwang^{3,4}, Hanns-Peter Liermann⁵, Duck Young Kim^{5,6}, Yu He^{5,7}, Tae-Yeol Jeon⁸, Tae Joo Shin⁹, Dongzhou Zhang^{10,11}, Dmitry Popov¹² and Yongjae Lee¹

1. Yonsei University, Seoul, Republic of Korea
2. Korea Atomic Energy Research Institute, Daejeon, Republic of Korea
3. Deutsches Elektronen-Synchrotron DESY, Hamburg, Germany
4. Gwangju Institute of Science and Technology, Gwangju, Republic of Korea
5. Center for High Pressure Science & Technology Advanced Research, Shanghai, China
6. Pohang University of Science and Technology, Pohang, Republic of Korea
7. Chinese Academy of Sciences, Guizhou, China
8. Pohang Accelerator Laboratory, Pohang, Republic of Korea
9. Ulsan National Institute of Science and Technology, Ulsan, Republic of Korea
10. University of Hawaii at Manoa, HI, USA
11. University of Chicago, IL, USA
12. Argonne National Laboratory, IL, USA

A new approach against 'forever chemicals'

X-rays probe key interactions that enhance removal of per- and polyfluoroalkyl substances from water using tailored metal-organic frameworks

Per- and polyfluoroalkyl substances (PFAS) have emerged as persistent accumulative pollutants, with severe risks to human and aquatic life. They are known as 'forever chemicals' due to their resilience to conventional degradation methods which makes remediation very challenging. Adsorption remains the most practical approach to treat PFAS, yet existing sorbents often lack efficiency for widespread environmental application. Metal-organic frameworks (MOFs) are an innovative class of porous materials with large potential for custom-chemical modification which can be harnessed to improve adsorption performance. Our study presents a new strategy to boost capture for a range of PFAS, using suitably tailored MOFs.

More specifically, in this work we leveraged the chemical versatility of Zr-MOFs to develop a series of adsorbents with enhanced capacities for capturing both short- and long-chain perfluorinated carboxylic acids—key PFAS compounds of global concern [1]. Using a chemistry-driven approach, we applied targeted, post-synthetic modifications to boost PFAS...MOF interactions, optimising these materials for coordinative bonding and hydrophobic effects (Fig. 1). Among the designed materials, the trifluoroacetic acid-functionalised MOF, TFA-MOF-808, exhibited notably high adsorption capacities, setting a benchmark for PFAS capture in MOF-based materials.

To initiate our investigations, we selected and synthesised the prototypical Zr-based MOFs, DUT-67 and MOF-808,

based on their exceptional water stability and scalable production via environmentally friendly synthetic procedures. These frameworks offer distinct advantages for PFAS remediation due to their structural and chemical properties. DUT-67 features inner cuboctahedral and octahedral cages with diameters of 14.2 Å and 11.7 Å, respectively, while MOF-808 contains hexagonal channels with an approximate diameter of 18 Å. Both MOFs also possess unsaturated Zr₆ inorganic nodes, providing a robust platform for post-synthetic functionalisation to optimise pollutant interactions. Their well-defined porosity allows them to accommodate PFAS molecules with varying chain lengths and kinetic diameters, making them particularly versatile for addressing the challenges posed by these persistent pollutants. The successful synthesis of DUT-67

and MOF-808 in highly crystalline forms was confirmed through extensive characterisation using Powder X-ray Diffraction (PXRD), ¹H Nuclear Magnetic Resonance (NMR), Fourier-transform Infrared Spectroscopy (FT-IR), Thermogravimetric Analysis (TGA), Scanning Electron Microscopy (SEM) and gas adsorption measurements. These analyses verified their structural integrity, porosity and suitability as advanced adsorbents, laying the ground work for targeted adsorption studies against PFAS in aqueous environments.

Detailed mechanistic studies were performed to validate these observations, including theoretical calculations and experimental characterisation techniques. As part of these efforts, X-Ray Pair Distribution Function (PDF) data were collected at PETRA III beamline P02.1 [2] for several MOF materials before and after treatment with PFAS. Differential PDF (dPDF) analysis (Fig. 2) of this data provided deeper insight into how PFAS interact with MOF structures at the molecular level, uncovering the specific driving forces that maximise adsorption performance: Changes in the local environment of the Zr centres indicated that PFAS coordinates into the MOF through a unique ligand exchange mechanism. Additional dPDF signals confirmed formation of strong F...F interactions between the pollutant and the framework. This dual interaction approach—utilising both coordinative bonding and hydrophobicity—proved essential for achieving high PFAS retention in aqueous conditions.

To summarise, this work demonstrates that through precise post-synthetic functionalisation, MOFs with unsaturated metal sites can be tailored for effective PFAS capture from water. The performance of TFA-MOF-808 for both short- and long-chain PFAS pollutants underscores the potential of MOFs as next-generation PFAS sorbents. The study offers a clear strategy for designing high-capacity

adsorbents and highlights the role of structural modifications in enhancing MOF performance. It also validates the use of synchrotron characterisation tools to uncover key mechanistic information behind these phenomena. Future research will expand on these findings by exploring the optimal MOF functionalisation strategies and evaluating a broader range of PFAS pollutants to extend the applicability of this approach.

Author contact: Ana Platero-Prats, ana.platero@uam.es
Edward Loukopoulos, edouardos.loukopoulos@uam.es
Andreas Mavrandonakis, andreas.mavrandonakis@icmm.csic.es

References

1. M. Sadia, I. Nollen, R. Helmus, T. L. ter Laak, F. Béen, A. Praetorius and A. P. van Wezel, 'Occurrence, Fate, and Related Health Risks of PFAS in Raw and Produced Drinking Water', *Environ. Sci. Technol.* 57, 3062–3074 (2023).
2. A.-C. Dippel, H.-P. Liermann, J. T. Delitz, P. Walter, H. Schulte-Schrepping, O. H. Seeck and H. Franz, 'Beamline P02.1 at PETRA III for High-Resolution and High-Energy Powder Diffraction', *J. Synchrotron Rad.* 22, 675–687 (2015).

Original publication

'Chemically tailored metal-organic frameworks for enhanced capture of short- and long-chain per- and polyfluoroalkyl substances from water', *Advanced Functional Materials* 34, 2409932 (2024). DOI: 10.1002/adfm.202409932

Edward Loukopoulos¹, Sergio Marugán-Benito¹, Dionysios Raptis², Emmanuel Tylianakis³, George E. Froudakis², Andreas Mavrandonakis⁴ and Ana E. Platero-Prats^{1,5}

1. Departamento de Química Inorgánica, Universidad Autónoma de Madrid, Madrid, Spain
2. Department of Chemistry, University of Crete, Heraklion, Greece
3. Department of Materials Science and Technology, University of Crete, Heraklion, Greece
4. Material Science Institute of Madrid (ICMM-CSIC), Madrid, Spain
5. Condensed Matter Physics Center (IFIMAC), Universidad Autónoma de Madrid, Madrid, Spain

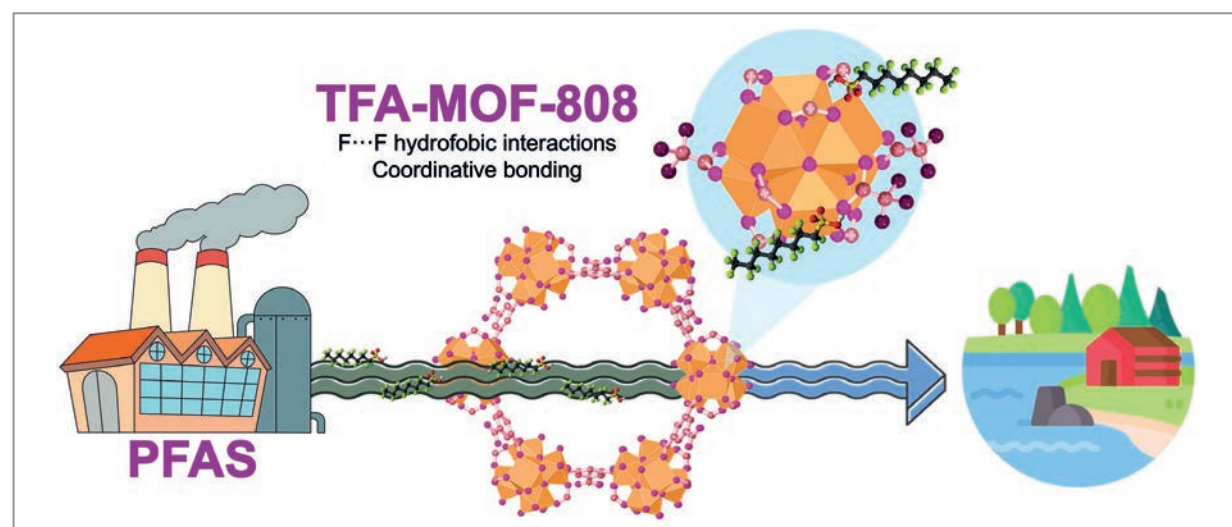
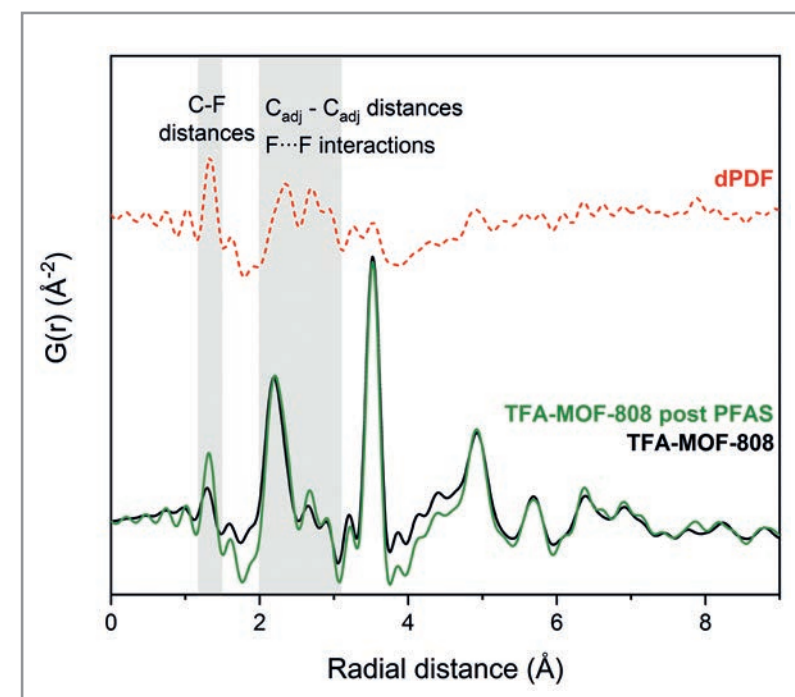


Figure 1 Schematic removal of PFAS pollutants from water, using a chemically tailored MOF-808 analogue. The insert under the magnifier could be larger so that one can see the atomic bonds better

Figure 2

Representative PDF data of TFA-MOF-808 before (black) and after (green) capture of perfluorooctanoic acid, including the corresponding dPDF signal (red).



A record resolution

The smallest ever focus of electromagnetic radiation

The resolution of a microscope is intrinsically linked to the wavelength of the radiation used. Achieving resolutions approaching 1 nm in an X-ray microscope, however, has been a challenge due to the weak interaction of X-rays with the materials of a focusing lens and the extreme precision required in its shape. We demonstrate a path to break the 1 nm barrier using multilayer Laue lenses and phase correctors. Since the properties of a microscope are determined by the properties of the light source and the quality of the lenses, high-resolution X-ray microscopy profits from high-brightness synchrotron sources and advances in X-ray optics.

We are developing multilayer Laue lenses (MLLs), which are diffraction-type X-ray optical elements, consisting of tens of thousands of diffracting layers and which we prepare using our custom magnetron sputtering systems [1]. The resolution is determined by the acceptance angle of the lens—also known as the numerical aperture (NA)—which is dependent on the minimum period that is present in the structure. High-aspect ratio structures needed for focusing shorter wavelength photons can be easily achieved using a sputtering approach, which then results in a high diffraction efficiency. The deposition of tens of thousands of layers requires extreme accuracy and precision since any deviation from a perfect structure leads to focus-spot broadening. Using wavefront interferometry developed in our group [2,3], we can measure wavefront aberrations with extreme sensitivity, even with a laboratory-based X-ray source [4]. This provides rapid feedback to our lens preparation, avoid-

ing a bottleneck that seriously hindered our progress in the past. With these improvements we demonstrated lenses that can focus 17.5 keV X-ray photons to below 5 nm [4]. Remaining residual errors can be corrected using a phase plate, as was used to improve aberrated compound refractive lenses (CRLs) [5]. However, the NA of our lenses is at least 10–30 times larger than the NA of a typical CRL, and since even the lowest-order aberration scales with the third power of the NA, the correction of our lenses requires a very high aspect ratio phase plate. To ease the fabrication of such a phase plate, we replaced it with an array of 3D-printed phase plates which we call a compound refractive corrector (CRC). We applied these CRCs to high-NA MLLs (Fig. 1) and demonstrated a $2.8 \times 2.9 \text{ nm}^2$ point spread function. Since multilayer structures with periods of 1.0 nm show high diffracting efficiency, this strategy should enable imaging at that resolution.

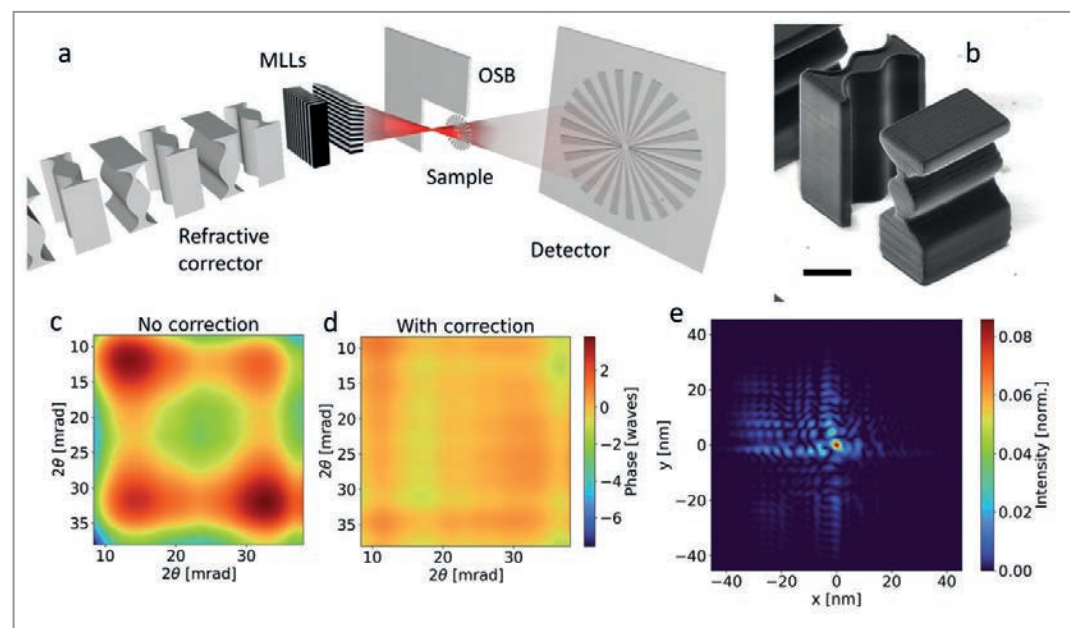


Figure 1 Wavefront correction using a compound refractive corrector. a) Schematics of the experimental setup showing the positions of the refractive corrector, MLLs, order sorting aperture (OSA), sample and detector. b) SEM image of a set of elements correcting along the vertical and horizontal direction. The scale bar is 20 μm . c) 2D wavefront map before and d) after correction. e) Point-spread function of the intensity distribution in the focal plane, normalised to an aberration-free lens pair.

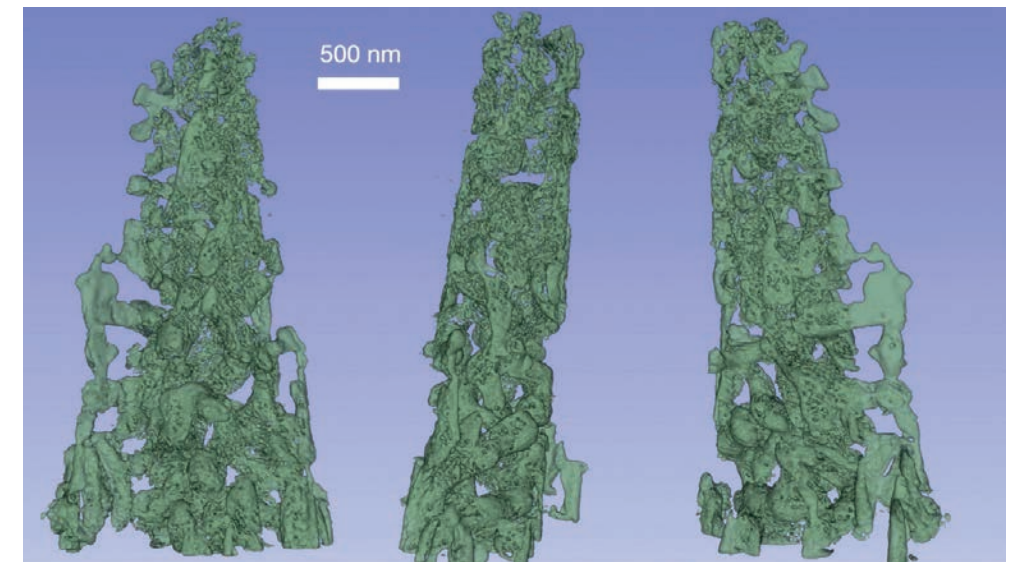


Figure 2 Three orientations of a high-resolution 3D rendering of nanoporous gold with pore sizes of 20 nm, reconstructed from projection holograms. The holograms were recorded directly on an Eiger 16M detector.

Our high-NA MLLs have enabled projection holography at very large magnifications. Figure 2 was obtained with our X-ray microscope at beamline P11 of PETRA III and depicts a nanoporous gold structure. The sample was placed out of focus, giving holograms magnified by a factor of more than 32000 which were recorded directly on an Eiger 16M detector. Each view of the sample was reconstructed using the method of near-field ptychography and then combined by 3D tomography. The resolution of the resulting images was well below 10 nm. In Fig. 2, three random orientations of the 3D rendering of the nanoporous gold with 20 nm pores are shown. The only other direct measurement of the structures' topological parameters, such as connectivity between the pores, was via a correlative high-resolution volume electron microscopy (SEM-FIB) reconstruction, but these measurements are currently limited to pore sizes larger than about 50 nm. High-resolution X-ray microscopy shows great potential to obtain 3D reconstruction of such hierarchical network structures, which will help to understand enhanced mechanical properties and how to make strong and lightweight materials.

The high NA of our MLLs has opened up other new applications such as convergent beam diffraction, which benefits from a beam spot size comparable to a single unit cell of the crystal. This method has been used in transmission electron microscopes for decades but up to now was not demonstrated with X-rays.

Extreme focusing is also needed in experiments where very high intensities are required, such as studying non-linear X-ray optics or creating dense plasmas; we have already demonstrated focusing XFEL pulses with MLLs at the European XFEL. Combined with the high spatial coherence of beams at the future PETRA IV synchrotron, our MLLs will enable high-throughput imaging of technological, biological and quantum materials.

Author contact:

J. Lukas Dresselhaus, jan.lukas.dresselhaus@desy.de
Saša Bajt, sasa.bajt@desy.de

References

1. S. Bajt et al., 'X-ray focusing with efficient high-NA multilayer Laue lenses', *Light: Sci. Appl.* 7, 17162 (2017).
2. A. Morgan et al., 'Ptychographic X-ray speckle tracking with multi-layer Laue lens systems', *J. Appl. Cryst.* 53, 927–936 (2020).
3. N. Ivanov et al., 'Robust ptychographic x-ray speckle tracking with multilayer Laue lenses', *Opt. Express* 30, 25450–25473 (2022).
4. J. L. Dresselhaus et al., 'Precise wavefront characterization of x-ray optical elements using a laboratory source', *Rev. Sci. Instrum.* 93 (2022).
5. F. Seiboth et al., 'Perfect X-ray focusing via fitting corrective glasses to aberrated optics', *Nat. Comm.* 8, 14623 (2017).

Original publications

'X-ray focusing below 3 nm with aberration-corrected multilayer Laue lenses', *Optics Express* 32, 16004–16015 (2024).
DOI: 10.1364/OE.518964



J. Lukas Dresselhaus¹, Margarita Zakharova², Nikolay Ivanov², Holger Fleckenstein², Mauro Prasciolu², Oleksandr Yefanov², Chufeng Li², Wenhui Zhang², Philipp Middendorf², Dmitry Egorov², Ivan De Gennaro Aquino², Henry N. Chapman^{1,2,3} and Saša Bajt^{1,2}

'Fast and efficient hard X-ray projection imaging below 10 nm resolution', *Optics Express* 32, 30879–30897 (2024).
DOI: 10.1364/OE.532037



Wenhui Zhang², J. Lukas Dresselhaus¹, Holger Fleckenstein², Mauro Prasciolu², Margarita Zakharova², Nikolay Ivanov², Chufeng Li², Oleksandr Yefanov², Tang Li², Dmitry Ergov², Ivan De Gennaro Aquino², Philipp Middendorf², Johannes Hagemann⁴, Shan Shi^{5,6}, Saša Bajt^{1,2} and Henry N. Chapman^{1,2,3}

1. The Hamburg Centre for Ultrafast Imaging, University of Hamburg, Hamburg, Germany
2. Center for Free-Electron Laser Science CFEL, DESY, Hamburg, Germany
3. Department of Physics, University of Hamburg, Hamburg, Germany
4. Center for X-ray and Nano Science CXNS, DESY, Hamburg, Germany
5. Institute of Materials Physics and Technology, Hamburg University of Technology, Hamburg, Germany
6. Helmholtz-Zentrum Hereon, Geesthacht, Germany

Extending frontiers with X-ray multibeam ptychography

Time-efficient nanoscale imaging without compromising field of view

X-ray ptychography is a powerful lensless scanning microscopy technique that achieves sub-10 nm resolution for imaging complex materials [1]. However, conventional single-beam ptychography is constrained by its reliance on coherent flux which limits imaging efficiency for large fields of view. Since each area must be scanned sequentially, high-resolution imaging requires significant beamtime. Additionally, thicker samples demand substantial coherent photon flux, but even advanced synchrotrons at 20 keV provide less than 10% of their total beam intensity as coherent flux, further restricting imaging efficiency [2].

X-ray multibeam ptychography addresses these limitations by splitting a single X-ray beam into multiple individually coherent yet mutually incoherent beams, each illuminating a separate region of a sample (Fig. 1) [3]. This technique significantly accelerates high-resolution imaging across large areas without sacrificing resolution. It is particularly advantageous for analysing intricate materials like catalytic compounds, energy devices and microelectronics, and it reduces the need for invasive sample preparation often required in electron microscopy. This approach marks a

substantial advancement in nanoscale imaging, enabling faster, more comprehensive imaging of complex samples.

The success of multibeam ptychography relies on two key advancements: (i) high-efficiency optics for generating multiple beams and (ii) effective separation of scattering signals. Advanced 3D-printing via two-photon absorption lithography enables the fabrication of high-aspect-ratio (1000:1) double-concave refractive lenses with sub-micrometre precision [4]. Stacked in arrays, these lenses split

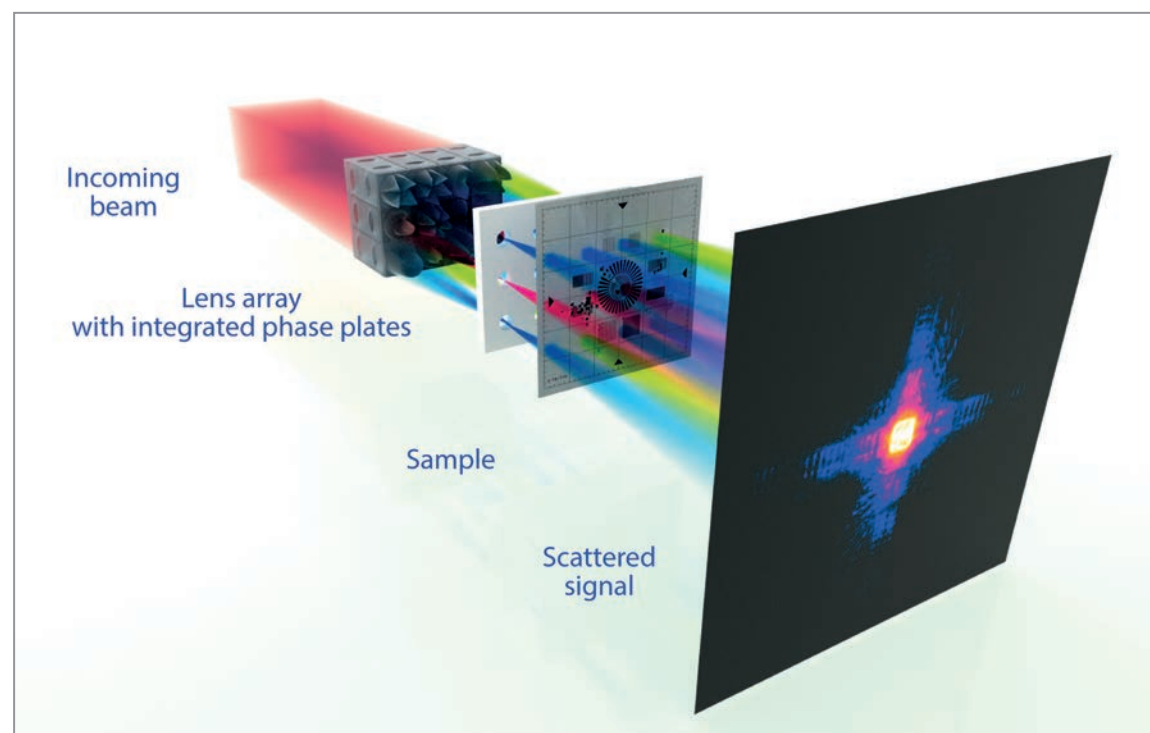


Figure 1
Schematic of the multibeam ptychography experiment setup shows primary beam division into individually coded beams that illuminate multiple sample points simultaneously. Scattered beams are directed to the detector, similar to traditional hard X-ray ptychography.

Figure 2
Ni/Al₂O₃ catalyst reconstruction with 45 µm diameter (prepared with FIB), achieving a resolution of 37 nm across an extensive 65 × 95 µm field. Measurements were done at 13 keV X-ray energy.

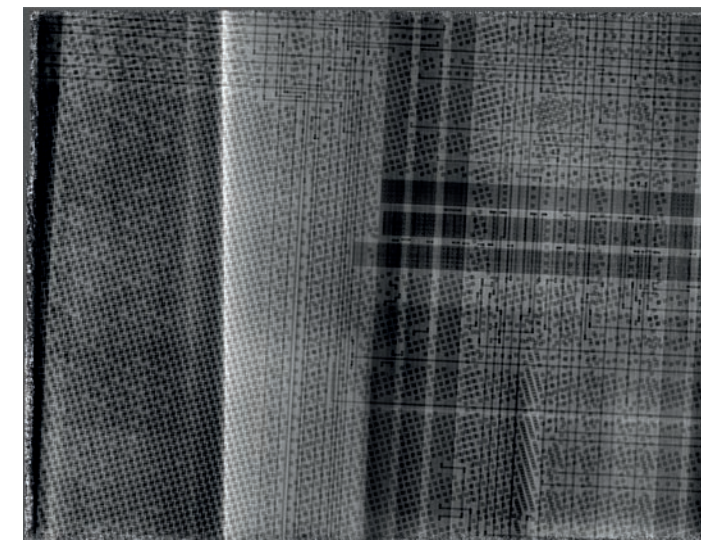
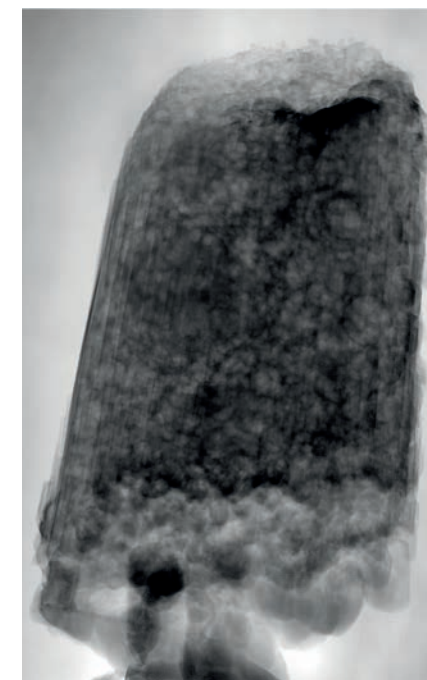


Figure 3
Microchip (without prior preparation) reconstruction, revealing circuits, transistors and contacts across multiple layers within a 95 × 125 µm field (measured at 20 keV energy).

the X-ray beam into up to 12 beams, each carrying unique phase information, ensuring accurate image reconstruction even with overlapping signals. Optimised for high photon energies, these lenses achieve over 90% transmission efficiency, making multibeam ptychography suitable for imaging dense, thick samples.

Applications in microelectronics and catalysis showcase the technique's versatility. Nanoscale structures, such as circuit elements and metal nanoparticles, are often embedded in materials containing high-Z metals (e.g., Zn, Au, Pt, Ag) alongside lighter elements (e.g., Si, Ge in electronics; Al, Ti in catalysis). These materials pose challenges due to high-contrast gradients and absorption, but multibeam ptychography overcomes these, achieving sub-40 nm resolution (Fig. 2 and 3). Here, demonstration studies on a hierarchically porous Ni/Al₂O₃ catalyst and a microchip sample are presented. The measurements were carried out at the P06 beamline of PETRA III (13 keV) and at ID13 of the ESRF-EBS (20 keV), respectively. Its rapid, high-resolution imaging also benefits studies of large heterogeneous samples across fields like biology, energy materials and advanced electronics where invasive preparation may alter results. Additionally, the technique's high-throughput, *in situ* imaging capabilities support real-time studies of catalytic and biological processes, enhancing its utility in both research and industry.

In the future, multibeam ptychography could be adapted for high-energy tomographic imaging, enabling non-destructive visualisation of larger samples at energies above 25 keV and reducing attenuation and phase artifacts. As synchrotron sources continue to evolve with greater coherent flux, the speed and scalability of multibeam ptychography will

improve, supporting real-time applications. Additionally, developing lab-based multibeam systems could make high-resolution 3D imaging more accessible, thereby reducing reliance on synchrotron facilities and expanding research opportunities globally.

Author contact: Tang Li, tang.li@desy.de
Mikhail Lyubomirskiy, mikhail.lyubomirskiy@desy.de

References

1. T. Aidukas et al., 'High-performance 4-nm-resolution X-ray tomography using burst ptychography', *Nature* 632, 81–88 (2024).
2. R. Khubbutdinov et al., 'Coherence properties of the high-energy fourth-generation X-ray synchrotron sources', *J. Synchrotron Rad.* 26, 1851–1862 (2019).
3. M. Lyubomirskiy et al., 'Multi-beam X-ray ptychography using coded probes for rapid non-destructive high resolution imaging of extended samples', *Sci. Rep.* 12, 6203 (2022).
4. M. Lyubomirskiy et al., 'Ptychographic characterisation of polymer compound refractive lenses manufactured by additive technology', *Opt. Express* 27, 8639–8650 (2019).

Original publication

'X-Ray Multibeam Ptychography at up to 20 keV: Nano-Lithography Enhances X-Ray Nano-Imaging', *Advanced Science* 11, 2310075 (2024). DOI: 10.1002/adv.202310075



Tang Li¹, Maik Kahnt², Thomas L. Sheppard³, Runqing Yang⁴, Ken V. Falch¹, Roman Zvagelsky⁵, Pablo Villanueva-Perez⁴, Martin Wegener³ and Mikhail Lyubomirskiy¹

1. Centre for X-ray and Nano Science CXNS, DESY, Hamburg, Germany
2. MAX IV Laboratory, Lund, Sweden
3. Karlsruhe Institute of Technology, Karlsruhe, Germany
4. Department of Physics, Lund University, Lund, Sweden
5. Karlsruhe Institute of Technology, Karlsruhe, Germany

Leveraging AI to extract weak signals

Denoising experimental X-ray diffraction data using deep convolutional neural networks

In recent years deep learning has revolutionised many scientific fields, including image restoration. Still, denoising scientific data presents unique challenges due to the complexity and variability of noise sources. In this work we apply deep convolutional neural networks to remove noise from X-ray diffraction data, enabling the detection of weak signals that are otherwise lost in noisy environments. By training neural networks on experimental data, we demonstrate significantly improved signal clarity and accuracy compared to traditional methods. As such, this approach offers exciting potential for advancing research in materials science.

While artificial intelligence (AI) has seen an exponential increase in applications for everyday use, it is less commonly applied in fundamental condensed matter research. One promising use case of AI is the advancement of current data analysis procedures. At present, supervised machine-learning approaches involving deep neural networks have been applied across various disciplines to address problems covering complex parameter spaces. Supervised algorithms excel in such cases by enabling the automatic identification of intricate patterns and relationships between input variables and target outcomes that are often inaccessible through traditional computational and analytical methods. One such discipline, where remarkable progress has been made, is the field of image denoising [1,2] where a typical benchmark problem is the removal of Gaussian noise using deep convolutional neural networks (CNNs) [3].

However, counting of events with time-independent probability is expected to follow Poisson statistics where the signal and the noise are no longer independent, posing denoising a bigger challenge. As such, virus-cell infection, radioactivity and particle scattering are examples that follow a Poisson distribution. Poisson noise can generally be reduced by using a sufficient acquisition time. However, long exposure times are not always possible. For example, for radiation of molecules, proteins or human tissue, low exposure times are required in order to avoid beam damage [4]. The removal of noise from experimental data is even more challenging because additional noise sources, such as readout noise, are a contributing factor. Finally, many experiments explore multi-dimensional parameter spaces which are almost impossible to cover completely with sufficient statistics. Thus, there is clear potential in

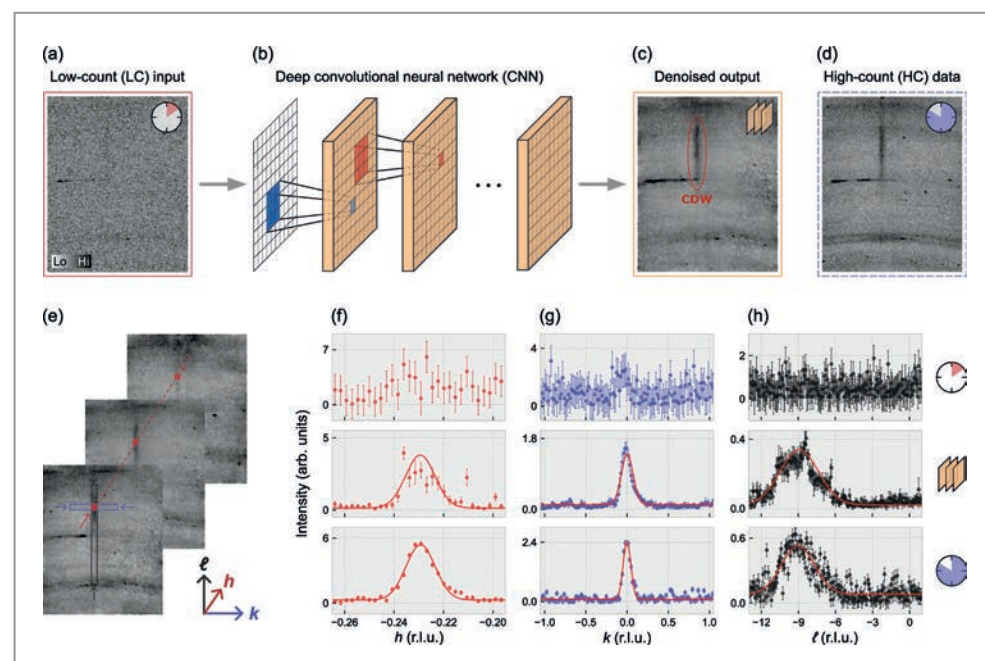
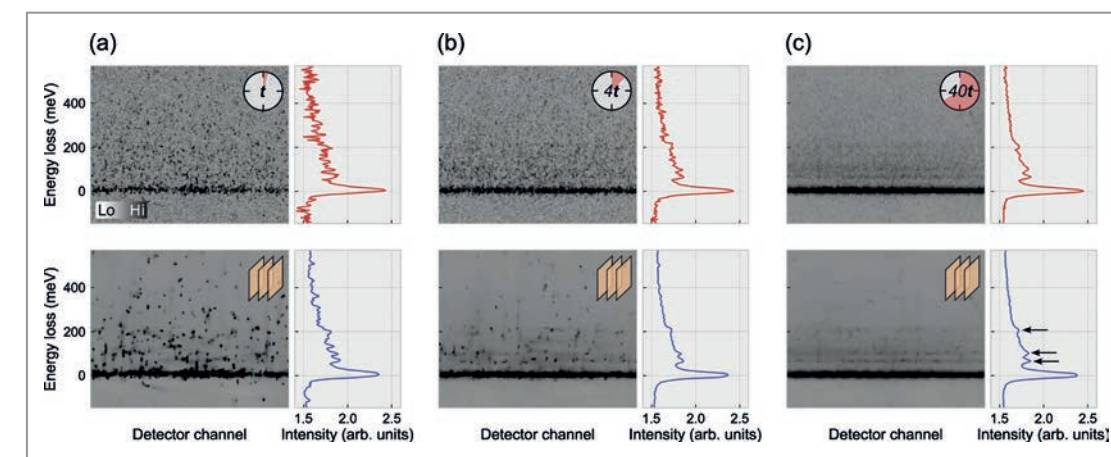


Figure 1
Example of denoising X-ray diffraction data using a deep CNN. a) A real experimental LC frame (exposure time 1 second) is used as an input to a deep CNN b) trained to remove the noise. c) The denoised output reveals a CDW signal (red) barely visible in the raw LC data. d) The real experimental HC frame (exposure time 20 seconds) for comparison. e-h) Line shape analysis of the CDW signal along the three reciprocal space directions (h, k, ℓ) demonstrates the CNN's effectiveness in significantly enhancing weak signals, achieving quality comparable to the HC data.

Figure 2
RIXS spectra recorded on SrTiO₃. a-c) Top row: RIXS spectra with counting statistics of 1, 4, and 40 times 3 minutes (t). Left: counting intensities as detector channel versus energy loss. Right: horizontally projected RIXS spectra. Bottom row: corresponding outputs from the neural network. The arrows in c) highlights three inelastic peaks.



developing robust methods to denoise low-count (LC) statistics data to produce results of a quality comparable to what would be obtained from high-count (HC) statistics data. By extension, noise filtering can speed up exploratory approaches by orders of magnitudes.

In our work we focus on experimental data recorded by X-ray diffraction on a prototypical high-temperature superconductor La_{1.88}Sr_{0.12}CuO₄ single crystal at the P21.1 beam-line at PETRA III. The dataset contains various signals with intensities varying over six orders of magnitude. We then train deep CNNs to remove the noise from the LC data, enabling the extraction of weak signals such as charge-density-wave (CDW) order which reveals itself as faint superlattice reflections. Such an example of denoising X-ray diffraction data is shown in Fig. 1a-c. The performance evaluation of the trained neural network is illustrated by one-dimensional line cuts (along the reciprocal h, k , and ℓ directions) through the CDW ordering vector, see Fig. 1e-h. We find that a CNN is highly effective in removing noise from the LC data, achieving results comparable to HC data while enabling a 20-fold reduction of the measurement time. We also observe that training on experimental data greatly improves the noise filtering compared to training on artificial noise. This conclusion holds true even when the amount of artificial training data is larger than the amount of experimental training data.

To illustrate the generality and robustness of our approach, we apply a CNN trained on solely X-ray diffraction data to resonant inelastic X-ray scattering (RIXS) data recorded on SrTiO₃ (Fig. 2 top row). Since the used RIXS detector does not offer single-photon sensitivity, the signal is not expected to follow pure Poisson statistics. Despite the dissimilar experimental technique, different sample and different noise distribution, the trained neural network achieves a noticeable noise reduction and consequently enhances the signal-to-background ratio (Fig. 2 bottom row). The successful denoising of RIXS data likely stems from the rich variation of signals and noise sources in the

X-ray diffraction training data. Our results, therefore, encourage the collection of even more diverse training data with different compositions of noise sources from other scattering, spectroscopy and microscopy techniques. By applying our method to future studies, a large amount of beamtime could be saved, or a fixed beamtime budget could be used more efficiently by, for example, being able to probe a larger parameter space.

Author contact: Jens Oppliger, jens.oppliger@physik.uzh.ch

References

- V. Jain and S. Seung, 'Natural image denoising with convolutional networks', In: *Advances in Neural Information Processing Systems Vol. 21* (eds D. Koller et al.) (Curran Associates, 2009).
- C. Tian et al., 'Deep learning on image denoising: an overview', *Neural Netw.* **131**, 251 (2020).
- K. Zhang, W. Zuo, Y. Chen, D. Meng and L. Zhang, 'Beyond a Gaussian denoiser: residual learning of deep CNN for image denoising', *IEEE Trans. Image Process.* **26**, 31423155 (2017).
- Z. J. W. A. Leijten, A. D. A. Keizer, G. de With and H. Friedrich, 'Quantitative analysis of electron beam damage in organic thin films', *J. Phys. Chem. C* **121**, 10552 (2017).

Original publication

'Weak signal extraction enabled by deep neural network denoising of diffraction data', *Nature Machine Intelligence* **6**, 180-186 (2024). DOI: 10.1038/s42256-024-00790-1



Jens Oppliger¹, M. Michael Denner¹, Julia Küspert¹, Ruggero Frison¹, Qisi Wang^{1,2}, Alexander Morawietz¹, Oleh Ivashko³, Ann-Christin Dippel³, Martin von Zimmermann³, Izabela Bialo^{1,4}, Leonardo Martinelli¹, Benoît Fauqué⁵, Jaewon Choi⁶, Miriam Garcia-Fernandez², Ke-Jin Zhou⁴, Niels Bech Christensen⁷, Tohru Kurosawa⁸, Naoki Momono^{8,9}, Migaku Oda⁸, Fabian D. Natterer¹, Mark H. Fischer¹, Titus Neupert¹ and Johan Chang¹

- Physik-Institut, Universität Zürich, Zurich, Switzerland
- Department of Physics, The Chinese University of Hong Kong, Hong Kong, China
- Deutsches Elektronen-Synchrotron DESY, Hamburg, Germany
- Faculty of Physics and Applied Computer Science, AGH University of Krakow, Krakow, Poland
- JEIP, USR 3573 CNRS, Collège de France, PSL University, Paris, France
- Diamond Light Source, Didcot, UK
- Department of Physics, Technical University of Denmark, Kongens Lyngby, Denmark
- Department of Physics, Hokkaido University, Sapporo, Japan
- Department of Applied Sciences, Muroran Institute of Technology, Muroran, Japan

Dose-efficient *in vivo* X-ray imaging of small samples

Bragg magnifier enables micrometre resolution imaging of tiny parasitoid wasps

X-ray imaging of morphodynamic and physiological processes in living organisms is hampered by the high radiation dose deposited in the sample. To overcome current limitations of conventional high-resolution detector systems, we combined propagation-based X-ray phase contrast, Bragg crystal optics and a single-photon counting detector, thereby considerably improving the dose efficiency. The developed method allows imaging at micrometre resolution with a minimal radiation dose. The method was applied to an *in vivo* behavioural study of parasitoid wasps in their hosts.

Hidden structures and processes in living cells and organisms can be visualised by X-ray imaging, but the possible observation period is limited due to ionising radiation. While conventional X-ray images only provide little soft tissue contrast due to the low absorption of X-rays in light elements, phase contrast methods can improve image contrast by taking advantage of the phase shift that the sample imprints on the incident X-ray wavefield. For soft tissue, this phase shift dominates absorption by three to four orders of magnitude, implying a significant reduction in radiation dose. One of the main approaches to visualise the phase variation is propagation-based phase contrast which exploits the self-interference of the transmitted wavefield behind the sample [1]. Despite this considerably improved image contrast, gentle imaging becomes increasingly difficult with higher resolution, requiring a higher dose. Moreover, the efficiency of high-resolution indirect detectors, which are conventionally used in X-ray imaging, decreases with increasing resolution [2]. These detectors consist of a scintillator that converts the X-rays into visible

light before the image is magnified by a microscope and detected by a CCD or CMOS camera. Because of the limited focal depth of the objective, the scintillator has to be very thin to achieve high resolution. Due to the low thickness, only a fraction of the X-ray photons are absorbed by the scintillator, leading to a low detection efficiency, especially at high X-ray energies. As a result, the radiation dose is further increased. In addition, the microscope of the indirect system has an incoherent optical transfer function which further suppresses image information at high spatial frequencies needed for high resolution.

We have developed an imaging system with micrometre resolution that uses radiation more efficiently. The system combines X-ray phase contrast with Bragg crystal optics [3–6] and a photon-counting detector [7]. Instead of converting the X-ray image to a visible light image and enlarging it with a microscope, the X-ray wavefield behind the specimen is coherently magnified before the intensity image is detected by a directly converting large-area

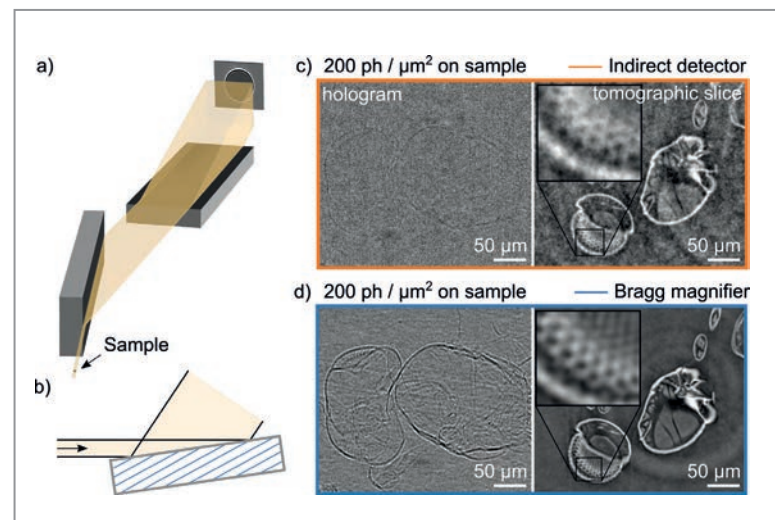
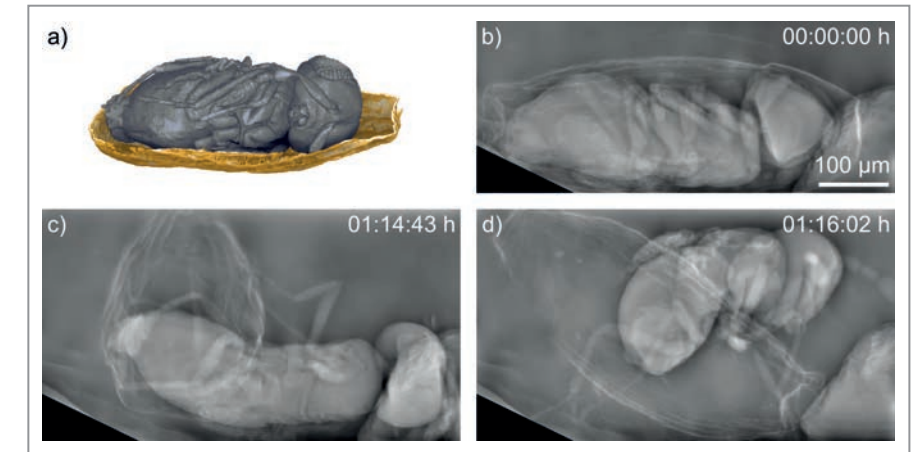


Figure 1
a) Schematics of the Bragg magnifier system consisting of two asymmetrically cut silicon crystals and a high-Z single-photon-counting detector. The sample is placed in front of the crystals. b) Principle of beam magnification by asymmetric Bragg diffraction. The lattice planes of the crystal are indicated in blue. c) and d) Comparison of imaging performance between c) a conventional high-resolution scintillator-based indirect detector system and d) the developed dose-efficient Bragg magnifier system. Both systems were operated at the same imaging parameters (67 ms exposure time, 30.5 keV X-ray photon energy). The flatfield-corrected holograms (left column) and the single-distance phase reconstructed tomogram (right column) show a critical point dried *Lariophagus distinguendus* chalcid wasp. (Figures adapted from original paper according to the Optica Publishing Group Open Access Publishing Agreement)

Figure 2
Trichogramma cacoeciae wasps were imaged *in vivo* with the Bragg magnifier system. a) Volume rendering of wasp inside the parasitised moth eggshell. b) to d) Phase-reconstructed radiographs of a wasp emerging from its host egg, acquired with 15 frames per second. The dose per frame was 7 mGy, and the total exposure time to X-rays was 30 min. The X-ray movie of the wasp is available in the supplemental material of the original paper. (Figures adapted from original paper according to the Optica Publishing Group Open Access Publishing Agreement)



detector. In this way, the high detection efficiency of single-photon counting detectors can be exploited while at the same time realising an image resolution of about 1 μm despite the large detector pixels of 55 μm [7]. The magnification is realised with a so-called Bragg magnifier [3–6]. The Bragg magnifier consists of two perfect silicon crystals (Fig. 1a) whose magnification effect results from the strongly asymmetric diffraction geometry used (Fig. 1b). Another big advantage of the Bragg magnifier is its uniform and high optical transfer function close to unity which enables almost lossless transfer of all spatial frequencies up to the resolution limit.

Thanks to the combination of propagation-based phase contrast with a Bragg magnifier and a photon-counting detector, all tailored to the optimum X-ray energy of 30 keV, the method approaches the theoretically highest possible dose efficiency for propagation-based X-ray phase contrast at micrometre resolution. This results in a more gentle imaging technique for small living organisms and allows for longer observation times.

In an experiment conducted at the P23 beamline at PETRA III, we showed that the new system can achieve a detection efficiency of over 90% while providing a resolution of up to 1.3 μm. Furthermore, the system's performance was compared with a conventional high-resolution detector system using the same sample, X-ray fluence and 30.5 keV X-ray energy. At this energy, we showed that the detective quantum efficiency of the Bragg magnifier system exceeds that of the conventional system by more than two orders of magnitude for the relevant high-resolution components of the image. This results in superior images (Fig. 1c,d) and enables a drastic reduction of the X-ray dose deposited in the sample.

We demonstrated the method in a pilot study of tiny parasitoid *Trichogramma* wasps widely used for biological pest control. Due to the minimal radiation dose, the wasps could be observed inside their host eggs and during their emergence from the eggs for more than 30 minutes at frame rates of 15 images per second (Fig. 2). We could observe the flexible biting capability of their mandibles while perforating the eggshell and the involvement of different body

parts during emergence. The developed method is suited for living samples and other types of radiation-sensitive specimens, opening up new opportunities in biology, biomedicine and materials science.

Author contact: Rebecca Spiecker, rebecca.spiecker@kit.edu
Carlos Sato Baraldi Dias, carlos.dias@desy.de
Tilo Baumbach, tilo.baumbach@kit.edu

References

1. S. Wilkins, T. E. Gureyev, D. Gao, A. Pogany and A. Stevenson, 'Phase-contrast imaging using polychromatic hard X-rays', *Nature* 384, 335–338 (1996).
2. L. Wollesen, F. Riva, P.-A. Douissard, K. Pauwels, T. Martin and C. Dujardin, 'Scintillating thin film design for ultimate high resolution X-ray imaging', *J. Mater. Chem. C* 10, 9257–9265 (2022).
3. W. J. Boettinger, H. E. Burdette and M. Kuriyama, 'X-ray magnifier', *Rev. Sci. Instrum.* 50, 26–30 (1979).
4. M. Stapanoni, G. Borchert, R. Abela and P. Rügsegger, 'Bragg magnifier: a detector for submicrometer x-ray computer tomography', *J. Appl. Phys.* 92, 7630–7635 (2002).
5. P. Modregger, D. Lübbert, P. Schäfer and R. Köhler, 'Magnified X-ray phase imaging using asymmetric Bragg reflection: experiment and theory', *Phys. Rev. B* 74, 054107 (2006).
6. P. Vagovič, D. Korytar, A. Cecilia, E. Hamann, L. Švéda, D. Pelliccia, J. Härtwig, Z. Zápražný, P. Obera, I. Dolbnya, K. Shawney, U. Fleschig, M. Fiederle and T. Baumbach, 'High-resolution high-efficiency X-ray imaging system based on the in-line Bragg magnifier and the Medipix detector', *J. Synchrotron Radiat.* 20, 153–159 (2013).
7. D. Pennicard, S. Smoljanin, B. Struth, H. Hirseman, A. Fauler, M. Fiederle, O. Tolbanov, A. Zarubin, A. Tyazhev, G. Shelkov and H. Graafsma, 'The LAMBDA photon-counting pixel detector and high-Z sensor development', *J. Instrum.* 9, C12026 (2014).

Original publication

'Dose-efficient *in vivo* X-ray phase contrast imaging at micrometer resolution by Bragg magnifiers', *Optica* 10, 1633–1640 (2023).
DOI: 10.1364/OPTICA.500978



Rebecca Spiecker¹, Pauline Pfeiffer², Adyasha Biswal^{3,4}, Mykola Shcherbin¹, Martin Spiecker⁵, Holger Hessdorfer³, Mathias Hurst³, Yaroslav Zharov¹, Valerio Bellucci^{1,6}, Tomáš Faragó³, Marcus Zuber³, Annette Herz⁷, Angelica Cecilia³, Mateusz Czyzycki¹, Carlos Sato Baraldi Dias¹, Dmitri Novikov⁸, Lars Krogmann², Elias Hamann³, Thomas van de Kamp^{1,3} and Tilo Baumbach^{1,3}

1. Laboratory for Applications of Synchrotron Radiation, Karlsruhe Institute of Technology, Karlsruhe, Germany
2. Department of Entomology, State Museum of Natural History, Stuttgart, Germany
3. Institute for Photon Science and Synchrotron Radiation, Karlsruhe Institute of Technology, Eggenstein-Leopoldshafen, Germany
4. Centre for Organismal Studies, Heidelberg University, Heidelberg, Germany
5. Physikalisches Institut, Karlsruhe Institute of Technology, Karlsruhe, Germany
6. European XFEL, Schenefeld, Germany
7. Julius Kühn-Institute, Institute for Biological Control, Dossenheim, Germany
8. Deutsches Elektronen-Synchrotron DESY, Hamburg, Germany

The dark side of transmission X-ray microscopy

Advancing high-resolution dark-field imaging to visualise scattering sources at the nanometre scale

Dark-field X-ray imaging—a technique that visualises sources of X-ray scattering within a sample—has gained popularity in diverse scientific fields. Dark-field imaging provides a distinct contrast mechanism by utilising only scattered, rather than attenuated, X-rays. Since scattering features can be smaller than the setup's spatial resolution, dark-field imaging is sensitive to structures undetectable by attenuation. However, most dark-field implementations are currently limited to microtomography setups. Based on a simple approach, we realised a dark-field imaging setup at a synchrotron-based full-field transmission X-ray microscope.

The ability to visualise and characterise the hierarchical 3D structure and inhomogeneities of materials is essential across scientific fields. Non-destructive imaging based on the attenuation of X-rays has therefore become invaluable for investigating material properties. However, its limitations in detecting subtle features have led to complementary modalities like dark-field imaging which highlights scattering-induced structural inhomogeneities invisible to conventional techniques [1]. Dark-field imaging aids in diagnosing lung diseases like emphysema [2], improving breast cancer detection [3], identifying defects in reinforced thermoplastics [4] and revealing porosity below pixel resolution [5]. Sensitive to small internal structures, it is crucial in materials science. Yet, dark-field imaging has been limited to micro-computed tomography setups. The novel full-field dark-field transmission X-ray microscope (TXM) approach overcomes this limitation and makes dark-field imaging for the first time available for full-field nanotomography.

The challenge posed by the new approach has been that the attenuated light, which passes through the object, had to be suppressed so that the less intense scattering image becomes visible. In our TXM, a beam-shaping condenser is

used which diffracts the incoming beam creating a flat-top illumination [6]. This illumination creates a well-defined pattern in the back-focal plane of the objective lens. Based on that knowledge, the bright field—the non-scattered light—can be blocked by apertures (Fig. 1). The scattered light, on the other hand, changes its direction when passing through the sample and can therefore pass by the apertures. This results in the so-called dark-field image, now accessible with nanometre resolution. The full-field dark-field TXM was developed and implemented at the nanotomography end station of the PETRA III beamline P05 operated by Helmholtz-Zentrum Hereon.

Our TXM setup is designed for speed and versatility [7-9]. The long distance between the sample and the detector, in combination with highly efficient optics, allows dark-field images to be captured with exposure times of 0.5 seconds and complete tomographic scans in less than 15 minutes while maintaining a spatial resolution of 117 nm (Fourier ring correlation). With the motorisation of the apertures by piezoelectric actuators, the setup offers seamless switching between attenuation and dark-field modes without realignment, thus maximising productivity and minimising

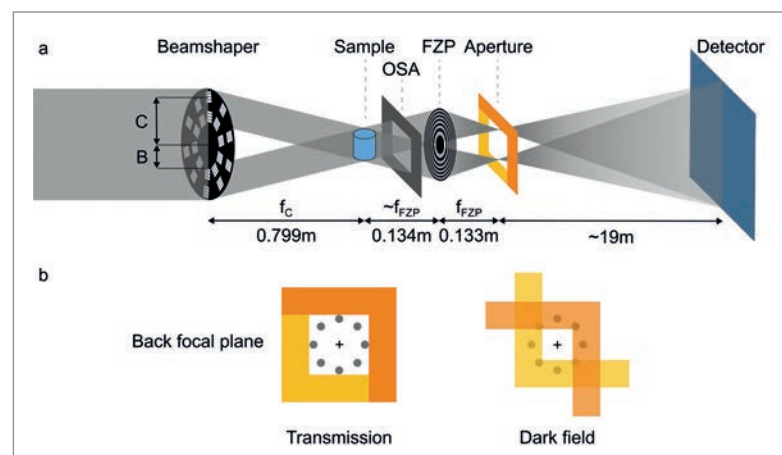


Figure 1
a) Schematic of the TXM dark-field setup. The beam-shaping condenser divides the X-ray beam into multiple deflected parallel beams, forming a ring of focused points in the back focal plane of the Fresnel zone plate (illustrated here with only two beams).
b) The two L-shaped apertures (yellow and orange) can be adjusted to fully block all focal spots (grey dots), thereby switching from transmission mode (left) to dark-field mode (right).

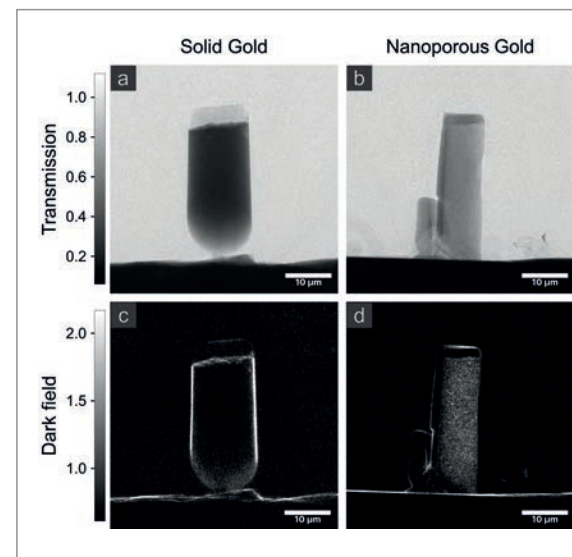


Figure 2
Two gold pillars were measured in the bright field a) and b) and in the dark field c) and d). The pillar in a) and c) consists of solid gold, while the pillar in b) and d) contains a nanoporous hierarchical inner structure. In the transmission projections, both pillars look homogeneous within the sample, whereas the intrinsic structure can be directly visualised using the dark-field signal. Each projection was taken with 1 s exposure time.

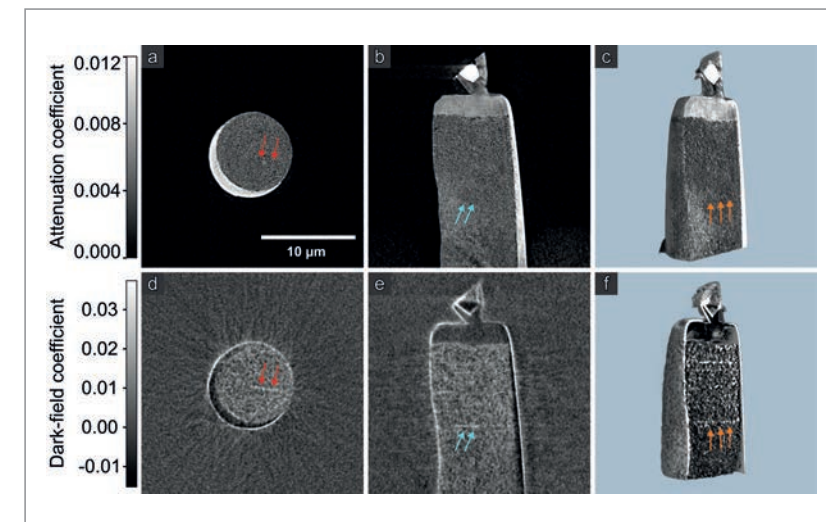


Figure 3
Reconstructed volume of a nanoporous gold pillar with structures in the range of 120 nm and below, which is at the resolution limit of the used TXM setup. a) shows the axial view and b) the coronal view, each displaying the local distribution of the attenuation coefficient. d) and e) show the local distribution of the dark-field coefficient, while c) and f) present the corresponding volume renderings. Arrows indicate grain boundaries that are visible in the dark-field signal but not in the attenuation coefficient. Each tomogram was acquired in under 15 minutes.

operational downtime. In our studies, this setup successfully revealed nanoscale porosities and boundary structures within hierarchical nanoporous gold samples, thus effectively highlighting features that conventional bright-field TXM imaging could not capture.

The contrast difference between the two imaging modalities becomes visible in Fig. 2, where a projection of the hierarchical nanoporous gold sample is compared to a solid gold pillar. Here, the dark-field image (Fig. 2c,d) immediately reveals the nanoporous internal structure not visible in attenuation (bright-field) (Fig. 2a,b). Figure 3 shows the 3D volume of the hierarchical nanoporous gold sample measured with standard attenuation (Fig. 3a,b,c) and in addition, using the newly developed dark field approach (Fig. 3d,e,f). The dark field image shows fine details that cannot be depicted by the attenuation modality alone. Therefore, the high-contrast dark-field images provide critical insights into material properties at the nanometre level which are essential for various scientific and industrial applications.

This method is also easily applicable to existing TXMs at other synchrotron facilities, thereby promising broader accessibility for high-resolution dark-field imaging. Applications of this technique extend to diverse fields, including biomedical research, industrial inspection processes as well as materials science, where understanding the fine structural details of advanced materials is essential. By offering additional structural information about cracks, voids and other sub-resolution features with strong changes in electron density, our dark-field TXM provides valuable informa-

tion that is crucial for non-destructive analysis and the study of hierarchical structures.

Author contact: Sami Wirtensohn, sami.wirtensohn@hereon.de

References

1. F. Pfeiffer et al., 'Hard-X-ray dark-field imaging using a grating interferometer', *Nat. Mater.* 7, 134–137 (2008).
2. T. Urban et al., 'Qualitative and Quantitative Assessment of Emphysema Using Dark-Field Chest Radiography', *Radiol.* 303, 119–127 (2022).
3. K. Scherer et al., 'Improved Diagnostics by Assessing the Micromorphology of Breast Calcifications via X-Ray Dark-Field Radiography', *Sci. Rep.* 6, 36991 (2016).
4. Ö. Öztürk et al., 'Defect detection in glass fabric reinforced thermoplastics by laboratory-based X-ray scattering', *Compos. B: Eng.* 252, 110502 (2023).
5. V. Revol et al., 'Sub-pixel porosity revealed by x-ray scatter dark field imaging', *J. Appl. Phys.* 110, 4 (2011).
6. K. Jefimovs et al., 'Beam-shaping condenser lenses for full-field transmission x-ray microscopy', *J. Synchrotron Radiat.* 15, 106–108 (2008).
7. S. Flenner et al., 'Pushing the temporal resolution in absorption and Zernike phase contrast nanotomography: enabling fast *in situ* experiments', *J. Synchrotron Radiat.* 27, 1339–1346 (2020).
8. S. Flenner et al., 'Hard X-ray nano-holography with a Fresnel zone plate', *Opt. Express* 28, 37514–37525 (2020).
9. E. Longo et al., 'X-ray Zernike phase contrast tomography: 3D ROI visualization of mm-sized mice organ tissues down to sub-cellular components', *Biomed. Opt. Express* 11, 5506–5517 (2020).

Original publication

'Nanoscale dark-field imaging in full-field transmission X-ray microscopy', *Optica* 11, 852–859 (2024), DOI:10.1364/OPTICA.524812.



Sami Wirtensohn^{1,2}, Peng Qi³, Christian David³, Julia Herzen², Imke Greving¹ and Silja Flenner¹

1. Helmholtz-Zentrum Hereon, Geesthacht, Germany
2. Technical University of Munich, Garching, Germany
3. Paul Scherrer Institut, Villigen, Switzerland

Chip-integrated ultrafast laser sources

Synthetic reflection and on-chip rare earth gain enable compact femtosecond lasers and high-energy pulse sources

Photonic chips are poised to revolutionise optics in the same way electronic chips transformed computing. By guiding photons instead of electrons, these chips enable integration of complex optical systems into compact, low-cost silicon photonic devices. One fascinating goal is to incorporate ultrafast laser sources within these chips. Such sources generate pulses of ultrashort duration measured in femtoseconds or picoseconds. Integrating these technologies into devices as small as a cell phone is expected to accelerate telecommunications, enhance computing efficiency and lead to portable laser sensors for self-driving cars, medical diagnostics and treatments. DESY scientists have recently made two major advances towards this goal.

One of the most promising approaches to integrating ultrafast laser sources onto chips is through microcombs [1]. These are created within microscopic optical resonators which are smaller than a human hair (Fig. 1). Nonlinear optical effects in these resonators can lead to the self-organisation and generation of femtosecond optical pulses known as dissipative Kerr solitons. However, practical implementation has been hindered by thermal effects and other instabilities intrinsic to silicon photonic chips. These factors make it difficult to precisely tune the pump laser, which powers the system, to the resonance frequency of the microresonator. As a result, generating soliton pulses has remained a challenge confining the technology to specialised laboratories. DESY scientists have established a new technique that inherently and predictably synchronises the pump laser with the microresonator by incorporating a

nanoscale periodic modulation into the resonator's geometry forming a photonic crystal microresonator. Though it is barely detectable under an electron microscope, this modulation has a big impact: It forms a wavelength-specific reflector within the resonator, directing light from the resonator back to the laser. This feedback mechanism allows the resonator to convey its resonance frequency to the laser which then emits light preferentially at that frequency through a process called injection-locking [2]. Because this mechanism responds faster than the system's inherent instabilities, it ensures stable and easily controllable operation. The DESY team demonstrated that their technique allowed the system to be miniaturised to a volume smaller than a cubic millimetre without sacrificing deterministic and self-starting performance. In a follow-up study they further optimised the laser's stability, making it suitable for some

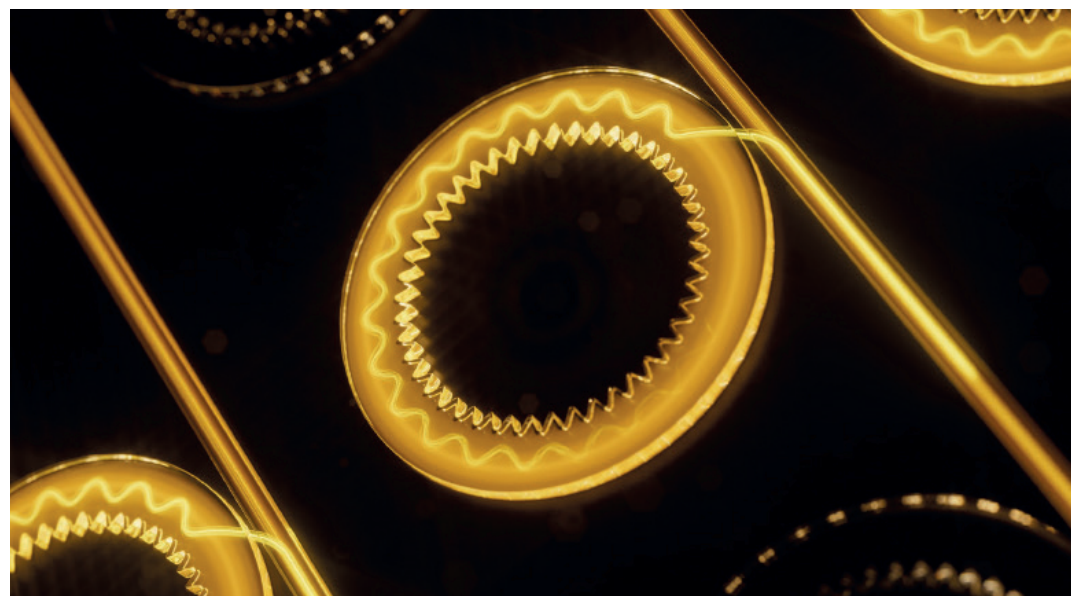


Figure 1
Artistic visualisation of the photonic crystal microresonator.

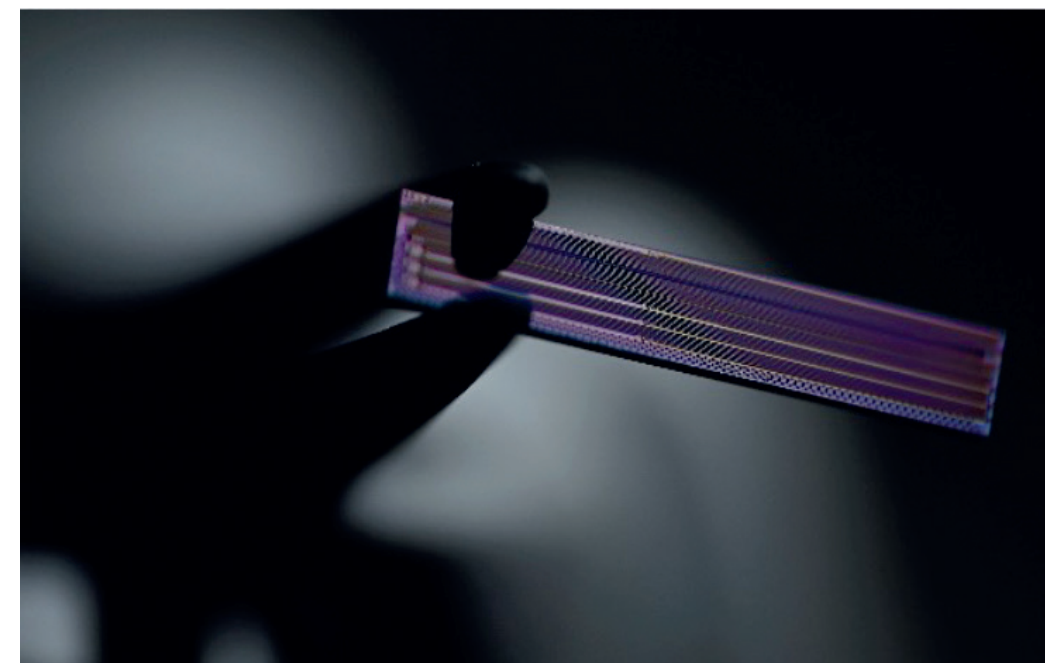


Figure 2
Photonic chip which can hold 10s of such laser sources held by a tweezer.

of the most precise measurements in physics, showcasing the vast potential of this new technology [3].

In a second study, DESY scientists tackled a different challenge: the typically low pulse energy of chip-integrated pulse sources. High-pulse energies have so far been achievable only with large, table-top laser systems. In such systems, large beam sizes efficiently interact with the energy-storing gain medium. However, in integrated photonics, the mode size is often millions of times smaller, fundamentally limiting the power that can be generated. By meticulously combining different materials and designing a waveguide geometry to optimise performance (Fig. 2), the DESY team managed to increase the mode size by over an order of magnitude, matching the level usually associated with optical fibres while also creating several centimetres of interaction length between the gain medium and the optical mode. To achieve this on a millimetre-scale chip, they folded the system into a compact structure no larger than a fingernail. With this approach, they successfully produced pulse energies comparable to those of many table-top systems.

These recent breakthroughs mark a significant step forward for chip-integrated laser technology. They hold immense promise for transforming advanced laser systems – currently accessible only in laser laboratories – into compact, low-cost, easily operable sources for out-of-laboratory applications that can meet critical societal and technological needs such as optical communication and precision sensing to emerging fields like photonic computing and quantum technology.

Author contact:
Alexander Ulanov, alexander.ulanov@desy.de

References

1. T. J. Kippenberg, A. L. Gaeta, M. Lipson and M. L. Gorodetsky, 'Dissipative Kerr solitons in optical microresonators', *Science* **361**, eaan8083 (2018).
2. N. M. Kondratiev et al., 'Recent advances in laser self-injection locking to high-Q microresonators', *Front. Phys.* **18**, 21305 (2023).
3. T. Wildi et al., 'Phase-stabilised self-injection-locked microcomb', *Nat. Commun.* **15**, 7030 (2024).

Original publications

'Synthetic reflection self-injection-locked microcombs', *Nature Photonics* **18**, 294–299 (2024).
DOI: 10.1038/s41566-023-01367-x

Alexander E. Ulanov¹, Thibault Wildi², Nikolay G. Pavlov², John D. Jost², Maxim Karpov² and Tobias Herr^{1,3}

1. Deutsches Elektronen-Synchrotron DESY, Hamburg, Germany
2. Enligna Sarl, Renens, Switzerland
3. University of Hamburg, Hamburg, Germany

'Silicon photonics-based high-energy passively Q-switched laser', *Nature Photonics* **18**, 485–491 (2024).
DOI: 10.1038/s41566-024-01388-0

Neetesh Singh¹, Jan Lorenzen^{1,2}, Milan Sinobad¹, Kai Wang³, Andreas C. Liapis⁴, Henry C. Frankis⁵, Stefanie Haugg⁶, Henry Francis⁷, Jose Carreira⁷, Michael Geiselmann⁷, Mahmoud A. Gaafar¹, Tobias Herr¹, Jonathan D. B. Bradley⁵, Zhipei Sun¹, Sonia M Garcia-Blanco³ and Franz X. Kärtner^{1,8}

1. Center for Free-Electron Laser Science CFEL, DESY, Germany
2. University of Kiel, Kiel, Germany
3. MESA+ Institute for Nanotechnology, University of Twente, Enschede, Netherlands
4. Aalto University, Espoo, Finland
5. McMaster University, Hamilton, Canada
6. The Centre for Hybrid Nanostructures CHyN, University of Hamburg, Hamburg, Germany
7. LIGENEC SA, Ecublens, Switzerland
8. University of Hamburg, Hamburg, Germany

Laser pulse control at extreme parameters using intense gas-borne ultrasound

Intense sound waves have been used to control laser pulses directly in air

Optical elements, the building blocks of light-based setups such as lasers or microscopes, today are primarily glass- or crystal-based. This includes lenses, mirrors and more advanced elements such as optical switches or fibres. The limiting parameters of these elements, most notably wavelength (due to absorption or dispersion) and peak power (due to nonlinear effects and damage thresholds) are typically defined by the solid materials. By using intense ultrasound, we mimic the properties of conventional elements by inducing a refractive index change through pressure waves – comparable to the effect of a mirage in the desert. In a first experiment, we implemented an acousto-optic modulator in ambient air capable of deflecting more than 50% of a high-power laser, exceeding the peak power records of today's acousto-optical modulators by three orders of magnitude.

Optical methods for shaping, guiding and modulating laser light primarily rely on interactions with solid media. However, these methods face limitations in advanced applications due to absorption in ultraviolet and infrared regions, nonlinear optical effects and potential light-induced damage. The refractive index, determined by the material, limits applicable wavelengths and peak power while the material's internal structure restricts the average power of light interaction. To address these constraints, we utilise gaseous media such as ambient air which offers broader transmissive windows to control laser light. Furthermore, gases are effectively damage-free and can sustain peak powers roughly three orders of magnitude higher than solid optical media.

In our study we present the use of gases as alternative optical media by employing intense ultrasound to tailor a suitable refractive index field resembling an optical grating for light deflection (Fig. 1). Prior research has documented gas-based refractive optics, including lenses and inefficient beam samplers [1,2] however, advanced control mechanisms, such as modulators, deflectors or phase shapers, have not yet entered the gas phase.

The required parameters involved in gas-phase sono-phonic approaches are extreme. The main reason is the

low refractive index variations that may be induced into gaseous media, even at high pressure: They are about four orders of magnitude lower than the refractive index difference at the boundary between the air and a glass lens.

For our initial experimental demonstration, we developed a 7 cm diameter ultrasound transducer operating at a frequency of 500 kHz with a sound pressure level (SPL) of approximately 140 dB which was further elevated to about 148 dB using a resonator configuration. This sound field acousto-optically modulates a laser beam at a nearinfrared wavelength ($\lambda = 1030$ nm) incident at the Bragg angle θ_B (Fig. 2a). This configuration allows the diffracted beam to be fully separated from the incident-collimated Gaussian beam (Fig. 2b) which exhibits interference fringes after diffraction (Fig. 2c). The diffraction orders are separated by $2\theta_B \approx 1.5$ mrad (Fig. 2d). We utilise laboratory ambient air without requiring additional housing or chambers and through a multi-pass scheme we achieve a diffraction efficiency surpassing 50%. This marks the first known efficient demonstration of an air-based acousto-optic modulator (AOM). Our experimental results agree very well with numerical simulations for both standing and traveling acoustic waves, even suggesting that higher SPLs could lead to greatly improved diffraction efficiency

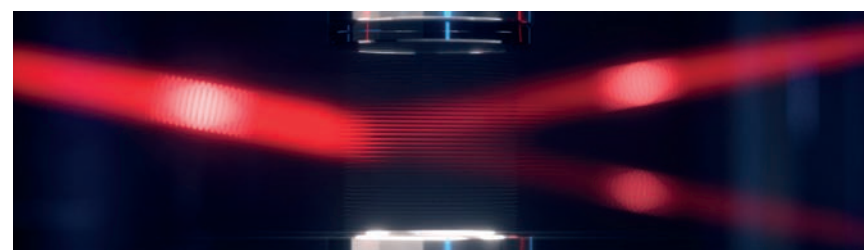


Figure 1
Illustration of a laser beam entering an air-borne ultrasound field at Bragg angle, where it diffracts and is partially deflected. (Credit: scicom-lab for DESY)

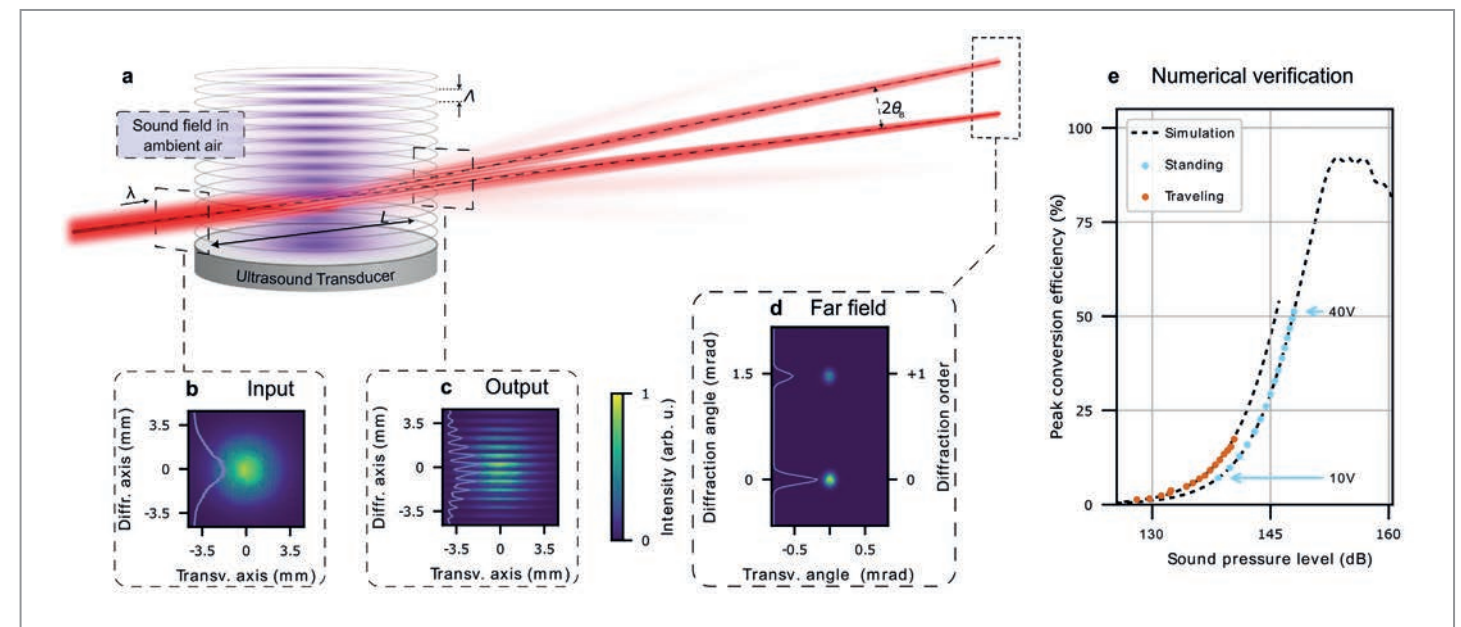


Figure 2
a) Schematic of AOM in a gas medium. b) The beam profile at the input: a Gaussian beam. c) The beam shape after the acousto-optic interaction, exhibiting interference fringes. d) The far-field showing separated transmitted and diffracted orders. e) Numerical simulations of AOM with (standing) and without reflector (traveling) and experimental results showing the diffraction efficiency at different SPL. (Credit: adapted from original publication published under CC BY 4.0)

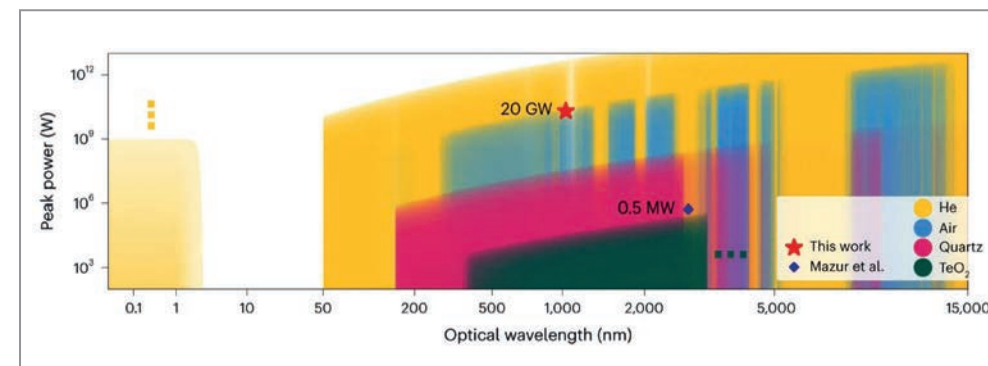


Figure 3
Possible parameter regimes of gas and bulk-based acousto-optic media limited by critical power and linear absorption displayed together with the reported result here (red star). Areas where data were not available are indicated using dotted line markers. The blue diamond indicates a $\text{KG}(\text{WO}_4)_2$ crystal as the AO medium [3]. (Credit: adapted from original publication published under CC BY 4.0)

around 90% which approaches the performance levels of conventional solid-based AOMs (Fig. 2e).

This innovative approach now opens up possibilities for developing a wide range of gas-phase sono-phonic optical elements beyond AOMs such as fast switches, lenses, optical waveguides and more, circumventing current limitations of photonic devices (Fig. 3).

Author contact: Yannick Schrödel,
yannick.schroedel@desy.de
Christoph M. Heyl, christoph.hey@desy.de

References

- L. Drescher et al., 'Extreme-ultraviolet refractive optics', *Nature* 564, 91–94 (2018).
- I. Grulkowski, D. Jankowski and P. Kwiek, 'Acousto-optic interaction with the use of cylindrical ultrasonic waves in the laser cavity', *Appl. Opt.* 48, C81 (2009).
- M. M. Mazur et al., 'Acousto-optic modulators of high-power laser radiation on the basis of KGW and KYW crystals', *Quantum Electron.* 50, 957–961 (2020).

Original publication

'Acousto-optic modulation of gigawatt-scale laser pulses in ambient air', *Nature Photonics* 18, 54–59 (2024).
<https://doi.org/10.1038/s41566-023-01304-y>



Yannick Schrödel^{1,2,3}, Claas Hartmann⁴, Jiaan Zheng¹, Tino Lang¹, Max Steudel⁵, Matthias Rutsch⁴, Sarper H. Salman^{1,2,3}, Martin Kellert⁴, Mikhail Pergament⁶, Thomas Hahn-Josef⁷, Sven Suppelt⁴, Jan Helge Dörsam⁴, Anne Harth⁵, Wim P. Leemans^{1,8}, Franz X. Kärtner^{6,8,9}, Ingmar Hartl¹, Mario Kupnik⁴ and Christoph M. Heyl^{1,2,3}

- Deutsches Elektronen-Synchrotron DESY, Hamburg, Germany
- Helmholtz Institute Jena, Jena, Germany
- GSI Helmholtzzentrum für Schwerionenforschung GmbH, Darmstadt, Germany
- Measurement and Sensor Technology Group, Technische Universität Darmstadt, Darmstadt, Germany
- Center of Optical Technologies, Aalen University, Aalen, Germany
- Center for Free-Electron Laser Science CFEL, DESY, Hamburg, Germany
- Inoson GmbH, St. Ingbert, Germany.
- Department of Physics, University of Hamburg, Hamburg, Germany
- The Hamburg Centre for Ultrafast Imaging CUI, University of Hamburg, Hamburg, Germany

Terahertz-driven ultrafast photogun: a practical novelty

New design brings proof-of-principle research to real-world applications

Ultrashort electron beams have emerged as powerful tools across diverse fields, with applications ranging from ultrafast electron diffraction and microscopy to the generation of ultrafast X-ray pulses. However, the traditional method for generating such electron beams primarily relies on radio-frequency (RF, 1–10 GHz) accelerators which require expensive, large-scale infrastructure and high power consumption, limiting their accessibility to a broader scientific community. Consequently, there is a strong motivation to develop novel, compact, laser-based technologies.

Recently, there has been significant interest in the use of THz-based particle acceleration and beam manipulation [1,2] which provide a compromise between the metre-scale RF- and the micrometre-scale laser-based technologies such as laser-plasma accelerators (LPAs) [3] and dielectric laser accelerators (DLAs) [4]. THz-based systems enable extreme acceleration gradients on the order of GV/m, allowing significant reductions in device size, cost and infrastructure. Moreover, they address key challenges such as the instability of plasma in LPAs and the stringent beam control tolerances required in DLAs. Additionally, all-optical approaches provide intrinsic synchronisation, promising precise timing control with attosecond temporal resolution. Although proof-of-principle demonstrations have shown

the feasibility of various THz-driven accelerator components, THz-driven photoguns with sufficient brightness, energy and control for use in demanding ultrafast applications have yet to be achieved.

A team of researchers from Shanghai Jiao Tong University, DESY and University of Hamburg have now developed the first practical THz-driven ultrafast photogun which leverages localised field enhancement and multi-function waveguides, realising comprehensive improvements in energy, field gradient, beam quality and control for such devices. For the first time, real applications in electron diffraction and microscopy were demonstrated, opening the door for future tabletop, ultrafast radiation sources.

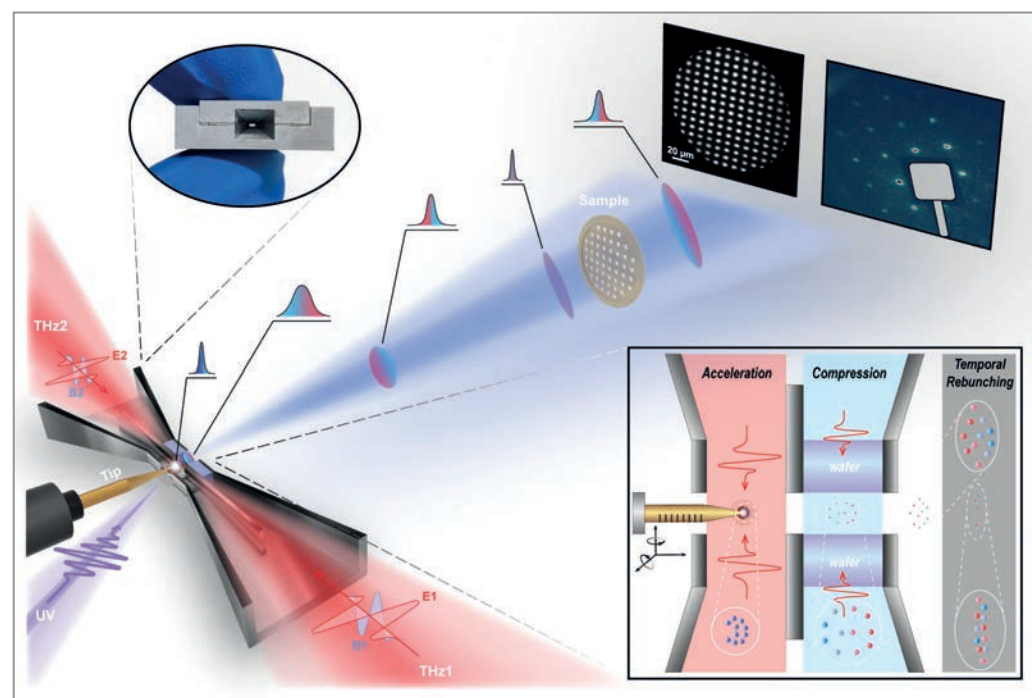
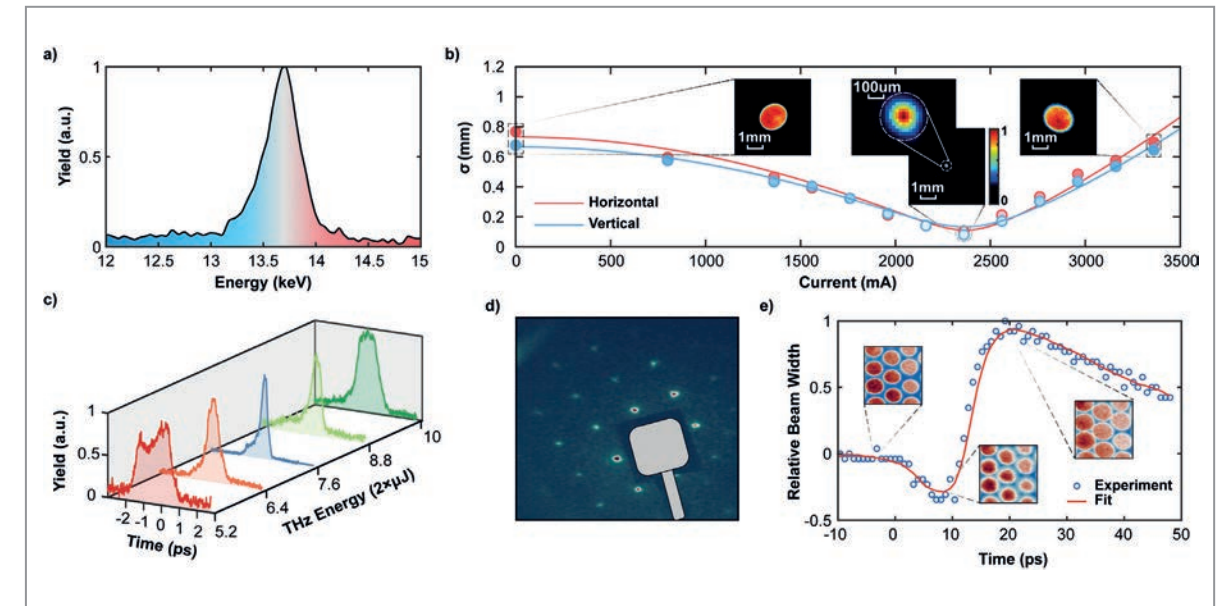


Figure 1 Experimental setup. The THz-powered photogun was driven by a UV pulse for photoemission and two single-cycle THz pulses that incident symmetrically for electron manipulation. Inset: enlarged view of the cross section of the THz-driven photogun and the schematic diagram of cascade acceleration and compression. (Adapted from original publication, © 2024 Springer Nature)

Figure 2

a) The measured electron energy spectra. b) The measured transverse emittance. c) The electron temporal distribution with different THz energies. d) The electron diffraction from a 35-nm thick single-crystalline silicon film. e) Differential transmission images as a function of the laser-electron delay time. (Adapted from original publication, © 2024 Springer Nature)



Technically, electrons are created by an ultrashort ultraviolet (UV) laser pulse at a tip-cathode via photoexcitation. Two THz pulses—serving as driving sources—are coupled into the THz waveguide cavity from the sides via symmetric horn structures with the electric field aligned parallel to the electron propagation direction (Fig. 1). The THz pulses are then transversely split by thin metal sheets into two beams for cascaded electron manipulation across separate interaction regions ('acceleration' and 'compression', see Fig. 1, inset). In the first cell, the tip-cathode enhances the electric field and is mounted on a motorised precision stage to optimise the interaction length. The relative delay between the two counter-propagating THz pulses sets the accelerating field while the UV delay controls the injection phase. In the second cell dielectric slabs with tailored lengths are inserted to match the arrival time of the THz wavefront with that of the electrons. A correct timing ensures that electrons pass through the zero-crossing point of the THz-field, accelerating the electron bunch tail while decelerating the bunch head, leading to ballistic longitudinal focusing ('compression').

The short THz driving pulses enabled a peak acceleration gradient of up to 3 GV/m, resulting in electron beams with energies reaching around 14 keV, an energy spread of 1% and exceptional beam quality with only about 0.02 mm-mrad transverse emittance. By integrating the rebunching cell, the scientists managed to compress the electron bunch by about 10 times to a duration of 167 fs, enhancing its utility for ultrafast applications. The generated high-quality electron beams indeed enable first applications in electron diffraction and projection imaging (Fig. 2d,e). Additionally, the researchers successfully mapped transient radial electric fields on a copper mesh with high spatio-temporal resolution, offering a potential avenue for plasma-based beam manipulation.

This is a critical step and milestone in the development of all-optical THz-driven electron devices, validating the technology's maturity and its use in precision applications. The exceptional performance and compactness of such THz-based photoguns make them very attractive for pursuing high-repetition rate and high-energy ultrafast electron bunches in the few- to sub-femtosecond range necessary for probing the fastest material dynamics.

Author contact: Franz X. Kärtner, franz.kaertner@desy.de
Dongfang Zhang, dongfangzhang@sjtu.edu.cn

References

1. D. Zhang et al., 'Segmented Terahertz Electron Accelerator and Manipulator (STEAM)', *Nat. Photon.* **12**, 336–342 (2018).
2. C. Kealhofer et al., 'All-optical control and metrology of electron pulses', *Science* **352**, 429–33 (2016).
3. V. Malka et al., 'Principles and applications of compact laser-plasma accelerators', *Nat. Phys.* **4**, 447–453 (2008).
4. R. Shiloh et al., 'Electron phase-space control in photonic chip-based particle acceleration', *Nature* **597**, 498–502 (2021).

Original publication

'High gradient terahertz-driven ultrafast photogun', *Nature Photonics* **18**, 758–765 (2024).
DOI: <https://doi.org/10.1038/s41566-024-01441-y>



Jianwei Ying¹, Xie He¹, Dace Su¹, Lingbin Zheng¹, Tobias Kroh^{2,3}, Timm Rohwer², Moein Fakhari², Günther H. Kassier², Jingui Ma¹, Peng Yuan¹, Nicholas H. Matlis², Franz X. Kärtner^{2,3} and Dongfang Zhang¹

1. Key Laboratory for Laser Plasmas (Ministry of Education), Collaborative Innovation Center of IFSA, School of Physics and Astronomy, Shanghai Jiao Tong University, Shanghai, China
2. Center for Free-Electron Laser Science CFEL, DESY, Hamburg, Germany
3. Department of Physics and The Hamburg Centre for Ultrafast Imaging, University of Hamburg, Hamburg, Germany



Light Sources and User Infrastructures

> FLASH	90
> PETRA III	94
> PETRA IV	98
> European Molecular Biology Laboratory Hamburg	102
> Hereon – the GEMS branch at PETRA III	104
> DESY NanoLab	106
> DESY Photon Science at the European XFEL	108

FLASH: FLASH2020+ upgrades in full swing

Taking FLASH1 to the next level

At FLASH, the year 2024 was divided into two main parts: In the first half of the year until early June, the FLASH team operated the machine for users and successfully completed 14 user experiments. Some of these experiments profited a lot from particular new FLASH2020+ upgrade features which had just been installed and commissioned. The second half of the year was devoted to the second longer FLASH2020+ upgrade shutdown which started in June 2024 and will continue until August 2025.

As for the user operation, the mobile 'CAMP2' instrument was assembled, commissioned and used in a first beamtime at the FLASH2 open port beamline FL24 (Fig. 1). The purpose of CAMP2 is to offer the capabilities of the permanent CAMP end station at FLASH1 [1] as well at open port beamlines at FLASH2 and at the soon seeded FLASH1 open ports. The permanent CAMP end station at beamline BL1 is a versatile instrument for atomic, molecular and optical physics (AMO), which allows for simultaneous use of large-area single-photon-counting pnCCD photon-detectors and velocity map imaging (VMI) electron- and ion-spectrometers, along with options for inhouse and user-provided sample delivery systems. Pulse energies of

few-10 μJ were predicted for the future seeded operation at FLASH1 and hence the experiments at CAMP. Comparing this to 100 μJ or more with SASE at FLASH2, we consider it likely that potential future single-particle imaging experiments using the pnCCDs will rather be conducted with CAMP2 at FLASH2. On the other hand, experiments which require a particularly narrow bandwidth and/or full polarisation control with moderate pulse energies can be well performed at the seeded FLASH1 at CAMP at BL1. In the previous years, the experiments at the non-monochromatic FLASH1 beamlines, such as BL1, were typically limited by the SASE FEL bandwidth and pulse-to-pulse jitter, resulting in about 1-2% effective spectral width. In contrast, the new seeded FLASH1 will yield a quasi-jitter-free bandwidth of 0.05 - 0.4%, and studies will benefit from high-spectral resolution and stability as well as the high longitudinal coherence. This would enable more precise experiments, for instance at CAMP, mapping out electronic and nuclear dynamics in molecules in more detail.

An important new feature for user operation at FLASH2 is the third harmonic afterburner undulator. It has been installed in the FLASH2 tunnel in September 2023 and

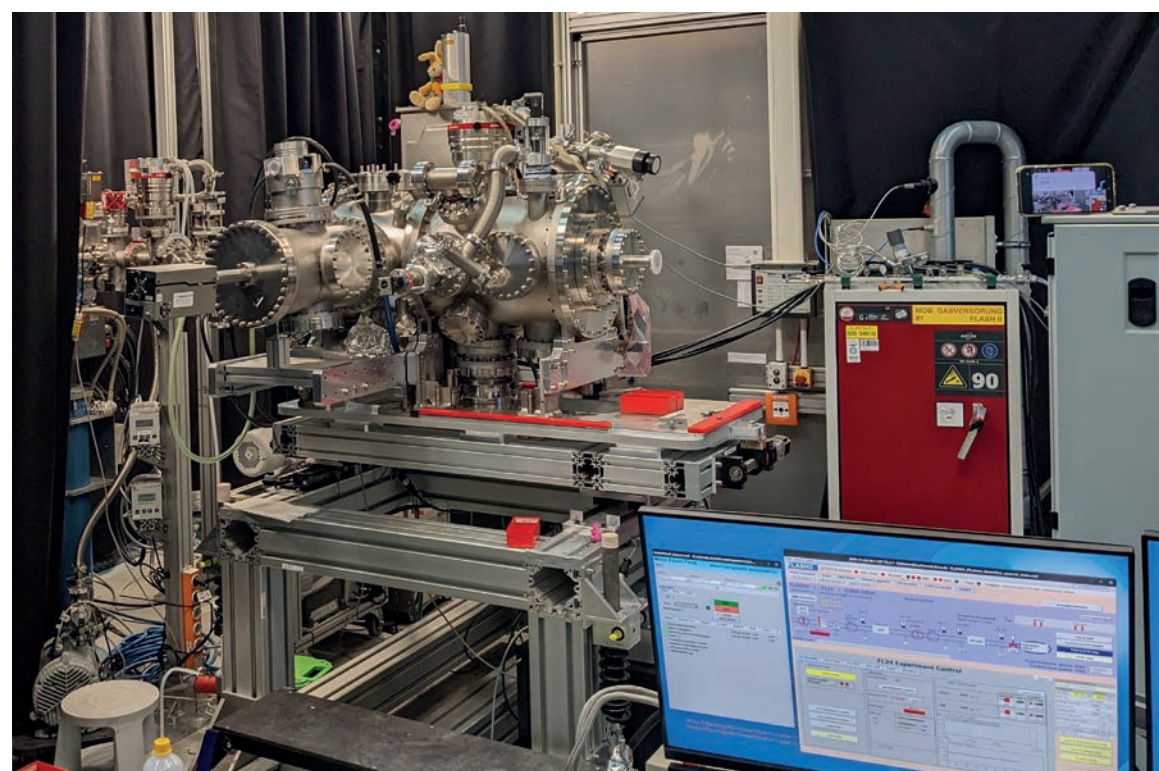


Figure 1
The new CAMP2 experimental chamber, which is fully compatible with all the usual CAMP instrumentation, here installed at beamline FL24 for the first FLASH2 user experiment with pnCCDs.

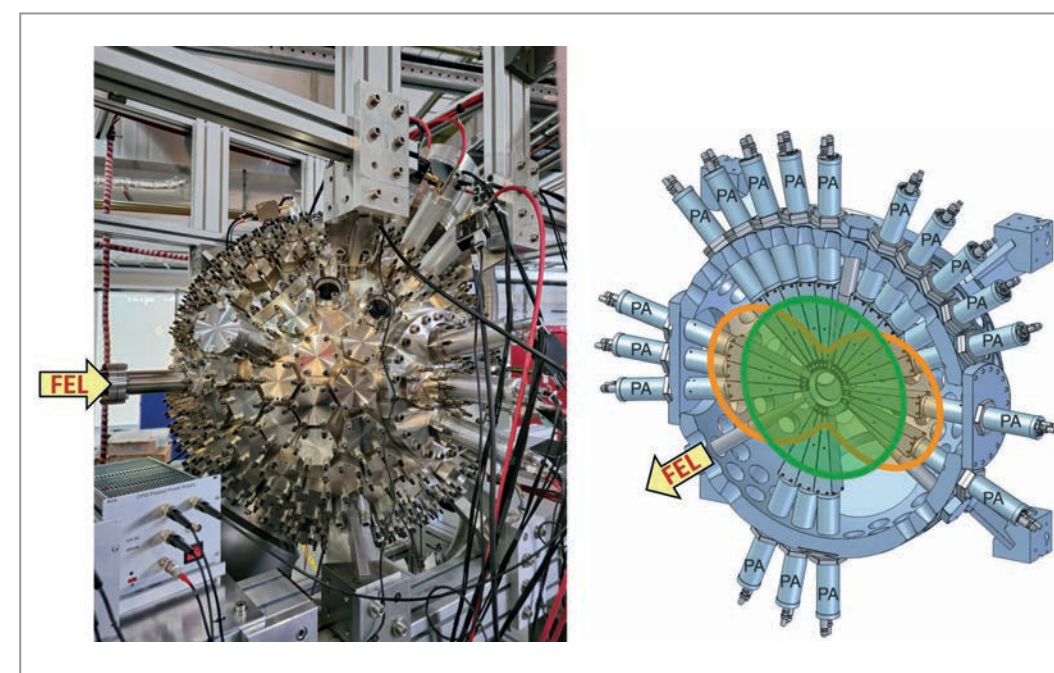


Figure 2
(Left) The so-called 'ball chamber' is used for diagnostics of the FEL polarisation, resulting from a certain magnetic setting of the afterburner undulator.
(Right) The sketch shows the cut of the CAD drawing seen from the rear side with overlapped photoelectron angular distributions for horizontal linear polarisation (orange curve) as well as circular polarisation (green curve). The 'PA' stands for 'Pre-amplifier' at the electron TOF spectrometers, which are mounted around the chamber.

was afterwards commissioned with respect to its spectral range and FEL polarisation properties. The polarisation characteristics were obtained with a setup of time-of-flight (TOF) photoelectron spectrometers circularly arranged in the plane perpendicular to the FEL propagation axis, as shown in Fig. 2. Different polarisation modes set with the afterburner can be distinguished by a measurement of the photoelectron angular distribution of gas targets. The angular distribution shows anisotropic patterns for linear polarisation and an isotropic pattern for circular polarisation. Details of the measurement principle are described in Ref. [2].

Directly after its successful commissioning, the afterburner undulator has been used for two magnetism experiments at the new pulse-length preserving double monochromator beamline FL23. The new optical laser system for FL23, employing a pulse-shortening technique based on multi-pass cells as described in last year's report, was also used for the first time during these FEL user experiments. The laser pulse was used to demagnetise the sample while the delayed FEL pulse was employed as a probe, sampling the circular X-ray magnetic dichroism. This was achieved with circularly polarised FEL pulses from the afterburner in the third harmonic of FLASH2, which were covering wavelengths scanned from 1.45 to 1.8 nm, i.e. around some of the 3d transition metal L-edges.

The FLASH user operation in 2024 ended with a successful test of a new 'Standardised Access Mode' (SAM) for users. Our motivation for offering SAM is to use beamtime more efficiently by pre-optimising the machine and experimental setup so that multiple experiments can be performed in quick succession. Unlike typical 5- to 6-day runs that require full optimisation before each individual experiment, this approach bundles experiments in a similar parameter space.

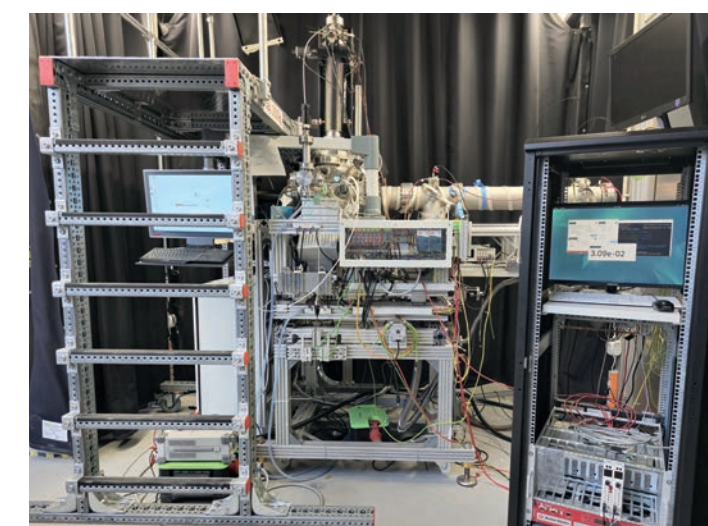


Figure 3
URSA instrument with its magnetic bottle electron spectrometer for AMO science and gas phase femto-chemistry [3]. The spectrometer is pointing to the right while the scaffolding at the left was required for frequently accessing the manipulator on top for sample exchange. The FEL beam is coming from behind.

We identified the community of scientists working in the field of gas-phase photochemistry as a test group. For their studies we offered a suitable standard parameter set using the URSA instrument, a flexible pump-probe instrument for electron spectroscopy at gas-phase samples [3]. Out of twelve submitted proposals from users, five were selected by our external project review panel (PRP) and were all-together completed in ten days with minimal sample-change interruptions. Pre-optimisation allowed consistent conditions throughout the run, yielding good data sets for each group. This operation mode proved to be efficient in terms of workload and machine hours. We are planning to offer further SAM access campaigns for other user communities. Parallel to the implementation of all the new features in the user experiments and operation



Figure 4
View into the emptied FLASH1 tunnel in autumn 2024, providing about 120 m of space for a new electron beamline, undulators, laser and photon beamlines and all the related infrastructure around.

schemes, we also pushed the limits of the accelerator further. In the last shutdown, two accelerator modules had been replaced by modern, better performing ones, yielding an energy gain of about 100 MeV. After a thorough commissioning of all accelerator modules, the new electron energy limit of 1.35 GeV is now fully accessible. This corresponds to a shortest wavelength of 3.2 nm (~390 eV) at FLASH2 with some headroom to reach even shorter wavelengths in the future. Furthermore, the new 'laser heater', which is an essential ingredient for optimising the future seeded FLASH1, could also be used to optimise the third harmonic afterburner with respect to polarisation contrast.

Regarding the characterisation of the FEL pulse properties, knowledge and control of the FEL pulse length is particularly important, if one strives for best temporal resolution of ultrafast dynamics. Therefore, the FLASH team conducted an extended campaign to compare pulse length measurements, using two entirely different approaches. On the one hand, the energy modulation of the electron bunch due to the FEL lasing process was monitored by using a transverse deflecting accelerator cavity named PolariX [4]. On the other hand, a direct measurement of the XUV pulse length was made by using a dedicated THz streaking setup at FLASH2 [5]. For standard operation of FLASH, a rather good agreement between the two complementary measurements was found. For specially tuned extreme settings, for instance with several charge spikes in an electron bunch or strong 'overheating' with the laser

heater, a more detailed analysis is required, combining the results from both methods.

All the described improvements on the instrument and the machine/accelerator side were complemented by building larger teams for operation of our instruments in the experimental halls. In the years before the pandemic, about one third of the experimental instruments were provided by the external user groups at FLASH. This number has now decreased to 10-15% which means that the largest portion of the experiments is now carried out at instruments provided by the facility. Those are typically operated in a three-shift-per-day mode which requires a growing facility staffing in particular areas of the instrumentation. We responded to these challenges of increased instrument responsibility by bundling expertise, also including the laser operations colleagues, into larger teams. Although triggered by the current tight staffing situation, this bundling will generally allow us to master the increasing and more diverse facility-operated science instrumentation in the future. Colleagues dedicated to AMO and gas-phase chemistry experiments are already forming an efficiently collaborating team for beamtimes. Particularly the first round of SAM experiments was a major group effort. Distributing the operation to more people than just the base team of the specific (in this case URSA) instrument, turned out to be essential for successfully conducting five experiments in a row in just ten days. We are currently building a similar overarching science team for the condensed-matter research.

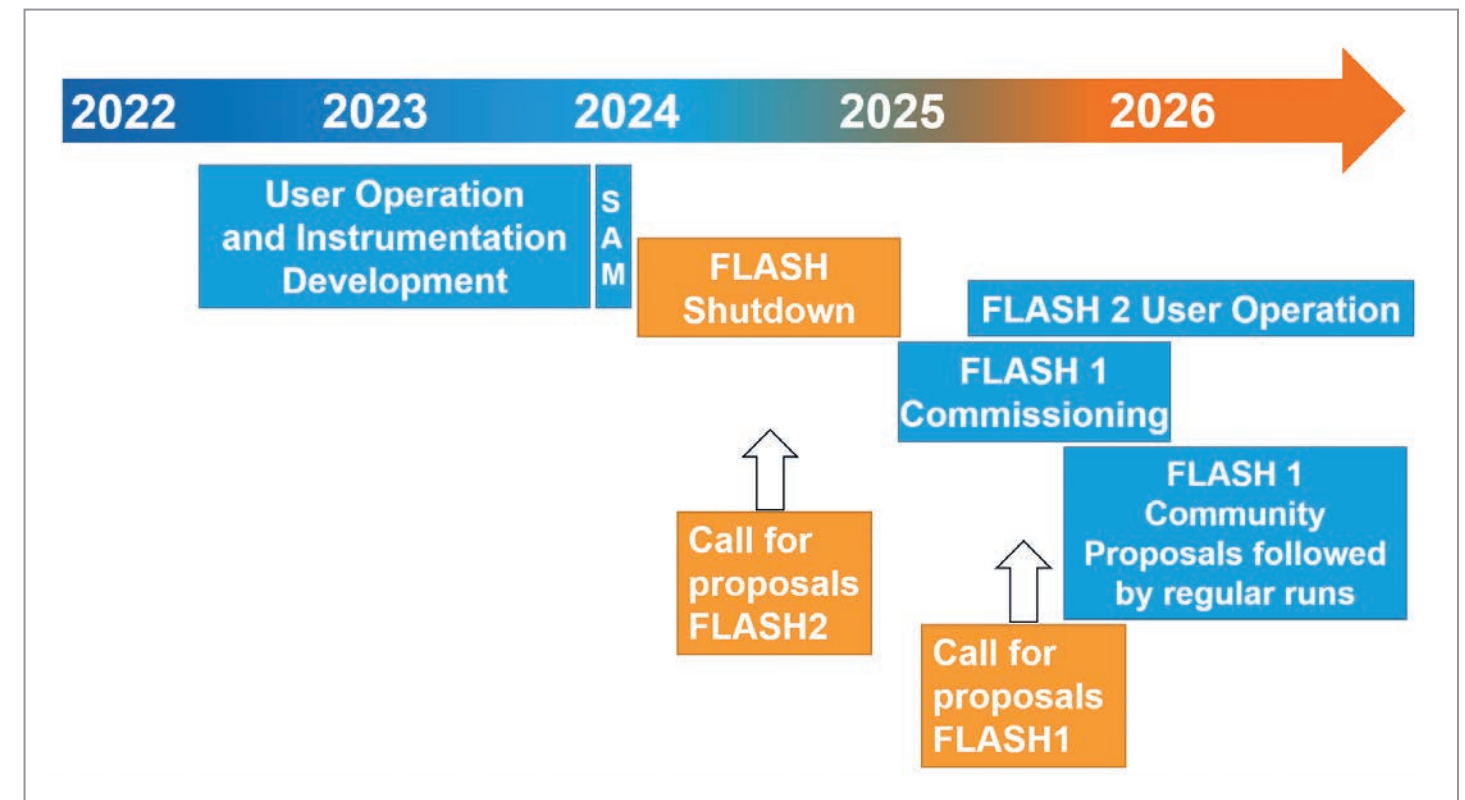


Figure 5
Envisioned timeline of FLASH shutdown and operation periods along with the corresponding calls for proposals.

In the second half of 2024, the operation of FLASH was stopped for the second shutdown of the FLASH2020+ upgrade campaign. Whereas the first upgrade shutdown in 2021/22 was mainly devoted to upgrades in the accelerator part and in the FLASH2 FEL branch, we are now going for a complete makeover of the FLASH1 branch, taking it to the 'next level' in the FEL parameter range. As described in more detail last year, the new FEL line will afterwards house:

- External seeding at MHz repetition rate (during a bunch train) via either high gain or echo-enabled harmonic generation. This is powered by an inhouse-developed seed laser system.
- New APPLE III-type undulators with variable gap and full polarisation control.
- A new photon transport beamline with pulse-resolved photon diagnostics tailored to seeded FEL pulses.
- A fully parallelised accelerator-based THz-generation capability.

The FLASH team already cleared the last 120 m of the FLASH1 tunnel (Fig. 4) to make space for all the new state-of-the-art equipment which will be installed until August 2025.

After the present upgrade shutdown, we will soon restart user operation at the FLASH2 branch. At the end of 2024, we issued a call for proposals related to the corresponding FLASH2 beamtimes in late 2025 and the first half of 2026. The new FLASH1 FEL branch, equipped with external seed-

ing, first needs to be commissioned from the end of 2025 until presumably early 2026. First experiments with the seeded FLASH1 will then be community-driven proposals, and all users are invited to join the process. After these user community experiments, we will continue with proposals running through the regular project review panel (PRP) process for FLASH1 as well. We expect to publish a call for FLASH1 proposals towards the beginning of 2026. This FLASH1 call will then be related to beamtimes from late 2026 on. At that point, FLASH will again be in regular user operation at both ends, with many new features as demanded by our user community. The overall timeline for the next years is sketched in Fig. 5.

Contact (FLASH and FLASH2020+):
Rolf Treusch, rolf.treusch@desy.de
Markus Gühr, markus.guehr@desy.de
Lucas Schaper, lucas.schaper@desy.de

References

1. Benjamin Erk et al., 'CAMP@FLASH - An End-Station for Imaging, Electron- and Ion-Spectroscopy, and Pump-Probe Experiments at the FLASH Free-Electron Laser', *J. Synchrotron Rad.* 25, 1529-1540 (2018).
2. G. Hartmann et al., 'Circular dichroism measurements at an x-ray free-electron laser with polarization control', *Rev. Sci. Instrum.* 87, 083113 (2016).
3. Jan Metje et al., 'URSA-PQ: A Mobile and Flexible Pump-Probe Instrument for Gas Phase Samples at the FLASH Free Electron Laser', *Appl. Sci.* 10, 7882 (2020).
4. B. Marchetti et al., 'Experimental demonstration of novel beam characterization using a polarizable X-band transverse deflection structure', *Sci. Rep.* 11, 3560 (2021).
5. Rosen Ivanov et al., 'Free-electron laser temporal diagnostic beamline FL21 at FLASH', *Opt. Express* 31, 19146-19158 (2023).

PETRA III

User operation and automation of beamlines



Figure 1
View into the PETRA III experimental hall 'Ada Yonath' which hosts five beamlines. (Photo: DESY)

In the year 2024 more than 3400 individual users, including mail-in and remote access, performed experiments at PETRA III beamlines. In total, 25 beamlines, including those operated by EMBL and Hereon, were operational and open for users. Two run periods of PETRA III for user operation were scheduled in 2024. The first period was from 23 February to 31 July, while the second period was from 2 September to 18 December. During the first run 2673 hours of user operation were provided, in the second run 2016 hours, resulting in a total of 4689 hours in 2024. Upon regular calls for proposals, in 2024, users submitted 1111 proposals, thereof 5 Block Allocation Group (BAG) proposals, 5 Long Term Proposals (LTP), 3 Targeted Challenge-Driven proposals (TCD) with focus on 'Molecular Water Science'. In addition, 101 rolling proposals were submitted (details on the new rolling access procedure are described below).

Further 143 proposals, including 76 BAG proposals, have been collected for the EMBL beamlines P12-P14 at PETRA III.

PETRA III – machine operation

In 2024, the overall availability of the PETRA III storage ring for synchrotron radiation users was 89.3% and is therefore significantly below the target value of at least 98%. Two major faults led to a complete loss of a total of 441 hours of user operation. PETRA III operates with two wiggler sections in the West and North of the ring, each equipped with a 6.1 meter-long absorber funnel designed to absorb the radiation power from the wigglers evenly along its length (Fig. 2). The first event was caused by the failure of these absorbers in the damping wiggler sections. In early May, the wiggler absorber in the West had a vacuum leak and was replaced with a spare, resulting in the loss of seven days of user operation. In early June, the absorber in the North showed similar problems. A temporary fix allowed to continue operating at 70% beam current until the service week in July, when the absorber was replaced with the previously repaired one. Both absorbers showed melted copper on the inside (Fig. 2). The main reason is

probably a manufacturing nonconformity of the absorber funnel as its inner dimension was found about 1 mm smaller compared to the original drawings. The second loss of beamtime was caused by a fire of a power supply rack at the pre-accelerator DESY II, causing a loss of 323 hours of user operation in November. The burned power supply rack dates back to the 1980s. Due to the risk of hazardous materials potentially released by the fire, a thorough inspection and risk assessment was conducted by trained personnel in full protective equipment, before cleaning and replacement of destroyed components could be completed.

In addition, as in previous years, a major fraction of beamtime losses were related to power interruptions, overall 12 events, mainly caused by glitches in the public electricity grid. Since DESY has no possibility to compensate sudden power drops yet, by using e.g. batteries or flywheels, power glitches almost always cause a beam dump. The PETRA III storage ring usually is back to operation within 15-45 minutes after such beam dumps, depending on the respective equipment failures caused.

As usual two different bunch filling modes were offered in the PETRA III storage ring: a mode for time-resolved experiments with 40 bunches and a 'multi bunch' mode with 480 bunches, with about equal time shares. This bunch mode distribution has proven to be an optimal scenario to provide a maximum number of 'timing mode' shifts while minimizing the radioactive activation of ring components as well as radiation damage of undulators. However, the two main faults mostly occurred during the 40 bunch mode which modified this ratio to 53.5:46.5.

PETRA III – new access model

At five PETRA III beamlines, a testing procedure of a *Generic Rolling Access* to beamtime for users has been implemented in mid-March 2024. This modification in the user access model has been introduced to address requests from commercial and academic users with urgent need for beamtime but also to allow faster scheduling of beamtime assigned to users via European projects such as NFFA or ReMade@ARI. Under the well-established bi-annual call-based access procedure, there is an average of eight to nine months between the submission of a proposal and the actual beamtime (see Fig. 3). Under the new access model users can apply for beamtime at any time without calls for proposals or deadlines. Proposals submitted under the new scheme are now being reviewed, evaluated and scheduled on a rolling basis. This rolling access procedure significantly reduces the time between submission and experiment. If required, the earliest possible experimental time can be scheduled within two months for academic proposals (after feasibility and scientific review), as illustrated in Fig. 3, or two weeks for commercial access (after feasibility review). This is now the main access route for these beamlines, offering the opportunity for single (up to 21 shifts) or multiple beamtime proposals (up to 72 shifts). The five PETRA III beamlines testing rolling access are the high-resolution diffraction beamline (P08), the *in situ* diffraction and imaging beamline (P23), the high-throughput macromolecular crystallography beamline (P11), the chemical crystallography beamline (P24) and the hard X-ray photoelectron spectroscopy beamline (P22). Supporting laboratories and groups, namely the chemistry laboratories, DESY NanoLab, safety group, DESY Innovation and Tech-

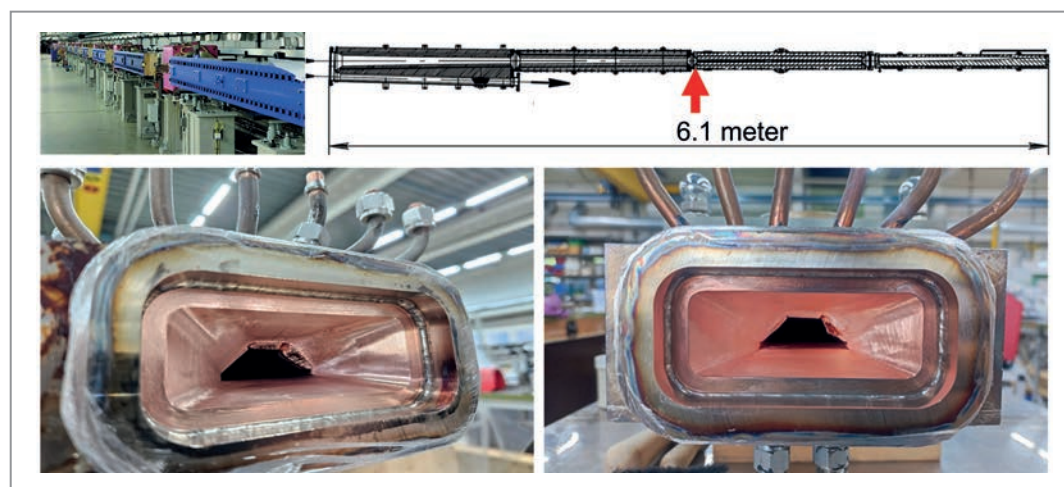


Figure 2
The top panel shows an image of one of the PETRA III wiggler sections and a schematic of the 6.1-meter-long adjacent absorber. The lower panel shows a view in the beam direction to the inside of the two damaged absorbers. (Photo: DESY)

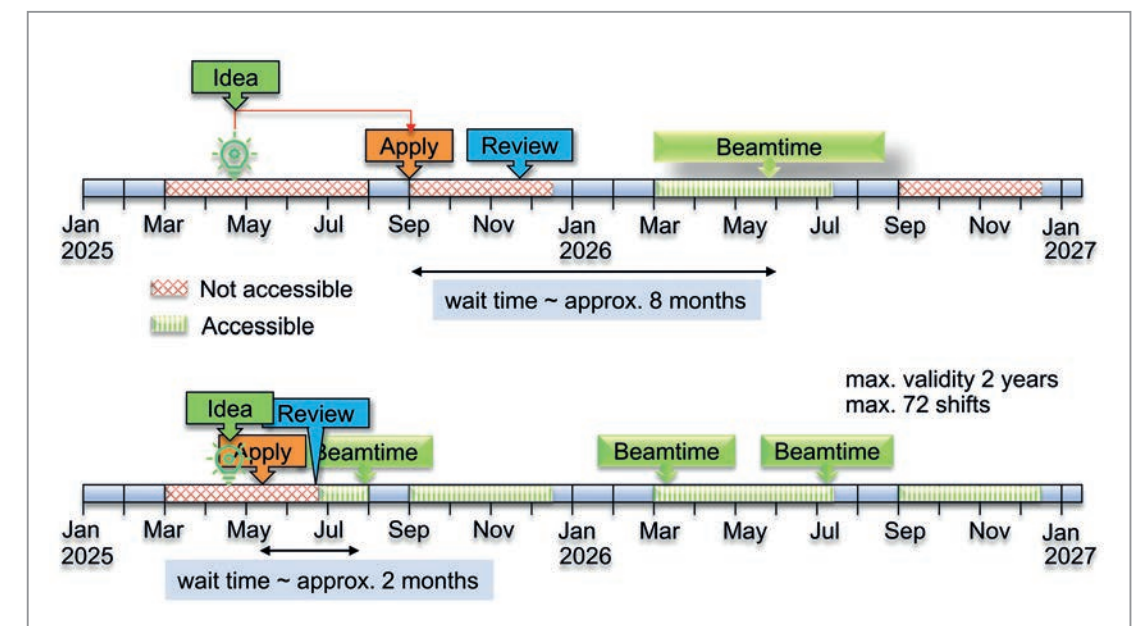


Figure 3
Timelines for proposal submission, review and beamtime for both the bi-annual call-based access (above) and the rolling access (below) at PETRA III. (Credit: DESY)



Figure 4
Universal robot at the PETRA III beamline P65 for sample handling (left), and the automated XAFS setup (right). (Credit: DESY)

nology Transfer group, also contribute to the evaluation and scheduling process on a rolling basis.

This new rolling access model offers advantages over regular call-based access models. These include a simplified proposal submission scheme, enhanced flexibility over longer periods up to two years and multiple accesses through a single proposal. Also, the resubmission of improved proposals, or the application of follow-up beamtimes is facilitated within this scheme. The preliminary response from the reviewers and users who have employed this new access model has been favorable. Through this new access model, some of the rolling beamlines succeed to attract a considerable number of new user groups. We will evaluate the new access procedure in the summer of 2025. If the results are as promising as expected, the new scheme may be permanently implemented and extended to other beamlines.

PETRA III – technical developments and automation

To develop automation procedures in X-ray absorption fine structure (XAFS) applications, the Helmholtz initiative 'Remote, Operando Controlled, Knowledge-driven, and IT-based' ROCK-IT has been started at PETRA III two years back, focusing on PETRA III beamline P65. This PETRA III beamline is specialised for XAFS applications and supports diverse research applications in catalysis, battery science, materials science, biology, environmental and geosciences, many of which align with industrial research needs. In 2024 through this ROCK-IT initiative, a significant progress has been made on the automation of XAFS measurements at the P65 (Fig. 4) using the 'BlueSky' control system and

'Daiquiri' web interface. Through the development of general support for 'Tango' servers to 'Ophyd-Async', the team has established communication with critical devices, such as the undulator, ionisation chambers, double-crystal monochromators, timers, stepper motors and a robot (Fig. 4) for sample handling. For sample management, a camera with AI capabilities now enables QR code reading and automatic detection of samples.

The PETRA III beamline P01 for Nuclear Resonant Scattering (NRS) and (Resonant) Inelastic X-ray Scattering ((R)IXS) for photon energies from 2.5 to 90 keV, is offering a high energy and spatial resolution. The Max-Planck-Gesellschaft (MPG) is contributing to the costs of this beamline and in return can use 40% of the total beamtime. In 2024, a second set of twelve individual X-ray-Raman (XRS) analysers (Fig. 5) has been installed on the spectrometer in the experimental hutch 2, thereby enabling the capture of both low q and high q data during XRS measurements at the same time. This enhances the experimental capabilities for users. Additionally, a new ^{57}Fe synchrotron Mössbauer source has been installed at P01. The source can be combined with the conventional nuclear forward scattering experiment, enabling both time and energy-domain Mössbauer spectroscopy to be measured from the same sample. This combination leverages the unique advantages of both methods, providing a more comprehensive analysis. For the RIXS instrument, the P01 beamline now extended the number of atomic resonance (Sulfur K, Chlorine K, Rhodium $L_{2,3}$ and Uranium $M_{4,5}$ -edges) in addition to the existing Ruthenium $L_{2,3}$ -edges available to users.

The Small-Angle X-ray Scattering Beamline for Materials Research (SAXSMAT) beamline P62, started user operation in 2021 and offers small- or wide-angle X-ray scattering (SAXS/WAXS) techniques (Fig. 6). In 2024, a new multi-modal imaging setup to produce simultaneously SAXS and WAXS Tensor Tomography and X-ray Fluorescence Computed Tomography (XRF-CT), has been successfully developed and commissioned and is now open for users. Another setup of pseudo-SAXS/WAXS-CT is being commis-

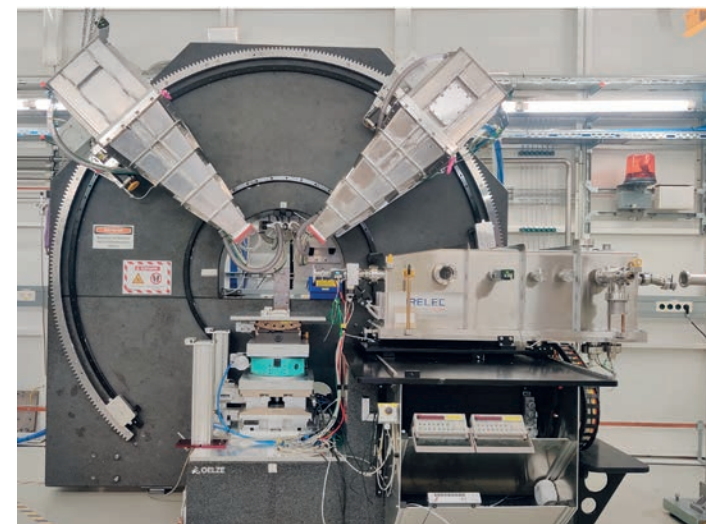


Figure 5
X-ray Raman setup with two sets of 12 bent silicon analysers each in two tanks adjustable in scattering angle at the PETRA III beamline P01. (Credit: DESY)

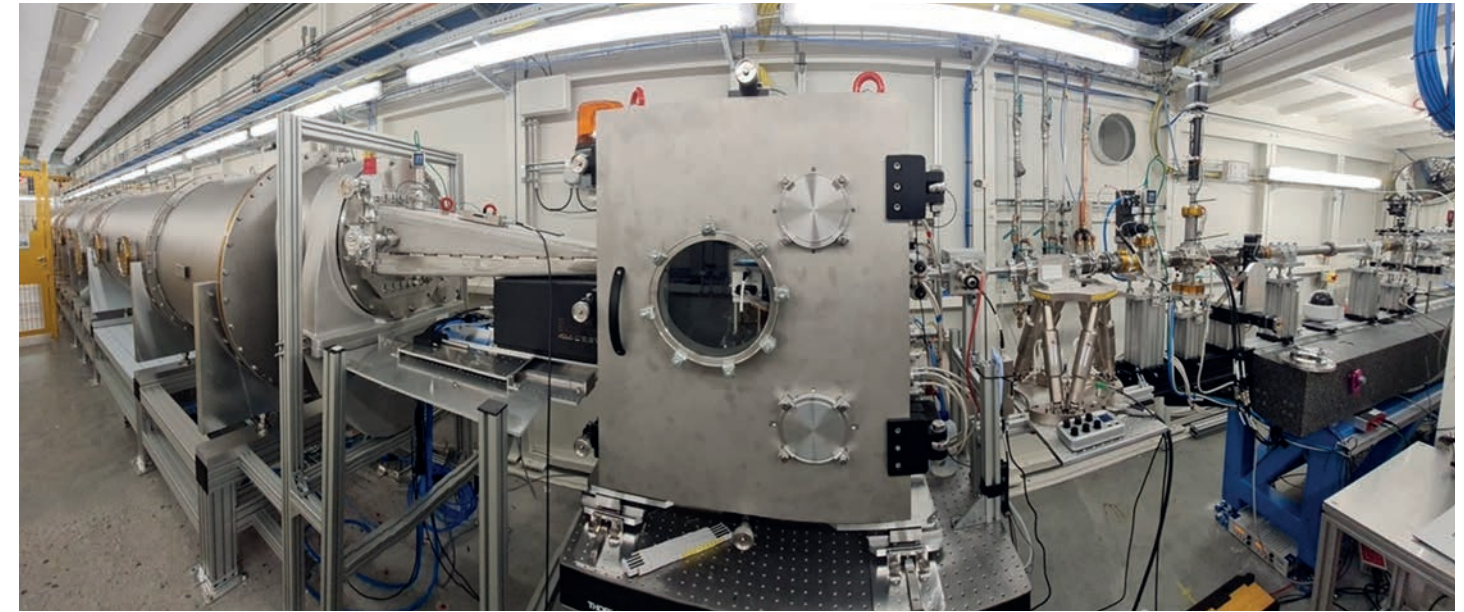


Figure 6
SAXS and WAXS tensor tomography setup at the PETRA III beamline P62. (Credit: DESY)

sioned and has already been successfully applied to investigate brain diseases such as Multiple Sclerosis, Alzheimer's, Parkinson's as well as fibrosis in the heart. This setup will also be available for users in the near future.

The PETRA III beamline P25 is being developed within the frame of an internal cooperation project at DESY with main funding from the Innovation and Technology Transfer (ITT) group. In 2024, the construction of the optics test hutch (for white beam operation), the experimental hutch and the control hutch were successfully completed and the beamline optics and supporting infrastructure are being installed. The experimental hutch is being equipped with fully automated powder diffraction station planned to serve many industrial clients using 'mail-in' operation, where the samples are sent to DESY and the beamline staff carries out the experiment. The hutch also hosts a setup for element-specific X-ray fluorescence microscopy and imaging with focus on biomedical applications in collaboration with the

University Medical Center Hamburg-Eppendorf (UKE) among others. The X-ray beam in the experimental hutch is expected to be available in the second half of 2025.

The support from the chemical, biological and sample preparation laboratories is an integral component of the academic and industrial user operations conducted at PETRA III. In 2024, an additional glove box (Fig. 7) was installed at the chemistry laboratory in the PETRA III experimental hall 'Ada Yonath' in order to accommodate the growing demand from especially from the community performing battery research. Additionally, an atomic force microscopy instrument (Fig. 7) has been installed in the PETRA III experimental hall 'Max von Laue' and is now operational.

Contact: Oliver Seeck, oliver.seeck@desy.de
Hans-Christian Wille, hans.christian.wille@desy.de
Arka Bikash Dey, arka.bikash.dey@desy.de



Figure 7
The new glove box in the chemistry laboratory in the PETRA III experimental hall 'Ada Yonath' (left) and the new atomic force microscopy instrument (Park SmartScan) in the experimental hall 'Max von Laue' (right). (Credit: DESY)

PETRA IV – The ultimate 4D-X-Ray microscope

Proposal submitted for the national prioritisation process for large-scale scientific infrastructures

PETRA IV is the planned ultra-low-emittance upgrade of the existing PETRA III storage ring. DESY's flagship project will deliver the brightest synchrotron light source in the world. Academic and industrial users will benefit from the enormous increase in coherent X-ray photon flux, the planned cutting-edge beamlines, the novel experimental possibilities and the new business model in preparation for the facility. It will provide easy on-demand access, extended services and support for non-expert synchrotron radiation users, especially for the processing and analysis of their data. PETRA IV will be a cornerstone of the Science City Hamburg Bahrenfeld and a central element of DESY's vision of a data- and information-driven solution ecosystem for academia and industry.

The main activities in 2024 were focused on the compilation of the proposal for the prioritisation process of large-scale scientific infrastructures (FIS) of the German Federal Ministry of Education and Research (BMBF) for PETRA IV, the preparation of draft conceptual design reports for all PETRA IV beamlines and the kick-off of the PETRA IV Preparation Project.

With the budget law passed in February 2024, 40 Mio. Euro were earmarked for the preparatory work for PETRA IV. The Authority for Science, Research, Equality and Districts (BWFG) of Hamburg granted an additional 4.4 Mio. Euro, so that DESY can spend 44.4 Mio. Euro in total for the three different pillars of the PETRA IV Preparation Project.

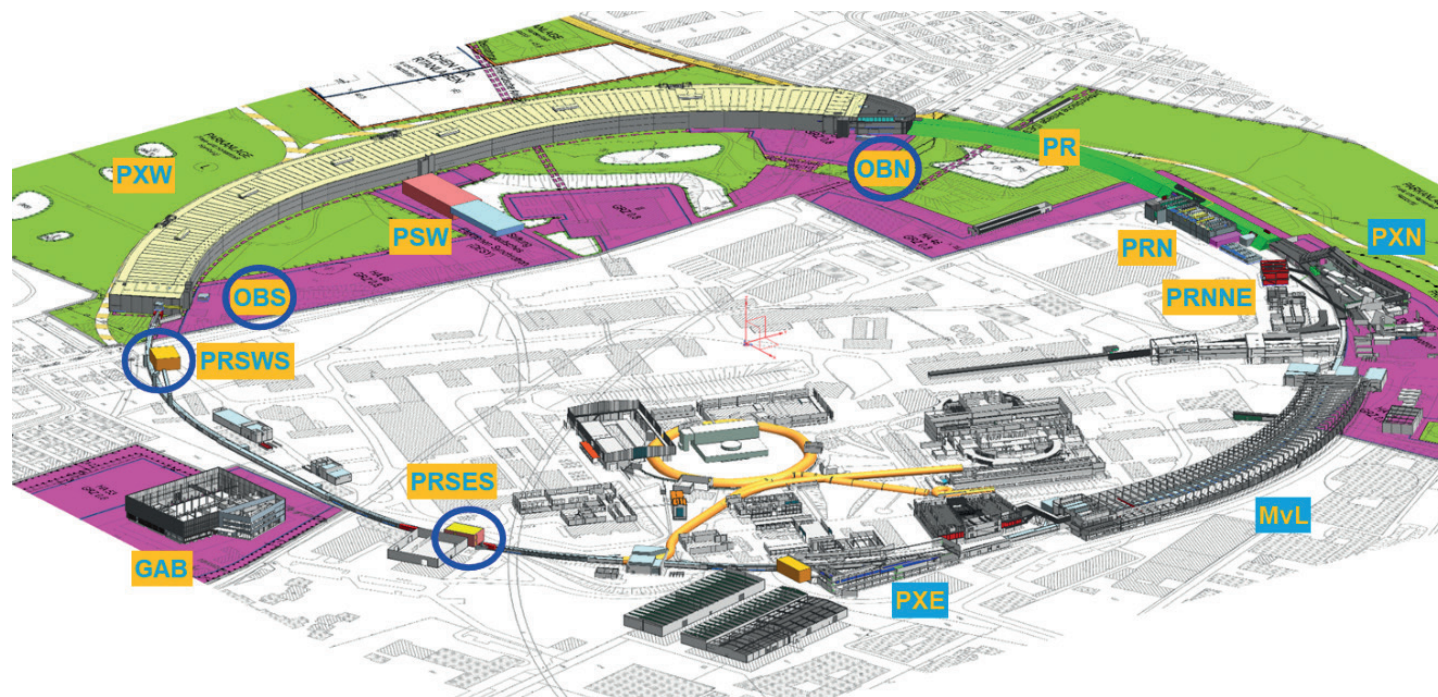


Figure 1
3D CAD model of the PETRA IV complex including existing PETRA III experimental halls 'Paul Ewald' (PXN), 'Max-von-Laue' (MvL) and 'Ada Yonath' (PXE) as well as new buildings (abbreviations PRNNE, PRN, PR, PXW, PSW, GAB show their place on the DESY campus in the figure). The buildings circled in blue (OBN, OBS, PRSWS, PRSES) are next in line for the preliminary CAD design. (Credit: DESY)

Pillar 1 will support two main activities: The first main activity covers the planning steps for the infrastructure for PETRA IV with focus mainly on the western and northern section of the PETRA complex on the Bahrenfeld campus (see Fig. 1). This area includes the new 550 m long PETRA Experimental Hall West (PXW), together with its office, laboratory and media supply buildings, the newly planned building for the RF system (PRN) of the electron storage ring in the long straight section in the North, and the renewal of the tunnel section (PR) between the PXW hall and the RF building North. In this context, the digitisation of civil construction and technical infrastructure planning will be advanced with the introduction of the 'Building Information Modelling' (BIM) methodology at DESY. The second main activity is the completion of the PETRA IV prototyping programme for the PETRA IV accelerators to ensure readiness for the immediate start of the execution of the main project once project approval is received.

Pillar 2 will advance the development of a full-energy (6 GeV) Laser-Plasma Accelerator (LPA) injector for the PETRA IV electron storage ring. Within the PETRA IV Preparation Project, two stages are foreseen. In stage one, a 450 MeV LPA will be built to inject electron bunches into the existing

DESY II booster synchrotron which serves as pre-accelerator for PETRA III. Stage two should deliver a 6 GeV LPA as proof-of-concept for a full-energy LPA injector. This includes an extension of the existing laser laboratory to accommodate the high-power laser required to accelerate electron bunches to the final kinetic energy of 6 GeV in a single step.

Pillar 3 is dedicated to important and necessary transformation measures in order to be prepared for PETRA IV once the project has been approved. These include changes in the internal organisation of DESY and user operation. These transformation measures are divided into four key projects: The digitisation of administrative processes at DESY, from personnel management to procurement. This modernisation is intended to simplify and streamline administrative processes. The development of new access modalities and extended services for users from science and industry in order to make PETRA more attractive for application-oriented users and non-X-ray experts. The broadening and expansion of the user community by joint business field developments between pilot partners from industry and DESY, complemented by the establishment of a start-up culture. Generative artificial intelligence tools will be established and prepared for their implementation for different applications at DESY and PETRA IV.

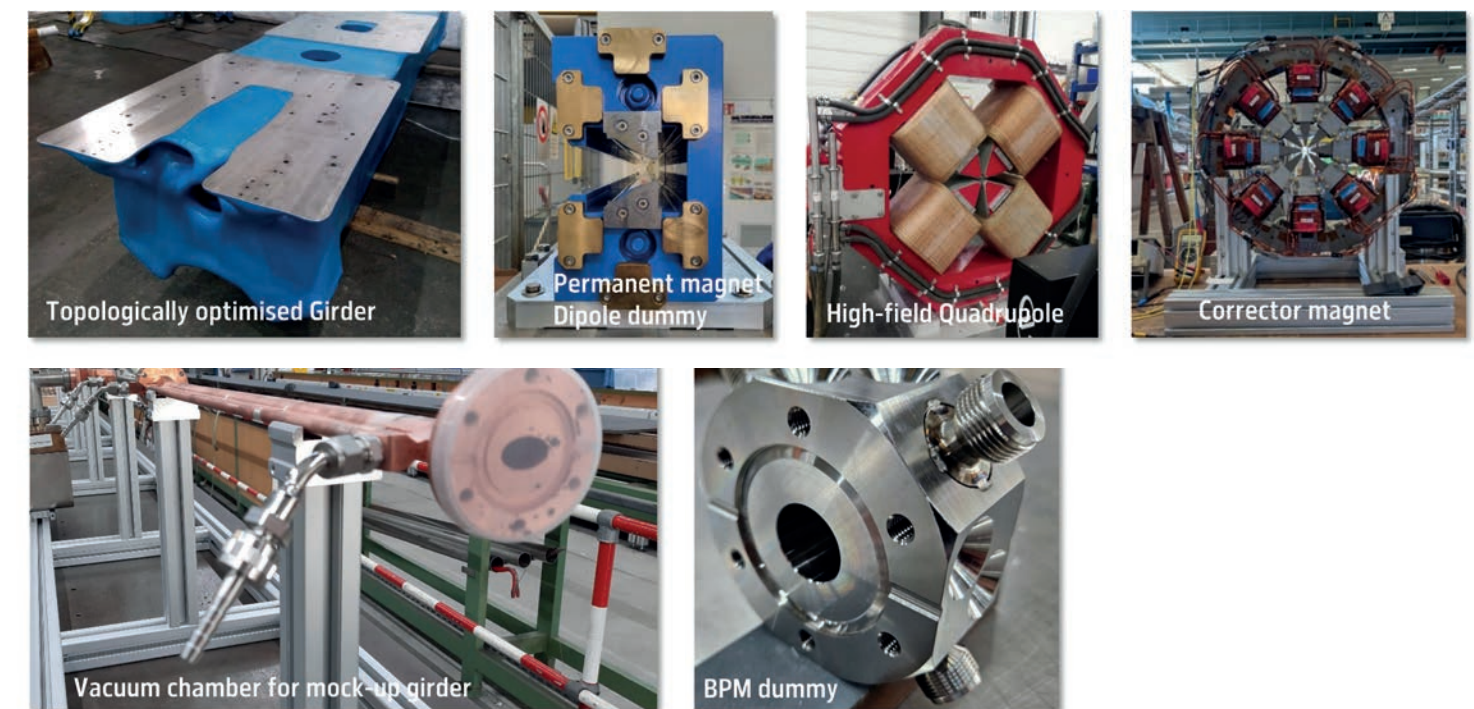


Figure 2
Collection of available prototypes of the beam transport technology for the PETRA IV storage ring. (Credit: DESY)

Pre-planning for the PETRA IV infrastructure has advanced significantly with the inhouse development of 3D CAD models for most of the buildings of the PETRA IV complex, which facilitates optimal use of space for the technical infrastructure, the accelerators and the experimental facilities (beamlines and laboratories). An overview of the current layout of the complex is shown in Fig. 1. The team has also started to advance elements of the execution planning to be able to further solidify the estimates for the duration of the long shutdown of PETRA. The results of these estimations have led the team to increase the targeted duration of the shutdown to 2.5 years owing to the massive amount of construction work to be executed during the shutdown (civil construction and installation of technical infrastructure mainly in the new experimental hall PXW).

With the PETRA IV Preparation Project, the prototyping programme initiated during the Technical Design phase will be extended and concluded by the end of 2026 (for some examples, see Fig. 2). The remaining technical risks are addressed to ensure readiness for the start of the call for tender in the execution phase of the project. The programme includes the completion of the magnets prototypes

with a high-gradient short quadrupole and a combined function dipole based on permanent magnets (DLQ). A higher harmonic RF system for bunch lengthening will be further developed, including an alternative prototype of the 1.5 GHz cavity and the corresponding solid-state amplifiers. Components for the Fast Orbit Feedback System will be finalised to ensure sub- μm stability of the electron beam at the source point of the undulators. These include the development of the electronics for the beam position monitors and fast corrector magnets. Sophisticated diagnostics to measure the characteristics of the ultra-low emittance electron beam will be developed. Other key deliverables include a damping wiggler, vibration-free nanostages for the future beamlines and lenses for nanobeam experiments. In 2024, the delivery of a complete assembled PETRA IV storage ring girder including the magnets, the vacuum chambers and beam diagnostics has been achieved.

Another major step forward has been the preparation of the draft Conceptual Design Reports (CDR) for all 31 PETRA IV beamlines, which are now under internal evaluation. The CDRs for the Phase I beamlines will be completed by March 2025 and those for the Phase II beamlines by April

2025. These documents will form the basis for the beamline TDR phase which will start as soon as the PETRA IV project is approved. In March 2025, the Phase I beamline CDRs will be reviewed by the PETRA IV project's Beamline Technical Advisory Committee (TAC). In 2024, many key developments have been advanced, such as the generic front-end design, the SPIDER nano-station (see Fig. 3), high-quality diamond compound refractive lenses (CRLs) and aberration-compensated lens cubes (see Fig. 4) and the TEMPUS and CoRDIA detector programme, including CZT (cadmium zinc telluride) sensors for high-flux hard X-ray detection.

In July 2024, the BMBF issued a call for proposals for a prioritisation exercise for large-scale scientific infrastructures (FIS), a shortlist of potential projects will be announced/published in summer 2025 by the BMBF. Applicants were asked to prepare a 30-page document, complemented by 11 different appendices, until 25 October 2024 as input for the evaluation of the planned new facility in three categories: the scientific relevance of the new facility, the potential of the new facility for innovation and transfer and the assessment of costs and risks over the full lifecycle of the facility (construction, operation, decommissioning) including aspects such as sustainability.

In August and September, the project team compiled the text, figures and tables for the proposal and conducted a full lifecycle assessment of the PETRA IV project over a 40-year time span with the full support of the DESY infrastructure groups. The documents were submitted in October and confirmation was received in November that all formal requirements set by the BMBF have been met. The proposal is now staged for the evaluation process scheduled from November 2024 to June 2025. No further feedback on the status of the draft proposal will be given until the final publication of the short list with the prioritised large-scale scientific infrastructures.

With the three main activities in 2024, the submission of the proposal for the prioritisation process for large-scale scientific infrastructures, the preparation of the beamline conceptual designs, and the kick-off of the PETRA IV preparation project, the project team reached several important strategic goals on the way to project approval for the PETRA IV main project. DESY and the project team will be ready for the implementation of PETRA IV as soon as the green light is given.

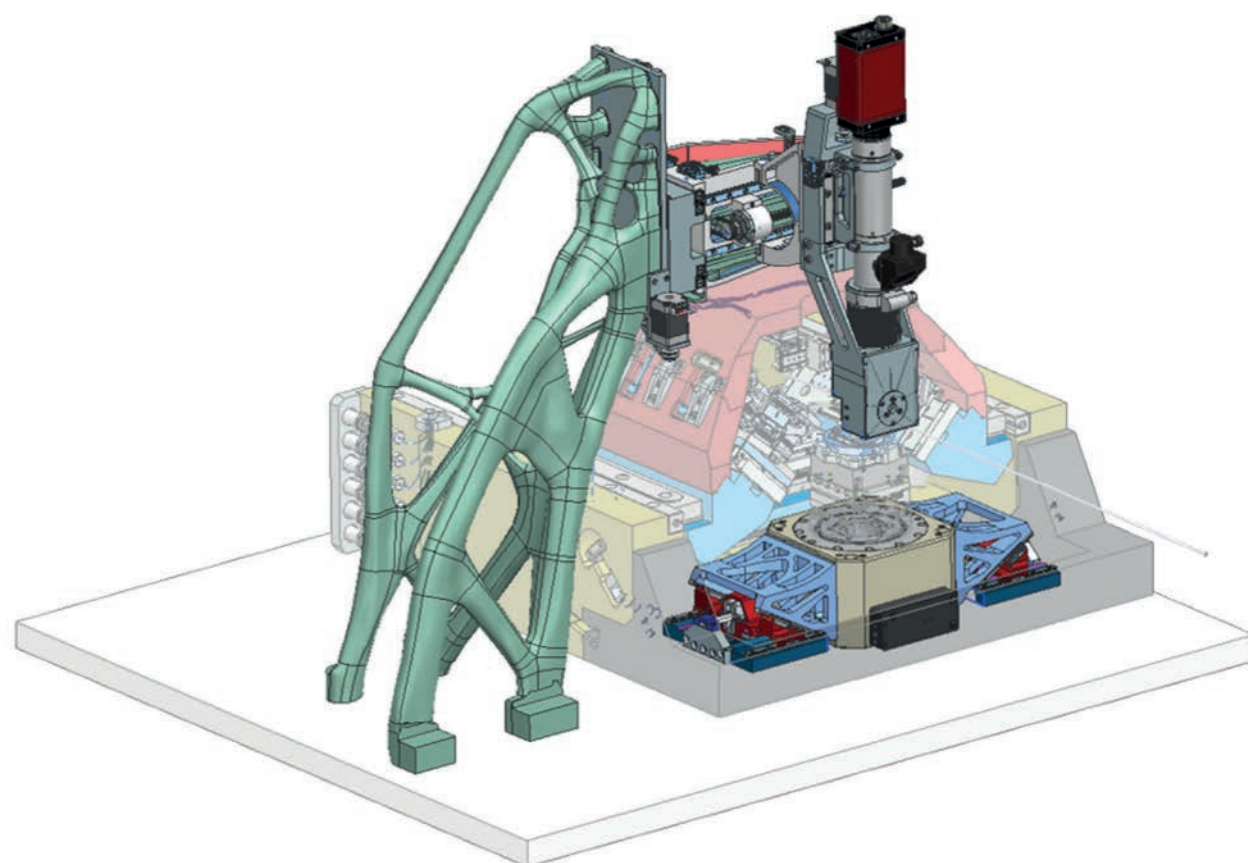


Figure 3
SPIDER nano-station for experiments with ultra-high spatial resolution. (Credit: DESY)

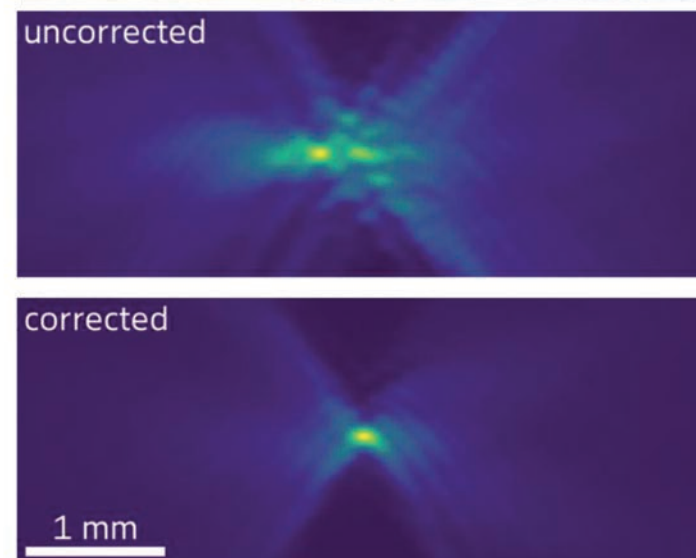


Figure 4
Aberration-compensated lens cubes with diamond lenses and integrated phase plates. The top figure shows the lens cubes implemented in the P06 PtyNAMI end-station. The lower figures show the beam caustics with and without phase plate correction. (Credit: DESY)

Contact: Harald Reichert, harald.reichert@desy.de
Riccardo Bartolini, riccardo.bartolini@desy.de
Karolin Baev, karolin.baev@desy.de
Selina Storm, selina.storm@desy.de
Kai Bagschik, kai.bagschik@desy.de
Stephan Klumpp, stephan.klumpp@desy.de

The European Molecular Biology Laboratory Hamburg Unit

Research and infrastructures for applications in the life sciences

The European Molecular Biology Laboratory (EMBL) unit in Hamburg provides access to three beamlines at PETRA III and to a sample preparation and characterisation (SPC) facility for users from academia and industry. Training is also offered. EMBL Hamburg carries out research with a focus on infection biology using structural biology and imaging tools at various scales. During the reporting period, EMBL Hamburg served 712 individual users at its facilities. External access to EMBL's facilities is supported by several European consortia: INSTRUCT, iNEXT-Discovery (until 2024), MOSBRI, ISIDORE and canSERV.

EMBL's sample preparation and characterisation (SPC) facility provides a high-throughput pipeline for optimising and characterising biological samples, tailored for structural and biophysical studies. The state-of-the-art crystallography and biophysics platforms have supported more than 160 users with latest technologies and expert staff, all in one location. A new Monolith MicroScale Thermophoresis has been added to the facility's portfolio. This technology enables the measurement of protein interactions in the picomolar range. Additionally, a new module 'ChiraKit' has been integrated into the eSPC Online Data Analysis Platform for analysing biomolecular conformation, unfolding parameters, spectral decomposition and secondary structure content.

Beamline P12 for biological small-angle X-ray scattering (BioSAXS) is specialised in studying biological macromolecules and biocomposites in solution, offering detailed insights into their structure and behaviour. This includes time-resolved studies of molecular dynamics and screening of environmental conditions, such as pH, salt or ligand concentration, providing deeper insights into their functional mechanisms.



Figure 1

Setting up the stopped-flow device for time-resolved SAXS experiments at the EMBL Hamburg beamline P12 at PETRA III. (Credit: Massimo Del Prete/EMBL)

A key improvement has been the integration of a new stopped-flow mixing device (μ SFM, Biologic), which significantly reduces the volume of biological samples required—previously a limiting factor—while maintaining experimental precision.

Our enhanced user support allows characterising samples and optimising their quality several weeks before their time-resolved beamtime to ensure more accurate predictions of experimental outcomes. Complementary techniques such as UV/VIS absorption and fluorescence spectroscopy can be applied in combination with the stopped-flow mixing device to track kinetics and optimise conditions.

These innovations have significantly broadened the beamline's research scope, providing users with a more versatile and informed experimental platform for investigating biological systems.

Beamlines P13 and P14 for macromolecular crystallography (MX) continue providing unique atomic-resolution structural information to a broad range of interdisciplinary studies, in academic, e.g. [1,2] as well as in an industrial setting [3]. While P13 is fully focused on high-throughput MX, P14 in 2024 has shared about 50% of its capacity with T-REXX and High Throughput Tomography (HiTT) imaging experiments (see below). Along with the standard high-throughput MX, P14 supports unique applications, requiring micro-beam, as e.g. for *in cellulo* and *in situ* serial crystallography [4], and high-energy photon applications combined with advanced data collection techniques [5] for ultra-high resolution studies in chemical enzymology.

As, with respect to 2023, the demand for MX beamtime significantly increased both for academic (over 20%) and industrial (over 100%) applications, the beamtime scheduling was adjusted to accommodate two user groups per day

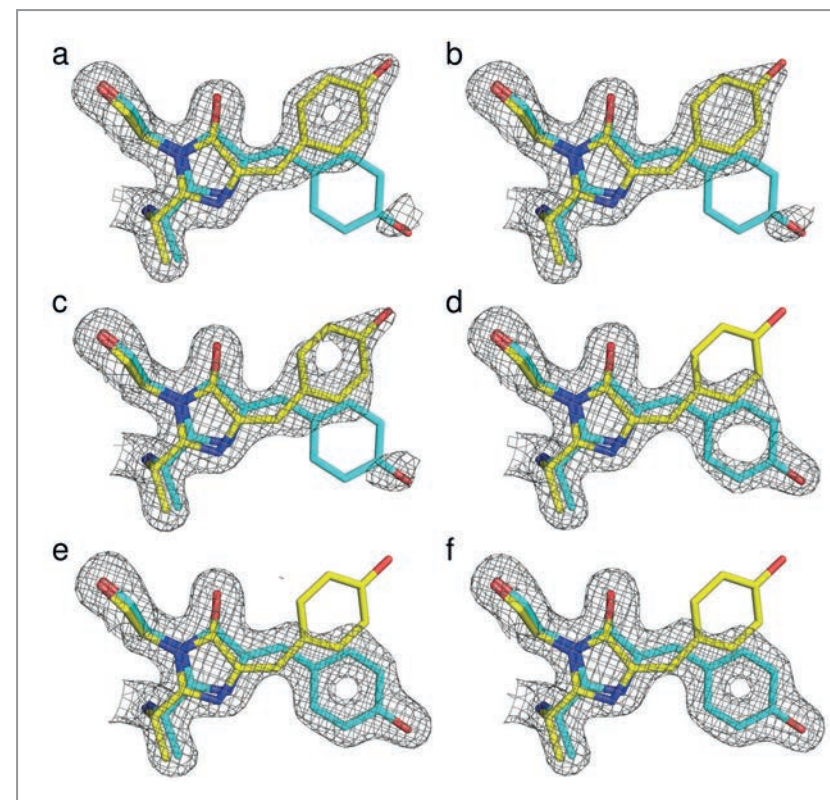


Figure 2

With increasing power of a 405 nm laser illuminating the crystal, the electron density (grey mesh) of the chromophore of the photo-switchable fluorescent protein rsKiir0 transitions from the trans (yellow) to the cis (cyan) conformation (a-f). (Figure from [6] published under CC-BY 4.0)

per beamline. An automated cryogenic sample-delivery-handling facility ('dewar hotel') acquired and installed in collaboration with DESY Photon Science (beamline P11) in 2023 allows much more efficient sample logistics.

The T-REXX end station of the P14 beamline

is dedicated to time-resolved serial macromolecular crystallography. A sophisticated setup employing excitation of crystals by two lasers of different wavelengths enabled studying the photoisomerisation of the reversibly switchable fluorescent protein rsKiir0 [6]; a possible repair-mechanism for a damaged human eye lens protein by illumination with UV light has been observed in crystals of gamma-D crystallin [7]. Different chip systems for presenting crystals have been evaluated in terms of usability in time-resolved crystallography experiments [8].

X-ray imaging at P14 beamline

In 2023, EMBL Hamburg issued its first call for proposals for X-ray imaging of biological samples on P14. Fourteen proposals were awarded beamtime in 2024 and covered samples ranging from plankton to mosquitos and scaffolds to tissue biopsies. All of the users took advantage of the pipeline established by the Duke team for HiTT (Fig. 3) [9].

Change in leadership

In 2024, Thomas R. Schneider was appointed as the Interim

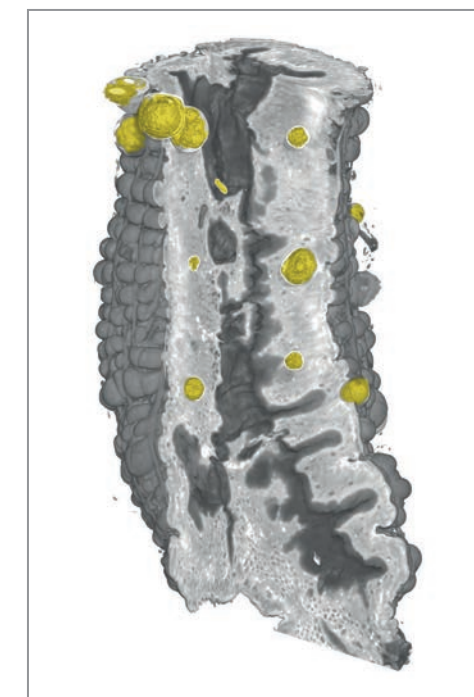


Figure 3

3D-rendering of an HiTT data set of an osmium-stained and resin-embedded mid-gut of an *Anopheles stephensi* mosquito which was infected with *Plasmodium berghei*. Oocysts formed by the parasites are segmented and visualised in yellow. (Figure from [9] published under CC-BY 4.0)

Head of EMBL Hamburg, succeeding Matthias Wilmanns, who had served as Head of EMBL Hamburg since 1997. During Wilmanns' tenure, the critical transition from DORIS III to PETRA III took place, accompanied by an expansion of research activities in integrated structural biology at EMBL Hamburg.

Training

EMBL Hamburg hosted the EMBO Practical Course 'Membrane protein expression, purification, and characterisation 3 (mPEPC3)', the EMBO Workshop 'Computational structural biology' and the EMBL Course 'Solution scattering from biological macromolecules'.

Contact: Dorota Badowska, dorota.badowska@embl-hamburg.de
Thomas R. Schneider, thomas.schneider@embl-hamburg.de

References

1. F.L. Sendker et al., *Nature* 628, 894–900 (2024).
2. G. Tamulaitiene et al., *Nature* 627, 431–436 (2024).
3. J. B. Ingraham et al., *Nature* 623, 1070–1078 (2023).
4. R. Schönherr et al., *Nat. Commun.* 15, 1709 (2024).
5. T. Donath et al., *J. Synchrotron Rad.* 30, 723–738 (2023).
6. J. M. Baxter et al., *J. Am. Chem. Soc.* 146, 16394–16403 (2024).
7. J. A. Hill et al., *Commun. Chem.* 7, 81 (2024).
8. R. Bosman et al., *Cell Rep. Phys. Sci.* 5, 101987 (2024).
9. J. Albers et al., *J. Synchrotron Rad.* 31, 186–194 (2024).

Hereon – the GEMS branch at PETRA III

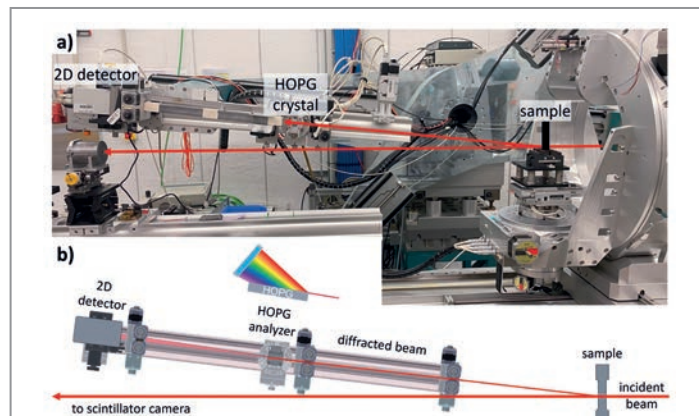
Diffraction and imaging techniques at our beamlines and instruments optimised for the needs of materials research

The Helmholtz-Zentrum Hereon operates the German Engineering Materials Science Centre (GEMS). The experimental stations of GEMS at PETRA III are being continuously developed and upgraded for engineering materials and bio-materials science users from institutions in Germany, Europe and around the world. The design and specifications of the successor beamlines at PETRA IV are currently being developed in order to meet future user demands for cutting-edge instrumentation optimised for materials science.

Diffraction

The High-Energy Materials Science (HEMS) beamline P07 at PETRA III has again seen an intense use of conical slits for residual stress analysis in 2024. They enable a spatial resolution along the photon beam and thus a 3D spatial resolution in thick samples. This led to starting a development of an experiment platform for conical slits that enable a fast setup at different experiment stations by combining all positioning devices for both, slits and sample, on one platform. This will be extremely useful to offer measurements to industrial customers on short notice, as setup times for the experiment are minimised. The sample environment for *in situ* experiments on laser powder bed fusion for additive manufacturing, which is a modified commercial machine, is now available, and first *in situ* experiments are planned for 2025. More and more users at P07 have started using the Pydidas software developed by Hereon [1] for the analysis of diffraction data. The concept of easy use with a graphic user interface for beginners while maintaining access to all functionalities via scripts seems to work, as there has been a lot of positive feedback.

The engineering materials station P61A of the white-beam beamline P61 had its first beamline review in spring 2024



with excellent feedback and a clear recommendation to continue with a white-beam beamline at PETRA IV. Further developments at P61A will follow the reviewers' recommendations. More high-speed radiography experiments (with frame rates up to 25 kHz) using the *in situ* Electron Beam Melting (EBM) additive manufacturing setup [2] were carried out in 2024 (see also the Science Highlights section of this report). Following one of the reviewers' recommendations, a development for simultaneous diffraction and radiography measurements was started; the first test setup is shown in Fig. 1. A Highly Oriented Pyrolytic Graphite (HOPG) crystal is used as an analyser for the diffracted beam that reflects different photon energies into different directions. In this way, the energy spectrum of the diffracted beam is transformed into a divergent beam that is detected with an area detector. Although the detector itself lacks energy resolution, the energy distribution can be reconstructed from the spatial information in the detector image. The test enabled frame rates of 500 Hz; after optimisation of the setup, frame rates of several kHz are expected to be possible for diffraction. In a recent user experiment at P61A, energy-dispersive diffraction was carried out with a 10 μm -wide beam, enabling a 10 μm spatial resolution on scan lines in a 25 mm thick steel sample. This example demonstrates the potential of the white beam for engineering applications.

Imaging

The X-ray imaging branch of GEMS maintains instruments at PETRA III beamlines P03, P05 and P07, all of which are optimised for *in situ/operando* studies with both, full-field and scanning imaging techniques. These capabilities are

Figure 1

Test setup for simultaneous diffraction and radiography at P61A. a) Setup with 2D detector mounted on the diffractometer arm. b) Sketch of the setup that uses a HOPG mosaic crystal as an analyser for the photon energy. The radiography camera is not included in these pictures. (Credit: G. Abreu Faria, Hereon)

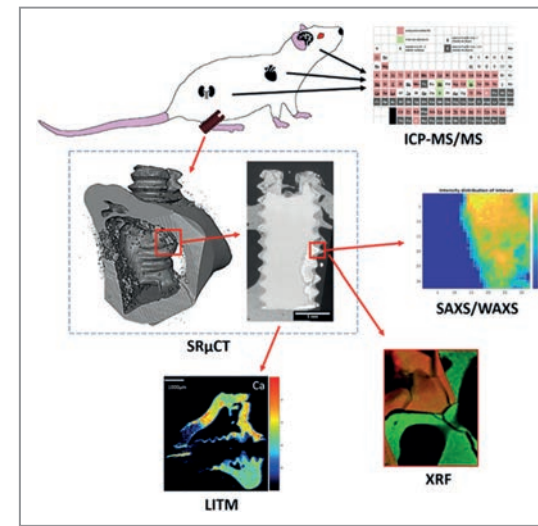


Figure 2

Scheme of the multi-modal magnesium implant study. Screws were implanted in the diaphysis of the rat's tibia. ICP-MS/MS: determination of element concentration in organs, SR μ CT: tomography volume rendering of a screw surrounded by bone and a cross-section slice, SAXS/WAXS: scanning nano-diffraction map of the (002) hydroxyapatite reflex, XRF: X-ray fluorescence map where green stands for bone and red stands for degradation layer, LITM: laser ablation time-of-flight mass spectrometry for high sensitivity element distribution analysis. (Figure from original publication [4]).

valued in materials science but are also broadly utilised in life science applications. Our range of continuously enhanced techniques offers a unique combination of high X-ray energies, ample space for sample environments, advanced phase contrast techniques and a wide range of spatial resolutions.

In the framework of a doctoral thesis a new method was developed at the P05 nano-CT station and published in *Optica* [3]. This development makes sub-resolution features visible which are not accessible with standard full-field transmission X-ray microscopy (TXM) and takes darkfield imaging, common in micro-CT, into the nano regime. Unlike classical full-field TXM, this method offers the possibility to capture only the scattered X-ray light and simultaneously block the transmitted signal from the sample. This way, it improves the detection of scattering nanostructures like small cracks, oriented nanoparticles as well as defects in materials which would not be visible in attenuation contrast. The method can be easily integrated into existing TXMs by adding motorised apertures and is described in greater detail in the Research Highlights section of this report.

Another in-house research example on magnesium implants demonstrates the added value of combining multiple imaging modalities [4]. The multimodal analysis of Mg-Gd alloys confirms their suitability as implant material through the combination of scanning nanodiffraction at P03 and microtomography at the beamlines P05 and P07

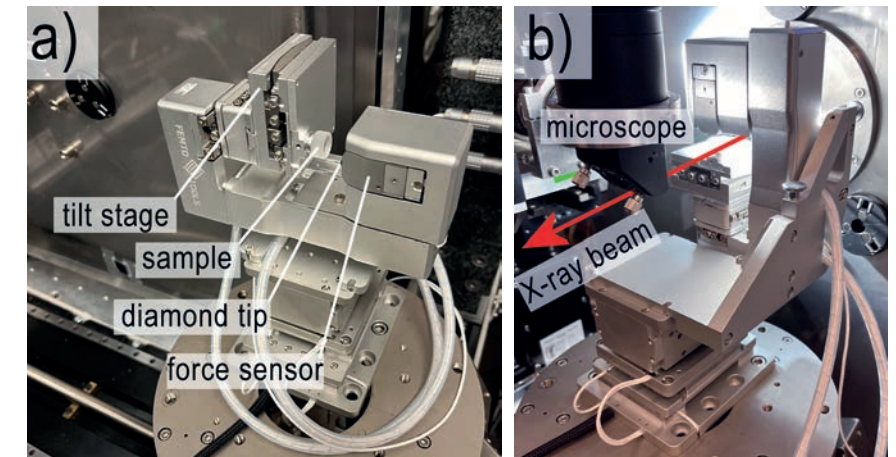


Figure 3

a) New nanoindenter installed at the Nanofocus Endstation of PETRA III beamline for synchronised micromechanical studies with *in situ* scanning X-ray nanodiffraction. b) The nanoindenter can be used in a vertical or horizontal mounting position (Credit: A. Davydok, Hereon)

along with X-ray fluorescence and light microscopy data from other instruments, as schematically shown in Fig. 2. The study detected no traceable Gd in the bone around the implant, no effect of the Mg-Gd degradation on the hydroxyapatite structure around implants and found Mg to be homogeneously distributed among the organs with a slightly lower concentration in liver and brain.

A further noteworthy technical development is the implementation of a newly designed nanoindenter at the P03 Nanofocus Endstation, as shown in Fig. 3. A commercially available nanoindenter (Femtools FT-NMT04) has been mechanically extended with an additional tilt-stage to support wedge-type indenter tips. At the same time the control software has been modified to enable a precise synchronisation between the nanoindentation process and the nanodiffraction data acquisition at the beamline. This new device complements our existing, self-built nanoindenter and enables complex, automated micromechanical test protocols under controlled strain-rate conditions. If required, the nanoindenter can be transferred into our FIB/SEM (Tescan Amber X) to perform micromechanical tests under the electron microscope. In addition, our suite of supporting laboratory instrumentation has recently been complemented by a new, large-volume X-ray micro-CT machine (RX Solutions, Easytom XL) which was put into operation at the beginning of 2024 and is now also available to our users.

Contact: Christina Krywka, christina.krywka@hereon.de
Peter Staron, peter.staron@hereon.de
Martin Müller, martin.mueller@hereon.de

References

1. M. Storm et al., <https://pydidas.hereon.de>
2. J. Ye et al., *J. Manuf. Mater. Process* 8, 103 (2024).
3. S. Wirtensohn et al., *Optica* 11, 852-859 (2024).
4. K. Iskhakova et al., *Bioact. Mater.* 41, 657-671 (2024).

The DESY NanoLab offers on-site methods for nanoscience that complement techniques and experiments at the DESY light sources and the European XFEL, including nanocharacterisation, nanostructuring and nanosynthesis techniques for investigation of atomic scale structure, chemical composition and magnetism.

The DESY NanoLab is providing high-level user support in its labs at the Centre for X-ray and Nanoscience (CXNS) for internal and external users and adjoining buildings which host its Scanning Auger Electron microscopy lab with chemical resolution at the nanoscale, X-ray labs and the DESY NanoLab's electrochemistry lab. Access is also offered to e-beam lithography in cooperation with the Centre for Hybrid Nanostructures (CHyN) of the University of Hamburg. A further specific offer for users is the 'nanotransfer protocol' that assists in the re-localisation of preselected microscopic regions of interest in focussed PETRA III X-rays.

The diverse dedicated instrumentation at the DESY NanoLab has already proven fruitful. An international research team led by DESY NanoLab scientists observed how the whitening agent titanium dioxide inactivates

viruses. Using atomic force microscopy at the DESY NanoLab and complementary measurements at the synchrotron light source PETRA III, the research team was able to decipher the exact process that takes place on the surface of the titanium dioxide.

The researchers used virus-like particles (VLPs) for their investigations on the photocatalytic inactivation capabilities which mimic real SARS-CoV-2 viruses but lack genetic materials. While the structure of the virus remained intact under nitrogen atmosphere and in the dark, the VLPs on the titanium dioxide surface were denatured and went under morphological changes as soon as ultraviolet (UV) light hit the sample in air. The air acts as a source of oxygen. The UV light triggers an oxidation process in the amino acid blocks of the VLP's protein which is facilitated by the titanium dioxide as a photocatalyst. This increases

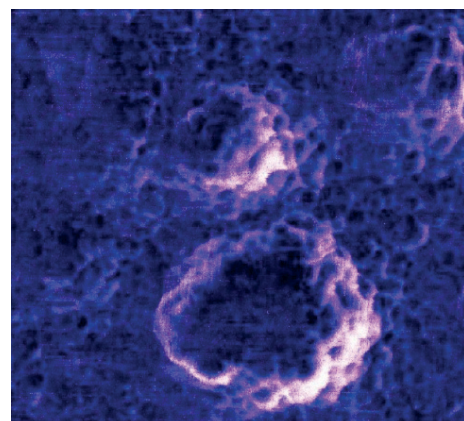


Figure 1
Atomic force microscopy shows the virus morphology (spherical particles in image) and the spike proteins.
(Credit: DESY NanoLab, Mona Kohantorabi)

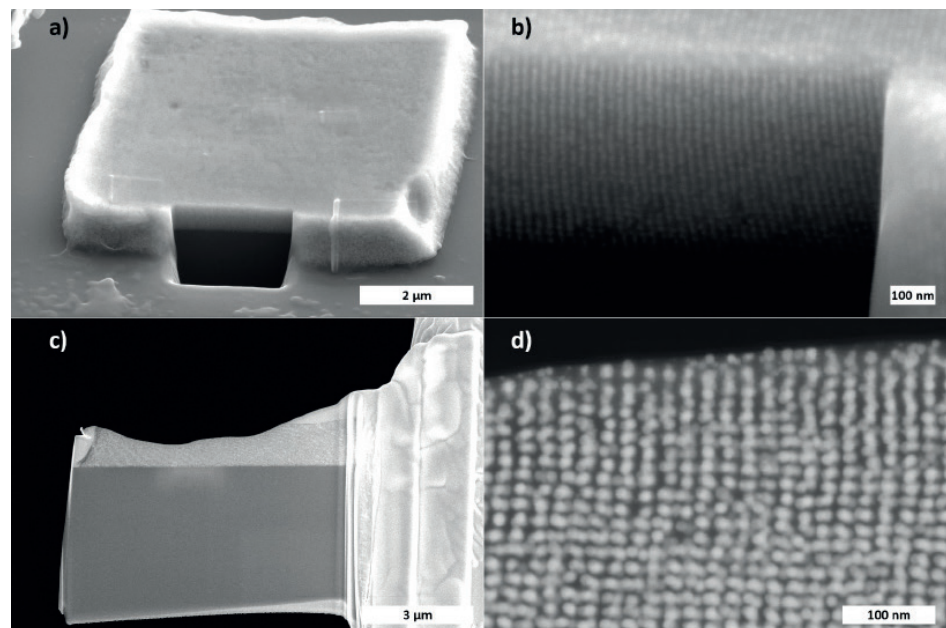


Figure 2
a) SEM overview image of a FIB-cut hetero binary AuEnc^(neg)/eFtn^(pos) crystal on a Si wafer. b) zoomed-in cross-section view, c) FIB-prepared ~ 50 nm thick lamella for transmission analysis, d) high-resolution high-angle annular dark-field (HAADF) transmission image. (Credit: DESY NanoLab, Satishkumar Kulkarni)

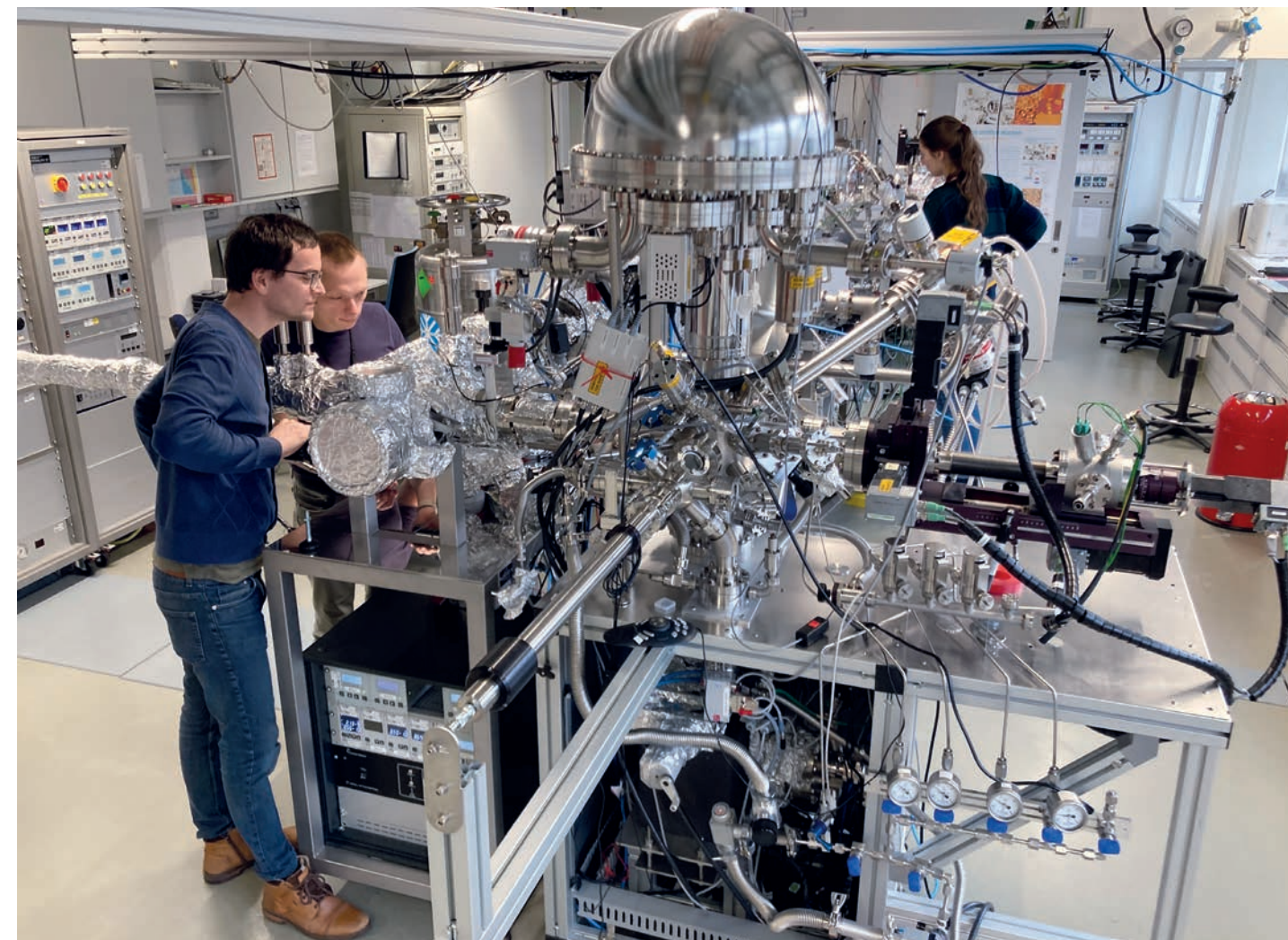


Figure 3
View into the DESY NanoLab: Spectroscopy and sample preparation laboratory. (Credit: DESY)

the size of the virus particle and ultimately destroys it. These findings are vital for the development and optimisation of self-cleaning materials, as they highlight the mechanisms that ensure the thorough inactivation of enveloped viruses like SARS-CoV-2 [1].

Another recent publication in material science highlights the importance of fabricating improved and combined materials with well-defined composition and intricate structures. It was supported by the DESY NanoLab utilising the focused ion beam (FIB) for sample preparation and the scanning electron microscope (SEM) for imaging.

The binary superlattice assemblies are based on the two differently sized protein cages encapsulin (Enc) and 'empty' ferritin (eFtn). They have an outer diameter of 24 nm and 12 nm, respectively. Fig. 2 shows the SEM images of a superlattice created from the negatively and positively charged variants Enc^(neg) and eFtn^(pos), respectively. The Enc^(neg) cage was filled with a gold nanoparticle (AuEnc) while the ferritin was left empty. The study showcases the use of nanoparticles as a contrast to gain insights into the structural details of crystalline biohybrid materials. It highlights the versatility of protein

nanocages for creating distinctive types of binary superlattices. With the support of the DESY NanoLab and its scientists, the study not only contributes to the expanding repertoire of nanoparticle assembly methods but also demonstrates the power of advanced characterisation techniques in elucidating the structural intricacies of these biohybrid materials [2].

A more detailed insight into research activities and user collaborations of the DESY NanoLab is provided in the Science Highlights section of this report.

Contact: [Andreas Stierle, andreas.stierle@desy.de](mailto:andreas.stierle@desy.de)

References

1. M. Kohantorabi, A. Ugolotti, B. Sochor, J. Roessler, M. Wagstaffe, A. Meinhardt, E. E. Beck, D. S. Dolling, M. Blanco Garcia, M. Creutzburg, T. F. Keller, M. Schwartzkopf, S. Koyiloth Vayalil, R. Thuenauer, G. Guédez, C. Löw, G. Ebert, U. Protzer, W. Hammerschmidt, R. Zeidler, S. V. Roth, C. Di Valentin, A. Stierle and H. Noei, 'Light-Induced Transformation of Virus-Like Particles on TiO₂', *ACS Appl. Mater. Interfaces* 16, 37275–37287 (2024).
2. M. Rütten, L. Lang, H. Wagler, M. Lach, N. Mucke, U. Laugks, C. Seuring, T. F. Keller, A. Stierle, H. M. Ginn and T. Beck, 'Assembly of Differently Sized Supercharged Protein Nanocages into Superlattices for Construction of Binary Nanoparticle-Protein Materials', *ACS Nano* 18, 25325–25336 (2024).

DESY Photon Science at the European XFEL

User consortia

DESY is not only responsible for the operation of the European XFEL linear accelerator but also plays an important role as a user. Moreover, DESY scientists are developing lasers and detectors for usage at the European XFEL and are involved in several user consortia including the three largest ones:

Serial Femtosecond Crystallography (SFX)

The SFX Consortium works with the 'Single Particles, Clusters and Biomolecules and Serial Femtosecond Crystallography' (SPB/SFX) instrument of the European XFEL to develop and provide instrumentation and methodology for structure determination using intense XFEL pulses.

By outrunning radiation damage with femtosecond X-ray pulses, high-quality crystal diffraction data can be acquired at ambient temperatures, allowing the study of macromolecular systems undergoing reactions, with temporal resolution ranging from femtoseconds to minutes. Such measurements can complement structure-based screening of drug targets by providing insights into the actual binding mechanisms and responses of the protein. An experiment carried out by the Consortium at the SPB/SFX instrument determined how the main protease, or M^{pro}, of the SARS-CoV-2 virus protects itself from oxidative damage [1]. This protein was the subject of a massive screening programme carried out during the pandemic at PETRA III, and subsequent studies showed that its activity was reduced by exposure to oxygen and then restored when the oxidative stress was removed. The SFX experiments revealed that the addition of oxygen creates a disulfide bond which protects the active cysteine by burying it in the core of the protein structure, giving an insight into how M^{pro} is regulated during the life cycle of the virus.

The European XFEL produces pulses at megahertz rates in the form of pulse trains which can potentially allow the highest achievable measurement speeds for SFX experiments. These must be coupled with fast and efficient sample delivery to avoid sample wastage between pulse trains. As part of a Block Allocation Group (BAG) proposal, the SFX Consortium recently tested drop-on-demand methods to achieve this. In addition, a new approach developed by Alke Meents and his work group at DESY sweeps the fast pulse train across a stationary membrane coated with protein microcrystals. The XFEL beam reflects off an assembly of two opposing mirrors rotating at 5 Hz located 2 m from the sample (Fig. 1). Within 1 μ s, the mirror turns by 31 μ rad, such that the reflected pulses are spaced by 124 μ m at the sample. Ten times per second, after each line of pulses, the sample is stepped in the direction perpendicular to the sweep. Two protein structures were obtained from diffraction recorded this way at a detector frame rate of 110 kHz, proving the feasibility and promise of the technique to measure at rates only limited by detector speed and capacity.

Helmholtz International Beamline for Extreme Fields (HIBEF)

The ReLAX laser in interaction chamber 1 and the diamond anvil cell platform are very well-established drivers of research at the HED-HIBEF in the diverse, international user community. After first successful beamtimes using the DiPOLE-100X laser in diffraction experiments in 2023, this laser was commissioned for spectroscopy investigations to

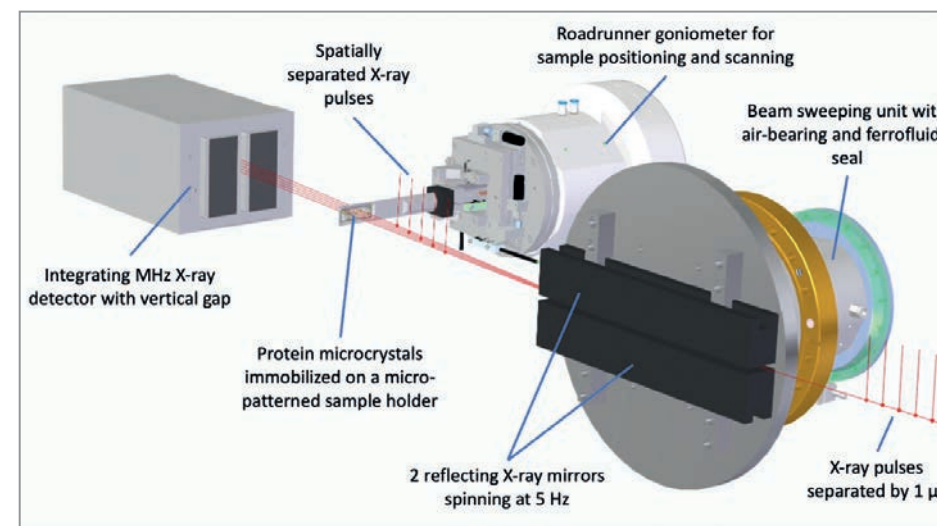
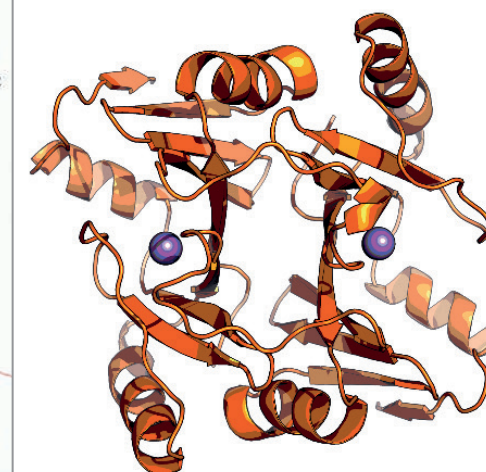


Figure 1

Schematic concept of MHz beam-sweeping fixed-target serial crystallography. A two-mirror assembly rotates at 5 Hz, causing a spatial separation of the X-ray pulses within a bunch train when they reach the target (left). Structure of the FosAKP protein as determined from 23 000 indexed diffraction patterns at the SPB/SFX instrument using this new approach (right). (Credit: DESY)



broaden the experimental possibilities in 2024. The uniqueness and excellent performance of the HIBEF-contributed experimental platforms as well as their operation were highlighted in the HED-HIBEF instrument review.

In 2024 for the first time, HIBEF priority access beamtime was used to push strategic technical developments and key scientific goals of the HIBEF consortium. The selected experiments focused on imaging of imploding wires, MHz imaging in the diamond anvil cell, development of a new detection scheme for vacuum birefringence, and a DiPOLE user community experiment.

The pulsed high-magnetic field setup was used for the first time in a user-assisted commissioning proposal to study the 'Intertwining electronic and spin order in superconducting cuprates and magnetoelectric materials'. Fields up to 50T were achieved in time-resolved diffraction experiments.

The final assembly of the HIBEF AGIPD 1M Si-detector is planned for the first quarter of 2025 and the installation at the HED instrument is scheduled for the third quarter of 2025. First successful tests for the selection of sensors for the high-Z version of this detector were performed.

Some of the scientific highlights achieved at HIBEF [2,3,4], are listed below.

Heisenberg Resonant Inelastic X-ray Scattering (hRIXS)

The hRIXS consortium includes partners from Germany, Switzerland, Finland, France, Sweden, Italy and the UK. The project is coordinated by Potsdam University in close collaboration with DESY and European XFEL.

hRIXS is in full user operation with alternating proposal calls for the modular solid-state and chemistry sample environments. Helmholtz research topics are investigated by the consortium, but the community has grown far beyond the initial proposers into a vibrant user community.

Contact:

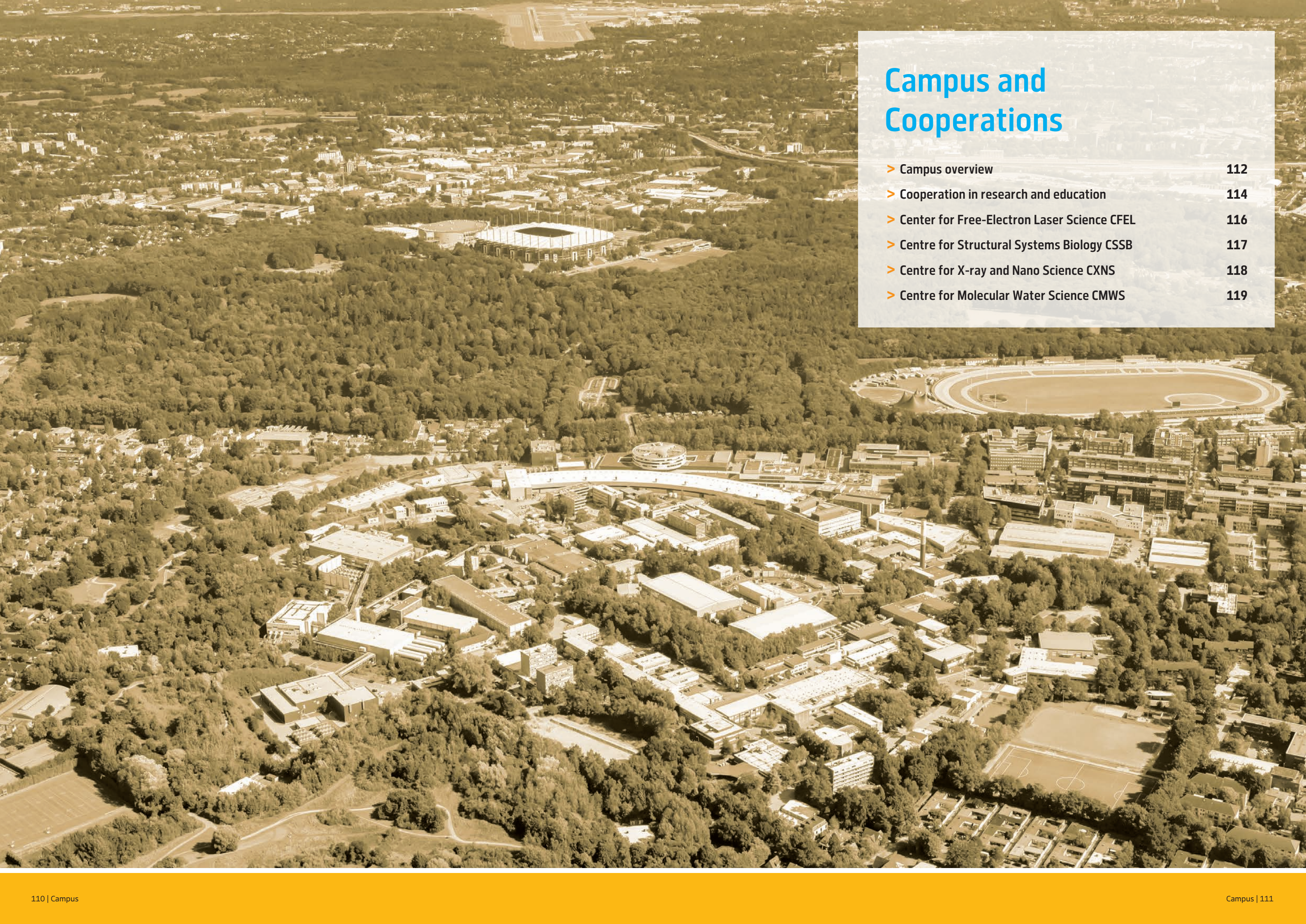
SFX: Henry Chapman, CFEL/DESY, henry.chapman@desy.de

HIBEF: Thomas Cowan, HZDR, t.cowan@hzdr.de

hRIXS: Alexander Föhlisch, Potsdam University and HZB, alexander.foehlich@helmholtz-berlin.de

References

1. P. Y. A. Reinke and R. Schubert et al., 'SARS-CoV-2 M^{pro} responds to oxidation by forming disulfide and NOS/Sonos bonds', *Nat. Comm.* 15, 3827 (2024).
2. M. Frost et al., 'Diamond precipitation dynamics from hydrocarbons at icy planet interior conditions', *Nat. Astron.* 8, 174–181 (2024).
3. A. Laso Garcia et al., 'Cylindrical compression of thin wires by irradiation with a Joule-class short-pulse laser', *Nat. Commun.* 15, 7896 (2024).
4. R. J. Husband et al., 'Phase transition kinetics of superionic H₂O ice phases revealed by Megahertz X-ray free-electron laser-heating experiments', *Nat. Commun.* 15, 8256 (2024). (and a highlight article in this report)



Campus and Cooperations

- > Campus overview 112
- > Cooperation in research and education 114
- > Center for Free-Electron Laser Science CFEL 116
- > Centre for Structural Systems Biology CSSB 117
- > Centre for X-ray and Nano Science CXNS 118
- > Centre for Molecular Water Science CMWS 119

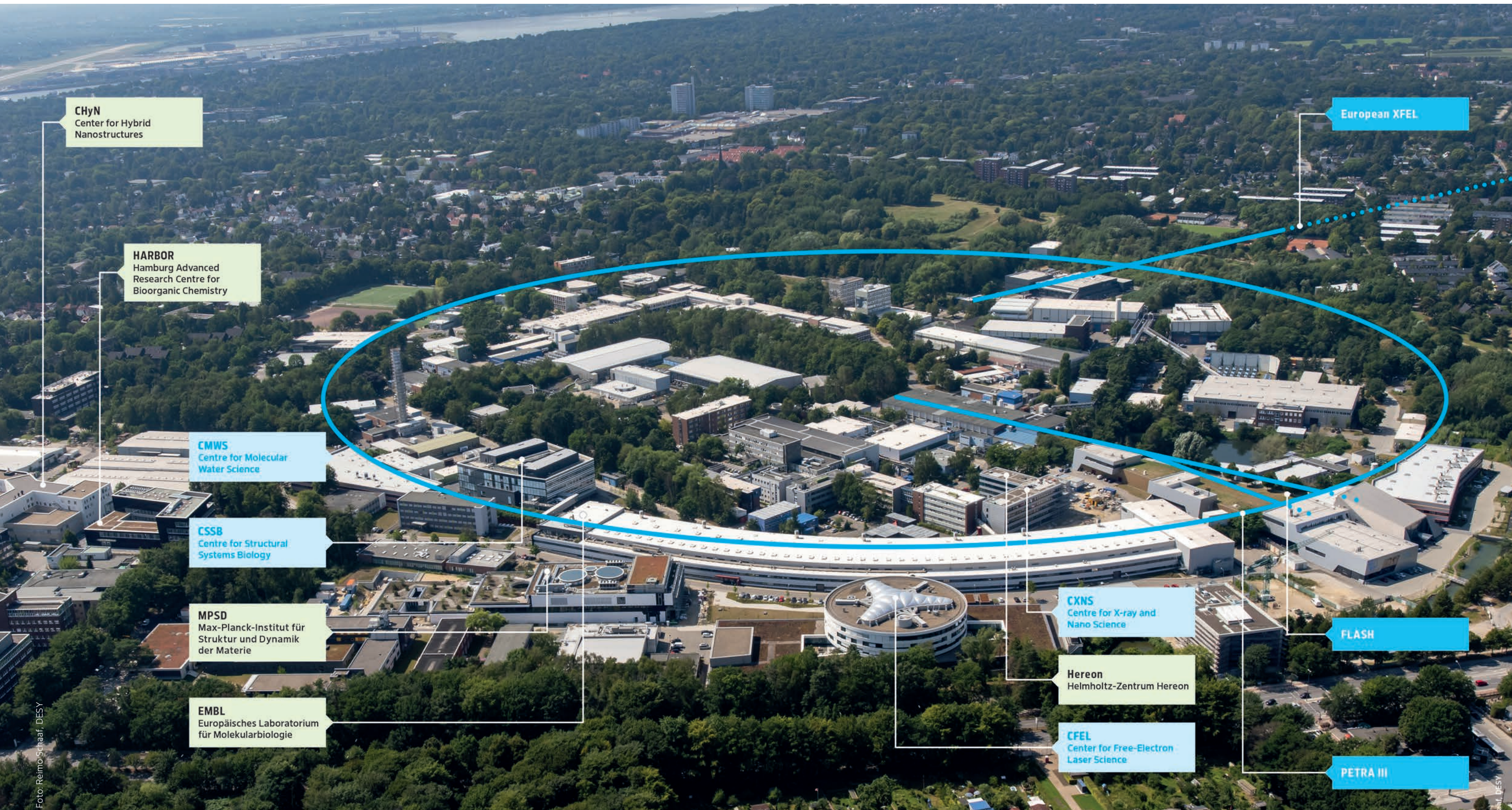
Campus overview

Research centres and cooperations

The research and cooperation landscape at DESY Photon Science includes local, national and international partners with a number of research centres as nuclei for cooperation. All benefit from the excellent scientific environment and research facilities on the Research Campus Bahrenfeld. The image below highlights the light sources, the four research centres in which DESY Photon Science is involved as well as the outstations of EMBL and HEREON and the research centres of the Universität Hamburg. Some major cooperative

activities with universities and the interdisciplinary research platforms on campus are reported on within this chapter.

German universities are also closely involved in developments at PETRA III and FLASH, for example through collaborative research projects funded via the BMBF programme ErUM-Pro. Major developments related to PETRA III, FLASH and European XFEL are described in the chapter 'Light Sources and User Infrastructures'.



Cooperation in research and education

Overview

Graduate Schools

• PIER Helmholtz Graduate School (PHGS)

PHGS is a joint graduate education programme of DESY and University of Hamburg. In 2024, about 270 doctoral researchers were members of the PHGS. They benefit from an outstanding research environment focused on particle and astroparticle physics, nanoscience, photon science, infection and structural biology, accelerator research, theoretical physics and artefact profiling. In addition, PHGS offers skills trainings, language courses, career guidance, a buddy programme and travel awards for young researchers.

During the 2024 PIER PhD Reception on 3 July at DESY, more than 90 doctoral researchers, supervisors, staff, friends and families met to welcome all new doctoral researchers and to honour this year's 55 graduates. The annual PIER Graduate Week, which in 2025 took place from 7-11 October, addresses young scientists and offers stimulating lectures and workshops in the wide range of the PIER research fields. This year's event was attended by 90 doctoral researchers. In the scientific colloquium, Detlef Lohse talked about the physics of soft condensed matter, while DESY alumnus Murali Ganesa gave an inspiring talk on his career as a data scientist at 'Porsche digital'. graduateschool.pier-hamburg.de



PHGS graduates participating at the PIER PhD Reception. (Credit: PHGS, K. Winkler)

• The Helmholtz-Lund International Graduate School (HELIOS)

HELIOS focuses on instrumentation development in particle physics, molecular physics, nano(bio)science and ultrafast photon science. A major aim is to prepare young scientists for the next generation of instrumentation. The involved partners are University of Hamburg, Lund University, City of Hamburg and DESY. In March, HELIOS successfully passed the midterm evaluation by the Helmholtz Association with praise for its scientific excellence, the recruitment of top international PhD students and tailored training programme.



HELIOS doctoral researchers and PIs at the spring retreat in Lund. (Credit: LINXS, S. Mufti)

Currently, 25 doctoral candidates are enrolled in HELIOS. The new HELIOS PhD students started in May 2024 during the HELIOS Spring Retreat hosted by the Institute for Advanced Neutron and X-ray Science (LINXS) in Lund. This training week focused on advanced technologies in the fields of photon science, nanophysics, nano(bio)science and particle physics with hands-on workshops and vivid discussions. A highlight was the keynote lecture given by Nobel Prize winner Anne L'Huillier.

The HELIOS Day 2024 on 15 October in Hamburg brought together scientists and PhD students for a full day of exchange and networking. heliosgraduateschool.org

• Data Science in Hamburg – Helmholtz Graduate School for the Structure of Matter (DASHH)

DASHH is one of six Helmholtz Information & Data Science (HIDS) Schools and is a joint project of DESY and eight partner institutions (UHH, TUHH, HSU, HAW, Hereon, HZI, MPSD, EuXFEL). DASHH's goal is to train young scientists in the field of novel data acquisition and analysis techniques to meet the challenges posed by the huge data sets generated at large-scale facilities. After the successful evaluation by the Helmholtz Association in 2023, the HIDS Schools have become a permanent Helmholtz activity: Funding is now secured until at least December 2029.

By now, 31 interdisciplinary PhD projects are supported by DASHH. A total of twelve PhD projects have been completed so far, seven of them in 2024; another expected by the end of the year. Participants at the DASHH Annual Retreat 2024 enjoyed a poster session, presentations and an inspiring keynote by Wolfgang Hildesheim.

In addition, PhD Seminars, a Data Science Colloquium and PhD Get Togethers promote regular exchange and networking. PhD students from all partner institutions can benefit from these offers through a DASHH associate membership. dashh.org



Impressions of the DASHH retreat. (Credit: DASHH)

Strategic networks

• LEAPS

The 'League of European Accelerator-based Photon Sources' is a strategic consortium of sixteen institutions operating 21 accelerator-based light sources across Europe. The pilot project LEAPS-INNOV develops the LEAPS Technology Roadmap and fosters a strong partnership with industry through joint technological developments and advanced research capabilities for industry. 'LEAPS Meets' is a thematic conference series that takes place every two years. The next event in spring 2025 will be dedicated to 'Advanced Materials for Energy'. leaps-initiative.eu

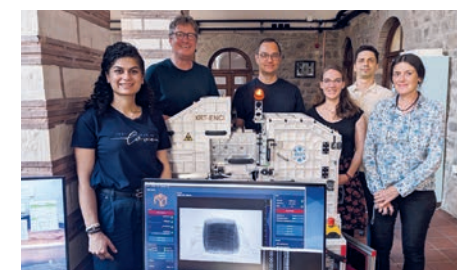
• PIER PLUS

PIER PLUS views itself as the Hamburg metropolitan region's scientific platform and is led by University of Hamburg. Aims are to strengthen Hamburg as a scientific center and to promote collaboration between the 22 involved universities and research institutes in six fields of interest: Science City Hamburg Bahrenfeld, Health and Infection, Climate and Coast, Conflict and Coordination, Climate-friendly Mobility and New Materials. pier-plus.de

Excellence clusters at the University of Hamburg

• 'CUI: Advanced Imaging of Matter'

Many of the DESY lead scientists and UHH professors are strongly involved in the cluster's research programme, with Francesca Calegari and Henry Chapman acting as two of the three spokespersons. CUI profits from Hamburg's excellent light sources as ideal environment for groundbreaking research and recognises the importance of education and equal opportunities, e.g. through the dynamENT mentoring programme.



The ENCI during the mission to Ankara with the team from DESY, UHH and CNRS/France. (Credit: DESY).

• 'Understanding Written Artefacts'

Christian Schroer, DESY lead scientist and UHH professor, is principal investigator and co-spokesperson of the cluster of excellence 'Understanding written Artefacts'. In the project 'Reading Closed Cuneiform Tablets Using High-Resolution Computed Tomography', his team has developed a portable tomography scanner (XRT-ENCI) to read cuneiforms directly in museums such as the Louvre in Paris or the Museum of Anatolian Cultures in Ankara.

Joint laboratories

• In the 'Helmholtz International Laboratory on Reliability, Repetition, Results at the most advanced X-ray Sources' (HIR3X), DESY, European XFEL and the US National Accelerator Laboratory SLAC jointly develop techniques and procedures for the reliable application of X-ray lasers.

• DESY is partner of the Helmholtz Institute Jena, an outstation of the GSI Helmholtz Center for Heavy Ion Research in Jena. The institute focuses on applied and fundamental research at the frontier of high-power lasers and particle accelerator facilities.

• The Ruprecht Haensel Laboratory is a joint research facility of Christians-Albrecht-Universität zu Kiel and DESY with state-of-the-art instruments and methods for nanoresearch offered to national and international partners. Joint appointments strengthen research-oriented teaching in the field of nanoscience and surface physics.

Collaborative research

• Tracking the active site in heterogeneous catalysis for emission control (SFB 1441), coordinated by Karlsruhe Institute of Technology

• Tailor-made multi-scale materials systems (SFB 986), coordinated by Technische Universität Hamburg (TUHH)

• Atomic scale control of energy conversion (SFB 1073), coordinated by Georg-August-Universität Göttingen

• Quantum Cooperativity of Light and Matter (QuCoLiMa) (TRR 306), coordinated by Friedrich-Alexander-Universität Erlangen-Nürnberg

• Center for Integrated Multiscale Materials Systems (CIMMS), coordinated by TUHH

• Center for Data and Computing in Natural Sciences (CDCS), coordinated by Universität Hamburg

• Extreme Light for sensing and driving molecular CHirality (ELCH) (SFB 1319), coordinated by Universität Kassel

• Data for PHoton and Neutron for a National Research Data Infrastructure (DAPHNE4NFDI), coordinated by DESY

• Basic Services for a German National Research Data Infrastructure (Base4NFDI), coordinated by Technische Universität Dresden

• Sustainability-driven nano- and materials science and technology with synchrotron radiation, cooperation with synchrotron radiation, cooperation between DESY and Technische Universität Bergakademie Freiberg.

• X-ray analyses on the PETRA III synchrotron radiation source and their evaluation, cooperation between DESY, Hereon, EMBL and Fraunhofer-Gesellschaft

Center for Free-Electron Laser Science CFEL

Three institutions working successfully together

DNA damage drives cancer, ageing and cell death. Therefore, DNA repair is crucial for all organisms, and a deeper understanding of this basic function helps us to better comprehend how life around us survives and thrives. An international team of researchers led by DESY groups at CFEL around Thomas J. Lane, with strong support of the University of Hamburg and European XFEL, reported in *Science* on 'Time-resolved crystallography captures light-driven DNA repair' [1]. In their study they used time-resolved crystallography to understand how the enzyme photolyase efficiently channels the energy of sunlight into DNA repair chemistry (see also article in the Science Highlights section of this report).

Superconductivity is a fascinating phenomenon which allows a material to sustain an electrical current without any loss. This collective quantum behaviour of matter only appears in certain conductors at temperatures far below ambient. Besides being capable of transporting electrical currents without loss, superconductors are also known to expel magnetic fields from their interior. This phenomenon, known in equilibrium conditions as the Meissner effect, is a direct consequence of the mutual coherence of the charge carriers and of their tendency to march in lockstep. However, measuring the expulsion of magnetic fields for light-induced superconductivity has been challenging because the effect only persists for a few picoseconds, making it impossible to measure magnetic field changes with precision. A team of re-

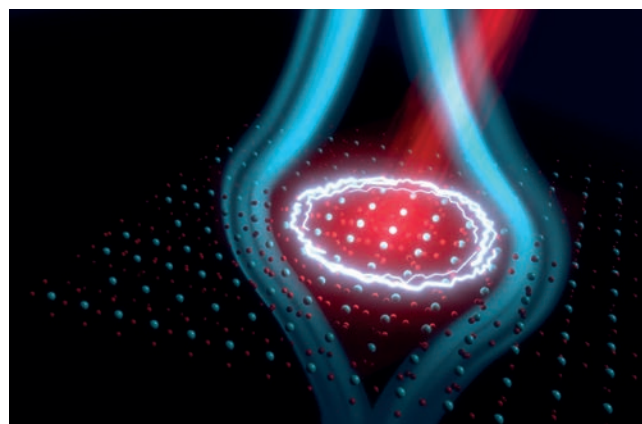


Figure 1
Mid-infrared laser pulses coherently drive atomic modes in $\text{YBa}_2\text{Cu}_3\text{O}_{6.48}$ and stabilise superconducting fluctuations at high temperature. This quantum coherence leads to the ultrafast expulsion of a static magnetic field. (Credit: Sebastian Fava, Jörg M. Harms, MPSD)

searchers at the Max Planck Institute for the Structure and Dynamics of Matter (MPSD) at CFEL, led by Andrea Cavalleri, has developed a new experiment capable of monitoring the magnetic properties of superconductors at very fast speeds. They have worked on laser-irradiated $\text{YBa}_2\text{Cu}_3\text{O}_{6+x}$, a compound for which static superconductivity is only seen down to about -200°C . They have discovered that photo-excited $\text{YBa}_2\text{Cu}_3\text{O}_{6.48}$, in addition to featuring near zero resistance, also expels a static magnetic field from its interior and reported on this in a *Nature* article 'Magnetic field expulsion in optically driven $\text{YBa}_2\text{Cu}_3\text{O}_{6.48}$ ' [2] (Fig. 1).

The DESY Attosecond Science group at CFEL led by Francesca Calegari has developed a novel light source capable of producing extremely short pulses for the investigation of UV-induced molecular dynamics with unprecedented temporal resolution. Their unique observations are described in a *Nature Communications* article 'Few-femtosecond time-resolved study of the UV-induced dissociative dynamics of iodomethane' [3] (Fig. 2). The group's lasers, among others, are now included in the network 'Lasers4EU', offering access to the European laser community.

Contact: Ralf Köhn, ralf.koehn@cfel.de

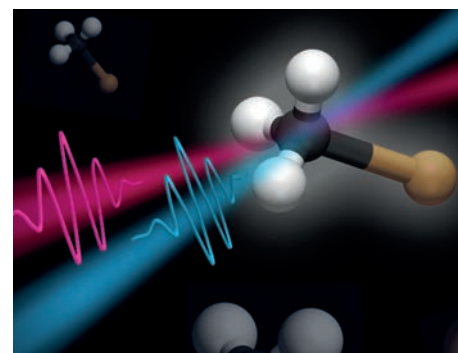


Figure 2
An ultrashort UV pulse causes photolysis of neutral iodomethane which can be avoided if a second laser pulse arrives within 5 femtoseconds after photo-excitation. (Credit: Nicoletta Calegari)

References

1. N. Christou et al., *Science* 382, 1015-1020 (2023).
2. S. Fava, *Nature* 632, 75-80 (2024).
3. L. Colaizzi et al., *Nat. Commun.* 15, 9196 (2024).

CFEL Partner Institutions

- Deutsches Elektronen-Synchrotron DESY, Hamburg, Germany
 - Max Planck Institute for the Structure and Dynamics of Matter, Hamburg, Germany
 - University of Hamburg, Hamburg, Germany
- www.cfel.de

Centre for Structural Systems Biology CSSB

A hub for molecular infection research

Scientific collaboration and exchange are at the heart of CSSB. Such interactions are also visible in research networks with our partner institutions. For example, several CSSB scientists are involved in the newly funded DFG Collaborative Research Centre (CRC) on 'Emerging Viruses: Pathogenesis, Structure, Immunity', which focuses on the mechanistic understanding of viruses, infection processes and immune reactions at the molecular level.

In June, CSSB participated in the Science City Day during which 14000 people visited the Bahrenfeld campus. Activities such as 'AI in Action', 'Cells Under the Microscope', 'Chromatography Lab' and 'Nuclear Pore Complex Basketball' highlighted our research for both adults and children.

Following Kay Grünewald, Holger Sondermann has taken over as Scientific Director of CSSB from 2024 to 2026.

Research highlights

CSSB scientists investigate the molecular mechanisms of infections. This year our scientists revealed new structural insights into how proteins secreted by Gram-negative bacteria's type III secretion system subvert the host cell's actin cytoskeleton during infection [1], examined the crucial role played by RNA in critical steps of the Lassa virus life cycle [2], revealed some key insights into the composition and structure of the Vaccinia virus core [3] (Fig. 1), uncovered crucial details on how herpesviruses exit the cell nucleus without compromising the integrity of the nuclear envelope [4] and uncovered the molecular details of how we absorb vitamin B1, paving the way to preventing dangerous hidden B1 deficiencies in patients [5].

Our scientists are also involved in the development of new tools and technologies for the infection and structural biology community such as TEMPy-ReFF, a new method for atomic structure refinement in cryo-EM density maps [6].

Awards:

Prof. Caroline Barisch (FZB) received the DGHM Advancement Award from the Deutsche Gesellschaft für Hygiene und Mikrobiologie, endowed with 3500 Euro, for her research on the molecular mechanisms by which pathogenic mycobacteria manipulate lipid metabolism and lipid transport pathways of their host to ensure their intracellular survival. Jan Kosinski (EMBL) together with three other researchers, received an ERC Synergy grant for their project

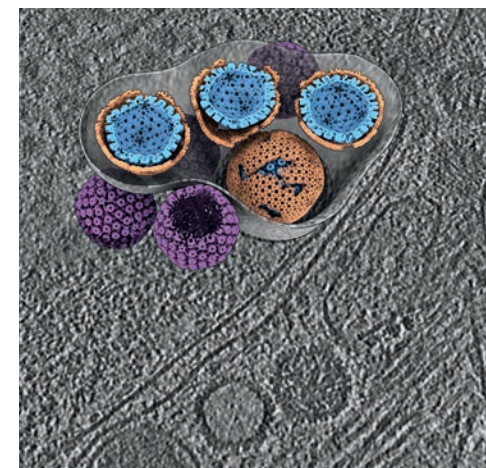


Figure 1
A slice through a tomogram and a backplotted three-dimensional representation of egress components. (Credit: Grünewald/LIV)

'TransFORM', for which they will receive funding of 14 million Euro (2.5 million for the Kosinski group) to be used over a period of six years.

Dr. Enrico Caragliano from the Bosse group (MHH) and Dr. Janine-Denise Kopicki from the Uetrecht group (DESY, Univ. Lübeck) both received an award for having one of the best theses of 2023/2024 in the Department of Chemistry at the Universität Hamburg. Dr. Sukrit Srivastava from the Kolbe group (HZI) received a Helmholtz Enterprise Field Study Fellowship.

Contact:

Holger Sondermann, holger.sondermann@cssb-hamburg.de

References

1. B. Yuan et al., *Sci. Adv.* 9, 49 (2023).
2. L. Sängler et al., *J. Am. Chem. Soc.* 145, 51 (2023).
3. J. Liu et al., *Nat. Struct. Mol. Biol.* 31, 1105 (2024).
4. V. Pražák et al., *Nat. Microbiol.* 9, 1842 (2024).
5. F. Gabriel et al., *Nat. Commun.* 15, 8542 (2024).
6. J.G. Beton et al., *Nat. Commun.* 15, 444 (2024).

CSSB Partner Institutions

- Bernhard Nocht Institute for Tropical Medicine (BNITM)
- Deutsches Elektronen-Synchrotron DESY
- European Molecular Biology Laboratory (EMBL)
- Hannover Medical School (MHH)
- Leibniz Institute of Virology (LIV)
- Helmholtz Centre for Infection Research (HZI)
- Research Center Borstel (FZB)
- Universität Hamburg (UHH)
- University Medical Center Hamburg-Eppendorf (UKE)

www.cssb-hamburg.de

Centre for X-ray and Nano Science CXNS

Widening the scope – research in materials science and nanoscience in a multi-institutional centre

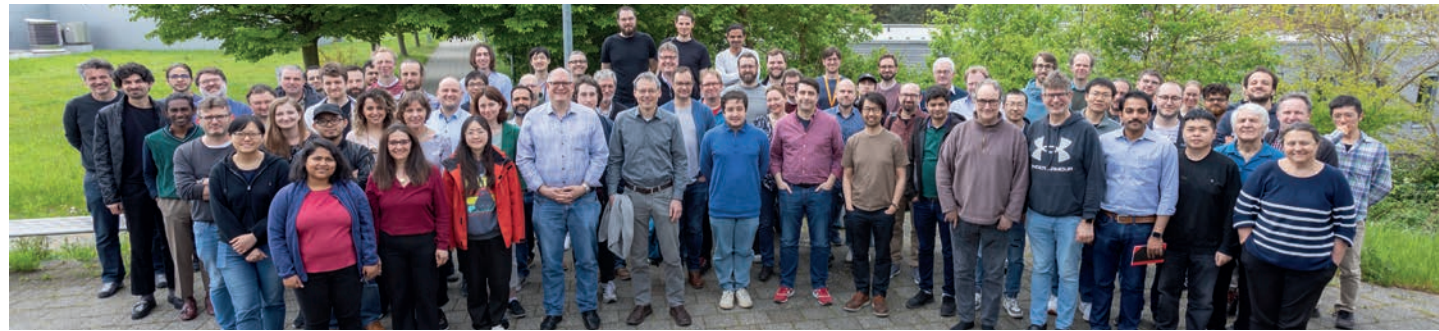


Figure 1
NanoMat Science Day 2024 at DESY. (Credit: M. Mayer, DESY)

The CXNS was established by the partners Helmholtz-Zentrum Hereon with its German Engineering Materials Science Center (GEMS), Kiel University (CAU) with the Ruprecht Haensel Laboratory (RHL), the Leibniz-Institut für Kristallzüchtung (IKZ) and the Hamburg University of Technology (TUHH) and DESY. All partners as well as DESY Photon Science groups profit from CXNS' lab infrastructure and its close proximity to the large-scale facilities PETRA III and FLASH. This infrastructure provides a huge variety of highly specialised methods for sample analysis to inhouse and guest researchers. It facilitates projects in the core research fields corrosion research, materials science, quantum research, as well as catalysis, hydrogen and medical research.

In April around 100 participants attended the NanoMat Science Day 2024 'Future opportunities at DESY's up-graded large-scale facilities'. The aim of the annual event is to advance and deepen inter-institutional exchange and cooperation, especially for young scientists from fields related to CXNS and its research priorities.

One example for outstanding research cooperation in CXNS research areas are new findings on nanoporous materials. In a cooperation between DESY, TUHH, Hereon, University of Hamburg and other institutions a team has investigated the mechanism of water transport without a mechanical pump from bottom to top. In nature driven by capillary forces in trees, this project revealed a pump mechanism in a special type of nanomaterial: a silicate glass permeated by innumerable, extremely fine pores which instead of contracting expands during water transportation. These results can be the basis for a promising new sensor technology. Measuring the length of a nanoporous material to determine its liquid content could aid in advancing liquid electrolyte-based batteries, supercapacitors and other future energy technologies. The CXNS partners from the RHL together with an Indian consortium performed *in situ* X-ray measurements of a

self-assembly process of 2D perovskite formation at the airwater interface. They found that the 2D single-crystalline films and flakes are suitable materials to develop broad-band white light emission across the entire visible range and to obtain lasing without external cavities [2].

Another research highlight in the field X-ray photonics is presented by IKZ's X-ray optics group together with the IKZ-DESY start-up company 'TXproducts'. They developed a fast and versatile solid-state X-ray pulse picker and presented a full characterisation of the main performance parameters of the device. Due to its small size and flexible adaptability, the pulse picker can be easily introduced into existing setups and facilitate measurements at synchrotron beamlines with high temporal resolution [3].

As a cooperation between the DESY NanoLab and the IKZ, a laser laboratory for the investigation of dynamics at the nanoscale has started operation. It hosts setups for ultrafast photoacoustic experiments complementing the existing portfolio. A new setup for time-resolved surface reflectance is under construction.

Contact: [Andreas Stierle, andreas.stierle@desy.de](mailto:andreas.stierle@desy.de)

References

1. J. Sanchez et al., PNAS 121, 38 (2024).
2. S. Chowdhury et al., Adv. Funct. Mater. 34, 2401334 (2024).
3. D. Schmidt et al., Optics Express 32, 5 (2024).

CXNS Partner Institutions

- Helmholtz-Zentrum Hereon, German Engineering Materials Science Centre (GEMS)
- Christian-Albrechts-Universität zu Kiel (CAU), Ruprecht-Haensel-Laboratory
- Deutsches Elektronen-Synchrotron DESY
- Technical University Hamburg (TUHH), Center for Integrated Multiscale Material Systems (CIMMS)
- Leibniz-Institut für Kristallzüchtung (IKZ Berlin)
photon-science.desy.de/research/centres_for_research/cxns

Centre for Molecular Water Science CMWS

Achieving a detailed molecular understanding of water

The CMWS brings together key experts to develop a detailed molecular understanding of the various structures, phenomena and dynamic processes in water and at water interfaces on different timescales relevant for green-energy technologies, health and environment. The research is organised in five pillars and coordinated by DESY with a combined theoretical and multimodal experimental approach. One important focus is the access to the light sources at DESY and European XFEL and complementary methods offered by other Helmholtz large-scale facilities and CMWS partners.

Founding declaration of CMWS

This year 47 partner institutions signed a founding declaration to establish the CMWS governance and mission. The first general assembly was held in October 2024; a festive inauguration ceremony is planned during the CMWS Water Days (25-27 February 2025).

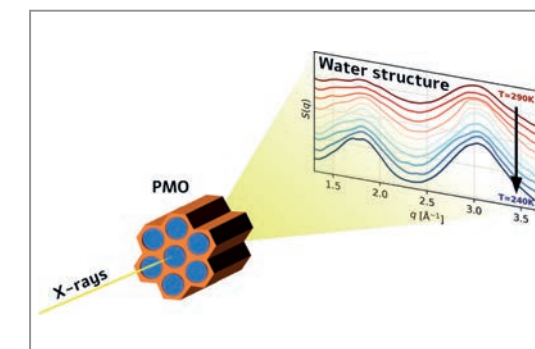


Figure 1
Probing scheme of the structure of water confined in nanopores by X-ray scattering [2].

Advancing water research

On the DESY campus, water-specific instrumentation has been further advanced, including high-level spectrometers in the two CMWS laboratories. A science programme was launched by DESY in 2019 to strengthen CMWS research and support PhD and Postdoc projects with focus on the research agenda of the CMWS White Paper [1]. The programme is jointly financed by DESY and CMWS partners and continued successfully in 2024. Water under spatial confinement exhibits structural and thermodynamic properties that differ from bulk water. One project [2] investigated the effect of pore wall chemistry and pore diameter on the structure of water confined in periodic mesoporous organosilicas (PMOs) (Fig. 1). A shift in the first structure factor peak reveals that smaller and more hydrophilic pores induce a lower density. Compared to larger and hydrophobic pores, smaller and more hydrophilic pores induce a more pronounced tetrahedral network in water.

A second project [3] focused on crystalline and amorphous water ices and characterised their vibrational overtone spectra in the near-infrared range (NIR) (Fig. 2). While at the conditions present at Earth's surface only hexagonal ice is observed, the p-T conditions at extraterrestrial sites allow for a large variety of topologically and morphologically distinct forms. The study identified the first overtone of the OH-stretching vibration as a powerful marker for structural features such as porosity, density and cubicity in ices. This provides reference data of astronomically relevant ices, allowing for remotely accessing properties for e.g. icy moons by the James Webb Space Telescope.

Events and activities

The CMWS Water DAYS 2024, with more than 80 participants, showcased research highlights from all scientific pillars and covered the outcome and lessons learnt from the first topical 'water calls' of PETRA III and European XFEL. Following that, a second round of topical calls for molecular-water science was launched in 2024, resulting in successful projects with significant CMWS contributions. The bi-weekly CMWS Seminar series provides a platform for knowledge exchange and introducing students to CMWS research areas through lectures by network and external experts.

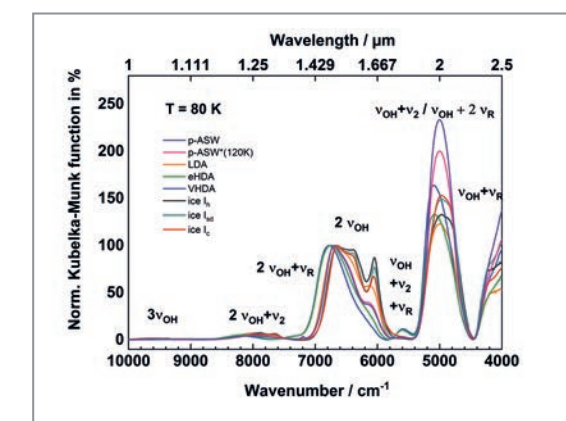


Figure 1
NIR spectra of crystalline and amorphous ices [3].

Contact: [Claudia Goy, claudia.goy@desy.de](mailto:claudia.goy@desy.de)

References

1. G. Gruebel et al. (eds.), DESY, 127 pp. (2021) DOI: 10.3204/PUBDB-2021-01859.
2. N. C. Giebelmann et al., J. Phys. Chem. C. 128, 1, 499 (2024).
1. C. M. Tonaer et al., The Astrophys. J. 970, 82 (2024).

CMWS Partner Institutions

47 partner institutions from 12 countries signed the founding declaration
www.cmws-hamburg.de



Facts and Numbers

FLASH

- > Experimental halls, machine and lasing parameters 122
- > Beamlines and laser systems 123
- > Beamtime statistics 125

PETRA III

- > Experimental halls and machine parameters 126
- > Beamlines 127
- > Beamtime statistics 129

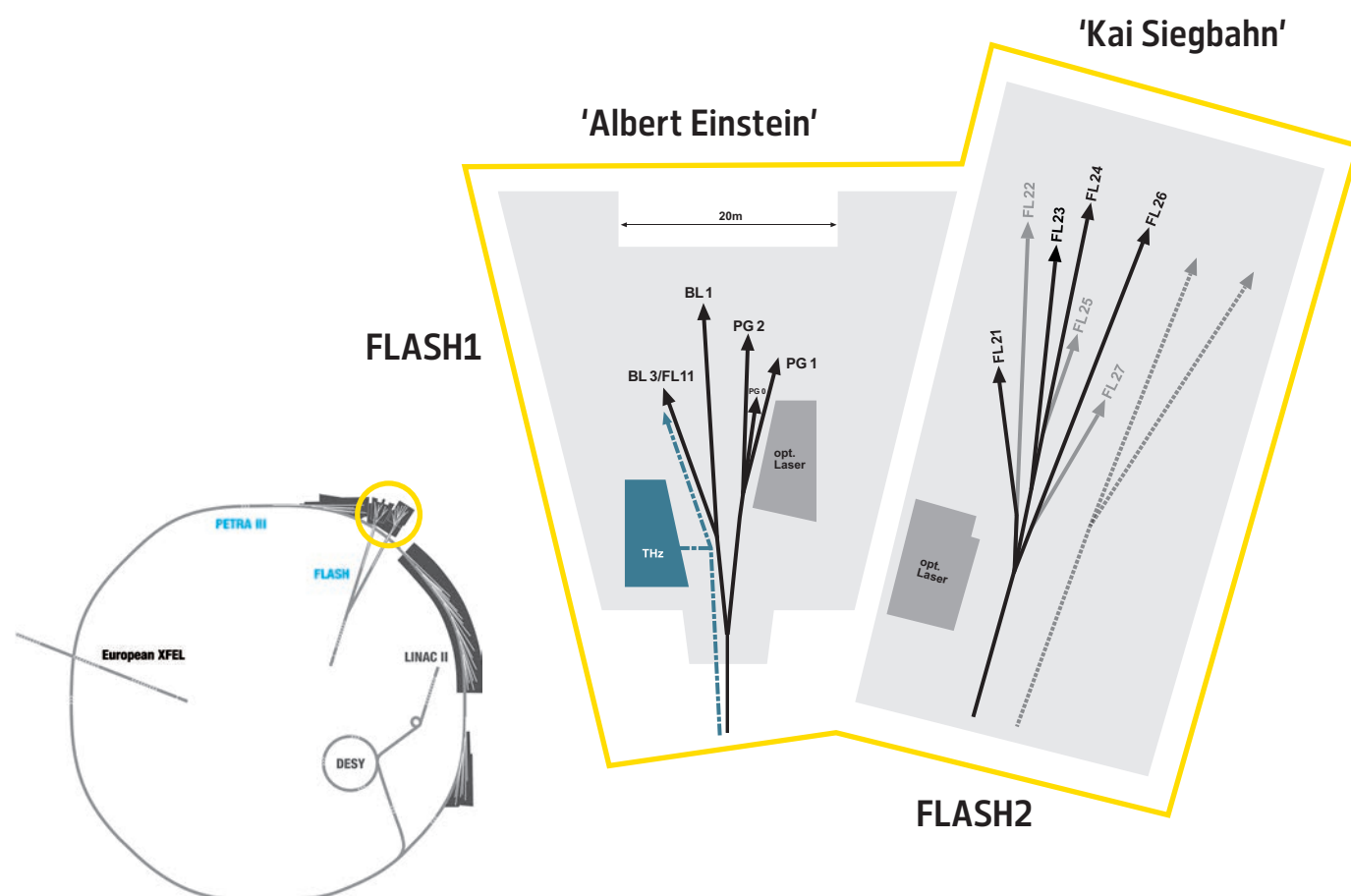
DESY NanoLab – instruments 130

Committees 131

Project Review Panels 132

FLASH

Experimental halls, machine and lasing parameters



FLASH - machine parameters

	FLASH1*	FLASH2
Electron energy range	0.35–1.35 GeV	0.4–1.35 GeV
Normalised emittance at 0.4 nC (rms)	0.4 mm mrad	0.4 mm mrad
Energy spread	200 keV	500 keV
Electron bunch charge	0.01–1.2 nC	0.01–1 nC
Peak current	1–2.5 kA	1–2.5 kA
Electron bunches per second (shared between FL1 and FL2)	5000	5000

*After completion of the present upgrade, FLASH1 will provide seeded FEL pulses with new parameters from 2026 on (to be documented in the Annual Report 2025).

FLASH - lasing parameters

	FLASH1	FLASH2
Photon energy fundamental	24–360 eV	14–370 eV
Wavelength fundamental	51–3.4 nm	90–3.3 nm
Photon pulse duration (FWHM)	30–200 fs	10–200 fs
Peak power	1–5 GW	1–5 GW
Single photon pulse energy (average)	1–500 μ J	1–1000 μ J
Spectral width (FWHM)	0.7–2%	0.5–2%
Photons per bunch	10^{11} – 10^{14}	10^{11} – 10^{14}
Peak brilliance photons/sec/mm ² /mrad ² /0.1%	10^{28} – 10^{31}	10^{28} – 10^{31}

FLASH

Beamlines and laser systems

FLASH1 experimental hall 'Albert Einstein'

BL1	non-monochromatic FEL photons Kirkpatrick-Baez (KB) focusing optics, FEL focal spot of $\approx 7 \mu\text{m} \times 8 \mu\text{m}$ (FWHM) split-and-delay unit for XUV pump – XUV probe experiments (mirrors for 13.57 nm, -30 ps to +650 ps delay) optical pump – probe laser not available before 2026 permanent end station: multipurpose CAMP chamber with pnCCD detectors, electron and ion spectrometers and collinear incoupling optics for optical laser	TU Berlin
BL3 (FL11)	Currently rebuilt into FL11, future capabilities in 2026: non-monochromatic FEL photons, wavelength range: 2–60 nm fundamental Kirkpatrick-Baez (KB) focusing optics with variable foci down to $< 10 \mu\text{m}$ (FWHM)/unfocused beam size ≈ 5 –10 mm (FWHM, depending on wavelength) optional pump – probe experiments using the new FLASH1 optical laser system for BL1 and BL3 (future FL11) optional pump – probe experiments using THz radiation: Double pulse scheme with tunable undulator source and broadband dipole source synchronised to X-ray pulses, new parameters to be confirmed after shutdown about 3 x 4 m platform for user-provided end station	
PG1	high resolution plane grating XUV monochromator (SX 700 type, $< 10^{-4}$ bandwidth, carbon coated optics): - variable combination of photon flux and resolution (from high flux to high resolution) - controlled temporal-spectral properties at moderate resolution for pump – probe experiments - high photon flux with harmonic filtering Kirkpatrick-Baez (KB) refocusing optics, FEL focal spot down to $5 \mu\text{m}$ FWHM (vertically, monochromator exit slit size dependent) permanent end station: - XUV-Raman spectrometer TRIXS for high-resolution and time-resolved RIXS measurements on solid samples (20–400 K, resolving power ≈ 1700 , time resolution 170–300 fs FWHM) - optional pump – probe experiments (RIXS; XAS and reflectivity with angular resolution) using the FLASH1 optical laser system for PG1 and PG2	
PG2	uses the same monochromator as PG1 50 μm focus XUV beam splitter with variable time delay (± 6 ps) for time resolved studies optional pump – probe experiments using FLASH1 optical laser system for PG1 and PG2 about 3 x 4 m platform for user-provided end station	

FLASH2 optical / NIR laser system for pump – probe experiments for beamline BL1 and BL3 (future FL11)

The FLASH1 pump probe laser for BL1 and BL3 has been decommissioned in 2024.
A new laser facility is in preparation, but will not be available in 2025.
The parameters of the laser serving BL1 and FL11 in the future will be similar to the laser provided for FL23.

FLASH2 optical / NIR laser system for pump – probe experiments for beamlines PG1 and PG2

central wavelength	1030 nm
spectral bandwidth	30 to 50 nm (pre-set for experiment)
intra-burst repetition rate	Up to 1 MHz
number of pulses per burst	1–800
pulse duration	60–100 fs FWHM
timing jitter to FEL	< 60 fs rms
pulse energy	0–30 μ J (at interaction point at 1030 nm)
polarisation	Linear (s or p)
peak intensity	$> 10^{14}$ W/cm ²
time delay to FEL	-1.5 ns to +1.5 ns, larger delays optional
energy stability	$< 10\%$ pulse-to-pulse peak (3% rms)
Harmonic generation conversion to (SHG) 515 nm, (THG) 343 nm or (FHG) 257 nm central wavelength is available with conversion efficiencies of $> 50\%$ SHG, $> 10\%$ THG, $> 6\%$ FHG.	

All FLASH beamlines provide online photon diagnostics for intensity, wavelength and beam position, fast shutter, aperture and filter sets.

FLASH1 experimental hall 'Kai Siegbahn'

FL21	diagnostics beamline – not available for user experiments
FL23	pulse-length preserving double grating monochromator beamline wavelength range: 2–20 nm fundamental plus 3. harmonic High transmission option (single grating) & high temporal resolution option (double grating) (effective) pulse duration <50 fs FWHM Kirkpatrick-Baez (KB) focusing optics with variable foci down to < 10 μm (FWHM)/unfocussed beam size ≈ 5–10 mm (FWHM, depending on wavelength) optional pump – probe experiments using FLASH2 optical laser system grazing incidence split-and-delay unit with -5/+18 ps time delay <i>Univ. Münster</i> about 3 × 4 m platform for user-provided end station
FL24	non-monochromatic FEL photons wavelength range: 4–90 nm fundamental Kirkpatrick-Baez (KB) focusing optics with variable foci down to < 10 μm (FWHM)/unfocussed beam size ≈ 5–10 mm (FWHM, depending on wavelength) optional pump – probe experiments using FLASH2 optical laser system grazing incidence split-and-delay unit with -5/+18 ps time delay <i>Univ. Münster</i> about 3 × 4 m platform for user-provided end station
FL26	non-monochromatic FEL photons wavelength range: 6–90 nm fundamental optional pump – probe experiments using FLASH2 optical laser system Laser-based high harmonic generation VUV source for VUV-XUV pump-probe experiments with up to 50 eV VUV photon energy <i>Univ. Hannover</i> permanent end station: <i>MPI-K Heidelberg</i> - reaction microscope (REMI) for time-resolved AMO spectroscopy - grazing incidence split-and-delay unit and refocusing optics: FEL focal spot < 10 μm × 10 μm (FWHM, depending on wavelength) - ± 2.7 ps time delay range, 1 fs precision - grating spectrometer for online spectral distribution monitoring and for transient absorption spectroscopy

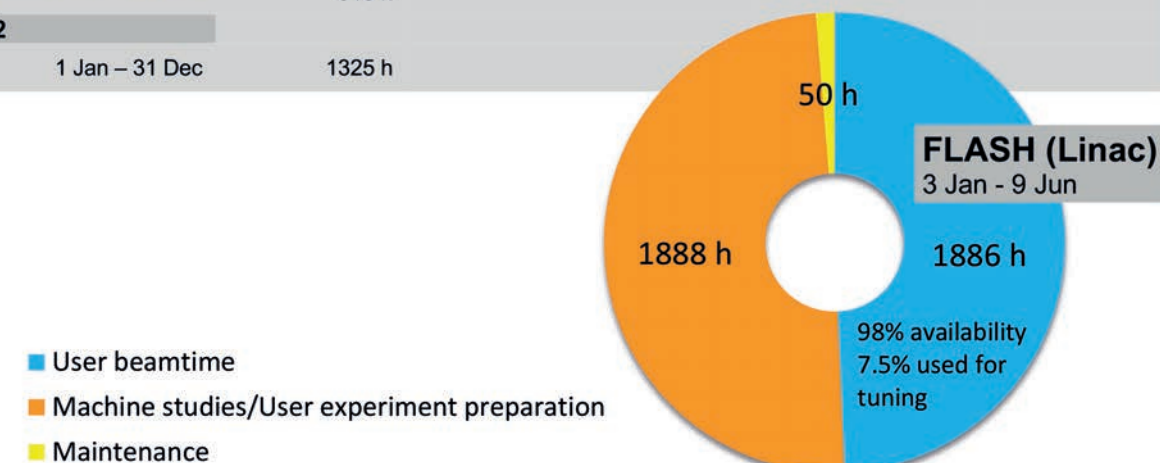
FLASH2 optical / NIR laser system for pump – probe experiments for beamline FL23

central wavelength	1030 nm
spectral bandwidth (@-10dB)	< 50 nm
intra-burst repetition rate	100 kHz
number of pulses per burst	80 (burst 800 μs flat)
pulse duration	> 70 fs (FWHM (compressed to 1.1 × bandwidth limit), >1000 fs FWHM (uncompressed))
timing jitter to FEL	t.b.d.
pulse energy	0–1.8 mJ (at interface with experimental chamber)
polarisation	Linear (s or p)
focus size (1/e ² diameter)	> 50 μm (1/e ²)
peak intensity	> 10 ¹⁵ W/cm ²
time delay to FEL	-1.5 ns to +1.5 ns, larger delays optional
energy stability	< 10% pulse-to-pulse peak (3% rms)
Harmonic generation conversion to 515, 343 and 257 nm central wavelength is available	

FLASH2 optical / NIR laser system for pump – probe experiments for beamline FL23 and FL26

central wavelength	700 to 900 nm (fast tuneable)
spectral bandwidth	30 to 140 nm (pre-set for experiment)
intra-burst repetition rate	100 kHz
number of pulses per burst	1–77
pulse duration	15–65 fs FWHM (compressed to 1.1 × bandwidth limit), ~1000 fs FWHM (uncompressed)
timing jitter to FEL	~ 30 fs rms (~ 15 fs rms with Laser Arrival Monitor [LAM])
pulse energy	0–120 μJ (at interaction region)
polarisation	Linear (s or p)
focus size (1/e ² diameter)	> 50 μm (1/e ²)
peak intensity	10 ¹³ W/cm ² (@50 μm)
time delay to FEL	-1.5 ns to +1.5 ns, larger delays optional
energy stability	< 10% pulse-to-pulse peak (3% rms)
Harmonic generation conversion to 400 nm (SHG) and 266 nm (THG) central wavelength is available with conversion efficiencies of > 10% SHG, > 3% THG, pulse durations are increasing.	

FLASH	Operation period 2024	User beamtime	Machine studies and user experiment preparation	Maintenance	Shutdown
FLASH (Linac)	1 Jan – 31 Dec	1886 h	1888 h	50 h	4960 h
FLASH1	1 Jan – 31 Dec	913 h			
FLASH2	1 Jan – 31 Dec	1325 h			



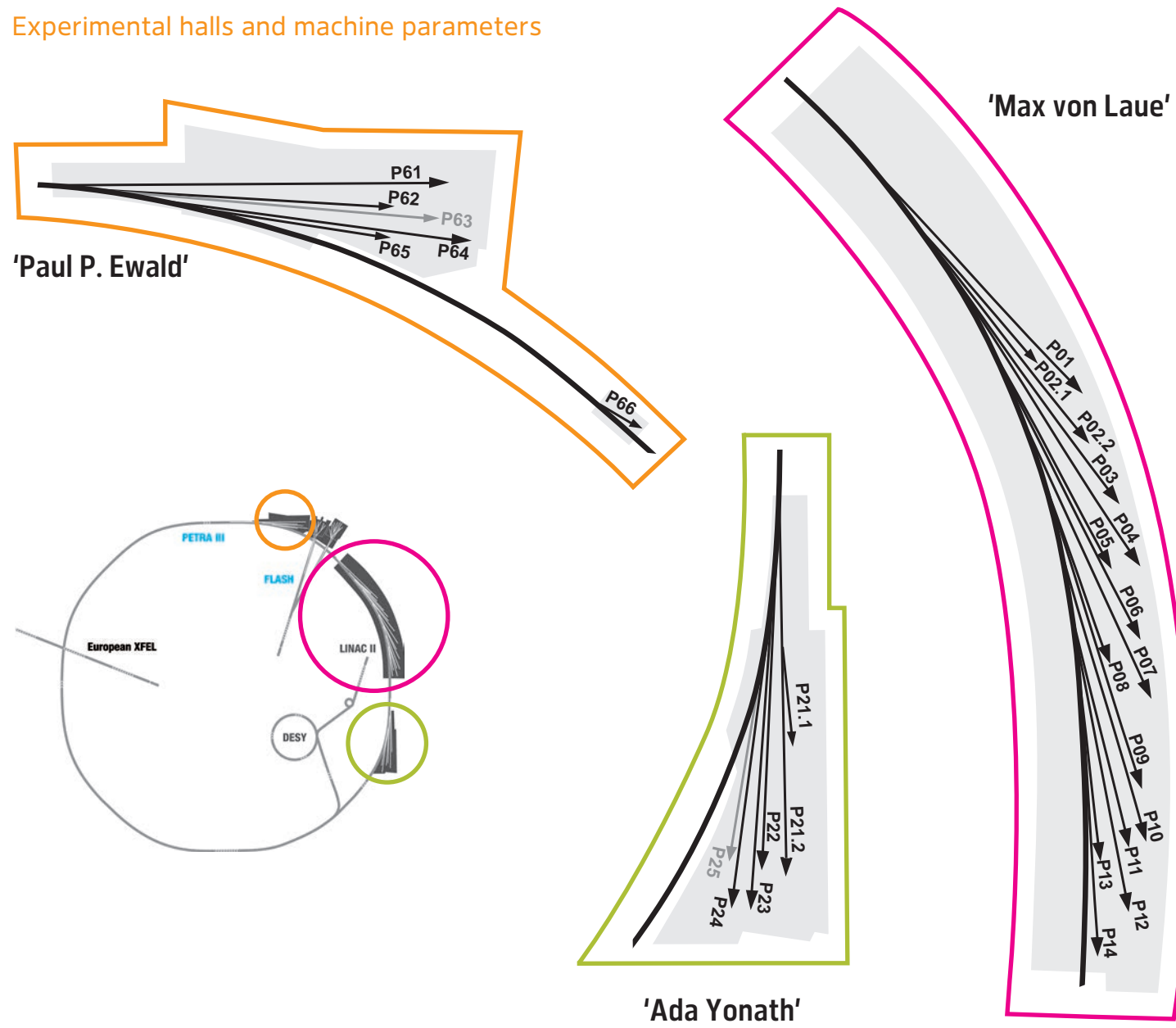
Please note that the machine operation period at FLASH ended on June 9. The second half of 2024 was devoted to the second FLASH2020+ upgrade shutdown (10 June 2024 until 3 August 2025).

Acknowledgement

We would like to acknowledge all contributions to the development and operation of FLASH and PETRA III beamlines and instruments provided within the framework of 'Verbundforschung/ErUM-Pro' of the Federal Ministry of Education and Research (BMBF), and as part of the collaboration 'India@DESY' with the Department of Science and Technology (Government of India).

PETRA III

Experimental halls and machine parameters



PETRA III - machine parameters

Electron energy	6.08 GeV
Circumference of the storage ring	2304 m
Number of bunches	40 (timing mode) 480 (continuous mode)
Bunch separation	192 ns (timing mode) 16 ns (continuous mode)
Electron beam current	100 mA (timing mode) 120 mA (continuous mode)
Horizontal electron beam emittance	1.3 nmrاد
Vertical electron beam emittance	0.01 nmrاد
Electron beam energy spread (rms)	0.1%
Horizontal × vertical beam size (rms) at 5 m undulator (high β section) and 10 keV photon energy	141 μm × 5.2 μm
Horizontal × vertical beam size (rms) at 5 m undulator (low β section) and 10 keV photon energy	36 μm × 5.7 μm

PETRA III

Beamlines

PETRA III experimental hall 'Max von Laue'

Beamline and instruments	Operated by
R — option for remote user operation M — option for mail-in service rolling — submission of proposals at any time under the rolling access scheme	
P01 High Resolution Dynamics 10 m U36 2.5–80 keV	DESY
Nuclear resonant scattering	DESY
Resonant inelastic X-ray scattering	DESY MPI
X-ray Raman scattering	DESY MPI
P02.1 Powder Diffraction and Total Scattering 2 m U23 60 keV	DESY
M Standard and <i>in situ</i> powder diffraction	DESY
M Standard and <i>in situ</i> total scattering	DESY
P02.2 Extreme Conditions 2 m U23 25.6 keV, 42.7 keV	DESY
R Laser heated experiment for diamond anvil cells (DACs)	DESY
R General purpose experiment for high pressure DAC applications	DESY
P03 Micro- and Nano-SAXS/WAXS 2 m U29 7–21 keV	DESY
Grazing incidence and transmission micro-beam small and wide-angle scattering	DESY
Nano-beam scattering and diffraction	DESY Hereon collaborators
P04 Variable Polarisation Soft X-rays 5 m UE65 250–2800 eV	DESY
UHV diffractometer and soft X-ray spectrometer	DESY collaborators
Photon-ion spectrometer (PIPE)	DESY collaborators
Ultra-high resolution angular resolved photoelectron spectroscopy (solids & liquids)	DESY collaborators
Soft X-ray absorption holographic imaging instrument	DESY collaborators
P05 Micro- and Nanoimaging 2 m U29 8–50 keV	Hereon
M Microtomography	Hereon
Nanotomography	Hereon
P06 Hard X-ray Micro- and Nanoprobe 2 m U32 5–45 keV	DESY
Microprobe	DESY
Nanoprobe	DESY
P07 High Energy X-ray Materials Science 4 m IVU21 50–200 keV	Hereon
Surface diffraction, grazing incidence total scattering, diffraction tomography	DESY
Heavy-load diffractometer	Hereon
Grain mapper	Hereon
High energy tomography	Hereon
P08 High Resolution Diffraction rolling 2 m U29 5.4–29.4 keV	DESY
M High resolution diffractometer	DESY
Liquid surface diffractometer	DESY collaborators
Langmuir trough in-plane diffractometer	DESY
P09 Resonant Diffraction / HiPhax 2 m U32 2.7–24 keV / 16 keV	DESY
Resonant X-ray diffraction at low temperatures (2 K < T < 750 K)	DESY
Resonant X-ray diffraction in high B-fields (2 K < T < 300 K; B < 14 T, B ⊥ Q)	DESY
Resonant X-ray diffraction at high pressure (4 K < T < 300 K; p < 30 GPa)	DESY
High-throughput Pharmaceutical X-ray screening (HIPHAX)	DESY
P10 Coherence Applications 5 m U32 4–20 keV	DESY
R X-ray photon correlation spectroscopy (SAXS/WAXS geometry) (5–15 keV)	DESY
R Bragg coherent diffraction imaging (5–13 keV)	DESY
R GINIX — Nanofocusing setup (8 and 13.8 keV)	DESY collaborators
P11 High-throughput Macromolecular Crystallography rolling 2 m U32 2.4–30 keV	DESY
R, M Macromolecular crystallography (6–26 keV)	DESY HZI Univ. Lübeck
M Serial crystallography (6–26 keV)	DESY

PETRA III

Beamlines

PETRA III experimental hall 'Max von Laue'

Beamline and instruments	Operated by
R — option for remote user operation M — option for mail-in service rolling — submission of proposals only under the rolling access scheme	
P12 Bio SAXS 2 m U29 4–20 keV	EMBL
R Small-angle and wide-angle X-ray scattering	EMBL
Time-resolved X-ray scattering	EMBL
Anomalous small-angle X-ray scattering	EMBL
P13 Macromolecular Crystallography 2 m U29 4.5–17.5 keV	EMBL
R Macromolecular crystallography	EMBL
P14 Macromolecular Crystallography and Imaging 2 m U29 6–32 keV	EMBL
R Macromolecular crystallography (7–27 keV)	EMBL
R Serial crystallography (7–18 keV)	EMBL
High throughput micro-tomography (6–32 keV)	EMBL
Time-resolved serial crystallography (12.7 keV)	EMBL U Hamburg

PETRA III experimental hall 'Ada Yonath'

Beamline and instruments	Operated by
R — option for remote user operation M — option for mail-in service rolling — submission of proposals only under the rolling access scheme	
P21.1 High-Energy Diffraction for Physics & Chemistry at the Swedish Beamline side branch: 2 m U29 54 keV, 88 keV, 102 keV	Center for X-rays in Swedish Materials Science (CeXS) DESY
Single crystal diffuse scattering and 3d- Δ PDF	CeXS DESY
Total scattering (transmission and grazing incidence)	CeXS DESY
P21.2 Swedish Materials Science Beamline 4 m IVU21 40–150 keV	Center for X-rays in Swedish Materials Science (CeXS) DESY
Wide-angle scattering (bulk and surface, grain resolved and averaged)	CeXS DESY
Small-angle-scattering (bulk and surface, grain resolved and averaged)	CeXS DESY
Imaging (CT and radiography)	CeXS DESY
P22 Hard X-ray Photoelectron Spectroscopy rolling 2 m U33 2.4–15 keV	DESY
R Hard X-ray photoelectron spectrometer (HAXPES)	DESY
Ambient pressure XPS (POLARIS)	DESY collaborators
Hard X-ray photoemission electron microscope (HAXPEEM)	DESY collaborators
R Hard X-Ray momentum microscope (HarMoMic)	DESY
P23 <i>In situ</i> Nanodiffraction Beamline rolling 2 m U32 5–35 keV	DESY
XRD and secondary processes, <i>in situ</i> and complex environments	DESY
Hierarchical X-ray imaging	KIT DESY
P24 Chemical Crystallography rolling 2 m U29 8 keV, 15–44 keV	DESY
Single crystal diffraction in complex sample environments	DESY
Small molecule crystallography	DESY
P25 Beamline for applied biomedical imaging, powder diffraction and innovation 2m U32 8–60 keV	DESY - ITT Start of operation planned for 2025
X-ray fluorescence imaging (milliprobe) (XFI)	DESY U Hamburg
Scanning X-ray microscopy (SAXM)	DESY
High throughput powder diffraction (15–35 keV)	DESY
PETRA IV test station (white beam)	DESY

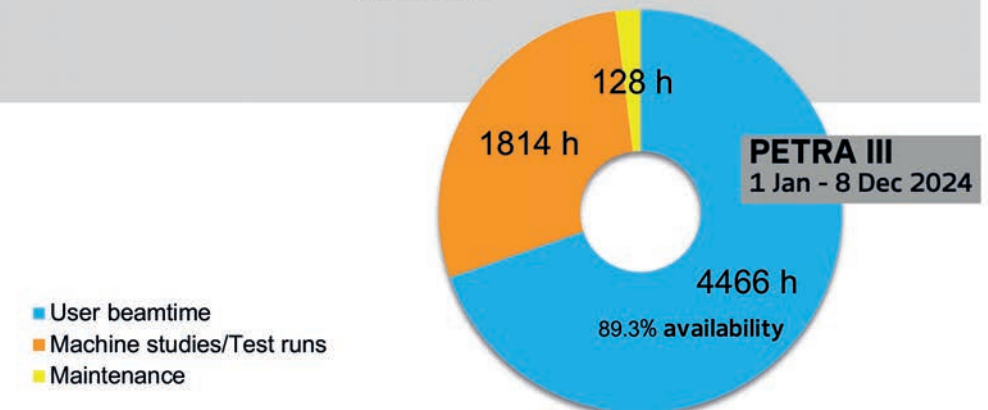
PETRA III experimental hall 'Paul P. Ewald'

Beamline and instruments	Operated by
R — option for remote user operation M — option for mail-in service rolling — submission of proposals only under the rolling access scheme	
P61 High Energy Wiggler Beamline 10 × 4 m damping wigglers white beam btw. 30–250 keV	DESY
High energy engineering materials science	Hereon
Large volume press — extreme conditions	DESY
P62 Anomalous Small-Angle X-ray Scattering 2 m U32 3.5–35 keV	DESY
Anomalous small-angle X-ray scattering	DESY
SAXS tomography	DESY
P63 Material Science Beamline	DESY MPI Start of operation: not yet defined
<i>Ex situ</i> and <i>in situ</i> XAFS with simultaneous scattering and diffraction	
P64 Advanced X-ray Absorption Spectroscopy 2 m U33 4–44 keV	DESY
<i>Ex situ</i> and <i>in-situ</i> XAFS	DESY
High-resolution X-ray emission spectroscopy (non-resonant and resonant)	DESY
QEXAFS	DESY
P65 Applied X-ray Absorption Spectroscopy 41 cm U33 4–44 keV	DESY
<i>Ex situ</i> and <i>in situ</i> XAFS of bulk samples	DESY
P66 Superlumi (between PETRA III halls 'Paul P. Ewald' and 'Max von Laue') Bending magnet 4–40 eV	DESY
Time-resolved luminescence spectroscopy	DESY

PETRA beamtime statistics 2024

PETRA III Operation period 2024				
	User beamtime	Machine studies and test runs	Maintenance	Shutdown
1 Jan – 8 Dec	4466 h thereof 504 h with only 70mA	1814 h	128 h	1824 h
9 Dec – 31 Dec (planned)	223 h	113 h thereof 96 h compensation for down-time DESY II after fire	7 h	209 h

User run periods:
23 Feb – 31 July
2 Sep – 18 Dec



Instruments	Operated by
Sample preparation (CXNS, ground floor, laboratory 006a and 006b)	DESY
2 UHV sample preparation chambers	DESY
Low energy electron diffraction	DESY
Zn evaporation chamber	DESY
Auger electron spectroscopy	DESY
UHV multi flange tunnel chamber	DESY
Surface spectroscopy (CXNS, ground floor, laboratory 006a and 006b)	DESY
UHV Infrared reflection absorption spectroscopy (IRRAS)	DESY
X-ray photoelectron spectroscopy (XPS)	DESY
Ultraviolet photoelectron spectroscopy (UPS)	DESY
X-ray diffraction (building 25, laboratory 023)	DESY
UFO chamber, 2 mini reactors, 2 gas mixer	DESY
2 <i>in situ</i> UHV chambers	DESY
Reflectometer	DESY
2 six-circle diffractometers	DESY
Microscopy and nanomanipulation (CXNS, ground floor, laboratories 001-004, 006a PETRA III experimental hall 'Max von Laue', 47c, laboratory L096)	DESY
Scanning Auger microscope (SAM)	DESY
Dual-beam focused ion beam (FIB-SEM)	DESY Univ. Bayreuth
High-resolution scanning electron microscope (HR-SEM)	DESY
Versatile high-resolution atomic force microscope (AFM)	DESY
UHV scanning tunnelling / atomic force microscope (UHV-STM/AFM)	DESY
Optical polarisation microscope	DESY
Surface optical reflectance microscope (SOR)	DESY
Sputter coater	DESY
Physical and magnetic sample characterisation (CXNS, ground floor, laboratories 014 and 015)	DESY
Superconducting magnet	DESY
Sample cryostat	DESY
Vibrating sample magnetometer	DESY
AC susceptibility	DESY
AC and DC resistivity and Hall effect	DESY
AC calorimetry	DESY
Thermal transport	DESY
Magnetic microscopy	DESY
Electrocatalysis and electrochemistry (building 25b, laboratory 027)	DESY
Rotating disc electrode surface X-ray diffraction setup	DESY
Combined infrared X-ray diffraction setup	DESY FAU Erlangen-Nürnberg
Hanging meniscus cell, flow cell	DESY
Langmuir trough	DESY CAU Kiel

Committees 2024

Photon Science Committee PSC — advises the DESY Photon Science management

Christian David (Chair)	Paul Scherrer Institut, Villigen, CH
Stefan Eisebitt (Vice Chair)	MBI and Technische Universität Berlin, DE
Serena DeBeer	MPI-CEC, Mülheim an der Ruhr, DE
Kristina Djinovic-Carugo	Universität Wien, AT
Jan-Dierk Grunwaldt	Karlsruher Institut für Technologie, Karlsruhe, DE
Mark Heron	Diamond Light Source Ltd, Didcot, UK
Simo Huotari	University of Helsinki, FI
Oxana Klementieva	Lund University, SE
Sarah Köster	Georg-August-Universität Göttingen, DE
Michael Krisch	ESRF, Grenoble, FR
Jan Lüning	Helmholtz-Zentrum Berlin, DE
Thomas Pfeifer	MPI for Nuclear Physics, Heidelberg, DE
Daniela Rupp	Eidgenössische Technische Hochschule Zürich, CH
Bernd Schmitt	Paul Scherrer Institut, Villigen, CH
Thomas Schröder	Humboldt-Universität zu Berlin and IKZ, Berlin, DE
Andrea Somogyi	Synchrotron SOLEIL, Saint-Aubin, FR
Stefan Vogt	Argonne National Laboratory, Lemont, US
Olga Vybornova, Hermann Franz (PSC Secretaries)	DESY, Hamburg, DE

Laser Advisory Committee LAC — advises DESY and European XFEL

Thomas Dekorsy (Chair)	Deutsches Zentrum für Luft- und Raumfahrt e.V., Stuttgart, DE
Jake Bromage	University of Rochester, USA
Miltcho Danailov	Elettra-Sincrotrone, Trieste, IT
Joseph Robinson	SLAC National Accelerator Laboratory, USA)
Clara Saraceno	Ruhr-Universität Bochum, DE
Emma Springate	STFC Rutherford Appleton Laboratory, US
Caterina Vozzi	Politecnico di Milano, Italy
Jörg Hallmann (LAC Secretary)	European XFEL, Schenefeld, DE
Karolin Baev (LAC Secretary)	DESY, Hamburg, DE

DESY Photon Science User Committee DPS-UC — represents the DESY Photon Science user community

Peter Müller-Buschbaum (Chair)	Technische Universität München, DE
Natalia Dubrovinskaia	Universität Bayreuth, DE
Hermann Duerr	Uppsala Universitet, SE
Julia Herzen	Technische Universität München, DE
Gregor Witte	Ludwig-Maximilians-Universität München, DE

Komitee Forschung mit Synchrotronstrahlung KFS — represents the German SR and FEL user community

Christian Gutt (Chair)	Universität Siegen, DE
Birgit Kanngießer (Vice Chair)	Technische Universität Berlin, DE
Jan-Dierk Grunwaldt	Karlsruher Institut für Technologie, Karlsruhe, DE
Bernd Hinrichsen	BASF SE, Ludwigshafen, DE
Dorota Kozej	Universität Hamburg, DE
Taisia Gorkhova	Universität Hamburg, DE
Martina Müller	Universität Konstanz, DE
Bridget Murphy	Christian-Albrechts-Universität zu Kiel, DE
Andrea Thorn	Universität Hamburg, DE

The European Synchrotron and FEL User Organisation ESUO (Executive Board)

Cormac McGuinness (ESUO President)	Trinity College Dublin, IRL
Carla Bittencourt	Université de Mons, BE
Wojciech Gawelda	Universidad Autónoma de Madrid, ES
Tom P. Hase	University of Warwick, UK
Rainer Lechner	Montanuniversität Leoben, AT
Derek Logan	Lund University, SE
Bridget Murphy	Christian-Albrechts-Universität zu Kiel, DE
Moniek Tromp	Rijksuniversiteit Groningen, NL

For national delegates please see: www.esuo.eu/user-representation/user-delegates-representatives/

Project Review Panels 2024

Bulk and surface diffraction

Rolling access — P08 | P23 | P24

Volodymyr Bon	Technische Universität Dresden, DE
Wuge Briscoe	University of Bristol, UK
Diane Dickie	University of Virginia, Charlottesville, US
Michal Dusek	Czech Academy of Sciences, Prague, CZ
Jan Ingo Flege	Brandenburgische Tech. Univ. Cottbus-Senftenberg, DE
Joerg Grenzer	Helmholtz-Zentrum Dresden-Rossendorf, DE
Yvonne Grunder	University of Liverpool, UK
Richard Harvey	Universität Wien, AT
Alexander Hinderhofer	Universität Tübingen, DE
Vladimir Kaganer	Paul-Drude-Institut für Festkörperelektronik, Berlin, DE
Bärbel Krause	Karlsruher Institut für Technologie, Karlsruhe, DE
SoHyun Park	Ludwig-Maximilians-Universität München, DE
Paul Raithby	University of Bath, Bath, UK
Carsten Richter	Leibniz-Institut für Kristallzüchtung, Berlin, DE
Aleksandr Virovets	Goethe-Universität Frankfurt am Main, Frankfurt, DE
Florian Bertram, Dimitri Novikov, Martin Tolkiehn (PRP Secretaries)	DESY, Hamburg, DE

Coherent applications

P10

Giacomo Baldi	Università di Trento, IT
Martin Bech	Lunds Universitet, SE
Ralf Busch	Universität des Saarlandes, Saarbrücken, DE
Birgit Hankiewicz	Universität Hamburg, DE
Michael Paulus	Universität Dortmund, DE
Ullrich Pietsch	Universität Siegen, DE
Barbara Ruzicka	Institute for Complex Systems, Roma, IT
Dina Sheyfer	Argonne National Laboratory, Lemont, US
Olivier Thomas	Aix-Marseille Université, Marseille, FR
Michael Sprung, Fabian Westermeier (PRP Secretaries)	DESY, Hamburg, DE

EXAFS

P64 | P65

Giannantonio Cibir	Diamond Light Source, Didcot, UK
Dmitry Doronkin	Karlsruher Institut für Technologie, Karlsruhe, DE
Nina Genz	University of Utrecht, Utrecht, NL
Giorgia Greco	Università di Roma 'La Sapienza', Roma, IT
Konstantin Klementiev	MAX IV Laboratory, Lund, SE
Dorota Koziej	Universität Hamburg, DE
Aleksej Kuzmin	University of Latvia, Riga, LV
Katherine Mazzio	Helmholtz-Zentrum Berlin, Berlin, DE
Dooshaye Moonshiram	Materials Science Institute of Madrid, ES
Christina Roth	Universität Bayreuth, DE
Claudia Schnohr	Universität Leipzig, DE
Roland Schoch	Universität Paderborn, DE
Kajsa Sigfridsson Clauss	MAX IV Laboratory, Lund, SE
Janis Timoshenko	Fritz-Haber-Institut der Max-Planck-Gesellschaft, Berlin, DE
Case van Genuchten	Geological Survey of Denmark and Greenland, København, DK
Andrea Zitolo	Synchrotron SOLEIL, Gif-sur-Yvette, FR
Aleksandr Kalinko, Edmund Welter (PRP Secretaries)	DESY, Hamburg, DE

Extreme conditions

P02.2 | P61 LVP

Eglantine Boulard	Sorbonne Université, Paris, FR
Martin Bremholm	Aarhus University, DK
Silvie Demouchy	Blaise Pascal University, Aubiere Cedex, FR
Lars Ehm	Stony Brook University, Stony Brook, US
Holger Kohlmann	Universität Leipzig, DE
Zuzana Konopkova	European XFEL, Schenefeld, DE
Sergey Lobanov	Helmholtz-Zentrum Potsdam, GFZ, Potsdam, DE
Paolo Lotti	Università degli Studi di Milano Statale, Milano, IT
Hauke Marquardt	University of Oxford, UK
Sergey Medvedev	MPI für Chemische Physik fester Stoffe, Dresden, DE
Bjoern Winkler	Goethe-Universität Frankfurt am Main, DE
Hanns-Peter Liermann, Robert Farla (PRP Secretaries)	DESY, Hamburg, DE

HAXPES

Rolling access — P22

Sara Blomberg	Lunds Universitet, SE
Francesco Borgatti	CNR, Istituto per la Studio dei Materiali Nanostrutturati, Bologna, IT
Felix Gunkel	Forschungszentrum Jülich GmbH, Jülich, DE
Maria Hahlin	Uppsala Universitet, Uppsala, SE
Andreas Lindblad	Uppsala Universitet, Uppsala, SE
Martina Müller	Universität Konstanz, DE
Slavomir Nemsak	Forschungszentrum Jülich GmbH, DE
Christoph Rameshan	Montanuniversität Leoben, AT
Anna Regoutz	University College London, GB
Frederik Schiller	Centro de Fisica de Materiales, Donostia - San Sebastian, ES
Michael Sing	Universität Würzburg, DE
Yasumasa Takagi	Japan Synchrotron Radiation Research Institute, Hyogo, JP
Christoph Schlueter (PRP Secretary)	DESY, Hamburg, DE

High energy diffraction

P07 (DESY) | P21.1 | P21.2

Frauke Alves	Georg-August-Universität, Göttingen, DE
Elizabeth Blackburn	Lund University, SE
Olaf Borkiewicz	Argonne National Laboratory, Lemont, US
Peter Broekmann	Universität Bern, CH
Per-Anders Carlsson	Chalmers Tekniska Högskola, Gothenborg, SE
Magnus Colliander	Chalmers Tekniska Högskola, Gothenborg, SE
Margit Fabian	Centre for Energy Research, MTA, Budapest, HU
Jens Gibmeier	Karlsruher Institut für Technologie, Karlsruhe, DE
Julia Herzen	Technische Universität München, Garching, DE
Nina Lock	Aarhus University, DK
Lindsay Richard Merte	Malmoe University SE
Matt Miller	Cornell University, Ithaca, US
Tobias Ritschel	Technische Universität Dresden, DE
Larissa Veiga	Diamond Light Source, Didcot, UK
Ann-Christin Dippel, Martin von Zimmermann, Ulrich Lienert (PRP Secretaries)	DESY, Hamburg, DE

Project Review Panels 2024

Imaging	P05 P06
Matthias Alfeld	Delft University of Technology, NL
Ulrike Boesenberg	European XFEL, Schenefeld, DE
Asuncion Carmona	Centre d'Etudes Nucléaires de Bordeaux Gradignan, FR
Fabien Chauveau	Lyon Neuroscience Research Center, Bron, FR
David Fenning	University of California, San Diego, US
Michael Heethoff	Technische Universität Darmstadt, DE
Sebastian Kalbfleisch	MAX IV Laboratory, Lund, SE
Andrew Kiss	Brookhaven National Laboratory, Upton, US
Ute Kraemer	Ruhr-Universität Bochum, DE
Florian Meirer	University of Utrecht, NL
Bert Mueller	Universität Basel, Allschwil, CH
Guillermo Requena	Rheinisch-Westfälische Technische Hochschule (RWTH) Aachen, DE
Roberto Terzano	Università degli studi di Bari, IT
Ulrich Vogt	Royal Institute of Technology, Stockholm, SE
Benjamin Wipfler	Zool. Forschungsmuseum Alexander Koenig, Bonn, DE
Fabian Wilde; Gerald Falkenberg (PRP Secretaries)	Helmholtz-Zentrum Hereon, Geesthacht; DESY, Hamburg, DE

Inelastic, magnetic and resonant scattering	P01 P09
Manuel Angst	Forschungszentrum Jülich GmbH, DE
Ilya Kupenko	European Synchrotron Radiation Facility, Grenoble, FR
Kristina Kvashnina	Helmholtz-Zentrum Dresden-Rossendorf, DE
Lars Lauterbach	Rheinisch-Westfälische Technische Hochschule, Aachen, DE
Catherine McCammon	Universität Bayreuth, DE
Daniel Merkel	Wigner Research Centre for Physics, Budapest, HU
Matteo Minola	Max Planck Institute for Solid State Research, Stuttgart, DE
Volker Schünemann	Technische Universität Kaiserslautern, DE
Joachim von Zanthier	Friedrich-Alexander-Universität Erlangen-Nürnberg, DE
Jonathan White	Paul Scherrer Institut, Villigen, CH
Ilya Sergeev, Sonia Francoual (PRP Secretaries)	DESY, Hamburg, DE

Materials science (Hereon)	P07 (Hereon) P61 (Hereon)
Jeremy Epp	Leibniz-IWT, Bremen, DE
Guillaume Geandier	Institut Jean Lamour, Nancy, FR
Julia Herzen	Technische Universität München, DE
Christian Krempaszky	Technische Universität München, DE
Ingo Manke	Helmholtz Zentrum Berlin für Materialien und Energie, Berlin, DE
Georg Schulz	Universität Basel, CH
Carsten Siemers	Technische Universität Braunschweig, DE
Petra Spoerk-Erdely	Graz University of Technology, AT
Dieter Lott (PRP Secretary)	Helmholtz-Zentrum Hereon, Geesthacht, DE

Powder diffraction	P02.1
Jozef Bednarcik	P.J. Safarik University, Košice, SK
Dorthe Bomholdt Ravnsbæk	Aarhus Universitet, Aarhus, DK
Robert Dinnebier	MPI für Festkörperforschung, Stuttgart, DE
Bernd Hinrichsen	BASF SE, Ludwigshafen, DE
Manuel Hinterstein	Karlsruher Institut für Technologie (KIT), Karlsruhe, DE
Kirsten Marie Jensen	Københavns Universitet, København, DK
Gregor Kieslich	Technische Universität München, Garching, DE
Michael Knapp	Karlsruher Institut für Technologie, Karlsruhe, DE
Daria Mikhailova	Leibniz-Institut f. Festkörper- und Werkstoffforschung Dresden, DE
Anatoliy Senyshyn	Technische Universität München, Garching, DE
Florian Spieckermann	Montanuniversität Leoben, AT
Claudia Weidenthaler	MPI für Kohlenforschung, Mülheim a.d. Ruhr, DE
Irmgard Weissensteiner	Montanuniversität Leoben, AU
Martin Etter (PRP Secretary)	DESY, Hamburg, DE

SAXS/WAXS/GISAXS	P03 P62
Jens Wenzel Andreasen	Danmarks Tekniske Universit, Roskilde, DK
Sabrina Disch	Universität Duisburg-Essen, DE
Marios Georgiadis	Stanford University, US
Ajay Gupta	University of Petroleum and Energy Studies, Dehradun, IN
Eva Herzig	Universität Bayreuth, DE
Tobias Kraus	Leibniz-Institut für Neue Materialien, Saarbrücken, DE
Rainer T. Lechner	Montanuniversität Leoben, AT
Eva Malmstroem	KTH Royal Institute of Technology, Stockholm, SE
Simone Mascotto	Universität Koblenz, DE
Peter Šiffalovič	Institute of Physics, Bratislava, SK
Qi Zhong	Zhejiang Sci-Tech University, Hangzhou, CN
Sarathlal Koyiloth Vayalil, Sylvio Haas (PRP Secretaries)	DESY, Hamburg, DE

Soft X-ray and VUV	P04 P66
Paola Bolognesi	CNR-ISM, Istituto di Struttura della Materia, Roma, IT
Sergey Borisenko	Leibniz-Institut für Festkörper- und Werkstoffforschung, Dresden, DE
Felix Buettner	Universität Augsburg, DE
Raimund Feifel	Göteborgs Universitet, SE
Jochen Geck	Technische Universität Dresden, DE
Nils Huse	Universität Hamburg, DE
Timo Kuschel	Universität Bielefeld, DE
Aleksandr Luštšik	University of Tartu, EE
Yasmine Sassa	Chalmers Tekniska Högskola, Gothenborg, SE
Anna Vedda	Università di Milano-Bicocca, Milano, IT
Moritz Hoesch, Aleksei Kotlov (PRP Secretaries)	DESY, Hamburg, DE

Soft X-ray FEL experiments	FLASH
Majed Chergui	École Polytechnique Fédérale de Lausanne, CH
Hermann Dürr	Uppsala Universitet, Uppsala, SE
Irene Groot	Universiteit Leiden, NL
Marion Harmand	Sorbonne Université, Paris, FR
Michael Meyer	European XFEL, Schenefeld, DE
Kevin Prince	Elettra-Sincrotrone Trieste, IT
Christian Schüssler-Langeheine	Helmholtz-Zentrum Berlin, DE
Marc Simon	Sorbonne Université, Paris, FR
Julia Stähler	Humboldt-Universität zu Berlin, DE
Elke Plönjes-Palm, Rolf Treusch (PRP Secretaries)	DESY, Hamburg, DE

PEC EMBL Life Science beamlines P12-P14 PRP Macromolecular Crystallography at P11 — Rolling access	
Pau Bernadó	CBS/CNRS, Montpellier, FR
Gwyndaf Evans	Diamond Light Source, Didcot, GB
Robert Fischetti	Argonne National Laboratory, US
Sebastian Glatt	Jagiellonian University Krakow, PL
Gergely Katona	University of Gothenburg, SE
Annette E. Langkilde	University of Copenhagen, DK
Andrea Mattevi	University of Pavia, IT
Javier Pérez	Synchrotron SOLEIL, Saint-Aubin, FR
Teresa Santos-Silva	Universidade NOVA de Lisboa, PT
Zehra Sayers	Sabancı University, Istanbul, TR
Thomas Lykke-Møller Sørensen	Aarhus University, Denmark
Norbert Sträter	Leipzig University, Germany
Joel L. Sussman	Weizmann Institute of Sciences, Rehovot, IL
Giedrė Tamulaitienė	Vilnius University, LT
Giuliana Tromba	Elettra-Sincrotrone Trieste, IT
Maria A. Vanoni	Università degli Studi di Milano, IT
Mark J. van Raaij	Centro Nacional de Biotecnología, Madrid, ES
Gregor Witte	Ludwig-Maximilians-Universität München, DE
Christian Schroer (DESY observer)	DESY, Hamburg, DE

Photographs and Graphics

Anton Davydok, Hereon
Attosecond Group, CFEL, DESY
Benjamin Motyka
CFEL
Christina Mänz, DESY
CMWS
CSSB
DASHH
DESY
Diana von Ilsemann, DESY
EMBL
European XFEL

Guilherme Abreu Faria, Hereon
Helmholtz-Zentrum Hereon
Jörg M. Harms, MPSD
Kevin Winkler, PHGS
Laila Tkotz, KIT
Lars Berg, DESY
Marlovits Group/CSSB
Marta Mayer, DESY
Massimo Del Prete/EMBL
Miriam Huckschlag, DESY
MPG
Nicoletta Calegari

pbr/nh studio
Reimo Schaaf, Hamburg
Robin Santra, DESY CFEL
Science Communication Lab, DESY
Sebastian Fava, MPSD
Shandana Mufti, LINXS
Sonja Smalian, PhoenixD
Susann Niedworok, DESY
Sylvio Haas, DESY
UKE
University of Hamburg

Acknowledgement

We would like to thank all authors and all who have contributed to the realisation of this Annual Report.

Imprint

Publishing and Contact:

Deutsches Elektronen-Synchrotron DESY
A Research Centre of the Helmholtz Association

Hamburg location:
Notkestr. 85, 22607 Hamburg, Germany
Tel.: +49 40 8998-0, Fax: +49 40 8998-3282
desyinfo@desy.de

Zeuthen location:
Platanenallee 6, 15738 Zeuthen, Germany
Tel.: +49 33762 7-70, Fax: +49 33762 7-7413

Photon Science at DESY
Tel.: +49 40 8998-2304, Fax: +49 40 8998-4475
photon-science@desy.de
photon-science.desy.de

www.desy.de

ISBN 978-3-945931-54-7
DOI 10.3204/PUBDB-2024-06624

Online version:

photon-science.desy.de/annual_report



Realisation:

Wiebke Laasch, Daniela Unger

Editing:

Sadia Bari, Krishnayan Basuroy, Lars Bocklage,
Christina Bömer, Günter Brenner, Ulrike Frühling, Claudia Goy,
Thomas Keller, Dmytro Kutnyakhov, Wiebke Laasch,
Britta Niemann, Christoph Schlueter, Sang-Kil Son,
Sebastian Trippel, Daniela Unger, Olga Vybornova

Layout: Sabine Kuhls-Dawideit, Büro für Grafik und Design,
Halstenbek

Printing and image processing: EHS Druck GmbH, Schenefeld

Copy deadline: December 2024

Reproduction including extracts is permitted subject
to crediting the source.

HELMHOLTZ

Deutsches Elektronen-Synchrotron DESY
A Research Centre of the Helmholtz Association

Helmholtz contributes to solving major challenges facing society, science and the economy through top-level scientific achievements in six research fields: Energy, Earth and Environment, Health, Information, Matter as well as Aeronautics, Space and Transport. With about 46 000 employees at 18 research centres and an annual budget of more than 6 billion euros, Helmholtz is Germany's largest scientific organisation. Its work is rooted in the tradition of the great natural scientist Hermann von Helmholtz (1821-1894).

www.helmholtz.de